

**PREPARATION AND CHARACTERIZATION OF ZIRCONIA
COATINGS ON STAINLESS STEEL DEVELOPED BY
HYDROTHERMAL PROCESS**

By

NIDHI GARG
(CHEM01201104021)

BHABHA ATOMIC RESEARCH CENTRE
Mumbai

*A thesis submitted to the
Board of Studies in Chemical Science Discipline*

*In partial fulfillment of requirements
For the Degree of*

DOCTOR OF PHILOSOPHY
of
HOMI BHABHA NATIONAL INSTITUTE

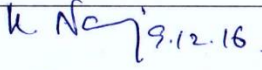


October, 2015

Homi Bhabha National Institute

Recommendations of the Viva Voce Committee

As members of the Viva Voce Committee, we certify that we have read the dissertation prepared by Nidhi Garg entitled “**Preparation and characterization of zirconia coatings on stainless steel developed by hydrothermal process**” and recommend that it may be accepted as fulfilling the thesis requirement for the award of Degree of Doctor of Philosophy.

Chairman- Dr. K. Nagarajan		Date	09-12-2016
Guide/Convener- Dr. S. Velmurugan		Date	09-12-2016
Examiner- Prof. V. S. Raja		Date	09-12-2016
Member 1- Dr. S. Rangarajan		Date	09-12-2016
Member 2- Dr. Santanu Bera		Date	09-12-2016

Final approval and acceptance of this thesis is contingent upon the candidate's submission of the final copies of the thesis to HBNI.

I hereby certify that I have read this thesis prepared under my direction and recommend that it may be accepted as fulfilling the thesis requirement.

Date: 09/12/16

Place: Kalpakkam


Guide

डॉ. एस. वेल्लुमुगन / Dr. S. VELMURUGAN
अध्यक्ष, ज.भा.रा.प्र. / Head, WSCD
भापअके सुविधाएँ / BARC Facilities
कल्पाक्कम / Kalpakkam-603 102.

STATEMENT BY AUTHOR

This dissertation has been submitted in partial fulfillment of requirements for an advanced degree at Homi Bhabha National Institute (HBNI) and is deposited in the Library to be made available to borrowers under rules of the HBNI.

Brief quotations from this dissertation are allowable without special permission, provided that accurate acknowledgement of source is made. Requests for permission for extended quotation from or reproduction of this manuscript in whole or in part may be granted by the Competent Authority of HBNI when in his or her judgment the proposed use of the material is in the interests of scholarship. In all other instances, however, permission must be obtained from the author.

Nidhi Garg

DECLARATION

I, hereby declare that the investigation presented in the thesis has been carried out by me. The work is original and has not been submitted earlier as a whole or in part for a degree / diploma at this or any other Institution / University.

Nidhi Garg

List of Publications arising from the thesis

Journal

1. "Preparation and characterization of tetragonal dominant nanocrystalline ZrO₂ obtained via direct precipitation", **Nidhi Garg**, Vinit K. Mittal, Santanu Bera, Arup Dasgupta, S. Velmurugan, Ceramic International, **2012**, 38, 2507-2512.
2. "Role of chemical composition of oxide layer on stainless steel for ZrO₂ coating by hydrothermal process", **Nidhi Garg**, Vinit K Mittal, Santanu Bera, P. Chandramohan, C.R. Das, S. Velmurugan, Thin Solid Films, **2013**, 545, 222-228.
3. "Study of Fe₂O₃-ZrO₂ interface of ZrO₂ coating grown by hydrothermal process on stainless steel", **Nidhi Garg**, Santanu Bera, G. Mangamma, Vinit K Mittal, R. Krishnan, S. Velmurugan, Surface and Coatings Technology, **2014**, 258, 597-604.
4. "Electrochemical and adhesion properties of hydrothermally deposited nano-ZrO₂ coatings on oxide layers of stainless steel", **Nidhi Garg**, Santanu Bera, G. Mangamma, C.R. Das, S. Kamaruddin, S. Velmurugan, Surface and Coatings Technology, **2015**, 281, 98-108.

Conferences

1. **Nidhi Garg**, Vinit K Mittal, Santanu Bera, S. Velmurugan, Adsorption of nano-ZrO₂ on 304L stainless steel in aqueous medium, 56th DAE SSPS-2011, AIP Conf. Proc. 1447 (2012) 735-736.
2. **Nidhi Garg**, Santanu Bera, V.S. Tripathi, Vijay Karki, S. Velmurugan, Optimum thickness evaluation of ZrO₂ coating on type 304L stainless steel for corrosion protection, In Proceedings of the symposium on water chemistry and corrosion in nuclear power plants in Asia-2015. (AWC-2015).

Dedicated

to

My Parents

ACKNOWLEDGEMENTS

I wish to express my deep sense of gratitude and sincere thanks to my research guide **Prof. S. Velmurugan** (Head, Water and Steam Chemistry Division (WSCD), Kalpakkam for his generous inspiration, guidance, encouragement, useful suggestions and good wishes throughout the research tenure. I also thank him for his guidance and for critically reviewing the thesis.

My sincere thanks to **Prof. B. N. Jagatap**, Director, Chemistry Group, BARC for his constant support and encouragement. I am grateful to Doctoral committee chairman **Prof. K. Nagarajan**, former Associate Director, Chemistry Group, IGCAR (currently, Raja Ramanna Fellowship, Kalpakkam) for his encouragement and insightful comments. I would like to thank **Prof. S. Rangarajan** (Section Head, Surface Characterization and Mass Transport Studies Section, WSCD and Member of Doctoral committee) for his guidance in carrying out experiments, valuable discussions and constant encouragement.

It is my great privilege to acknowledge **Dr. Santanu Bera** of WSCD (Member of Doctoral committee) for scrutinizing my entire research work and offered invaluable scientific suggestions during the course of this research work. He spent extensive time on my research work while preparing the thesis and manuscripts for journals. It is a great privilege for me to work with him. Thanks are due to his constant inspiration, legacy towards learning, and keen interest in the subject. I am deeply obliged to his constructive suggestions, meticulous planning, and effective analytic approach.

I would like to extend my warm wishes to **Dr. Vinit K. Mittal** of TWMP, NRB, Tarapur and **T. Saravanan** of WSCD for their help and support in day to day experiments. I must thank **Dr. G. Mangamma**, Materials Science Group, IGCAR for AFM analysis. I also thank **Dr. P.**

Chandramohan, WSCD for his contribution in Raman experiments. I would also want to place on records the help received from **Dr. V. S. Tripathi**, RPCD, BARC, Mumbai and **Mrs. Sumathi Suresh**, WSCD for the electrochemical measurements.

I would like to thank **Mr. T.V.K. Mohan** (Section Head, Engineering Simulation Studies Section) and all the members of the Engineering Group for their cooperation and constant support. I would like to acknowledge **Dr. C.R. Das**, **Dr. Arup Dasgupta** and **Dr. Vani Shankar** of Metallurgy and Materials Group, IGCAR for their contribution in SEM and TEM measurements. I also thank **Dr. P. Gangopadhaya**, **Dr. R. Krishnan**, **Dr. R. Ramaseshan**, **Mrs. D. T. Sunitha**, **P. C. Clinsha** and **N. G. Krishna** of IGCAR for their timely help. I sincerely appreciate the help rendered by **Dr. P. A. Hassan**, **Dr. Gunjan Verma** and **Dr. S. J. Keny** of Chemistry Group, BARC, Mumbai. I wish to express my gratitude to all WSCD staff members for their help in the time of need.

My affectionate thanks to my friends **Molly**, **Usha**, **Sudhir**, **Namrata**, **Bakkiyam**, **Abdul**, **Kiran**, **Debashis**, **Fransis**, **Raghvendra** for their love, affection and encouragements during my Ph.D. I must thank God for giving me a loving and caring family without whose support, encouragements and dedication, I would not be able to complete my PhD. I must thank my father **Shri. Vijender Garg**, mother **Smt. Maya Garg**, brother **Mr. Kapil Garg**, sister **Ms. Sonia Garg** and my husband **Mr. Nitin Garg** for their love, affection, care and support that have made me confident to overcome all the difficulties in life.

CONTENTS

	Page No.
Abstract	i-iii
List of Figures	iv-xi
List of Tables	xii-xiii
List of Abbreviations	xiv-xv
Chapter 1 Introduction	1-28
1.1 Introduction	1
1.2 SCC problem in BWR nuclear reactors	1
<i>1.2.1 The factors responsible for SCC</i>	3
<i>1.2.1.1 Material aspects</i>	4
<i>1.2.1.2 Environmental aspects</i>	6
<i>1.2.1.3 Stress aspects</i>	6
1.3 Methods adopted in past to mitigate SCC problem in BWR	7
<i>1.3.1 Hydrogen water chemistry (HWC)</i>	7
<i>1.3.2 Noble Metal Chemical addition (NMCA)</i>	8
<i>1.3.3 Inhibitive Protective coating (IPC)</i>	9
1.4 Use of zirconia as the coating material	12
1.5 Properties of ZrO ₂	14
1.6 Stabilization of pure tetragonal zirconia polycrystals at room temperature	16
<i>1.6.1 Role of surface energy</i>	16
<i>1.6.2 Role of interfacial and strain energies</i>	17

1.7. Hydrothermal deposition of ZrO ₂ coating on the SS surfaces	18
<i>1.7.1 Importance of hydrothermal deposition for NPPs</i>	18
<i>1.7.2 Hydrothermal deposition process</i>	19
1.8 Aim and scope of the study	20
1.9 References	21
Chapter 2 Materials and Methods	29-63
2.1 Objective of the study	30
2.2 Experimental setup	31
<i>2.2.1 Glassware setup for ZrO₂ nano-particle preparation and deposition</i>	31
<i>2.2.2 Autoclave setup for pre-oxidation of SS and ZrO₂ coatings</i>	31
2.3 Sensitization of SS specimens	32
2.4 Pre-oxidation of the SS surfaces	33
<i>2.4.1 Pre-oxidation of the SS surfaces in static autoclave</i>	33
<i>2.4.1.1 Reducing water chemistry environment</i>	33
<i>2.4.1.2 Oxidizing water chemistry environment</i>	34
<i>2.3.2.3 Oxidizing in H₂O₂ environment</i>	34
<i>2.4.2 Pre-oxidation of the SS surfaces in dynamic loop</i>	34
<i>2.4.3 Pulsed laser deposition (PLD) of α-Fe₂O₃ on SS surfaces</i>	35
<i>2.4.3.1 Target Preparation</i>	35
<i>2.4.3.2 α-Fe₂O₃ thin film deposition on SS surface</i>	36
2.5 Nanocrystalline ZrO ₂ powder preparation	37
2.6 Deposition of ZrO ₂ nanoparticles on pre-oxidized stainless steel in aqueous medium	38

2.7 Hydrothermal deposition of ZrO ₂ using ZrO(NO ₃) ₂ and Na-EDTA	38
2.7.1 Hydrothermal deposition process	38
2.7.2 Preparation of samples to study the mechanism of growth of ZrO ₂ on α-Fe ₂ O ₃	39
2.7.3 ZrO ₂ coating thickness enhancement by hydrothermal deposition process	39
2.7.3.1 By increasing the precursor concentration	39
2.7.3.2 Multiple rounds of ZrO ₂ deposition with the fresh reactants	40
2.8 Thickness measurement of coatings	40
2.8.1 Surface Profilometry	40
2.8.2 Dissolution Method for ZrO ₂ coatings thickness estimation	40
2.8.3 Cross-sectional SEM analysis	42
2.9 Characterization of materials and coatings	42
2.9.1 Optical microscopy	42
2.9.2 Scanning electron microscopy/Energy dispersive x-ray spectroscopy	43
2.9.3 Raman Spectroscopy	43
2.9.4 X-ray Photoelectron Spectroscopy (XPS)	45
2.9.5 X-Ray Diffraction	47
2.9.6 Transmission electron microscopy	48
2.9.7 UV-Vis spectroscopy	50
2.9.8 Zeta potential	50
2.9.9 Atomic Force Microscopy	52
2.9.9.1 Topography Imaging	52

2.9.9.2 Atomic Force Acoustic Microscopy	53
2.9.9.3 Force-distance (FD) spectroscopy	54
2.10 Electrochemical corrosion techniques	55
2.10.1 <i>Electrochemical cell setup</i>	55
2.10.2 <i>Sensitization study</i>	56
2.10.2.1 <i>Oxalic acid etch test</i>	56
2.10.2.2 <i>Double-loop electrochemical potentiokinetic reactivation Test</i>	57
2.10.3 <i>Corrosion resistant properties by electrochemical analysis</i>	58
2.10.3.1 <i>Potentiodynamic polarization</i>	58
2.10.3.2 <i>Electrochemical impedance analysis</i>	59
2.11 References	61
Chapter 3 Pre-oxidation of stainless steel surfaces	64-96
3.1 Introduction	65
3.1.1 <i>SEM</i>	66
3.1.2 <i>Raman Spectroscopy</i>	66
3.1.3 <i>XPS</i>	67
3.1.4 <i>GI-XRD</i>	68
3.1.5 <i>AFM</i>	68
3.2 Pre-oxidation of SS in static autoclave in reducing water chemistry conditions	69
3.2.1 <i>Pre-oxidation for 5 days</i>	69
3.2.2 <i>Pre-oxidation for 21 days</i>	71
3.2.3 <i>Mechanism of oxide film formation</i>	73
3.3 Pre-oxidation of SS in static autoclave under normal water conditions	75

3.3.1	<i>Specimens prepared in 14 days</i>	75
3.3.2	<i>Specimens prepared in 21 days</i>	77
3.3.3	<i>Mechanism of oxide film formation</i>	80
3.4	Pre-oxidation of SS in dynamic autoclave under simulated BWR water chemistry	81
3.4.1	<i>Characterization of specimen</i>	81
3.4.2	<i>Mechanism of oxide film formation</i>	84
3.5	Pulsed laser deposition (PLD) of α -Fe ₂ O ₃ on SS surface	85
3.5.1	<i>Characterization of PL deposited α-Fe₂O₃ films on SS surface</i>	86
3.5.2	<i>Mechanism of PL deposition of α-Fe₂O₃</i>	90
3.6	Conclusions	91
3.7	References	95
Chapter 4 Preparation, characterization and adsorption of nano-ZrO₂ on SS surface		97-118
4.1	Introduction	98
4.2	Preparation and characterization of nanocrystalline ZrO ₂ powder	99
4.2.1	<i>Preparation of ZrO₂ powder</i>	99
4.2.2	<i>Characterization of prepared ZrO₂ powder</i>	99
4.2.2.1	<i>Microstructure and phase analysis by TEM and XRD</i>	99
4.2.2.2	<i>Phase and volume fraction analysis from Raman spectroscopy</i>	103
4.2.2.3	<i>Chemical analysis from X-ray photoelectron spectroscopy</i>	104
4.2.3	<i>The role of chemical conditions during ZrO₂ powder formation</i>	105
4.2.3.1	<i>The role of solvent</i>	105
4.2.3.2	<i>The role of PEG-8000 as surfactant</i>	107

4.2.3.3	<i>Role of $ZrO(NO_3)_2$ as the starting material</i>	107
4.2.3.4	<i>Role of temperature</i>	108
4.2.4	<i>Zeta potential of the zirconia powder in aqueous suspension</i>	109
4.3	Adsorption of nano- ZrO_2 on SS304L in aqueous medium	111
4.3.1	<i>Adsorption of nano-ZrO_2 on SS304L surfaces at room temperature</i>	112
4.3.2	<i>Adsorption of nano-ZrO_2 on SS304L surfaces at 90°C</i>	112
4.3.3	<i>Adsorption of nano-ZrO_2 on SS304L surface at 150°C</i>	114
4.4	Conclusions	116
4.5	References	116
Chapter 5	Development of ZrO_2 coating from zirconyl salt and role of chemical composition of pre-oxidized layer	119-152
5.1	Introduction	120
5.2	Role of chemical composition of oxide layer on stainless steel surface for hydrothermal deposition of ZrO_2 coating	121
5.2.1	<i>Preparation and characterization of the ZrO_2 coatings on pre-oxidized SS surfaces</i>	121
5.2.1.1	<i>SEM-EDX characterization and thickness analysis</i>	122
5.2.1.2	<i>Raman and GI-XRD analysis</i>	124
5.2.1.3	<i>XPS analysis</i>	126
5.2.2	<i>Interaction of ZrO_2 with pre-oxidized SS surfaces</i>	128
5.3	Study of Fe_2O_3 - ZrO_2 interface and mechanism of ZrO_2 coating	130
5.3.1	<i>Preparation of ZrO_2 coated samples at different durations and temperatures</i>	131
5.3.2	<i>Surface Morphology by SEM and AFM</i>	131

5.3.3	<i>Phase Analysis by Raman Spectroscopy and GI-XRD</i>	134
5.3.4	<i>Chemical state analysis by XPS</i>	137
5.3.5	<i>Interaction and growth mechanism of ZrO₂ on the α-Fe₂O₃ surface</i>	142
5.3.5.1	<i>Formation of Na-salt of Zr-EDTA in aqueous solution</i>	143
5.3.5.2	<i>Interaction between α-Fe₂O₃ surfaces with Na salt of Zr-EDTA</i>	144
5.3.5.3	<i>Nucleation and growth of crystalline ZrO₂ coating</i>	146
5.4	Conclusions	148
5.5	References	152
Chapter 6	Electrochemical and adhesion properties of ZrO₂ coatings	153-190
6.1	Introduction	154
6.2	Sensitization of Type 304L stainless steel	155
6.2.1	<i>Oxalic acid etch test</i>	156
6.2.2	<i>DL-EPR Test</i>	157
6.3	Electrochemical studies of sensitized and non-sensitized SS 304L specimens	158
6.3.1	<i>PDP measurements</i>	158
6.3.2	<i>EIS measurements</i>	159
6.4	Pre-oxidation of sensitized SS specimens	161
6.5	Preparation and surface characterization of ZrO ₂ coated samples	162
6.5.1	<i>SEM-EDS results</i>	162
6.5.2	<i>XPS and Raman analysis</i>	164
6.6	Topography and adhesion studies by AFM	166
6.7	Electrochemical studies of zirconia coatings at room temperature	171
6.7.1	<i>Potentiodynamic polarization test</i>	171

6.7.2 <i>Electrochemical Impedance Spectroscopy</i>	174
6.8 Electrochemical studies of zirconia coatings at 90°C	179
6.8.1 <i>Potentiodynamic polarization tests</i>	180
6.8.2 <i>EIS studies</i>	181
6.9 Impact of coating physical properties on adhesion and corrosion resistance	183
6.10 Zirconia coating on SS specimen pre-oxidized in simulated BWR environment	185
6.11 Conclusion	187
6.12 References	188
Chapter 7 Increase of zirconia coating thickness and electrochemical measurements	191-211
7.1 Introduction	192
7.2 ZrO ₂ coating thickness improvement by increasing the precursor concentrations	193
7.2.1 <i>Improvement of ZrO₂ coating thickness on POH-21</i>	193
7.2.1.1 <i>Surface characterization</i>	193
7.2.1.2 <i>Electrochemical studies</i>	195
7.2.2 <i>Improvement of ZrO₂ coating thickness on POO-21</i>	196
7.2.2.1 <i>Surface Characterization</i>	196
7.2.2.2 <i>Electrochemical Characterization</i>	198
7.3 Improvement of ZrO ₂ coating thickness by multiple rounds of ZrO ₂ deposition	200
7.3.1 <i>Surface characterization of Zirconia coated samples</i>	200
7.3.2 <i>Electrochemical studies</i>	203
7.3.2.1 <i>Potentiodynamic polarization test</i>	203
7.3.2.2 <i>EIS studies</i>	204
7.4 Mechanism of film thickening by hydrothermal method	208

7.5 Conclusions	210
7.6 References	211
Chapter 8 Conclusions	212-216
8.1 Conclusions	213
8.2 Future directions	216

Abstract

Stress corrosion cracking (SCC) of the structural components fabricated of type 304/304L/304LN stainless steel (SS) is a critical issue for the structural integrity of boiling water reactors (BWRs). SCC problem is also expected in future advanced heavy water reactors (AHWRs) because of the use of type 304LN SS as the structural material and its coolant water chemistry being similar to BWR. Hydrogen water chemistry (HWC) and noble metal chemical addition (NMCA) are the most widely used techniques for mitigation of SCC in nuclear reactors. But these techniques are not suitable to provide protection at certain locations of structural materials. In addition, HWC technology leads to significant increase of radiation dose in main steam line. To get rid of these drawbacks, inhibitive protective coating of zirconia on SS surface is proposed to mitigate the SCC problem. The insulating nature of the zirconia inhibits the redox reactions at the surface by cutting off the electrical connection between oxidants in water and the metal components. Hydrothermal method is the only applicable method for industrial scale deposition of zirconia on SS surface.

Two methods of zirconia deposition on SS by hydrothermal process are presented in this thesis. The first one is adsorption of nano-zirconia on pre-oxidized SS surfaces. Adsorption of nano-zirconia on pre-oxidized SS surfaces was carried out in aqueous solution at different temperatures. Although this method led to the deposition of nano-zirconia on SS surface, but did not provide a full substrate surface coverage. The second method involves the deposition of zirconia in a static autoclave by using aqueous solution containing $\text{ZrO}(\text{NO}_3)_2 \cdot 6\text{H}_2\text{O}$ salt, Na-EDTA (disodium salt dehydrate) and sodium dodecyl sulphate (SDS). This method was found to

be promising and led to deposition of continuous, tetragonal nano-zirconia coating on pre-oxidized SS surfaces.

Intermediate SS surface oxide layer (also termed as pre-oxidized layer) is necessary to deposit adherent zirconia coating on SS surface. Chemical composition, oxide particle size and morphology of the pre-oxidized SS surface influence the zirconia coating properties like adhesion, continuity and thickness. The pre-oxidized SS specimens with different chemical compositions and surface morphologies are prepared. SS surfaces pre-oxidized in a static autoclave in reducing water chemistry environment showed the formation of spinel oxides like ferrites and chromites. The pre-oxidized SS specimens prepared in static autoclave in normal water showed that the surface oxide layer is composed of rhombohedral oxides like α -Fe₂O₃, α -Fe_{2-x}Cr_xO₃ and spinel oxides. To prepare stoichiometric α -Fe₂O₃ on SS surface, pure α -Fe₂O₃ films were developed on stainless steel surface by pulsed laser deposition technique. Deposited α -Fe₂O₃ particles were spherical and uniform in size. SS surface composed of α -Fe₂O₃ was found to be the most suitable for continuous and thick zirconia coating while the pre-oxidized layer composed of spinel oxides resulted in thin and discontinuous coating.

The mechanism of the growth of zirconia on the most favorable surface oxide (α -Fe₂O₃) has been explored. It is shown that Na salt of Zr-EDTA is formed in the solution prior to the interaction of Zr-precursor with the pre-oxidized surface. Interaction of Na salt of Zr-EDTA with α -Fe₂O₃ surface resulted in the formation of metastable Fe₂O₃-ZrO₂ compositions at around 200°C which provided the suitable interface for the growth of tetragonal ZrO₂ coating. X-ray photoelectron spectroscopy studies established the formation of Fe-O-Zr bonding states at the interface. ZrO₂ particles grew in the form of islands on the α -Fe₂O₃ surface at the initial stage and these islands grew and coalesce to form the continuous and thick coating.

The electrochemical properties of the zirconia coated SS samples have been studied with respect to the pre-oxidized SS specimens and plain SS at different temperatures. The coating developed over spinel oxide surface was porous, discontinuous and could not act as an insulated barrier. Still it showed improvement in the corrosion resistance compared to the uncoated surface. Zirconia coating developed over nano α -Fe₂O₃ showed the best corrosion resistance, lowest porosity and insulating barrier like characteristics. Nano-mechanical properties like adhesion, hardness at nano-scale using atomic force acoustic microscopy and force-distance spectroscopy are discussed. Grains and grain boundaries of the zirconia coating showed the significant impact on corrosion resistance and hardness. The substrate surface morphology plays major role in deciding the adhesion, thickness and compactness of ZrO₂ coatings. Small particle size and hills/valley type morphology of the pulsed laser deposited α -Fe₂O₃ films provide large surface area for interaction with Na salt of Zr-EDTA during the hydrothermal process which improves the adhesion.

Thickness of ZrO₂ coatings are improved by multiple repetitions of hydrothermal deposition process with fresh reactants. Multiple rounds of deposition of ZrO₂ coating on the pre-oxidized SS surface led to the improvement of coating thickness from 200 nm to ~1.2 μ m after four repetitions. Corrosion resistance of the ZrO₂ coated samples at room temperature increased remarkably with the increase in thickness and stabilized after third repetition where coating thickness was around 1 μ m. Electrochemical measurements like potentiodynamic polarization test and electrochemical impedance spectroscopy are used for the optimization of ZrO₂ coating thickness for corrosion resistance applications.

List of Figures

Figure No.	Caption	Page No.
1.1	Critical factors for SCC	4
1.2	Schematic of crack growth in BWR oxidizing environment	11
1.3	Evan diagram of stainless steel specimens before and after IPC treatment [46, 47]. The blue lines (E_{corr1} , I_{corr1}) represent the uncoated specimens while the red lines (E_{corr2} , I_{corr2}) represent the coated SS specimens	12
1.4	Crystal structures of ZrO_2 (a) cubic, (b) tetragonal and (c) monoclinic	15
1.5	Schematic free-energy diagram of monoclinic and tetragonal ZrO_2 nanoparticles	17
2.1	Glassware setup used for experiments below 90°C	31
2.2	Schematic of autoclave setup	32
2.3	Schematic diagram of PL deposition process on the target surface	35
2.4	Raman spectra of α - Fe_2O_3 pallet	36
2.5	Plot of maximum absorbance vs Zr concentration by UV-Vis spectrometer	41
2.6	Roughness distribution curve	53
2.7	Schematics of an electrochemical cell for corrosion study	56
2.8	Schematics of DL-EPR test	57
3.1	AFM micrographs of the (a) Si (100) (b) Plain polished SS	68
3.2	SEM image of the pre-oxidized SS specimen POH-5	70
3.3	Raman spectra the pre-oxidized SS specimen POH-5	70
3.4	XPS wide scan of the POH-5	70

3.5	Micrographs of POH-21 specimen (a) SEM image, (b) AFM topographic image	71
3.6	(a) Raman spectra of POH-21, (b) GI-XRD of the POH-21	72
3.7	XPS wide scan of the POH-21	72
3.8	XPS elemental scan of the POH-21 specimen (a) Fe2p, (b) Cr2p, (c) Ni2p and (d) O1s	73
3.9	SEM image of POO-14	75
3.10	Raman spectra of the specimen POO-14	75
3.11	XPS wide scan of the specimen POO-14	76
3.12	Micrographs of POO-21 specimen (a) SEM image, (b) AFM topographic image	77
3.13	Raman spectra of the pre-oxidized SS specimen POO-21, arrows indicate the signals from α -Fe ₂ O ₃	77
3.14	GI-XRD pattern of the pre-oxidized SS specimen POO-21	78
3.15	XPS wide scan of the pre-oxidized SS specimen POO-21	79
3.16	XPS elemental scan of the pre-oxidized POO-21 SS specimen; (a) Fe2p, (b) Cr2p, (c) Ni2p and (d) O1s	79
3.17	Micrographs of POL specimen (a) SEM image, (b) AFM topographic image	81
3.18	(a) Raman spectra (b) GI-XRD of the pre-oxidized SS specimen POL	82
3.19	XPS wide scan of the pre-oxidized SS specimen POL	83
3.20	XPS elemental scan of the pre-oxidized SS specimen POL (a) Fe2p, (b) Cr2p, (c) Ni2p, (d) O1s	83
3.21	Raman spectra of the SS specimen pre-oxidized in H ₂ O ₂ environment at 200°C	86
3.22	Micrographs of the PL deposited SS specimen (POP) (a) SEM image, (b) AFM image	87
3.23	(a) Raman spectra (b) GI-XRD of the PL deposited SS specimen POP	87

3.24	XPS wide scan of the PL deposited pre-oxidized SS specimen POP	88
3.25	XPS elemental scan of the PL deposited pre-oxidized SS specimen POP (a) Fe2p, (b) O1s	89
4.1	Bright field TEM micrographs of the ZrO ₂ powder showing the nano sized particles	100
4.2	Dark field TEM micrograph of the powder particles showing nanocrystalline ZrO ₂	100
4.3	ZrO ₂ crystallite size distribution obtained from analysis of TEM dark field micrograph	100
4.4	Selected area electron diffraction pattern	101
4.5	(a) Electron diffraction pattern evaluated from the image processing technique from SAD pattern shown in Fig. 4.4, and (b) X-ray diffraction pattern (d vs Intensity) of the nano ZrO ₂ powder	101
4.6	X-ray diffraction pattern (2θ vs Intensity) of the nano-crystalline ZrO ₂ powder	102
4.7	Raman spectrum of the ZrO ₂ powder showing the presence of both tetragonal and monoclinic phases (marked on the spectrum)	103
4.8	XPS analysis of ZrO ₂ powder on indium foil showing the composition of the powder	104
4.9	Zr 3d photoelectron electron spectra of the ZrO ₂ powder	105
4.10	Near Fermi level spectral features of the ZrO ₂ powder	105
4.11	The zeta potential of the nano- ZrO ₂ at different temperature, (a) 25°C, (b) 40°C and (c) 70°C, where pHPzc was seen to reduce with increase in the temperature	109
4.12	The zeta potential of (a) nano-ZrO ₂ in the aqueous solution containing SDS (b) α-Fe ₂ O ₃ in the aqueous solution containing SDS	109
4.13	SEM images of the pre-oxidized SS specimen after the adsorption of nano-ZrO ₂ in the aqueous solution at 90°C (a) without any surfactant (b) containing SDS as surfactant; EDS results at two different zones showing different counts of zirconium	113

4.14	XPS wide scan of the pre-oxidized SS specimen after the adsorption of nano-ZrO ₂ in the aqueous medium (a) without any surfactant at 90°C, (b) containing SDS as surfactant at 90°C and (c) without any surfactant at 150°C	114
4.15	SEM images (a) and EDS results (b) of the pre-oxidized SS specimen after the adsorption of nano-ZrO ₂ in aqueous solution at 150°C	115
5.1	SEM micrographs of ZrO ₂ coated Samples (a) ZPOH, (b) ZPOO and (c) ZPOP	122
5.2	EDS results of the ZrO ₂ coated Samples (a) ZPOH, (b) ZPOO and (c) ZPOP	122
5.3	EDS results of ZrO ₂ coated ZPOO specimen at two different places showing different counts of zirconium	123
5.4	Raman spectra of ZrO ₂ coated specimens (a) ZPOH, (b) and (c) ZPOO at two different points and (d) ZPOP	124
5.5	GIXRD patterns obtained from ZrO ₂ coated samples (a) ZPOH, (b) ZPOO and (c) ZPOP; T - tetragonal zirconia	125
5.6	XPS of ZrO ₂ coated specimens (a) ZPOP, (b) ZPOO and (c) ZPOH	126
5.7	a) Deconvolution of Zr 3d _{5/2} photoelectron peak acquired from ZrO ₂ coated specimen (ZPOP) showing the presence of ZrO ₂ (182.2 eV) and small amount of zirconium hydroxide (183.0 eV), (b) the same peak after Ar ⁺ ion sputtering	127
5.8	SEM micrographs of samples before and after ZrO ₂ deposition; (a) thin film of α-Fe ₂ O ₃ on stainless steel, (b) ZrO ₂ deposited for 30 min, (c) ZrO ₂ deposited for 60 min and (d) ZrO ₂ deposited for 5 days	132
5.9	AFM images in 2D and 3D profiles; (a & b) stainless steel surface pre-oxidized in H ₂ O ₂ environment, (c & d) Plain SS and, (e & f) mirror finished Si(100) surface	133
5.10	AFM images in 3D and 2D profiles; (a & b) thin film of α-Fe ₂ O ₃ deposited on stainless steel and (c & d) ZrO ₂ deposited on α-Fe ₂ O ₃ for 5 days	134
5.11	Raman spectra of samples prior and after ZrO ₂ deposition; (a) thin film of α-Fe ₂ O ₃ on stainless steel, (b) ZrO ₂ deposited for 30 min, (c) ZrO ₂ deposited for 60 min and (d) ZrO ₂ deposited for 5 days	135

5.12	GIXRD patterns obtained from samples prior and after ZrO ₂ deposition; (a) thin film of α -Fe ₂ O ₃ on stainless steel, (b) ZrO ₂ deposited for 30 min, (c) ZrO ₂ deposited for 60 min and (d) ZrO ₂ deposited for 5 days. T- tetragonal zirconia	136
5.13	XPS of different samples prior and after ZrO ₂ deposition; (a) thin film of α -Fe ₂ O ₃ on stainless steel, (b) ZrO ₂ deposited for 30 min, (c) ZrO ₂ deposited for 60 min and (d) ZrO ₂ deposited for 5 days	137
5.14	Fe2p photoelectron spectra obtained from samples, (a) thin film of α -Fe ₂ O ₃ on stainless steel, (b) ZrO ₂ deposited for 30 min, (c) ZrO ₂ deposited for 60 min	139
5.15	Zr3d photoelectron spectra from samples, (a) ZrO ₂ deposited for 30 min, (b) ZrO ₂ deposited for 60 min and (c) ZrO ₂ deposited for 5 days	139
5.16	Valance band spectra of (a) thin film of Fe ₂ O ₃ on stainless steel, (b) ZrO ₂ deposited on Fe ₂ O ₃ for 30 min, (c) ZrO ₂ deposited on Fe ₂ O ₃ for 60 min and (d) ZrO ₂ deposited on Fe ₂ O ₃ for 5 days	140
5.17	XPS wide scan of the ZrO ₂ coated sample prepared at 90°C for 5 hours	141
5.18	XPS of ZrO ₂ coated sample prepared at 90°C for 5 hrs, (a) Zr 3d spectrum, (b) C1s spectrum, (c) N1s spectrum and (d) Na KLL Auger peak	142
5.19	Binuclear complex structure of Na-salt of Zr-EDTA	144
5.20	Interaction mechanism of Zr-EDTA complex with α -Fe ₂ O ₃ in the hydrothermal conditions	145
6.1	Optical micrographs of the SS specimens after 10% oxalic acid etching at 1A/cm ²	156
6.2	DL-EPR curves of SS specimens (a) non-sensitized (as received), (b) sensitized at 650°C for 24 hrs and (c) sensitized at 625°C for 100 hrs	157
6.3	Potentiodynamic polarization plot of plain 304 SS specimens in 0.1 M sodium sulphate solution (a) non-sensitized SS and (b) Sensitized SS	158
6.4	Impedance spectra of plain 304 SS specimens in 0.1 M sodium sulphate solution (a) non-sensitized SS and (b) Sensitized SS	160

6.5	Equivalent circuit used for fitting the electrochemical data of plain non-sensitized and sensitized 304L SS specimens	160
6.6	SEM micrographs of ZrO ₂ coated samples; (a) ZPOH, (b) ZPOO and (c) ZPLD, cross-sectional SEM micrographs of ZrO ₂ coated samples; (d) ZPOH, (e) ZPOO and (f) ZPLD	162
6.7	EDS patterns of the ZrO ₂ coated samples; (a) ZPOH, (b) ZPOO and (c) ZPLD	163
6.8	XPS of ZrO ₂ coated samples (a) ZPLD, (b) ZPOO and (c) ZPOH	165
6.9	Raman spectra of ZrO ₂ coated samples (a) ZPOH, (b) ZPOO and (c) ZPLD	165
6.10	AFM 2D and 3D topographic images of ZrO ₂ coated samples; (a, b) ZPLD, (c, d) ZPOO and (e, f) ZPOH	166
6.11	Acoustic 2D and 3D images acquired during AFAM scans ZrO ₂ coated samples (a, b) ZPLD, (c, d) ZPOO and (e, f) ZPOH	169
6.12	Force-distance curves for the (a) Si, (b) Plain SS and ZrO ₂ coated samples (c) ZPOH, (d) ZPOO, (e) ZPLD. Force is given in terms of cantilever deflection (DFL). The particular zones from where the FD curves are presented are marked by circles in AFM images in the insets of FD curves	170
6.13	Potentiodynamic polarization plots of plain SS and pre-oxidized SS specimens in 0.1M sodium sulphate solution (a) Plain SS, (b) POH-21, (c) POO-21 and (d) POP	171
6.14	Potentiodynamic polarization plots of plain SS and ZrO ₂ coated SS samples in 0.1M sodium sulphate solution (a) Plain SS, (b) ZPOH, (c) ZPOO and (d) ZPLD	173
6.15	Impedance spectra (Nyquist plot) of plain SS and pre-oxidized specimens in 0.1 M sodium sulphate solution (a) Plain SS, (b) POH-21, (c) POO-21 and (d) POP	175
6.16	Bode-phase plot of plain SS and pre-oxidized specimens in 0.1 M sodium sulphate solution (a) Plain SS, (b) POH-21, (c) POO-21 and (d) POP	175
6.17	Equivalent circuit used for fitting the electrochemical data of pre-oxidized SS specimen POO-21	175

6.18	Impedance spectra (Nyquist plot) of plain SS and ZrO ₂ coated samples in 0.1 M sodium sulphate solution (a) Plain SS, (b) ZPOH, (c) ZPOO and (d) ZPLD, The inset shows the enlarged view of the (a) plain SS, (b) ZPOH and (c) ZPOO	177
6.19	Bode-phase plot of plain SS and ZrO ₂ coated samples in 0.1 M sodium sulphate solution (a) Plain SS, (b) ZPOH, (c) ZPOO and (d) ZPLD	177
6.20	Equivalent circuit used for fitting the electrochemical data of ZrO ₂ coated samples	178
6.21	Potentiodynamic polarization plots of plain, pre-oxidized and ZrO ₂ coated SS samples in 0.1M sodium sulphate solution at 90°C (a) Plain SS, (b) POH-21, (c) POO-21, (d) ZPOH and (e) ZPOO	180
6.22	Impedance spectra of the plain SS and pre-oxidized SS specimens (POH-21 and POO-21) in 0.1M sodium sulphate solution at 90°C	182
6.23	Impedance spectra of the plain SS and ZrO ₂ coated SS specimens (ZPOH and ZPOO) in 0.1M sodium sulphate solution at 90°C	182
6.24	(a) SEM image of the ZPOL sample and (b) EDS results for the ZPOL sample	185
6.25	The AFM images of the ZPOL sample; (a) AFM topographic image and (b) Acoustic image acquired during AFAM scan	186
6.26	Potentiodynamic polarization plots of (a) pre-oxidized POL specimen and (b) ZrO ₂ coated ZPOL sample in 0.1M sodium sulphate solution at 90°C	187
7.1	SEM micrographs of the zirconia coated SS samples (a) ZPOH and (b) 2ZPOH	193
7.2	XPS survey scan of the pre-oxidized and ZrO ₂ coated SS samples (a) POH, (b) ZPOH and (c) 2ZPOH	194
7.3	A. Potentiodynamic polarization plots of ZrO ₂ coated SS samples obtained at 25°C (a) ZPOH and (b) 2ZPOH, B. Potentiodynamic polarization plots of ZrO ₂ coated SS samples obtained at 90°C (a) ZPOH and (b) 2ZPOH	195
7.4	A. Impedance spectra of ZrO ₂ coated samples in 0.1 M sodium sulphate solution at 25°C, (a) ZPOH and, (b) 2ZPOH, B. Impedance spectra of ZrO ₂ coated samples in 0.1 M sodium sulphate solution at 90°C, (a) ZPOH and, (b) 2ZPOH	196

7.5	SEM micrographs of the ZrO ₂ coated SS samples; (a) ZPOO, (b) 2ZPOO and (c) 3ZPOO	197
7.6	XPS survey scan of the pre-oxidized and ZrO ₂ coated SS samples, (a) POO, (b) ZPOO and (c) 2ZPOO	198
7.7	A. Potentiodynamic polarization plots of ZrO ₂ coated SS samples at 25°C (a) ZPOO and (b) 2ZPOO, B. Potentiodynamic polarization plots of ZrO ₂ coated SS samples at 90°C (a) ZPOO and (b) 2ZPOO	199
7.8	SEM images of several rounds of ZrO ₂ coated SS samples; (a) POO2Z: second, (b) POO3Z: third and (c) POO4Z: fourth round	201
7.9	Cross-sectional images of several rounds of ZrO ₂ coated SS samples (a) ZPOO, (b) POO2Z, (c) POO3Z and (d) POO4Z	201
7.10	Raman spectra of the several rounds of ZrO ₂ coated SS samples (a) ZPOO (b) POO2Z, (c) POO3Z and (d) POO4Z	202
7.11	Potentiodynamic polarization plot of several rounds of ZrO ₂ coated SS samples (a) ZPOO (b) POO2Z, (c) POO3Z and (d) POO4Z	203
7.12	Nyquist plots of the several rounds of ZrO ₂ coated samples (a) POO2Z, (b) POO3Z and (c) POO4Z; the inset of figure shows the Nyquist plot for first round of ZrO ₂ deposited sample	205
7.13	Enlarged view of the several rounds of ZrO ₂ deposited samples (a) POO2Z, (b) POO3Z and (c) POO4Z; markers represent the experimental data whereas solid lines represent the fitted spectrum	205
7.14	Equivalent circuit used for fitting the electrochemical data of POO3Z and POO4Z	207
7.15	Bode plot of ZrO ₂ coated sample POO3Z (a) Bode-plot ($ Z $ vs frequency) (b) Bode-phase plot (phase angle vs frequency)	208

List of Tables

Table No.	Caption	Page No.
3.1	Analysis of Raman spectra acquired from different pre-oxidized SS specimens	92
3.2	Atomic concentration (at%) and binding energy of different photoelectron peaks obtained from pre-oxidized SS specimens	93
3.3	Properties of pre-oxidized SS specimens prepared under different environments	94
5.1	The details of substrate surfaces used for studying the role of substrate surface during ZrO ₂ deposition	121
5.2	Point of zero charge (PZC) values of ZrO ₂ and different iron oxides	129
5.3	Lattice parameters of tetragonal ZrO ₂ , α -Fe ₂ O ₃ and spinel oxides	129
6.1	Average value of polarization parameters for as received 304L SS and sensitized 304L SS in 0.1 M sodium sulphate	159
6.2	Parameters of electrical equivalent circuits for plain SS non-sensitized and sensitized 304L SS specimens	160
6.3	Surface chemical composition and morphology of the pre-oxidized layers on SS	161
6.4	Average value of polarization parameters for plain, pre-oxidized and ZrO ₂ coated 304L SS in 0.1 M sodium sulphate	173
6.5	Parameters of electrical equivalent circuits for sample plain SS and pre-oxidized specimens	176
6.6	Parameters of electrical equivalent circuit for ZrO ₂ coated samples	178

6.7	Average value of polarization parameters for plain, pre-oxidized and ZrO ₂ coated 304L SS in 0.1 M sodium sulphate at 90°C	181
6.8	Equivalent circuits used for fitting the electrochemical data of samples	182
6.9	Parameters of electrical equivalent circuit for different samples at 90°C	182
6.10	Comparison of properties of ZrO ₂ coated samples for different pre-oxidized SS surfaces	184
7.1	Average value of polarization parameters for the ZrO ₂ coated 304L SS samples in 0.1 M sodium sulphate	199
7.2	Parameters of electrical equivalent circuits for ZrO ₂ coated 304L SS samples in 0.1 M sodium sulphate	200
7.3	Average value of polarization parameters for the multiple rounds ZrO ₂ coated 304L SS samples in 0.1 M sodium sulphate	204
7.4	Parameters of electrical equivalent circuits for ZrO ₂ coated samples	206

List of Abbreviations

SS	<i>Stainless steel</i>
YSZ	<i>Yttria stabilized zirconia</i>
NPP	<i>Nuclear power plant</i>
SCC	<i>Stress corrosion cracking</i>
BWR	<i>Boiling water reactor</i>
XPS	<i>x-ray photoelectron spectroscopy</i>
XRD	<i>x-ray diffraction</i>
AFM	<i>Atomic force microscopy</i>
AFAM	<i>Atomic force acoustic microscopy</i>
FD	<i>Force-distance</i>
PLD	<i>Pulsed laser deposition</i>
SEM	<i>Scanning electron microscope</i>
EDS	<i>Energy dispersive x-ray spectroscopy</i>
OCP	<i>Open circuit potential</i>
PDP	<i>Potentiodynamic polarization</i>
EIS	<i>Electrochemical impedance spectroscopy</i>
I_{corr}	<i>Corrosion current density</i>
E_{corr}	<i>Corrosion potential</i>

<i>R_s</i>	<i>Solution resistance</i>
<i>R_{ct}</i>	<i>Charge transfer resistance</i>
<i>R_{pore}</i>	<i>Pore resistance</i>
<i>R_a</i>	<i>Average roughness</i>
<i>SDS</i>	<i>Sodium dodecylsulphate</i>
<i>PEG</i>	<i>Polyethylene glycol</i>
<i>PZC</i>	<i>Point of zero charge</i>
<i>IGC</i>	<i>Intergranular corrosion</i>

Chapter 1

Introduction

1.1 Introduction

Stress corrosion cracking (SCC) is the major degradation problem of Type 304 stainless steel (SS) in boiling water reactors (BWR) and is an unresolved issue throughout the world [1-6]. The basic reason for SCC of SS 304 in BWR is the presence of oxidizing species in the coolant water. Several techniques like hydrogen water chemistry (HWC), noble metal chemical addition (NMCA), hydrazine addition, inhibitive protective coating (IPC) have been proposed and studied to mitigate this problem. Although NMCA combined with HWC is the widely used technique till now, inhibitive protective coating of zirconia on the stainless steel surface is the most promising. Zirconia is a suitable material for corrosion resistant ceramic coatings on stainless steel surfaces to alleviate the SCC problem. The electrical, thermal, mechanical and neutron adsorption properties of ZrO_2 make it suitable to use as IPC material in nuclear power plants (NPPs). Hydrothermal deposition is the most suitable technique that can be applied for zirconia film deposition at plant scale. In this chapter, SCC mechanism and the available methods for reducing the SCC problem have been discussed. The advantages of inhibitive protective coatings of zirconia for SCC mitigation over the other methods have been briefed. The superiority of hydrothermal deposition of ZrO_2 coating over the other thin film deposition techniques is also discussed.

1.2 SCC problem in BWR nuclear reactors

SCC problem have been reported worldwide in BWRs since mid 1970s [1, 2]. There are more than 1000 number of incidents of SCC have been reported in BWRs from 1974 to 1991 [3]. These incidents spread over a wide variety of structural components including primary piping systems, core internals and some parts of reactor pressure vessel like incore monitor housings and control rod drive stub tubes [6]. Many types of pipe cracking incidences had been observed

like failure in main recirculation piping (diameter 24 inches and 28 inches), bypass lines (diameter 4 inches) as well as core spray lines (diameter 10 inches) [3, 5]. In mid-1980s, SCC of recirculation system piping led to significant reductions in US reactor operation, reaching a maximum capacity loss of about 15% [6]. In India also, over the years, many SCC failures have been observed in primary system pipelines in twin unit BWRs (TAPS#1 & TAPS#2) at Tarapur Atomic Power Station [7]. SCC problem is expected to be one of the main material degradation factors in future Advanced Heavy Water Reactor (AHWR) which uses boiling light water as a coolant in a high-pressure main heat transport system. It also uses austenitic SS (Type 304 LN SS) as structural material for core components. The 100 years of design life time of AHWRs increases their susceptibility towards SCC.

The worldwide SCC incidences could lead to severe accidents and cause safety hazard. As replacement of these failed components is difficult and costly, a wide range of basic and applied research activities were initiated to develop a mechanistic understanding of SCC problem in BWR piping and devise a suitable method to mitigate this problem.

1.2.1 The factors responsible for SCC

SCC is a significant ageing degradation mechanism for some components in boiling water reactors (BWRs) made of austenitic stainless steels and nickel based alloys. SCC is the brittle failure of susceptible alloys under the influence of tensile stress and a corrosive environment that lead to crack initiation and sub-critical crack growth. The crack propagates at a certain slow rate and continues till the unbroken ligament cannot bear the operating load. When the crack length reaches a critical length, brittle failure takes place. The crack can grow along the grain boundaries as well as within the grains. When the crack grows within the grains, mode of SCC is called transgranular stress corrosion cracking (TGSCC) and the mode of SCC where

crack grows along the grain boundaries is called intergranular SCC (IGSCC). The occurrence of IGSCC or TGSCC or mixed modes in the alloy, depend on the environment, the materials and the stress/strain state. For SCC to occur, three following preconditions are necessary and must be present simultaneously (Fig 1.1).

1. A susceptible material
2. A tensile stress component
3. An aqueous environment.

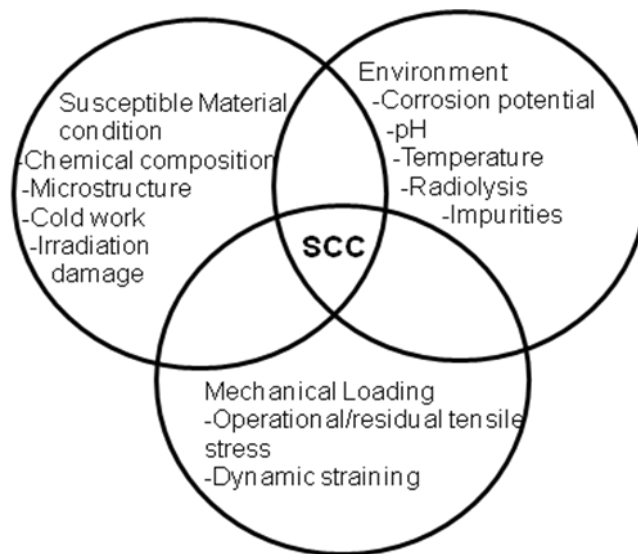


Fig 1.1: Critical factors for SCC

1.2.1.1 Material aspects: Austenitic stainless steel (~70Fe-18Cr-10Ni alloy) shows good resistance to general corrosion because of the formation of thin Cr rich passive surface film [8]. Heterogeneities like inclusion, precipitates, phase and grain boundaries in the alloy leads localized weakening/breakage of surface passive films [9]. Breakage of passive film at certain positions makes these materials prone to localized corrossions like pitting, intergranular corrosion

(IGC). Thermal sensitization and cold work are the two major material factors that contribute to SCC of austenitic stainless steels in BWR primary coolant systems.

Thermal sensitization: Sensitization is the precipitation of chromium carbides (Cr_{23}C_6) on grain boundaries and a concomitant depletion of chromium in the adjacent grains [10]. 2% reduction in Cr concentration than bulk concentration is sufficient to reduce the passivity adjacent to the grain boundaries relative to the grains themselves and lead to susceptibility to IGSCC [11]. Austenitic stainless steels are sensitized upon exposure in the temperatures between approximately 500°C–800°C [12]. This temperature range is encountered during welding, stress relief heat treatments and high temperature services[6].

Sensitization is often developed in recirculation pipelines of BWRs although most of the BWRs operate below 500°C. During welding, if Cr rich carbides just nucleate at the grain boundaries, the material can pass the IGC test. At reactor operation temperature of around 300°C, prolonged operations of the power plants lead to the diffusion of Cr from austenitic matrix to the Cr carbide particles at grain boundaries. These pre-existing Cr carbide nuclei in the weldment of austenitic stainless steel grow at temperature below 500°C and leads to IGC/IGSCC. This phenomenon when the sensitization occurs at temperature lower than the range of sensitization temperature is known as low temperature sensitization [13].

Cold work: Cold working is the plastic deformation of alloys below the recrystallization temperature. The major cold working operations are squeezing, bending, shearing and drawing [4]. If the initial cracking is transgranular that later changes to an intergranular cracking mode [14], then the initial transgranular cracking is associated with a surface layer of cold work induced by grinding or other severe surface machining techniques. In cold bent pipes, these types of failures have been observed. There may be an unfavorable interaction between deformation

induced martensite, high residual stresses and localized deformation that causes cold work induced SCC [4].

Irradiation Effects: The stainless steel core components of BWRs suffer from large number of cracking induced by radiation induced segregation (RIS). The Cr depleted grain boundaries develop due to the exposure of threshold influence of high energy ($E > 1\text{MeV}$) neutrons [14]. This type of cracking is referred as irradiation assisted stress corrosion cracking.

1.2.1.2 Environmental aspects

In BWR primary coolant, the presence of oxidizing radiolysis products, O_2 and H_2O_2 , dissolved in the high temperature water influence the electrochemical potential (ECP) of the stainless steel [15]. SCC can occur and propagate in stainless steel if the $\text{ECP} \geq -230 \text{ mV SHE}$ (Standard hydrogen electrode) [16]. The crack growth rate of stainless steels increases in sigmoidal manner with increasing potential [17]. Flow conditions, temperature and presence of impurities such as sulphate and chloride also influence the occurrence of SCC.

1.2.1.3 Stress aspects

In BWR components, majority number of SCC failures occurs in the vicinity of welds where residual stress is present. This stress is responsible for damaging the passive layer during crack initiation and propagation. SCC propagates mainly through heat affected zones developed during welding in austenitic stainless steels. Both applied and residual stress can accelerate the process of crack initiation. Fabrication flaws, welding defects, imperfections increase the local stress and act as starting point for SCC. Machining, grinding, surface finishing operations induce cold working that can generate local near surface stresses. Cold work can allow the local near surface stresses to remarkably exceed the original yield strength of the bulk material [18, 19]. Crack growth stress dependence has been quantified by some researchers [20, 21]. It is

driven by the total operational and residual manufacturing stresses and can be correlated with the local stress intensity factors. Improved welding techniques, post welding heat treatments and peening can reduce the stresses.

1.3 Methods adopted in past to mitigate SCC problem in BWR:

The severity of SCC in the structural components of BWRs leads to the development of several methods to mitigate this problem. The initiation and growth of SCC centers in sensitized SS is promoted by normal oxidizing environment of BWR [22]. The normal water chemistry (NWC) condition in a BWR in general signifies the presence of 100-300 ppb of dissolved oxygen (O_2), 200 ppb-500 ppb of hydrogen peroxide (H_2O_2) in primary coolant (light water) [23, 24]. Earlier days, corrosion potential (ECP) was commonly adopted as diagnostic indicator of the SCC susceptibility of SS components in BWRs. The approaches are followed to reduce the corrosion potential below the threshold potential of $-230mV_{SHE}$. Later on, studies are focused on more appropriate parameters like corrosion current density of structural components. Various methods have been adopted in past to mitigate the SCC problem in BWRs. Among them, the most studied ones are hydrogen water chemistry (HWC), catalytic treatment by noble metals [25-29] known as NMCA, and inhibitive treatment of SS surface by insulating chemicals [22, 30-34].

1.3.1 Hydrogen water chemistry (HWC)

The corrosion potential of SS pipes increases when the level of oxygen rises in the coolant system. It provides an unfavorable environment for the structural material by inducing SCC. Hydrogen injection to feed water systems is effective for suppressing water radiolysis and reducing the bulk oxygen concentration in reactor water to a level immune from SCC of stainless steel. The HWC technology is able to induce a reducing environment in the primary coolant through the injection of sufficient amount of H_2 (1.2-2ppm) into the feed water line of a BWR.

Dissolved oxygen concentration (100-300 ppb) in the primary coolant system will reduce to 20 ppb or less by maintaining the feed water hydrogen level at 1.5 ppm [35-37].

The HWC provide the protection against SCC for only few regions in the primary coolant circuit such as the lower ‘downcomer’ and the recirculation system. [37]. The two-phase flow condition in the reactor core, which renders the stripping of volatile H₂ from the liquid phase to the vapor phase and in turn leads to insufficient dissolved H₂ levels in regions close to the core-exit. Regions like core channel, upper plenum, stand pipe, mixing plenum, and sometimes the upper downcomer are prone to SCC even after HWC treatment [37-39]. In addition, an undesirable effect of HWC was that the increase in main stream line radiation dose of BWR when the [H₂]FW is greater than 0.5 ppm. The stable form of N¹⁶ in water soluble nitrate (NO₃) is converted into a volatile form NO_x or NH₃ and enters the steam generator tube along with steam. The partitioning of volatile species containing N¹⁶ into the steam phase will result in a four to six-fold increase in the radiation exposure relative to the situation of no hydrogen addition. Under the HWC, increase in shutdown radiation fields have been observed due to enhanced deposition of activation products like Co⁶⁰ from the reactor water [40].

1.3.2 Noble Metal Chemical addition (NMCA)

In the mid-1990s, the technology of noble metal chemical addition (NMCA) was brought into practice by ‘General Electric’ to enhance the effectiveness of HWC by employing the catalytic property of noble metals [41]. It is expected that only a stoichiometric amount of hydrogen is required to achieve the same level of SCC protection (reduction in ECP) as by HWC with the NMCA and radiation level in the BWR plant can be minimized [26]. Low level HWC [H₂]FW of 0.15 to 0.35 ppm is sufficient to meet the M_{H/O} requirement (molar ratio of hydrogen to oxidants; M_{H/O} >2). A thin layer equivalent of an atom layer of noble metal particles, such as

Pt, Rh, Ir, Os, Pd etc. are deposited onto the alloy surface in order to catalyze the redox reactions like oxidation of H₂ and reduction of O₂ and H₂O₂ to form water. The concentration of oxidants at the aqueous solution adjacent to an NMCA treated metal surface will decrease to a very low level in comparison to the bulk coolant. The aqueous environment adjacent to the metal surface would be relatively reducing and the ECP of the metal is substantially lowered. The primary coolant circuits of BWRs coated with noble metals show the effective reduction in ECP (< - 0.23V) by NMCA when M_{H/O} in the reactor is greater than 2. So, ECP specification can be achieved at low hydrogen concentration without suppressing all the radiolysis and there was no increase in main steam line radiation due to N¹⁶. Except lowering the requirement of H₂ injection, online NMCA allows sufficient noble metal penetration into cracks/crevices with a relatively uniform distribution and reduce the crack growth rate.

The noble metals are expensive; still other drawbacks of NMCA are more severe compared to the cost of noble metals. The undesirably enhanced corrosion in the SS components has been observed where the sufficient ratio of H₂ to O₂ cannot be maintained in the BWR coolant [28, 29]. The SS components at certain locations of BWR (e.g. in the vicinity of the core spray and top guide), remain susceptible to SCC where the water begins to boil. Here, H₂ partitions preferentially into the steam and sufficient amount of H₂ cannot be maintained in solution [41, 42].

1.3.3 Inhibitive Protective coating (IPC)

Inhibitive protective coating (IPC) on the SS surfaces has been proposed in the recent years and still remains in the research stage for implementing in the power plants [1, 31, 43]. In principle, the redox reactions like reduction of O₂, H₂O₂ coupled with metal oxidation lead to initiation and growth of cracks along the grain boundaries and aggravate inter-granular

corrosion cracking [1, 22, 34]. IPC treatment on the SS surface inhibits all the reactions like oxidation of H_2 , reduction of O_2 , reduction of H_2O_2 at the SS surface in the aqueous solution (Fig. 1.2). Electrical connection between external (high oxidant) water and the metal component substrate will be lost due to the insulating nature of the depositing material. The metal oxidation (dissolution) at crack the tip will also be stopped as it is coupled with the reactions at the SS surface [38, 43-46]. Dielectric coating arrest the crack growth by inhibiting the redox reactions corresponding to corrosion at grain boundaries of stainless steel in oxidizing environment. IPC treatment prevents the need of H_2 addition in BWR coolant as it suppresses the metal dissolution and SCC on the structural components of BWRs without the addition of hydrogen. The insulated protective coating restrict the mass transport of oxidants to the underlying metal substrate to a very low rate, thus prevents an electrochemical crevice cell from being formed.

The approach of IPC for mitigating SCC has been addressed by many researchers. In the work by Kim and Andresen [33], yttria stabilized zirconia (YSZ) was coated on SS by plasma spray method. It has been reported by them that the coating mitigates the SCC problem in high temperature water. Insulating coating doped with noble metal like Pt or Pd is also observed to be very effective in suppressing the ECP below -230 mV [47]. Zirconia coatings were produced on SS by hydrothermal technique at the decomposition temperature of Zr-compounds such as Zirconium acetyl acetone, Zr- EDTA, Zirconium citrate ammonium complex. But adherent and compact coating was obtained from the decomposition of Zr-EDTA only [22]. T. K. Yeh et. al. used ZrO_2 nano particle of size around 100 nm to form the coating on pre-oxidized SS [1]. Even with the discontinuous and porous ZrO_2 coatings, they observed the improvement in the corrosion resistance properties of the coated specimens. The technique of ZrO_2 coating on SS

using Zr-organometallic compound along with chelating agent and surfactant was started by Zhou et al [2, 34, 46] and the coating was seen to be continuous, compact and thick (~ 1 micron).

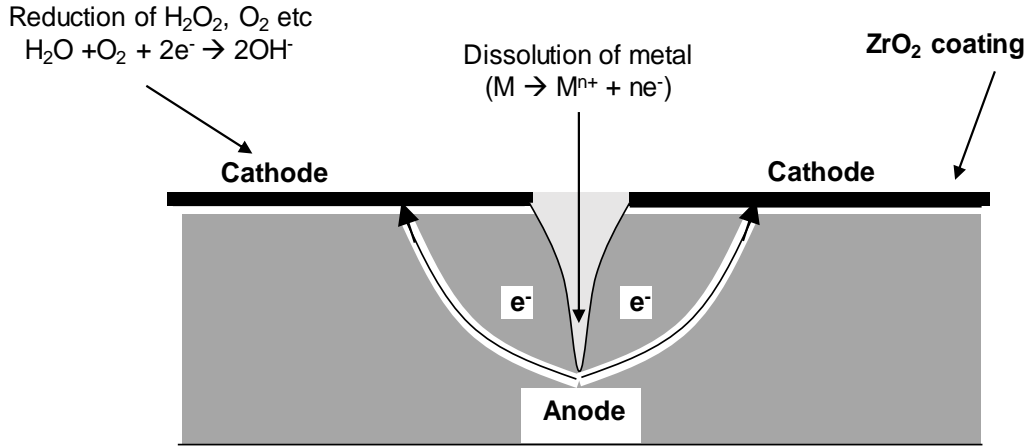


Fig. 1.2: Schematic of crack growth in BWR oxidizing environment

Potentiodynamic polarization (PDP) is one of the easiest techniques to evaluate the susceptibility of the SCC of the coated specimens. PDP studies involves the comparison of PDP plots from the coated specimens with the uncoated specimens [22, 28, 29]. The decrease in corrosion current is explained as the reduction in susceptibility of the SCC. In addition, the measurement of ECP at ~288°C is found to be a good parameter to estimate the improvement of the SCC resistance in the alloys. Laboratory experiments have been conducted in past in simulated BWR environments to verify the effectiveness of IPC [1, 31, 47]. It was observed that the exchange current densities (ECDs) of the O_2 and H_2O_2 reduction and SS oxidation reactions are effectively decreased and the corrosion of SS components is significantly alleviated after the IPC. The corrosion potential (ECP) of the Type 304 stainless steel (SS) of in purely oxygenated environments may increase or decrease after the IPC treatment [1, 31, 47, 48]. Evan diagrams (Fig. 1.3) show that the corrosion potential of the metal (E_{corr}) will decrease after the IPC if the

decrease in ECD of metal oxidation reaction is significantly higher than that of O_2 reduction (Fig. 1.3a). If decrease in ECD of metal oxidation is lower than the decrease in ECD of O_2 reduction then the E_{corr} value will rise after the IPC treatment (Fig. 1.3b). The corrosion current density of the metal decreases in both the cases [1, 32, 47, 49]. So, ECP is not the appropriate parameter to indicate the initiation and its propagation in the case of IPC treated surfaces. Corrosion of SS components will be significantly alleviated if ECDs of the redox reactions on the base metal surface decrease [46].

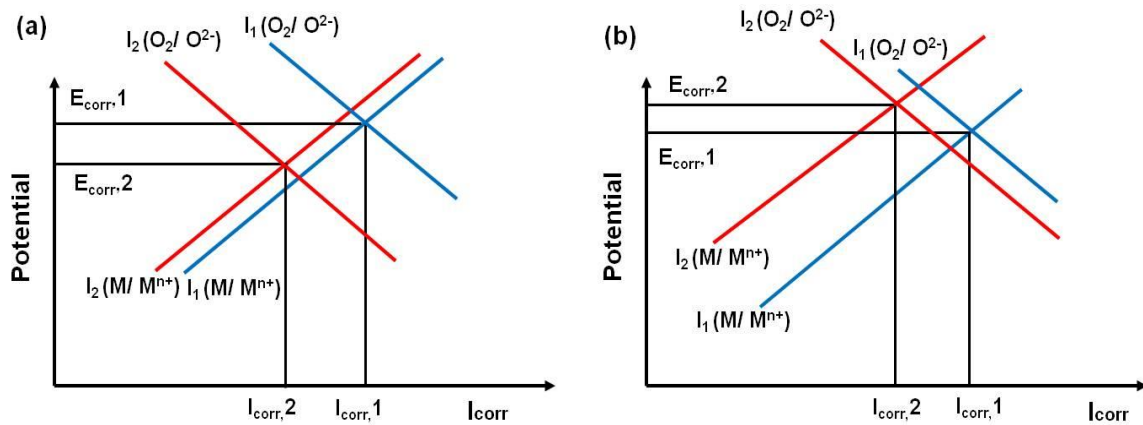


Fig. 1.3: Evans diagram of stainless steel specimens before and after IPC treatment [46, 47]. The blue lines ($E_{corr,1}$, $I_{corr,1}$) represent the uncoated specimens while the red lines ($E_{corr,2}$, $I_{corr,2}$) represent the coated SS specimens

1.4 Use of zirconia as the coating material

There are only very few potential materials available that can be used as the IPC on BWR structural material for corrosion resistant applications. The material should satisfy the following requirements for being used as the IPC material in BWR.

1. Material should be reactor friendly, foreign materials should be avoided in the nuclear reactor system.

2. It should have low neutron absorption coefficient to avoid the radioactivity build up in the coolant system.
3. Highly insulating to act as a protective barrier film for redox reactions.
3. It should withstand high temperature and high pressure.
4. Thermal expansion coefficient should match with SS to avoid the strain between substrate and deposited material at operating conditions.

TiO₂, Al₂O₃ and ZrO₂ are the potential materials proposed suitable as IPC materials. ZrO₂ coating was found to be better against the TiO₂ coating for corrosion protection applications [1, 50]. The higher band gap of ZrO₂ (5–7 eV) makes it an insulating material while TiO₂ generally behave as a semiconductor (band gap ~3 eV) [51, 52]. Al₂O₃ have the band gap as high as zirconia [53], and show the better mechanical properties compare to ZrO₂. The lower thermal expansion coefficient of Al₂O₃ (~8.2*10⁻⁶/°C) [ASTM-C372] compare to SS (10.1-17.3*10⁻⁶/°C) makes it unsuitable for performing at high temperature [54]. Thermal expansion coefficient of SS and ZrO₂ (10.5*10⁻⁶/°C) are similar and make the ZrO₂ a suitable material for high temperature protective coating applications. Al₂O₃ has higher dissolution rate in water at 288°C compare to ZrO₂. Zr-alloys are widely used as the cladding material (Zircaloy) for fuel rods in most of the nuclear power plants due to its low neutron absorption cross-section. So the entry of foreign elements in the reactor system can be avoided by the use of ZrO₂. ZrO₂ is very stable in high temperature water, both structurally (e.g., it is not prone to spalling and is not susceptible to environmentally assisted cracking) and chemically (e.g., it does not dissolve or react). Low thermal conductivity (20% that of alumina) of zirconia also make it a preferable material as heat loss during coolant circulation will be less. Highly insulating, wide band gap, low neutron adsorption cross-section, thermal expansion coefficient close to SS and its already established

wide use in nuclear reactor system make it an appropriate material for IPC on BWR structural components. ZrO_2 coatings are found to be effective for mitigating IGSCC problem and the ten times reduction in intergranular crack growth rate is observed for the zirconia coated SS samples compared to uncoated SS samples by Zhou et. al. [55].

1.5 Properties of ZrO_2

Zirconia is an important ceramic material due to its versatile properties [56]. The intrinsic physical and chemical properties like hardness, wear resistance, low coefficient of friction, chemical inertness, ionic conductivity, electrical properties, low thermal conductivity and high melting point make it important for engineering applications. Other than its suitability for IPC applications, it is being used for various applications like biomaterials [57-60], solid oxide fuel cells (SOFCs) [61, 62], oxygen sensors [63], transformation-toughened ceramics [64], catalysis [65] and optics [66, 67]. Thin films of ZrO_2 have numerous technological applications such as optical coating, insulating layers, thermal barrier, catalysis or catalytic supports, hard coatings and wear resistant coatings. High thermal expansion coefficient and low thermal conductivity ($\sim 2 \text{ W/(m.K)}$) make it a suitable material for thermal barrier coatings on metallic alloys [68-70]. Its high mechanical strength and fracture toughness make it a superior material over other ceramics.

Zirconia has three stable crystal forms: monoclinic (up to 1170°C), tetragonal ($1170\text{--}2370^\circ\text{C}$) and cubic ($2370\text{--}2680^\circ\text{C}$) [71, 72]. The structure of three phases of ZrO_2 is given in Fig. 1.4. [73]. Blue spheres are representing zirconium atoms while red spheres are representing oxygen atoms.

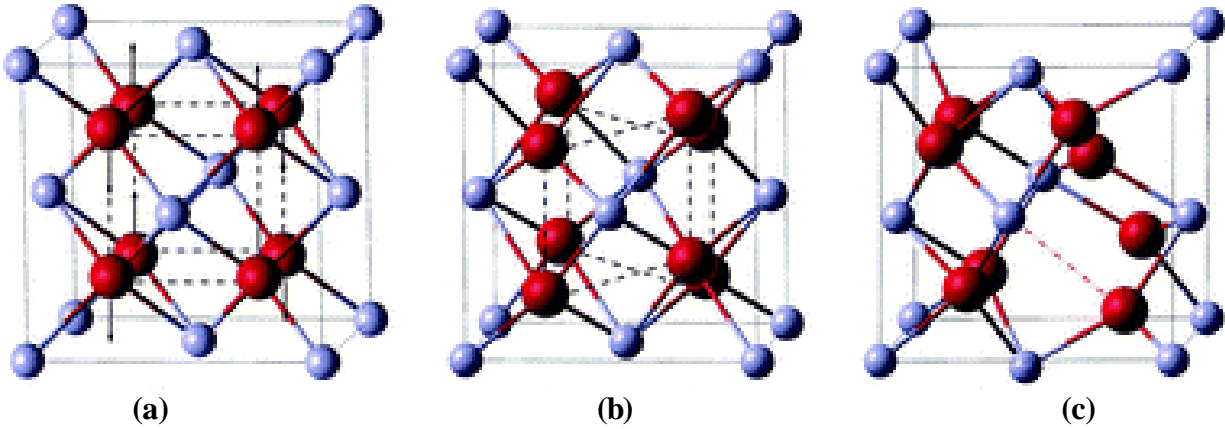


Fig. 1.4: Crystal structures of ZrO_2 (a) cubic, (b) tetragonal and (c) monoclinic

Monoclinic phase (m- ZrO_2) have the space group $P21/c$, $a=5.169\text{\AA}$, $b=5.232\text{\AA}$, $c=5.341\text{\AA}$, $\beta=98.9^\circ$), tetragonal phase (t- ZrO_2) have the space group $P42/nmc$, $a=3.591\text{\AA}$, $b=5.169\text{\AA}$ and cubic phase (c- ZrO_2) have the space group $Fm\bar{3}m$, $a=5.12\text{\AA}$) [74-77]. The c- ZrO_2 has a fluorite-type structure where Zr atom octahedrally coordinated with equi-distant eight oxygen atoms and oxygen atoms are tetrahedrally coordinated to four equidistant Zr atoms. In the t-phase, Zr atoms are octahedrally coordinated to the oxygen atoms, but the eight oxygen atoms are no longer equidistant. Four oxygen atoms are approximately 15% closer to the Zr atoms than the other four oxygen atoms. This phase has a distorted crystal structure which is termed face centered tetragonal. The m- ZrO_2 is also has a distorted tetragonal crystal structure. This phase is unique in that the Zr atoms have seven fold co-ordination with the oxygen at varying bond lengths and angles [73-77].

Any phase of ZrO_2 is capable of providing the inhibitive nature of the coating, but tetragonal phase of ZrO_2 is normally used in coating applications due to its superior mechanical properties over the other phases. Thin films (nm range) of t- ZrO_2 show more stability [78]. High strength, density, fracture toughness and transformation toughening in the tetragonal ZrO_2 make it a desirable phase compare to thermodynamically stable monoclinic zirconia. Garvie et al.

proposed that tetragonal to monoclinic transformation can improve both the toughness and strength of ceramics [79]. In thin films, when metastable t-ZrO₂ particles experience localized tensile stresses around a propagating crack, t-ZrO₂ particles can transform to the monoclinic phase at the crack tip zone. The tetragonal to monoclinic phase transformation is accompanied with 4% increase of volume strain due to the higher density of t-ZrO₂ compare to m-ZrO₂ [80]. The volume expansion in the vicinity of propagating crack reduce the stress intensity at the crack tip, crack tip compresses which retards crack growth. This process is called transformation toughening and it results in exceptional fracture toughness of the coatings made with metastable t- ZrO₂ particles [81-83].

1.6 Stabilization of pure t- ZrO₂ at room temperature

High temperature polymorphs of zirconia like tetragonal and cubic form cannot be quenched at room temperature. The addition of dopants like Y³⁺, Gd³⁺, Ce⁴⁺ etc. or the preparation of fine grained pure zirconia (> 30 nm) nano-crystals can only stabilize the tetragonal zirconia at room temperature [84-86]. The addition of dopants can stabilize the coarse zirconia particles (> 1 μm size) in metastable phase at room temperature by creation of oxygen vacancies around the Zr atom. The tetragonal phase stabilization mechanism for nano-crystalline zirconia is different from micro-crystalline zirconia and depends on many important factors like critical crystallite size effect, surface free energy of particles, interfacial energy and strain energy [87-89]. Few important factors for the stabilization of pure nano-crystalline zirconia are discussed.

1.6.1 Role of surface energy

The theory of occurrence of metastable t-ZrO₂ as the crystallite size effect was first put forth by Garvie and illustrated in Fig. 1.5 [85].

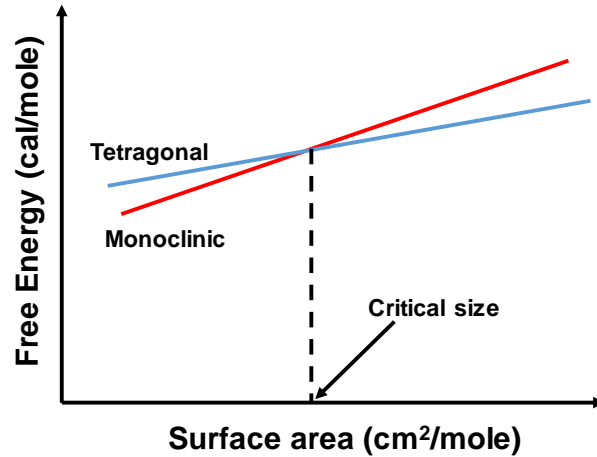


Fig. 1.5: Schematic free-energy diagram of monoclinic and tetragonal ZrO_2 nanoparticles

The tetragonal structure of ZrO_2 is thermodynamically stable at room temperature below the critical size of 10 nm within the isolated, strain free ZrO_2 nanocrystals. Below 10 nm, the surface energy of spherical ZrO_2 nanocrystal overcomes its volume free energy and high temperature tetragonal phase can be stabilized. The transformation temperature of monoclinic to tetragonal phase is a function of crystallite size for the nano-crystalline zirconia. Transformation temperature decreases very rapidly as the size decreases within the range of 100-10 nm, it is observed to be 25°C for 10 nm zirconia crystals in an isolated, strain free environment [90].

1.6.2 Role of interfacial and strain energies

Several parameters like interfacial energy, strain energy along with surface energy decide the critical size for stabilization of metastable tetragonal phase at room temperature. Highly agglomerated ZrO_2 domains show the tetragonal phase stabilization within the range of 10-190 nm as severe strain in the agglomerated ZrO_2 nano-particles alter the energy balance for stabilization of metastable phase. The processes like mechanical grinding or ball milling (non-hydrostatic strain energy) of metastable tetragonal zirconia triggers the tetragonal to monoclinic transformation by inducing lattice defects [91-93]. Hydrostatic and non-hydrostatic stresses

increase the critical size for stabilization of tetragonal phase at room temperature for both isolated and aggregated particles [87]. In addition to this, internal hydrostatic stresses and oxygen ion vacancies also play a role during room temperature stabilization of metastable tetragonal zirconia.

1.7 Hydrothermal deposition of ZrO₂ coating on the SS surfaces

1.7.1 Importance of hydrothermal deposition for NPPs

Several methods are available for developing the ZrO₂ coating on SS surfaces. Techniques like r.f. sputtering [94], hydrothermal [50, 95, 96], sol-gel [97, 98], electro-deposition [99], pulsed laser deposition [100], chemical vapor deposition [101] or plasma spray [102] have been adopted for developing the ZrO₂ coatings on SS surface by many researchers. Most of the routes followed for coating deposition are the physical deposition techniques and difficult to implement at power plant scale and for intricate structures. Wet chemical routes like sol-gel deposition and hydrothermal deposition should be followed for the deposition of zirconia at the industrial scale. Wet chemical methods allow the film deposition for the interior surfaces of the recirculation piping system or the reactor vessel of BWRs and complex designs systems. Sol-gel preparations result in very high quality of coatings, but it has some limitations in terms of applicability. The sol-gel process involves the deposition of material on the substrate surface followed by high temperature heating for drying and phase formation. The deposited film will be amorphous, with high C content, mainly constituting of metal hydroxides and may not be adherent to the substrate surface without heating. Post deposition heat treatment is not possible for the large systems like BWR structural components. Tensile stress may develop during heating and it can lead to cracks formation in the film. High temperature heating may sensitize the stainless steel and cancel the benefits of coating.

Hydrothermal route is the most suitable deposition method in terms its applicability at plant scale and for complex designs. It is simple, economically viable and convenient for forming the coating on intricate steel structures.

1.7.2 Hydrothermal deposition process

Hydrothermal method involves the formation of thin films/ powders directly from solution and post heating treatment/ calcination is not required to obtain crystalline thin film [103]. Hydrothermal is a homogeneous or heterogeneous chemical reaction in the presence of an aqueous solvent above room temperature and at pressure greater than 1 atm in a closed system [104]. It uses high temperature high pressure conditions to dissolve and recrystallize materials that are relatively insoluble under ordinary conditions. Both nano-particles and bulk materials can be crystallized by this method. The precursor based chemical approach in hydrothermal synthesis drastically reduces the temperature and pressure conditions for material processing. Nucleation and growth of crystallites are the two main steps of a hydrothermal synthesis. Nucleation is slow process and rate determining step while crystal growth is rate limiting step [102]. During the thin film deposition, the molecular level chemical interaction takes place in between depositing material and substrate surface at high temperature and high pressure of the hydrothermal conditions. Atom to atom interaction between substrate and depositing material is essential for the development of adherent, smooth and uniform deposition of insulating material on the substrate surface.

The modeling of hydrothermal reactions prior to the actual experiment helps in predicting the experimental conditions to achieve a desirable phase, size and shape [105, 106]. Hydrothermal reaction conditions like temperature, pressure and pH provides control over phase purity, size, chemical composition, minimized grain boundary effect, dense particles and higher

crystallinity over conventional physical deposition techniques [107, 108]. Surfactants and chelates controls the nucleation of desired phase in nanoparticles and phase homogeneity, size, shape and dispersibility can be achieved [108]. The different regions of pH correspond to different mechanisms of nucleation of nano-particles and each mechanism is associated with particular phase or phases.

1.8 Aim and Scope of the Study

The development target of this study is to produce a compact, adherent and electrically insulating ZrO_2 film on the SS surfaces by hydrothermal technique. The coating procedure must enable the treatment of SS components of intricate structures and complex designs. The adherence, thickness and surface coverage of the ZrO_2 coatings decide their effectiveness towards corrosion protection. ZrO_2 does not adhere on SS surface without the intermediate surface oxide layer. Pre-oxidation of the SS surface prior to ZrO_2 deposition is an essential step for developing adherent coating. Chemical composition, crystal structure, particle size and morphology of the pre-oxidized layer on SS strongly influence the zirconia coating properties like adhesion, continuity, density and thickness. The role of the pre-oxidized layer on SS for the growth of the ZrO_2 coatings by hydrothermal process has been discussed in detail. Different possible oxides on stainless steel like spinel oxides and rhombodral oxides are selected for these studies.

The specialty of the hydrothermal technique is that, it's a slow process but brings the atom to atom contact for the growth of the coatings. In this work the mechanism of the growth of ZrO_2 on pre-oxidized SS is explained. This understanding is crucial to produce compact and adhesive coatings, which has direct consequences on the corrosion resistance properties of the coated specimens. Thickening on the coatings by hydrothermal process is an important issue.

Typical laboratory scale experiments are performed to increase the thickness of the ZrO₂ coatings on SS. These experiments resemble a continuous precursor supply enabled circulating system, where the continuous supply of low concentration zirconia precursor material in a dynamic loop for longer duration will lead to a thick coating. The optimum thickness of the ZrO₂ coating for the best corrosion resistance properties have also been discussed in detail. The SCC susceptibility of the coated stainless steel specimens has been evaluated by the measurement of corrosion currents of the coated specimens by electrochemical potentiodynamic polarization process. Corrosion resistance of zirconia films improves with the increase in thickness of zirconia coatings. The optimization of the coating thickness has been estimated from the electrochemical corrosion current measurement.

1.9 References

- [1] T.-K. Yeh, M.-Y. Lee, C.-H. Tsai, J. Nucl. Sci. Technol. 39 (2002) 531–539.
- [2] Z.F. Zhou, E. Chalkova, S.N. Lvov, P.H. Chou, J. Nucl. Mater. 378 (2008) 229–237.
- [3] D.R. Diercks, J. Mater. Eng. Perform. 2 (1993) 799-806.
- [4] IAEA Nuclear Energy Series Technical Reports, Stress Corrosion Cracking in Light Water Reactors: Good Practices and Lessons Learned, Vienna 2011, ISSN 1995–7807; no. NP-T-3.13.
- [5] S.H. Bush, A.D. Chockie, An Overview of Stress Corrosion in Nuclear Reactors from the Late 1950s to the 1990s, February 1996, SKI Report 96:24, ISSN 1104-1374 ISRN SKI-R--96/24—SE.
- [6] S.M. Bruemmer, G.S. Was, J. Nucl. Mater. 216 (1994) 348-363.

- [7] N.K. Roy, N.K. Dhanmeher, A. Jabbar, C.S. Mali, A.P. Kulkarni, N.S. Gulavani, A.K. Singh, Ravindranath, R.K. Gargye, Proceedings of the National Seminar & Exhibition on Non-Destructive Evaluation NDE 2011, December 8-10, 2011.
- [8] L.S. Kumar, S.M.Verma, P. Radhakrishnaprasad, P.K. Kumar, T. Sivashanker, International journal of engineering trends and technology 2 (2011) 28-33.
- [9] D.D.N. Singh, Localized corrosion and component failures-Causes, mechanism and remedial measures, proceedings: COFA-1997 ©NML Jamshedpur, pp. 169-211.
- [10] R.K. Dayal, N. Parvathavarthini, B. Raj, Int. Mater. Rev. 50 (2005)129 –155.
- [11] N. Parvathavarthini, in: Corrosion of Austenitic Stainless Steels. Mechanism, Mitigation and Monitoring, Narosa Publishing House, New Delhi, 2002, pp. 117 – 138.
- [12] R. Singh, G. Das, P.K. Singh, and I. Chattoraj, Metall. Mater. Trans. A 40A (2009) 1219-1234.
- [13] S.C. Bali, V. Kain, V. S. Raja, Corrosion 65 (2009) 726-740.
- [14] T. Onchi, K. Dohi, M. Navas, W. Karlsen, Nucl. Sci. Technol. 43 (2006) 851–865.
- [15] J. R. Weeks, B. Vyas, H. S. Isaacs, Corros. Sci. 25 (1985) 757-768.
- [16] M. Roßkamp, N. Albrecht, U. Ilg, H. Neder, U. Reitzner, B. Riedmüller, D. Rutschow, VGB guideline for the water in nuclear power plants with light water reactors (BWR), VGB-R 401 J (2006).
- [17] P.L. Andresen, M.M. Morra, J. Nucl. Mater. 383 (2008) 97–111.
- [18] R.M. Horn, G.M. Gordon, F.P. Ford, R.L. Cowan, Nucl. Eng. Des. 174 (1997) 313-325
- [19] F.W. Brust, E.F. Rybicki, J. Pressure Vessel Technol. 103 (1981) 226-232.
- [20] R.J. Dimelfi, W.D. Nix, International Journal of Fracture 13 (1977) 341-348.
- [21] P. J. Noronha, P.F. Packman, Eng. Fract. Mech. 10 (1978) 289-297.

- [22] B. Stellwag, R. Killan, Water Chemistry of Nuclear Reactor Systems 8, BNES (2000) 127-131.
- [23] G.R. Johnson, W.H. Cook, Eng. Fract. Mech. 21(1985) 31-48.
- [24] T.-K. Yeh, F. Chu, Nucl. Sci. Eng. 139 (2001) 221-233.
- [25] Y.-J. Kim, P.L. Andresen, S. Hettiarachchi, T. P. Diaz, Hydrothermal formation and distribution of noble metal particles on type 304 SS in high temperature water, NACE International, Corrosion (2007) Nashville, Tennessee, NACE-07604.
- [26] S. Hettiarachchi, R.J. Law, T.P. Diaz, R.L. Cowan, in: 8th Int. Conf. on Environmental Degradation of Materials in Nuclear Power System-Water Reactors(1997) 535–540.
- [27] S. Hettiarachchi, T.P. Diaz, J.A. Varela, R.A. Seeman, L.C. Tran, 13th International conference on environmental degradation of materials in nuclear power systems, Materials Science (S36) (2007) Canadian Nuclear Society, ISBN 0-919784-89-5.
- [28] T.-K. Yeh, D.D Macdonald, J. Nucl. Sci. Technol. 43 (2006) 1228-1236.
- [29] T.-K. Yeh, C.-H. Tsai, J. Nucl. Sci. Technol. 41 (2004) 116-125.
- [30] X. Zhou, I. Balachov, D.D. Macdonald, Corros. Sci. (1998) 1349-1362.
- [31] T.K. Yeh, C.T. Liu, C.H. Tsai, J. Nucl. Sci. Technol. 42 (2005) 809-815.
- [32] T.-K. Yeh, Y.-C. Chein, B.-Y. Wang, C.-H. Tsai, Corros. Sci. 50 (2008) 2327–2337.
- [33] Y-J. Kim, P.L. Andresen, Corrosion 54 (1998) 1012-1017.
- [34] Z.F. Zhou, E. Chalkova, S.N. Lvov, P. Chou, R. Pathania, Corros. Sci. 49 (2007) 830-843.
- [35] C.C. Lin, F.R. Smith, R.L. Cowan, Nucl. Eng. Des. 166 (1996) 31-36.
- [36] R.J. Law, M.E. Indig, C.C. Lin, R.L. Cowan, Water chemistry of nuclear reactor systems 3, 1 (1983) ISBN 0-7277-0201-7.
- [37] T.K. Yeh, D.D. Macdonald, Nucl. Sci. Eng. 123 (1996) 295-304.

- [38] D.D. Macdonald, *Corrosion* 48 (1992) 194-205.
- [39] S. Hettiarachchi, proceedings of the 12th international conference on environmental degradation of materials in nuclear power system-water reactors-TMS (The Minerals, Metals & Materials Society), 2005, 925-862-4217.
- [40] C. C. Lin, F.R. Smith, R.L. Cowan, *Nucl. Eng. Desig.* 166 (1966) 31-36.
- [41] S. Hettiarachchi, G.P. Wozadlo, P.L. Andresen, T.P. Diaz, R.L. Cowan, in: proceedings of 7th International Symposium on Environmental Degradation of Materials in Nuclear Power System-Water Reactors, NACE, Houston, TX, 1995, pp. 735–744.
- [42] Y.-J. Kim, P.L. Andresen, in: 11th Int. Conf. Environmental Degradation of Materials in Nuclear Systems, Stevenson, WA, August 10–14, 2003, pp. 526–537.
- [43] Y.J. Kim, P.L. Andresen, *Corrosion* 96, NACE, Denver, Colorado, March 24–29, 1996, Paper No. 105.
- [44] D.D. Macdonald, T.K. Yeh, A.T. Motta, *Corrosion* 95, 1995, Paper No. 403.
- [45] D.D. Macdonald, P.-C. Lu, M. Urquidi-Macdonald, T.-K. Yeh, *Corrosion* 52(1996) 768-785.
- [46] Z.F. Zhou, E. Chalkova, V. Balasov, P. Chou, S.N. Lvov, *Interfacial electrochemistry and chemistry in high temperature media*, Issue 27, *ECS Transactions* 11 (2008) 181-188.
- [47] T.K. Yeh, C. H. Tsai, Y. H. Cheng, *J. Nucl. Sci. Technol.* 42 (2005) 462-469.
- [48] T.K. Yeh, B.Y. Wang, Y.C. Chien, C.H. Tsai, *J. Nucl. Sci. Technol.* 44 (2007) 1436-1447.
- [49] T.K. Yeh, Po-I. Wu, C. H. Tsai, *Prog. Nucl. Energ.* 57 (2012) 62-70.
- [50] Y.-J. Kim, T.M. Angelio, P.L. Andresen, F.P. Ford, United States Patent Application, Patent No. 2004/ 006724854 B1.
- [51] J.P. Chang, Y.-S. Lin, K. Chu, *J. Vac. Sci. Technol. B* 19 (2001) 1782-1787.

- [52] W.J. Yin, S. Chen, J.H. Yang, X.G. Gong, Y. Yan, *Appl. Phys. Lett.* 96 (2010) 221901-1-3.
- [53] M. Yazdanmehr, S.J. Asadabadi, A. Nourmohammadi, M. Ghasemzadeh, *Nanoscale Research Letters* 2012, 7:488.
- [54] ASM Handbook Volume 1 - Properties and Selection: Irons, Steels, and High-Performance Alloys.
- [55] X. Zhou, I. Balachov, D. Macdonald, *Corros. Sci.* 40 (1998) 1349-1362
- [56] F. Heshmatpour, R.B. Aghakhanpour, *Powder Technol.* 205 (2011) 193–200.
- [57] M. Srinivas, G. Buvaneswari, *Trends Biomater. Artif. Organs* 20(1) (2006) 24-30.
- [58] O. Roualdes , M.-E. Duclos , D. Gutknecht , *Biomaterials* 31 (2010) 2043–2054.
- [59] C. Oetze, E.R. Clase, *J. Mater Sci.* 41 (2006) 8130–8137.
- [60] X. He, Y.Z. Zhang, E.J.P. Mansell, E.B. Su, *J. Mater. Sci. Mater. Med.* 19 (2008) 2743–2749.
- [61] B.C.H. Steele, A. Heinzel, *Nature* 414 (2001) 345-352.
- [62] Y.W. Zhang, Y. Yang, S. Jin, S.J. Tian, G.B. Li, J.T. Jia, C.S. Liao, C.H. Yan, *Chem. Mater.* 13 (2001) 372-378.
- [63] S.B. Yu, Q.H. Wu, M. Tabib-Azar, C.C. Liu, *Sens. Actuators B* 85 (2002) 212-218.
- [64] R.H.J. Hannink, P.M. Kelly, B.C. Muddle, *J. Am. Ceram. Soc.* 83 (2000) 461-487.
- [65] M.P. Kapoor, A. Raj, Y. Matsumura, *Microporous Mesoporous Mater.* 44-45 (2001) 565-572.
- [66] A. Hartridge, M.G. Krishna, A.K. Bhattacharya, *Thin Solid Films* 384 (2001) 254-260.
- [67] Y.W. Zhang, S. Jin, C.S. Liao, C.H. Yan, *Mater. Lett.* 56 (2002) 1030-1034.
- [68] A.S. Kao, C. Hwang, *J. Vac. Sci. Technol.* A8(1990) 3289–3294.
- [69] M. Shane, M.L. McCartney, *J. Mater. Sci.* 25 (1990) 1537–1544.

- [70] A.S. Kao, G.L. Gorman, *J. Appl. Phys.*, 67(1990) 3826–3834.
- [71] M. Rühle, *Adv. Mater.* 9 (1997) 195-217.
- [72] E.C. Subbarao, in: *Science and Technology of Zirconia, Advances in Ceramics 3* (American Ceramic Society, Westerville, OH, 1981) p. 1.
- [73] F. Gallino, C. Di Valentin, G. Pacchioni, *Phys. Chem. Chem. Phys.* 13 (2011) 176-67-75.
- [74] J.D. McCullough, K.N. Trueblood, *Acta. Cryst.* 12 (1959) 507-511.
- [75] D.K. Smith, H.W. Newkirk, *Acta. Cryst.* 18 (1965) 983-991.
- [76] N. Igawa, Y. Ishii, T. Nagasaki, Y. Morii, S. Funahashi, H. Ohno, *J. Am. Ceram. Soc.* 76 (1993) 2673-2676.
- [77] R. Srinivasan, R.J. De Angelis, G. Ice, B.H. Davis, *J. Mater. Res.* 6 (1991) 1287-1292.
- [78] O. Bernard, A.M. Huntz, M. Andrieux, W. Seiler, V. Ji, S. Poissonnet, *Appl. Surf. Sci.* 253 (2007) 4626–4640.
- [79] R.C. Garvie, *Nature* 258 (1975) 703-704.
- [80] G. Rauchs, D. Munz, T. Fett, *Comp. Mater. Sci.* 16 (1999) 213–217.
- [81] R.H. French, S.J. Glass, F.S. Ohuchi, Y.-N. Xu, W.Y. Ching, *Physical Review B* 49 (1994) 5133-5142.
- [82] G.N. Heintze, R. McPherson, *Surf. Coat. Tech.* 36 (1988) 125–132.
- [83] J. Chevalier, L. Gremillard, A.V. Virkar, D.R. Clarke, *J. Am. Ceram. Soc.* 92 (2009) 1901-1920.
- [84] L. Borchers, M. Stiesch, F.-W. Bach, J.-C. Buhl, C. Hubsch, T. Kellner, P. Kohorst, M. Jendras, *Acta Biomater.* 6 (2010) 4547–4552.
- [85] T. Chraska, A.H. King, C.C. Berndt, *Mater. Sci. Eng. A* 286 (2000) 169–178.

- [86] L. Chen, T. Mashimo, E. Omurzak, H. Okudera, C. Iwamoto, A. Yoshiasa, *J. Phys. Chem. C* 115 (2011) 9370-9375.
- [87] R.C. Garvie, *J. Phys. Chem.* 82 (1978) 218–224.
- [88] R.C. Garvie, *J. Phys. Chem.* 69 (1965) 1238-1243.
- [89] S. Block, J.A.H. Da Jornada, G.J. Piermarini, *J. Am. Ceram. Soc.* 68 (1985) 497-499.
- [90] S. Shukla, S. Seal, *Int. Mater. Rev.* 50 (2005) 1-20.
- [91] T. Mitsuhashi, M. Ichihara, U. Tatsuke, *J. Am. Ceram. Soc.* 52 (1974) 97–101.
- [92] M. Ruhle, A.H. Heuer, in: *Advances in ceramics*, Vol. 12, (ed. N. Claussen et al.), 14–32; 1983, Columbus, OH, American Ceramic Society.
- [93] Y. Kannon, *J. Mater. Sci.* 25 (1990) 1987–1990.
- [94] Y. Hayashi, M. Masuda, J. Lee, M. Kojima, *Mater. Sci. Eng. A* 198 (1995) 71-74.
- [95] L. Amelinckx, M. Kamrunnahar, P. Chou, D.D. Macdonald, *Corros. Sci.* 48 (2006) 3646-3667.
- [96] X. Zhou, Z.F. Zhou, S.N. Lvov, D.D. Macdonald, United States patent application, Pub. No. US 2004/0086648 A1.
- [97] M. Atik, M.A. Aegerter, *J. Non-Cryst. Solids* 147–148 (1992) 813-819.
- [98] R. Di Maggio, L. Fedrizzi, S. Rossi, P. Scardi, *Thin Solid Films* 286 (1996) 127-135.
- [99] E. Setare, K. Raeissi, M.A. Golozar, M.H. Fathi, *Corros. Sci.* 51 (2009) 1802-1808.
- [100] K. Rodrigo, J. Knudsen, N. Pryds, J. Schou, S. Linderoth, *Appl. Surf. Sci.* 254 (2007) 1338-1342.
- [101] J.R. Vargas Garcia, T. Goto, *Sci. Technol. Adv. Mater.* 4 (2003) 397-402.
- [102] N. Iwamoto, N. Umesaki, S. Endo, *Thin Solid Films* 127 (1985) 129-138.
- [103] S. Somiya, T. Akiba, *J. Eur. Ceram. Soc.* 19 (1999) 81-87.

- [104] K Byrappa, M Yoshimura, Handbook of hydrothermal technology (2001), Noyes Publications, New Jersey, USA.
- [105] Y. Hao, A.S. Teja, J. Mater. Res. 18 (2003) 415-422.
- [106] M.M. Lencka, A. Andreko, R.E. Riman, J. Am. Ceram. Soc. 78 (1995) 2609-2618.
- [107] R.P. Denkwicz Jr, K.S. TenHuisen, J.H Adair, J. Mater. Res. 5 (1990) 2698-2705.
- [108] M. Yoshimura, K. Byrappa, J. Mat. Sci 43 (2008) 2085-2103.

Chapter 2
Materials and Methods

2.1 Objective of the study

The main objective of this research program is to develop a hydrothermal method for deposition of ZrO₂ coatings on stainless steel (SS) surfaces to improve its corrosion resistance properties. The alloy used in this study is austenitic Type 304L SS (composition in wt %: C, 0.028; Si, 0.55; Mn, 1.75; Mo, 0.021; Cr, 17.7; Ni, 10.4; Fe, balance, dimension: 15 × 10 × 2 mm³). The pre-oxidization of SS surface prior to ZrO₂ deposition is mandatory to get an adherent ZrO₂ film on the surface. The composition and morphology of the pre-oxidized layer decide the thickness, uniformity and adhesion of ZrO₂ coatings deposited. Susceptibility of SCC of SS after the ZrO₂ coating formation has been measured by electrochemical methods. Detailed electrochemical studies are carried out to assess the improvement in corrosion protection of SS surfaces after the ZrO₂ coatings.

- (i) It has been observed that composition and morphology of the oxide film on stainless steel surface prior to the ZrO₂ deposition plays a very important role [1, 2]. Type 304L stainless steel specimens were pre-oxidized under different conditions to form different types of oxide surfaces.
- (ii) ZrO₂ coating was developed on pre-oxidized SS surfaces by hydrothermal method. Pre-oxidized and the ZrO₂ coated surfaces were characterized by SEM-EDX, XPS, Raman spectroscopy and GI-XRD to understand the oxide structure, surface morphology, chemical states and crystal structure of the coatings. It led to establish the most suitable pre-oxidized layer as well as mechanism of formation of ZrO₂ coating on stainless surfaces.
- (iii) The Potentiodynamic polarization studies and electrochemical impedance spectroscopy studies are performed to analyze the corrosion resistance behavior of

ZrO₂ coatings. The SPM was used for qualitative analysis of nano-mechanical properties of ZrO₂ coatings.

2.2 Experimental setup

2.2.1 Glassware setup for ZrO₂ nano-particle preparation and deposition

A glass setup was used for ZrO₂ nano-particle preparation as shown in Fig. 2.1. The glass setup was the combination of 1 liter round bottomed flask, condenser, thermometer and a heating & stirring mantle. One neck of the round bottomed flask was used for online addition of base through burette.

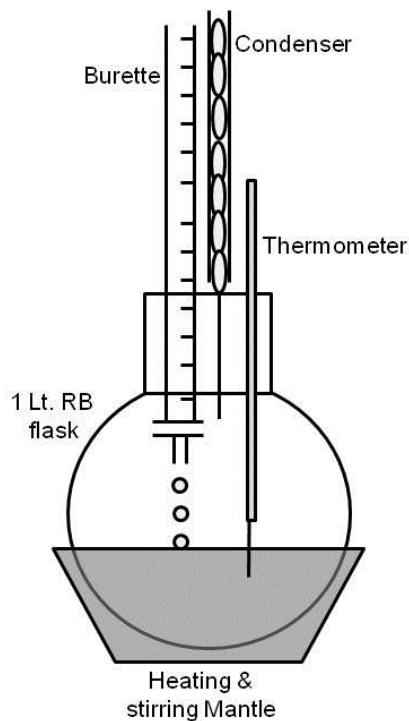


Fig. 2.1: Glassware setup used for experiments below 90°C

2.2.2 Autoclave setup for pre-oxidation of SS and ZrO₂ coatings

An autoclave setup was used to perform the pre-oxidation and ZrO₂ coating experiments as shown in Fig. 2.2. The autoclave setup was constituted of 1 liter vessel made up of SS 316L,

Teflon coated from inside. The setup involves a ceramic heater, thermocouple, sample holder (Teflon coated SS), digital temperature indicator and pressure gauge. The samples are placed inside the autoclave with the help of sample holder. All samples have a small hole at the corner and are tied to the sample holder through Teflon tape. Samples are positioned at the middle of the solution, neither at bottom where precipitates may be present, nor at top where sample may see only the vapors at high temperature.

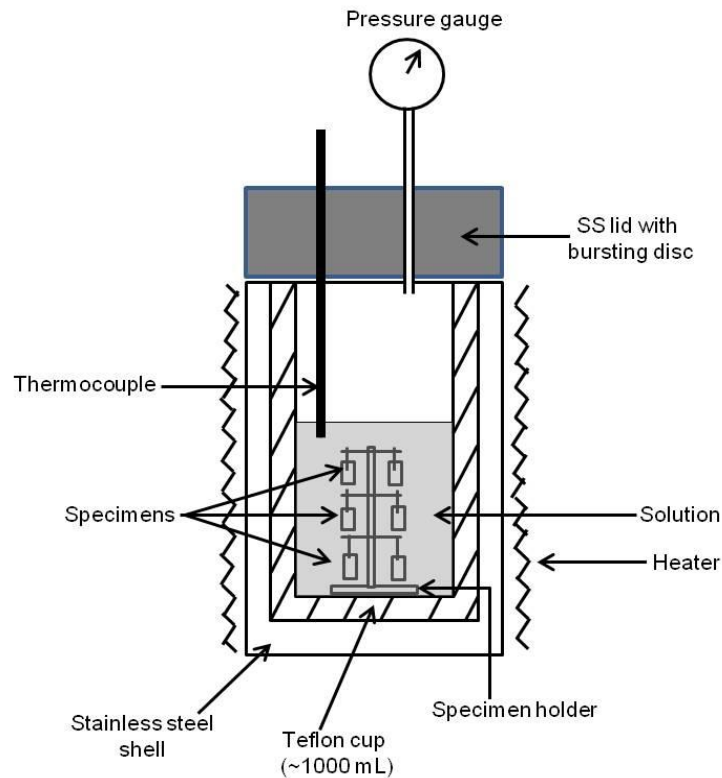


Fig. 2.2: Schematic of autoclave setup

2.3 Sensitization of SS specimens

The SS specimens were thermally sensitized in a vacuum furnace. The two different kinds of sensitization conditions were followed. Samples were sensitized at 650°C for 24 h and at

625°C for 100 h. After the heating, samples were spontaneously cooled to room temperature in vacuum furnace. Both types of sensitized samples and the non-sensitized samples were mechanically polished, cleaned and dried. The SS specimens were undergone oxalic acid etch test and double loop electrochemical potentiokinetic reactivation (DL-EPR) test to quantify the degree of sensitization (DOS). The degree of sensitization for the non-sensitized SS specimens, SS specimens sensitized at 650°C, 24 h and for the specimens sensitized at 625°C, 100 h was found to be approximately 0%, 3-4% and 25±5% respectively. The SS specimens with higher degree of sensitization (25±5%) were chosen for further experiments. Prior to all experiments, the sensitized SS specimens were mechanically polished using silicon carbide lapping (1000 grit), cleaned with acetone followed by methanol in an ultrasonic bath for 15 minutes, washed by deionized water and dried.

2.4 Pre-oxidation of the SS surfaces

2.4.1 Pre-oxidation of the SS surfaces in static autoclave

The autoclave was used for the pre-oxidation of the 304L SS surfaces in aqueous solutions at high temperature. Pre-oxidation experiments were carried out under different water chemistry conditions as described below:

2.4.1.1 Reducing water chemistry environment

The specimens were oxidized in an autoclave under reducing water conditions at pH 10.3 containing 24 ppm hydrazine and heated at 240°C, 33 atm pressure. The pH of the solution was adjusted with the help of lithium hydroxide. Prior to heating the autoclave, Ar gas was purged for 60 minutes to remove dissolved gases like O₂, CO₂ etc. from the solution. One set of SS specimens were oxidized for 5 days while another set of specimens were oxidized for 21 days.

2.4.1.2 Oxidizing water chemistry environment

The specimens were oxidized in normal water at 240°C. The initial oxygen concentration in solution was measured to be 7000 ppb. One set of samples were oxidized for 14 days while another set were oxidized for 21 days. Few of these specimens were used for pulsed laser deposition (PLD) of α -Fe₂O₃.

2.4.1.3 Oxidizing in H₂O₂ environment

The specimens were oxidized in an autoclave in the oxidizing water chemistry condition containing 5 ppm of H₂O₂ at 200°C (15.3 atm pressure) for 14 days. These specimens were used as substrates for the PLD of α -Fe₂O₃.

2.4.2 Pre-oxidation of the SS surfaces in dynamic loop

The specimens used for these pre-oxidation experiments were circular in shape with diameter 16 mm and thickness of 3 mm. The specimens were exposed to BWR coolant chemistry environment in a dynamic loop. Normal water (H₂O) is the BWR coolant and circulating normal water was used as solution. The initial pH of solution was 7 and the initial oxygen concentration in solution was measured to be 8000 ppb. Specimens were exposed for 4400 hrs (~ 6 months) at temperature 285±5°C. At high temperature, dissolved oxygen concentration was monitored several times and it is observed to be 200-300 ppb. Dissolved O₂ concentration was maintained by adding very small (~ 1ppm) amount of hydrazine. The flow rate of water was 11.2 liter per minute and the conductivity of water was <4µs/cm. After 6 months of exposure, SS specimens were retrieved from the dynamic loop system. Samples were washed with de-ionized water, dried and taken for characterization and further experiments.

2.4.3 Pulsed laser deposition (PLD) of α -Fe₂O₃ on SS surfaces

PLD is a thin film fabrication technique that include laser ablation of the target material by the bombardment of high energy pulsed laser beam at a certain vacuum pressure. The laser shooting areas of the targets experience the transition from the solid to the vapor phase, the development of a plasma plume with high energetic ions, electrons as well as neutrals take place. It is followed by the crystalline growth of the film on the heated substrate. The brief diagram of the PLD process is given in Fig. 2.3.

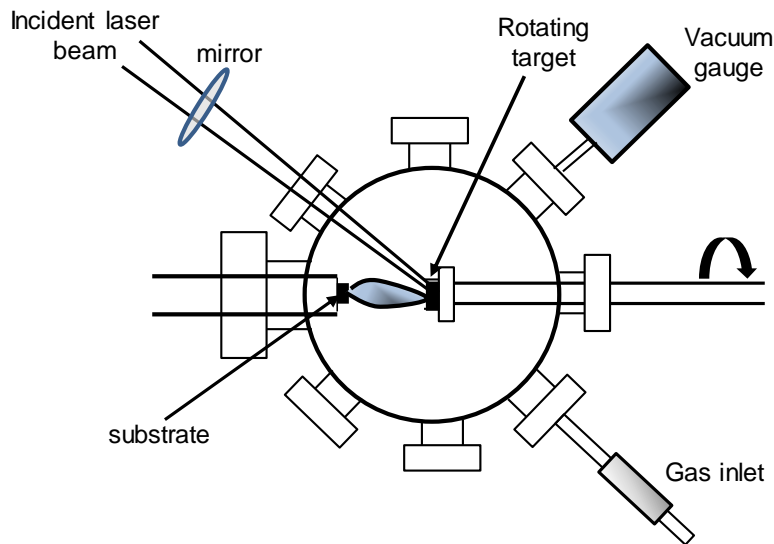


Fig. 2.3: Schematic diagram of PL deposition process on the target surface

2.4.3.1 Target Preparation

Dense and homogeneous targets are required to prepare good quality films by PLD. It avoids melting of target as well as particulate formation [3]. α -Fe₂O₃ target was prepared from commercially available α -Fe₂O₃ powder of ~99.99% purity. The powder was fine ground and compacted to a pellet of 20 mm diameter and 3 mm thickness. The pellet was sintered at 1000°C for 6 hours. The pellet had a sintered density ~90%. The pellet was characterized by Raman

spectroscopy and Fig. 2.4 shows the laser Raman spectra of α -Fe₂O₃ pallet. In the laser Raman spectra of the α -Fe₂O₃ pellet, several Raman modes at 225, 243, 288, 408, 497, 609 and 1311 cm⁻¹ are observed. All the peaks observed belong to the α -Fe₂O₃ only [4, 5].

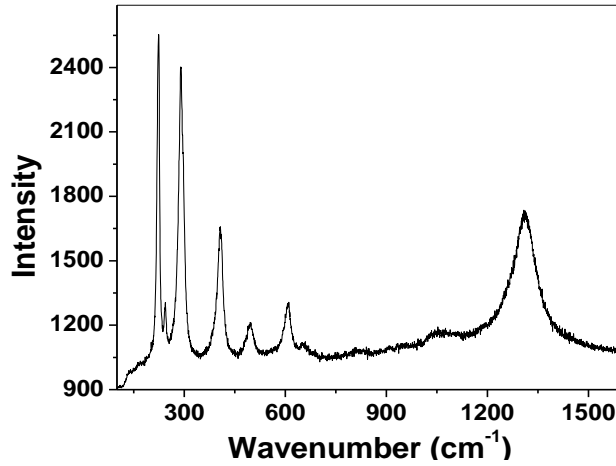


Fig. 2.4: Raman spectra of α -Fe₂O₃ pellet

2.4.3.2 α -Fe₂O₃ thin film deposition on SS surface

PLD technique was used to deposit α -Fe₂O₃ on type 304L SS surface. It has been observed that when α -Fe₂O₃ was directly deposited on stainless steel surface, the coating was non-adherent and peeled off from the substrate. It might be due to mismatch in lattice parameters of 304L SS and α -Fe₂O₃ which inhibited the growth of α -Fe₂O₃ directly on stainless steel substrate. So, α -Fe₂O₃ could not be grown on stainless steel without prior pre-oxidation. So pre-oxidized (in H₂O₂ and normal water) SS specimens were used as substrate for deposition of α -Fe₂O₃.

The target (α -Fe₂O₃) was mounted on to the target carousel using silver paste. The cleaned pre-oxidized SS substrates were mounted onto the substrate holder. The beam was focused to 2 mm on a rotating target. The substrate was kept at a distance 3 cm from the rotating

target. Deposition chamber was evacuated by using a rotary and turbo pump combination to a base pressure of ~ 0.002 Pa. After the base vacuum was achieved, the substrates were heated using a resistive heater (which is under the substrate holder). Oxygen gas was released into the chamber using a mass flow controller. In the present study, Nd-YAG laser (M/S Quanta System, 1064 nm wavelength) was used as the energy source for the deposition of thin films. The laser light was focused onto the target and the depositions were carried out with pulse width and energy of 5 ns and 450 mJ respectively. The substrate temperature was kept at 600°C and oxygen partial pressure was adjusted to 1.0 Pa. Thin film of $\alpha\text{-Fe}_2\text{O}_3$ was deposited for 30 minutes. Hematite coating formed over pre-oxidized steel substrate was found to be adherent and smooth.

2.5 Nanocrystalline ZrO_2 powder preparation

To carry out the direct deposition the ZrO_2 nano powder on stainless steel surface by hydrothermal process, ZrO_2 nanocrystalline powder is prepared [6, 7]. Nanocrystalline ZrO_2 was prepared through direct precipitation process by using $\text{ZrO}(\text{NO}_3)_2 \cdot 6\text{H}_2\text{O}$ (Fluka), $\text{NH}_3 \cdot \text{H}_2\text{O}$ (Merck), Ethanol (Merck), polyethylene glycol (PEG) 8000 and ultrapure water. Initially, 0.25M solution of zirconyl nitrate was prepared by dissolving $\text{ZrO}(\text{NO}_3)_2 \cdot 6\text{H}_2\text{O}$ in water containing ethanol (18% v/v). PEG-8000 (2.5% w/v) was added into the $\text{ZrO}(\text{NO}_3)_2$ solution. The $\text{NH}_3 \cdot \text{H}_2\text{O}$ (0.5 M) solution was added drop-wise (3 ml/min) to the $\text{ZrO}(\text{NO}_3)_2$ solution kept at 80°C with continuous stirring. The pH of the solution was adjusted to 9. A white, gelatinous precipitate obtained was filtered, washed with ethanol (18% v/v), dried at 100°C for 2 h, finely ground in pestle mortar and then calcined at 550°C for 4 h. Prepared powder was characterized by different techniques to get a complete understanding of its particle size, crystallographic phases and chemical state of zirconium.

2.6 Deposition of ZrO₂ nanoparticles on pre-oxidized stainless steel in aqueous medium

Adsorption of ZrO₂ nanoparticles on the plain polished and pre-oxidized SS surfaces was carried out by hydrothermal method. Aqueous solution containing 3.33 mM ZrO₂ nanoparticles of ~10 nm size were used for the study. Initial pH was adjusted to 6.2. The solution was sonicated for 1 h prior to the experiments to avoid agglomeration between suspended zirconia particles. The adsorption experiments were carried in the stirring condition for 5 days at 25°C, 90°C and 150°C. To study the adsorption at 25°C and 90°C, glassware setup (round bottom flask with condenser) and heating mantle with stirring facility was used. Autoclave setup with stirring facility was used for the adsorption of ZrO₂ at 150°C. For few specimens 10% w/w_{ZrO₂} sodium dodecyl sulphate (SDS) was used as surfactant to improve the coating coverage. After the deposition experiments, sample were washed with de-ionized water, dried and characterized.

2.7 Hydrothermal deposition of ZrO₂ using ZrO(NO₃)₂ and Na-EDTA

2.7.1 Hydrothermal deposition process

Zirconia coating on pre-oxidized SS specimens discussed earlier were deposited in a Teflon lined static autoclave. ZrO(NO₃)₂.6H₂O salt (3.33 mM) and Ethylenediaminetetraacetic acid disodium salt dihydrate (Na-EDTA) were dissolved in deionized water in 1:1 molar ratio. Sodium dodecyl sulphate (SDS) (10% w/w_{Zr-salt}) was used as the surfactant. pH of the solution was measured to be ~3.0 and it was maintained to 6.2 by addition of dilute NaOH. The white solution at pH 3.0 was transformed to a transparent solution while adjusting the pH to 6.2. Pre-oxidized SS specimens on which the zirconia coating is required are exposed with the above solution in Teflon lined static autoclave for 5 days at 200°C, 15.3 atm pressure. After the zirconia deposition experiment, ZrO₂ coated samples were retrieved from the autoclave, washed with deionized water, dried and characterized [2].

2.7.2 Preparation of samples to study the mechanism of growth of ZrO_2 on $\alpha-Fe_2O_3$

To understand the mechanism and interface of ZrO_2 coating on pre-oxidized SS surfaces, ZrO_2 coatings were grown for very short duration on $\alpha-Fe_2O_3$ surfaces in a 1000 ml Teflon lined static autoclave [8]. The experimental conditions of hydrothermal deposition process are same as described above (section 2.3.7.1). ZrO_2 coating was developed for different duration at $200^\circ C$. It took around 120 min to get the water temperature $200^\circ C$ and the samples were heated for different durations, viz 30 min and 60 min after reaching the desired temperature. The moment solution temperature reached $200^\circ C$, is considered as zero time. After 30 min and 60 min, the heating was stopped and the autoclave was rapidly cooled to room temperature. It took around 15-20 min to bring down the solution temperature to the room temperature. After the experiments, samples were retrieved from autoclave, washed with deionized water, dried and characterized by different techniques.

A low temperature ZrO_2 coating experiment was carried out under the same chemistry conditions at $90^\circ C$ for 5 h to understand the role of EDTA in the deposition of ZrO_2 [8].

2.7.3 ZrO_2 coating thickness enhancement by hydrothermal deposition process

Preparation of thick zirconia coating by hydrothermal method is necessary for the enhancement in corrosion resistance properties of zirconia coated samples. Two methods are adopted for the preparation of thick zirconia coatings.

2.7.3.1 By increasing the precursor concentration

Zirconia coatings on pre-oxidized SS specimens were developed in a Teflon lined static autoclave (1000 ml). $ZrO(NO_3)_2 \cdot 6H_2O$ salt and Na-EDTA (disodium salt dehydrate) were dissolved in deionized water in 1:1 molar ratio in the presence of the surfactant sodium dodecyl sulphate (SDS) (10% w/wZr-salt). 6.6 and 10.0 mM concentrations of reactants were chosen for

ZrO₂ coating experiments instead of 3.33 mM concentrations. Initial pH of the solution was maintained at 6.2 by using dilute NaOH. Pre-oxidized specimens were kept in the solution for 5 days at 200°C.

2.7.3.2 Multiple rounds of ZrO₂ deposition with the fresh reactants

ZrO₂ coating experiments were repeated for four times with the 3.33 mM concentrations of reactants. Every time, old solution was discarded and fresh reactants were used for deposition. After the second, third and fourth rounds of ZrO₂ deposition, samples were retrieved from autoclave, washed, dried and characterized by different techniques. This method enhances the coating thickness and has been discussed in details in chapter 7.

2.8 Thickness measurement of coatings

2.8.1 Surface Profilometry

Thickness of α -Fe₂O₃ films developed by PLD process was measured by a profilometer (DEKTAK6M Veeco-stylus profiler). This method is useful to measure the thickness in the range of 20 nm-1 mm with 1 nm accuracy. α -Fe₂O₃ was deposited on Si substrate along with the SS substrate and a step was created by putting mask on the Si substrate. The diamond profiler of diameter 12.5 microns was made to travel on the film across the mask on the substrate. Vertical Resolution is - 1.5nm, Error- ~ 5%. The step size was measured by taking the difference between the height of coated and uncoated regions of the sample. Three values of the steps are measured and the average has been taken. The average thickness was found to be approximately 0.5 μ m (500 nm).

2.8.2 Dissolution Method for ZrO₂ coatings thickness estimation

Average thickness of zirconia coating for some of the samples was measured by chemically descaling the coating followed by UV-Vis Spectroscopy [9].

Dissolution of ZrO₂ coatings: 5 ml of concentrated HNO₃ and 7 ml of 40% HF were mixed to prepare the solution for ZrO₂ coating dissolution. ZrO₂ coated sample was immersed in this solution and heated at 60°C for 15-30 minutes. It was observed that all the types of ZrO₂ coatings got dissolved at these conditions. The solutions were filtered through Whatman filter paper and diluted to a fixed volume of 50 ml.

Solution preparation for UV-Vis spectroscopy: The Zr solution, blank and standards of Zr were prepared for Zr analysis by taking absorption spectra using UV-Vis spectroscopy. The Zr solution was prepared by taking the 20 ml of the solution from the Zr solution. It is mixed with 50 ml HCl (1:1), 10 ml of 0.005M SDS and 2 ml of 0.2% (w/v) arsenazo-III solution and this solution was made up to 100 ml. For preparing the Zr⁴⁺ standards of 0.1, 0.2, 0.3 and 0.4 ppm of standard solution were prepared. ZrO(NO₃)₂·6H₂O was taken as the Zr⁴⁺ source. After 30 minutes of preparation of solutions, the wavelength (nm)-absorbance spectra was recorded for blank. The maximum absorbance is observed at 680 nm wavelength. The maximum absorbance was recorded for all the samples at 680 nm against blank. The maximum absorbance is plotted vs Zr concentration for standards (Fig. 2.5).

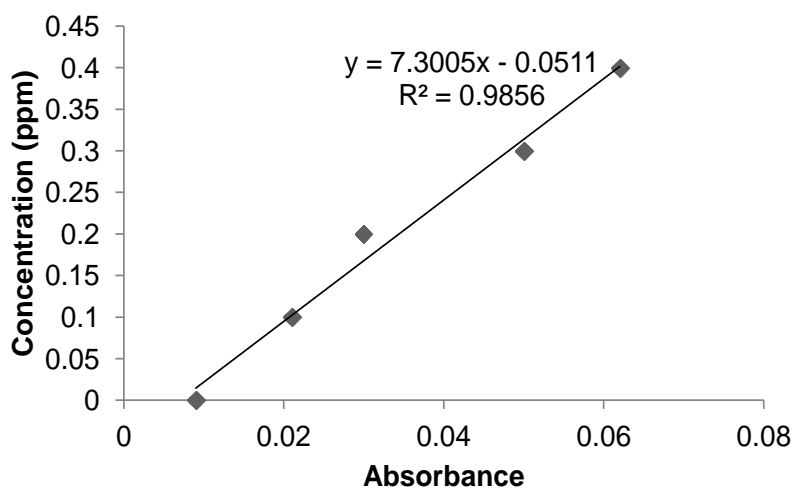


Fig. 2.5: Plot of maximum absorbance vs Zr concentration by UV-Vis spectrometer

The straight line is obtained for maximum absorbance vs Zr concentration in solution. Zr concentration in the unknown solutions was determined by fitting the absorbance value in that straight line. By taking the Zr concentration, surface area of SS sample and density of ZrO₂, thickness of ZrO₂ coating can be calculated by equation 2.1.

$$\text{Thickness of ZrO}_2 \text{ coating (cm)} = (C_{\text{Zr}} \cdot 50 \cdot \rho_{(\text{ZrO}_2)} \cdot (\text{At. wt.})_{\text{Zr}}) / A_{(\text{sample})} \cdot (\text{Mol. wt.})_{\text{ZrO}_2} \quad 2.1$$

Where, C_{Zr} = Zr concentration in solution ($\mu\text{grams/grams}$), $\rho_{(\text{ZrO}_2)}$ = Density of ZrO₂ (g/cm^3), $A_{(\text{sample})}$ = area of sample (cm^2).

Atomic weight of Zr, molecular weight of ZrO₂ and density of the ZrO₂ coating were taken as 94g, 124g and 5.68g/cm³ respectively.

2.8.3 Cross-sectional SEM analysis

Thicknesses and thickness uniformity of the few ZrO₂ coatings were studied by cross-sectional SEM images of the films. For cross-sectional SEM analysis, one side of the zirconia coated sample is mechanically polished by 1200 grade emery paper followed by diamond polishing of 0.5 μm size. The samples were ultrasonically cleaned with soap solution, water and methanol. The polished side of the zirconia coated samples was analyzed by SEM (model CAMSCAN 3200, UK). The cross-section images acquired by tilting the stage to approximately 10-15° with respect to normal beam.

2.9 Characterization of materials and coatings

2.9.1 Optical microscopy

Optical microscope (OLYMPUS, Japan make GX71 model) was used for the imaging of the sensitized SS samples after the etching in oxalic acid [10]. It has been used to see the step, dual and ditch kind of structures in sensitized SS samples.

2.9.2 Scanning electron microscopy/Energy dispersive x-ray spectroscopy

Scanning electron microscope (SEM) is an advanced imaging tool for high-resolution imaging of surfaces. The high energy electron beam scans the specimen and interaction of scanning electrons and the atoms of the specimen produce signals. These signals provide the information about the specimen's surface topography and composition. The high energy incident electrons interact elastically and in-elastically with the sample's surface and near-surface material and produce various types of electrons like secondary electrons (SE), backscattered electrons (BSE) and x-rays. SE and BSE are used for imaging while x-rays are used for compositional analysis. The inelastic scattering results in emission of lower-energy electrons ($\leq 50\text{eV}$) called secondary electrons (SE). The SE can be formed by collision of scanning electrons with the nucleus that results in substantial energy loss or by the ejection of loosely bound electrons from the sample atoms. Different detectors are used for detecting the SE and x-rays. Energy dispersive x-rays are emitted from the sample when it is bombarded with a high energy electron beam and the technique called energy dispersive spectroscopy (EDS). EDS is used for composition analysis

In the present thesis, SEM attached with energy dispersive x-ray spectroscopy (EDS) was used for surface imaging and elemental composition analysis of pre-oxidized as well as ZrO_2 coated samples. Following models of SEM were used in the present thesis: (1) CamScan 3200 microscope, UK and (2) FEG-SEM (model Hitachi S-4800 Type I). EDS of OXFORD model INCA attached with all the systems was used.

2.9.3 Raman Spectroscopy

Raman spectroscopy is a nondestructive technique, used to study the structure, symmetry, and phase of the material [11]. It involves molecular and crystal lattice vibrations and is

therefore, sensitive to the composition, bonding, chemical environment, phase and crystalline structure of the material [12]. Raman spectroscopy deals with the inelastic scattering of light after its interaction with material, resulting in a difference in incident and scattered energy. In Raman spectroscopy, the scattered light is observed in perpendicular direction to the incident light. Scattered light consists of two types of light: (i) light due to Rayleigh scattering, where the frequency is same as that of the frequency of incident light (ν_0) and (ii) Raman scattering where the light frequency is either greater or less than that of the incident light. In Raman spectroscopy, the shift in frequency from that of the incident frequency is measured. The shift in frequency ($\Delta\nu$) in Raman spectroscopy can be written as (equation 2.2).

$$\Delta\nu = \nu_0 \pm \nu_m \quad (2.2)$$

where $\nu_0 + \nu_m$ and $\nu_0 - \nu_m$ lines are called the Stokes and anti-Stokes lines, respectively [13]. In this thesis, all Raman spectra were obtained using a dispersive micro Raman Spectrometer (HORIBA Jobin Yvon, France, HR-800) equipped with 1800 grooves/mm holographic grating and 100x objective lens. Argon ion (Ar^+) laser of wavelength 514.5 nm was used as the excitation source. Laser was focused using a 100x LD objective lens on the sample surface with laser power of $\sim 0.5\text{mW}$. Raman spectra were acquired with spectral coverage from 100 to 2000 cm^{-1} with spectral resolution of $< 1\text{cm}^{-1}$ with 30 s data acquisition time and using a charge coupled device (CCD) detector. The spectrometer is fitted with an optical microscope that gives the advantage of acquiring the Raman spectrum at different locations. In this work, Raman spectroscopy included the study of ZrO_2 nano-powder, pre-oxidized and ZrO_2 coated SS samples

The phase fraction of the nano-crystalline ZrO_2 powder was estimated by Raman spectroscopy. The fraction of the monoclinic phase (f_m) in the nanocrystalline ZrO_2 powder was calculated using equation 2.3 [14],

$$f_m = \sqrt{0.19 - \frac{0.13}{X_m - 1.01}} - 0.56 \quad (2.3)$$

$$\text{Where } X_m = \frac{I(180) + I(192)}{I(148) + I(180) + I(192)} \quad (2.4)$$

'I' stands for the peak area under respective Raman modes.

2.9.4 X-ray Photoelectron Spectroscopy (XPS)

XPS is a surface sensitive spectroscopic technique that measures the elemental composition, empirical formula, chemical state of the elements in the material. XPS spectra are obtained when the x-ray beam hitting the specimen and simultaneously measuring the kinetic energy and number of electrons that escapes from the top 0 to 10 nm of the specimen surface. The bombardment of soft x-rays to a sample in ultrahigh vacuum (UHV) leads to the emission of photoelectrons from the materials. The kinetic energy of emitted photoelectrons (KE) is measured. The binding energy (BE) of the atomic orbital from which the photoelectron generates is calculated by equation 2.5.

$$BE = h\nu - KE - \Phi \quad (2.5)$$

Where $h\nu$ is the energy of incident x-ray and Φ is the work function of the spectrometer. The typical value of the spectrometer work function is around 4.5 eV. XPS equipment require UHV ($P < 10^{-9}$ millibar) to avoid the energy loss of photoelectrons due to scattering by molecules of air and also to avoid the surface contamination due to adsorption of gas molecules during the course of the experiment. In XPS, the transition of the vacuum from atmospheric pressure (1 atm = 760 bar) to UHV ($P < 10^{-9}$ millibar) is achieved by the combination of two or more different vacuum pumps. The pumps used for preliminary pumping are rotary pumps and turbo molecular pumps. The ion pumps are used to reach UHV level with auxiliary titanium sublimation pumps.

XPS provides both qualitative and quantitative information about the elemental composition, oxidation states of elements of solid surfaces. A low resolution, wide scan of XPS spectra gives the information about the presence of various elements and elemental composition on the sample surfaces. A high resolution scan peaks (narrow scan) provide information about the oxidation state of elements and molecular environment around the atom by analyzing photoelectron chemical shift and valence band structure.

For this work two different XPS models have been used. (i) Some experiments were done using the instrument Model VG ESCALAB MK200X. Al $k\alpha$ with beam energy 1486.6 eV and FWHM 0.85 eV was used as the X-ray source. The wide scan spectra and the narrow scan spectra were collected with pass energy of 100 eV and 20 eV respectively. The binding energy resolution of the XPS spectra is approximately ~ 1.0 eV. (ii) Some experiments are performed using SPECSLab2, Germany with monochromatic Al $k\alpha$ (1486.7 eV) as X-ray source. The wide scan spectra and the narrow scan spectra were collected with pass energy of 50 eV and 10 eV respectively. The resolution obtained from the photoelectron spectra is approximately ~ 0.5 eV. Hemispherical analyzer with 150 mm mean diameter fitted with channeltron electron multiplier was used for the photoelectron detection [15]. Carbon 1s peak at 285.1 eV was taken as internal standard for binding energy measurement of charging samples. The calibrations of the instruments were performed by acquiring Au 4f_{7/2}, Ag 3d_{5/2}, Cu 2p_{3/2} line at 84.0, 368.2 and 932.5 eV respectively [16].

'Eclipse V2.1' software was used for the deconvolution of the spectra. The component spectra were fitted with a Gaussian-Lorentzian peak functions on a Shirley background. The XPS was used in this thesis for the following studies:

1. Elemental composition and oxidation state analysis of all the pre-oxidized SS specimen surfaces and ZrO₂ coated samples.
2. Stoichiometry of nano-crystalline ZrO₂ powder, study of adsorption of (atomic%) ZrO₂ nano powder on pre-oxidized SS surfaces.
3. To study the interaction of ZrO₂ with α-Fe₂O₃ and the formation of interface for the adhesion of ZrO₂.

The elemental composition of the pre-oxidized SS surface and the atomic concentration of Zr are determined by using following equation:

$$C_A = (I_A/S_A) / \sum_n (I_n/S_n) \quad (2.6)$$

Where C_A = atomic percent of element A (%), I_A = intensity of element A, S_A = sensitivity factor for A, I_n = intensity of element n, S_n = sensitivity factor for n.

2.9.5 X-Ray Diffraction

X-ray diffraction (XRD) is a nondestructive technique used to determine the microstructure, crystallinity, phase and stress of the material. An XRD pattern is a plot of intensity versus diffraction angle (2θ) where 2θ position represents the angle of diffraction of a particular plane from which the d-spacing as well as lattice parameter can be derived. The full width at half maximum (FWHM) of the peaks provide the crystallite size of the nano-particles and stress in the material. Microstructural characterization of the ZrO₂ nano-powder, thin films of ZrO₂ and pre-oxidized SS specimens were carried out by XRD. The diffraction patterns for ZrO₂ nano-powder were recorded by using a XRD system (model Philips (XPRT MPD). Cu k α radiation was used for scanning 2θ from 20° to 70° with 2θ scanning speed of 0.05 degree/minute. λ for Cu k α is 1.5418 Å. From the 2θ values, d-spacings (d) were calculated using Bragg's equation [17].

$$n\lambda = 2d\sin\theta \quad (2.7)$$

where n is the order of reflection, λ is the Cu $k\alpha$ wavelength, d is the spacing between the planes in the atomic lattice and θ is the Bragg's angle. The peaks were indexed with reference to JCPDS files of the respective material.

XRD measurements of thin films was performed by grazing incidence x-ray diffractometer (GIXRD, Siemens D500, Germany, STOE, Germany) to avoid the inference signals from the substrate and get stronger signal from the film. In the GIXRD scan, 2θ is scanned with a fixed grazing angle of incidence of 0.5° and diffraction data was recorded for the 2θ range of 20 - 65° . GIXRD was used for the characterization of ZrO_2 coatings and pre-oxidized SS surfaces. Gaussian fitting of the peaks gives the 2θ and FWHM values and those values were used to calculate the average crystallite size.

The particle size of nano-crystalline ZrO_2 (D) powder and ZrO_2 films were calculated by using the Scherrer's formula (Equation 2.8),

$$D = 0.9\lambda / \beta\cos\theta \quad (2.8)$$

where $\beta^2 = B^2 - b^2$, B and b are the angular half-widths for the sample under investigation and a standard sample, respectively. Analytically pure, crystalline Si powders have been used as the standard sample. Particle size is estimated by taking the average of the particle sizes obtained from 3 diffraction planes (2θ).

2.9.6 Transmission electron microscopy

TEMs use very high energy electrons (few KeV-1MeV) as "source" and their much lower wavelength makes it possible to get a resolution of the order of a few angstrom (10^{-10} m). The greatest advantages of TEM are the high magnification ranging and its ability to provide both image and diffraction information from a single sample.

The elastic scattering of electrons by specimen gives rise to diffraction of electron beams at certain angles satisfying Bragg's law. The diffracted beams are collected at the back focal plane and are observed as electron diffraction pattern. An image is formed in TEM analysis from the interaction of electron beam with the specimen, as the electron beam passes through the specimen. The image is magnified and focused onto an imaging device, such as a fluorescent screen, on a layer of photographic film, or to be detected by a sensor such as a CCD camera. If the transmitted beam is selected to generate images it is called bright field (BF) image, while the diffracted beam is selected it is called dark field (DF) image.

The diffraction image on the screen of the TEM consists of a series of spots. Each spot corresponds to a satisfied diffraction condition of the sample's crystal structure. In TEM, user can choose the part of the specimen to obtain the diffraction pattern. This is called selected area electron diffraction (SAED). SAED is referred to as "selected" because selected area aperture is located below the sample holder in the TEM column which can be inserted into the beam path to block the beam. Selected area aperture is a thin strip of metal containing several different size holes. It can be moved to block all of the electron beam except for the small fraction passing through one of the holes. By moving the aperture hole to the particular section of the sample, particular area is selected by the aperture, and only this section will contribute to the SAD pattern on the screen. SAD can be used to identify crystal structures and examine crystal defects. It is similar to x-ray diffraction, but it can examine the area as small as several hundred nanometers in size. SAD patterns are a projection of the reciprocal lattice, with lattice reflections showing as sharp diffraction spots. SAD is essential for setting up dark-field imaging conditions. SAD of nanoparticles or nanocrystals give ring patterns analogous to those from x-ray powder

diffraction, and can be used to identify texture and discriminate nanocrystalline material from amorphous phases.

TEM studies were carried out in a Philips CM200 ATEM using a LaB₆ filament and an acceleration potential of 200kV. TEM was used for size and phase distribution study of ZrO₂ nano powder prepared. The ZrO₂ powder were first dispersed in ethanol, sonicated for about 10 min, spread on a 3mm diameter carbon coated copper grid and finally dried at 40°C.

2.9.7 UV-Vis spectroscopy

UV-Visible spectrophotometer is an instrument useful for measurement of optical properties of materials using Beer-Lambert law. When light of intensity I₀ passes through a material, both transmission and absorption occur. The % of transmittance is given by equation 2.9.

$$\%T = I / I_0 * 100 \quad (2.9)$$

The relation between absorbance and transmittance is given by equation 2.10.

$$A = \log (1/T) \quad (2.10)$$

where A is the absorbance of the film and T is the transmittance of the film [18].

The UV-Vis spectroscopy was used to estimate the average thickness of ZrO₂ on pre-oxidized SS surfaces. Absorption spectra of the Zr-complex solutions were collected on a UV-visible spectrophotometer Thermo Nicolet Evolution 500 (Thermo Electron Corporation, Waltham, MA, USA).

2.9.8 Zeta potential

When a solid particle is suspended in a liquid, it develops some charge around it. The liquid layer surrounding the particle exists as two regions. The inner region where the ions are strongly bound to the solid surface known as Stern layer and an outer (diffuse) region where they

are less firmly associated [19]. There is a notional boundary in the diffuse layer inside which the ions and the particles form a stable entity. When a particle moves, ions within the boundary move with it. Those ions beyond the boundary stay with the bulk dispersant solution. The potential at this boundary (surface of hydrodynamic shear) is called the zeta potential.

In this thesis, zeta potentials of ZrO_2 nano-particles were determined with a Nanosizer Z (Malvern Instruments, Malvern, UK) by phase analysis light scattering with applied field strength of 2.5×10^3 V/m. The light source was He-Ne laser operated at 633 nm operating at 4.0 mW. The zeta potential values are calculated from the electrophoretic mobility data using Smoluchowsky approximation. The experiment was carried out using a quartz cuvette (universal 'dip' cell) with 10 mm light pathway. The zeta potential of ZrO_2 was measured in aqueous solution with concentration of ZrO_2 , 0.01% (wt/vol.) at different pH. The initial pH measured of the ZrO_2 solution was 5.0. The various ZrO_2 suspensions of pH varying from 4 to 9 were prepared. The pH of the solutions were maintained by the addition of dilute HNO_3 or dilute NaOH . Prior to zeta potential measurements, all the solutions were sonicated for 1 hr and then allowed to settle for 24 h to get a stable suspension. The zeta potential measurements were performed at 25, 40 and 70°C. The effect of dispersant sodium dodecyl sulfate (SDS) on the zeta potential of nanocrystalline ZrO_2 and $\alpha\text{-Fe}_2\text{O}_3$ was also studied as a function of pH at 25°C. The suspensions were prepared using the same concentration 0.01% (wt/vol) for both ZrO_2 and $\alpha\text{-Fe}_2\text{O}_3$. The 10% ($w_{\text{SDS}}/w_{(\text{ZrO}_2/\text{Fe}_2\text{O}_3)}$) surfactant was used. Initial pH of the ZrO_2 and Fe_2O_3 suspension in the presence of SDS was measured to be 6.4 and 9.3 respectively. The pH of the suspensions was adjusted to the pH range varying from 4 to 9 and the suspensions were sonicated for 1 hr prior to zeta potential measurements.

2.9.9 Atomic Force Microscopy

Atomic force microscopy (AFM) is a type of scanning probe microscopy (SPM) that provides very high-resolution imaging of the solid surface in the angstrom level. The AFM probes the surface of a sample with a sharp tip, integrated to the free end of a spring cantilever that is 100 to 200 μm long. Forces involved in the tip sample interaction affect the interaction of probe with the sample. Van der waals interactions are the dominant interactions at short probe-sample distances in the AFM.

2.9.9.1 Topography Imaging

The topography imaging is the most common application of an AFM instrument. It is based on the interaction between tip and sample and provides important information about the surface morphology such as surface roughness and grain size. During topography mapping, as the tip moves across the surface, the interatomic potential makes the cantilever to bounce up and down with the changes in contours of the surface. Thus, topographic features of the samples can be mapped out by measuring the cantilever deflection. A laser and a detector are used to monitor the cantilever motion and atomic force between the sample and tip. Initially, surface topography of cleaned silicon substrate was mapped using SPM. The change in Z signal ($\sim\Delta Z$) or Z elevation as a function of X and Y co-ordinates were obtained and plotted. Mean and full width half maximum values from these plots were obtained and then actual values of roughness were calculated. More than two areas of surfaces of each sample were scanned. Then average value was achieved. Roughness distribution curve is given in Fig. 2.6.

Surface roughness can be represented by both average (R_a) and root mean square (RMS) values, but each is calculated differently. R_a is calculated as the roughness average of a surface measured microscopic peaks and valleys. RMS is calculated as the Root Mean Square of a

surface measured microscopic peaks and valleys. Each value uses the same individual height measurements of the surfaces peaks and valleys, but uses the measurements in a different formula as above. Average roughness (R_a) values are reported in this thesis.

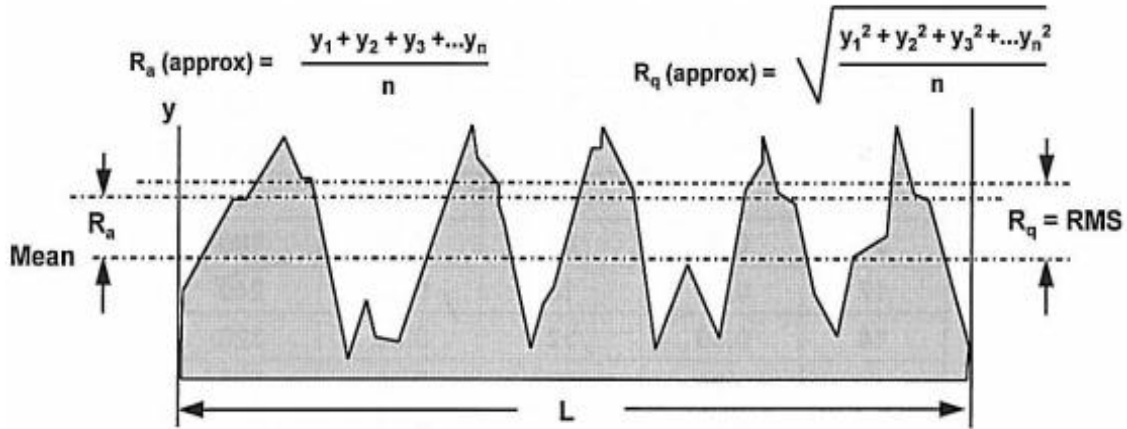


Fig. 2.6: Roughness distribution curve

2.9.9.2 Atomic Force Acoustic Microscopy

AFM based techniques can be used to test the mechanical properties like hardness, elastic modulus, Young's modulus on a nanoscale [20]. Atomic Force Acoustic Microscopy (AFAM) is a modified commercial version of AFM, in which increased dynamic stiffness of cantilever is exploited for quantitative measurement and imaging of mechanical properties. In AFAM, sample under investigation is made to vibrate at ultrasonic frequency. While sample is vibrating at ultrasonic frequency, cantilever is scanning the sample surface through the tip in contact mode. The cantilever remains above the sample surface and vibrates at characteristic frequencies. The frequency values depend on the cantilever shape, dimensions, and mechanical properties such as density and Young's modulus. In this work, rectangular shape cantilever is attached rigidly on one end and free on the other. AFAM technique can be used in spectroscopy mode and imaging mode. Only Imaging mode is used in this thesis. In AFAM imaging mode, the cantilever scans

the sample surface and the amplitude of cantilever vibrations is measured. The imaging mode of AFAM is used for qualitative analysis of nano-mechanical properties. The qualitative amplitude image can be obtained by exciting the signal at a fixed frequency. The contrast of the image strongly depends on the excitation frequency. Although the elastic properties cannot be quantified by AFAM images but the images are indicative of the uniformity/ differences in elastic properties of sample.

2.9.9.3 Force-distance (FD) spectroscopy

FD spectroscopy is useful for analysis of local mechanical properties like adhesion and elasticity at nano-metric level. It is the study of interaction forces between the cluster of atoms in the AFM cantilever tip and the sample surface. AFM actually measures the distance between the cantilever and the sample (Z), not the distance between the sample and the tip (d). Z is controlled during the measurement but ' Z ' and ' d ' are related by the following equation.

$$d = Z - (\delta_c + \delta_s) \quad (2.11)$$

F vs Z curve can be converted into F vs d curve. When the fixed end of the cantilever is extended towards and retracted from the sample, it's free end deflects. The force measurements are performed by recording the deflection of cantilever free end. A triangular wave-voltage pattern is applied to the electrodes for the Z -axis scanner. The scanner expands and contracts in the vertical direction; it generates the relative motion between the cantilever and the sample. The cantilever deflection is measured at many points. By multiplying the cantilever deflection (δ_c) and spring constant, force sensed by the AFM probe can be calculated. During FD spectroscopy, degree of deformation of nano coatings (δ_s) is influenced by the surface adhesive strength and thin film-substrate adhesion forces are calculated by measurement of force required to

separate the tip from the surface of thin film [21]. A complete force-curve records the force between tip and the sample during tip approach as well as retraction.

In this thesis, characterization of the samples was carried out by a Scanning Probe Microscope (model: NTEGRA Multimode, Russia). Topographic images of plain SS, pre-oxidized and zirconia coated samples are obtained with respect to Si(100). Qualitative nano-mechanical properties of the zirconia coated samples have been studied by AFAM with respect to mirror finished Si(100) and SS. In contact mode AFM, AFAM images were obtained for SS and zirconia coated samples along with the surface topography. Larger area AFAM imaging gives the information about stiffness uniformity of coatings and smaller area scans reveals the variation in stiffness along with local nano-structures. Stiff cantilever and constant force was used for all the samples during AFAM experiments. FD spectroscopy was carried in contact mode AFM for measuring the adhesive properties of zirconia thin films to the different pre-oxidized SS surfaces. The adhesion force values are measured with error bar of <10%.

2.10 Electrochemical corrosion techniques

2.10.1 Electrochemical cell setup

The electrochemical cell comprises of specimen as working electrode, platinum as non-polarizable counter electrode and saturated calomel electrode as reference electrode. Counter electrode is used for completing the circuit and the potential has to be applied with respect to reference electrode. The schematic of the electrochemical cell for carrying out electrochemical experiments is shown in Fig. 2.7. Ar purging was used for DL-EPR tests only. Reference electrode is separated from the solution by luggin probe, and is placed close to the working electrode to eliminate the effect of solution resistance. The experiments were performed at room temperature and 90°C using a potentiostat/ galvanostat (model SP-300 from Biologic Science

Instruments) system. The electrochemical cell is heated by using heating mantle for the experiments conducted at 90°C. A condenser (water) is attached to one neck of the given electrochemical cell to maintain the temperature for the experiments performed at 90°C.

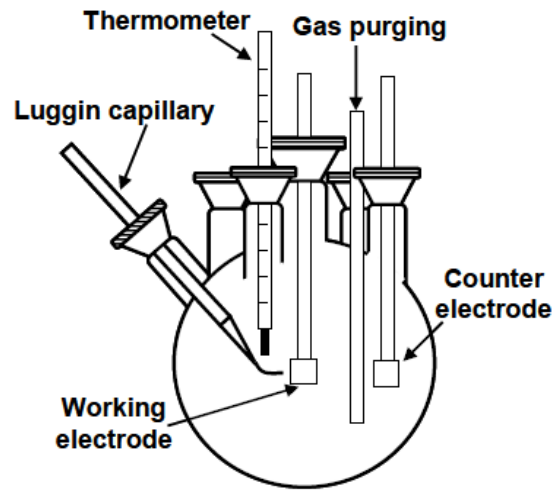


Fig. 2.7: Schematics of an electrochemical cell for corrosion study

2.10.2 Sensitization study

SS specimens were sensitized under different conditions in a vacuum furnace. Following methods were used to detect the SCC susceptibility.

2.10.2.1 Oxalic acid etch test

There are five methods described by ASTM A 262 [22] (Practice A - Practice E) for detecting the susceptibility to intergranular corrosion (IGC) in austenitic stainless steel. Practice A is the oxalic acid etch test for classification of etch structures of austenitic stainless steels which is the most simple and can be performed in few minutes. In this test, electroetching is performed in 10% oxalic acid at a current density of 1A/cm². After this, the samples are washed,

dried and viewed under optical microscope and the resultant structures are classified as "Step", "dual" or "ditch" based on grain boundary etching.

2.10.2.2 Double-loop electrochemical potentiokinetic reactivation Test

DL-EPR method is the advanced version of EPR method for quantitative measurement of the degree of sensitization [23]. In the DL-EPR test, the specimen is polarized anodically from the corrosion potential through the active region followed by the reactivation scan in the reverse direction by the same scan rate. During the anodic polarization, formation of a passive film takes place on the surface of the specimen. When the reverse scan is carried out, the passive film breaks down on chromium depleted area. Fig. 2.8 shows that two loops are generated, an anodic loop and a reactivation loop during the test.

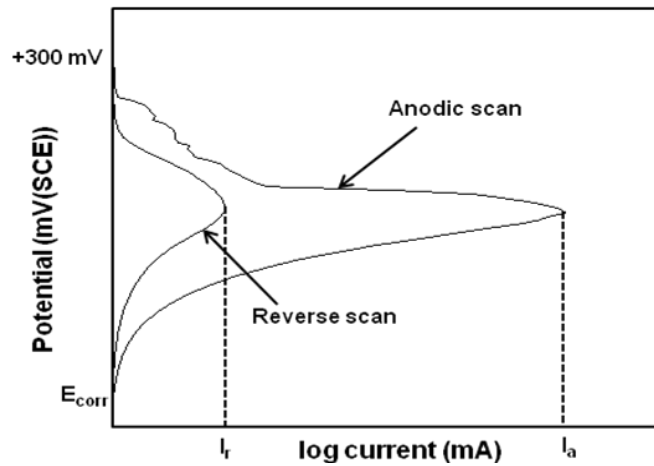


Fig. 2.8: Schematics of DL-EPR test

DL-EPR tests are conducted in 0.5 M sulphuric acid containing 0.0001 M ammonium thiocyanate (NH_4SCN), taken in a polarization cell at room temperature. NH_4SCN is a strong corrosive agent and a grain boundary activator. It has been used as a depassivating agent in the test, since it reactivates the Cr depleted regions by destroying preferentially the oxide films

formed on those regions [24, 25]. Dry, oxygen free argon gas was purged for one hour before and during the test, to remove dissolved oxygen from the aqueous solution. The mounted specimen was immersed in the solution and the OCP was noted for 60 minutes. The potential is scanned from the open circuit potential to +300 mV (SCE) and then immediately scanned back to the open circuit potential at a scan rate of 100 mV/minute. The maximum anodic current (I_a) and maximum reactivation current (I_r) were measured from the anodic and reactivation anodic curves respectively and degree of sensitization (DOS) was calculated using the following equation [26-28]

$$\text{DOS \%} = I_r/I_a * 100 \quad (2.12)$$

where I_r is the reactivation peak current density and I_a is the anodic peak current density. In this thesis, the DL-EPR test was carried out to measure the DOS for the non-sensitized and sensitized SS specimens.

2.10.3 Corrosion resistant properties by electrochemical analysis

The corrosion resistant properties of plain SS, pre-oxidized SS specimens and zirconia coated samples were studied by potentiodynamic polarization and electrochemical impedance spectroscopy (EIS). All the electrochemical studies were performed in 0.1 M Na_2SO_4 aqueous solution. In the present investigations OCP vs. time measurements were carried prior to all electrochemical measurements for 60 minutes for attaining stability at the electrode-electrolyte interface. Electrochemical tests are performed at least three times to check the reproducibility for various types of specimens examined in the present investigation.

2.10.3.1 Potentiodynamic polarization

Potentiodynamic polarization (PDP) is a DC technique that provides the information regarding corrosion rate, corrosion mechanism, pitting susceptibility, passivity and corrosion of

specific materials in designated environments. PDP method involves changing the potential of the working electrode at a fixed rate, and monitoring the current density which is produced as a function of potential [29].

The PDP studies are carried out at room temperature and 90°C using a potentiostat/galvanostat system. The polarization behavior of the samples is obtained by polarizing the working electrode from -0.6V to +1.2V with respect to OCP at a scan rate of 0.5mV per second. The corrosion current (i_{corr}) was determined from the intersection of anodic and cathodic Tafel lines or from that of E_{corr} with the suitable Tafel line. In this thesis, PDP studies are performed for the plain sensitized SS specimen, different types of pre-oxidized specimens and zirconia coated SS samples. Corrosion resistance behavior of zirconia coatings developed on different pre-oxidized SS surfaces, different thicknesses of zirconia coatings on the single pre-oxidized surface are compared by PDP studies.

2.10.3.2 Electrochemical impedance analysis

Electrochemical impedance spectroscopy (EIS) is a widely used technique to analyze the complex material properties like dielectric properties, mass transport, defect density, passive film stability and coating degradation [30-34]. Impedance is the ratio of applied voltage to the resulting current which means it is the opposition to the flow of current. In an electrochemical system, it is the combination of resistance and reactance [30]. The impedance technique makes the use of very small amplitude signal without disturbing the desired properties of materials to be measured. Mostly, it is non-destructive and provides a rapid way of measurements with potentiostat and frequency response analyzers and data processing using appropriate software programs.

This technique involves the determination of cell impedance, in response to a small AC (alternating current) signal at any constant DC potential (preferably at the OCP to minimize the DC currents), over frequencies ranging from a micro to mega-hertz. The locus of impedance as a function of angular frequency is called impedance spectrum. The most common approach for data interpretation is based on the equivalent circuit concept, exemplified in the model of Randles [35]. Impedance Z , can be expressed in complex number notation as equation 2.13.

$$Z = Z' + jZ'' \quad (2.13)$$

where Z' represent the real (resistance) and Z'' represents the imaginary components (reactant). Nyquist plot and Bode plot are the two most commonly used diagrams for the graphical representation of impedance data. In the Nyquist plot, the impedance is represented by a real part and an imaginary part. Therefore, the Nyquist plot is termed as the complex plane impedance plot. In the Bode plot, the modulus of the impedance and the phase angle are both plotted as a function of frequency.

EIS data from different samples were recorded at OCP by applying a sinusoidal voltage of ± 10 mV in the frequency range of 10^5 –0.01Hz. The impedance data obtained were analyzed by the commercial software package EC-Lab V10.1x. In this thesis, EIS experiments were carried out at room temperature and 90°C. EIS studies were done for the plain polished SS specimens, different types of pre-oxidized SS specimens and zirconia coated SS samples. EIS measurements help in study of optimizing the zirconia coating thickness on SS surface for corrosion resistant applications.

2.11 References

- [1] T.-K. Yeh, Y.-C. Chein, B.-Y. Wang, C.-H. Tsai, *Corros. Sci.* 50 (2008) 2327–2337.
- [2] N. Garg, V.K. Mittal, S. Bera, P. Chandramohan, C.R. Das, S. Velmurugan, *Thin Solid Films* 545 (2013) 222–228.
- [3] D.B. Chrisey, G.K. Hubler, “Pulsed laser deposition of thin films”, Wiley Interscience Publication (1994) (ISBN No. 0-471-59218-8).
- [4] D. Bersani, P.P. Lottici, A. Montenero, *J. Raman Spectrosc.* 30 (1999) 355-360.
- [5] D.L.A. de Faria, S. Venâncio Silva, M.T. de Oliveira, *J. Raman Spectrosc.* 28 (1997) 873-878.
- [6] N. Garg, V.K. Mittal, S. Bera, A. Dasgupta, V. Sankaralingam, *Ceram. Int.* 38 (2012) 2507-2512.
- [7] S. Wang, X. Li, Y. Zhai, K. Wang, *Powder Technol.* 168 (2006) 53–58.
- [8] N. Garg, S. Bera, G. Mangamma, V.K. Mittal, R. Krishnan, S. Velmurugan, *Surf. Coat. Technol.* 258 (2014) 597–604.
- [9] P.R. Patnaik, G.P. Panigrahi, *current science* 83 (2002) 695-696.
- [10] <http://www.molphys.leidenuniv.nl/monos/students/pdf/smon02.pdf>
- [11] G. Gouadec, P. Colomban, *Prog. Cryst. Growth Charact. Mater.* 53(2007) 1.
- [12] <http://alpha1.infim.ro/cost/pagini/handbook/chapters/raman.htm#4.1.7.1>.
- [13] J.R. Ferraro, K. Nakamoto, C.W. Brown, *Introductory Raman Spectroscopy* (Second edition) Elsevier, 2003, ISBN: 978-0-12-254105-6.
- [14] E. Djurado, P. Bouvier, G. Lucazeau, *Journal of SolidState Chemistry* 149 (2000) 399-407.
- [15] D.A. Skoog, F.J. Holler and T.A. Nieman, “Principles of Instrumental Analysis”, Harcourt Asia Pte Ltd., 2001.

- [16] C.D. Wagner, W.M. Riggs, L.E. Davis, J.F. Moulder, G.E. Mullenberg, Handbook of XPS, P.E. Corporations (1979) Minnesota.
- [17] T.J.B. Holland, S.A.T. Redfern, J. Appl. Crystallogr. 30 (1997) 84.
- [18] M. Fox, "Optical Properties of Solids", OxfordUniversity Press, ISBN No: 0-19-850612-0., D. F. Swainhart, J. Chem. Educ. 39 (7) (1962) 333.
- [19] E.J.W. Verway, J.Th.G. Overbeek, Theory of the Stability of Lyophobic Colloids, Elsevier, Amsterdam, 1948.
- [20] F. Marinello, P. Schiavuta, S. Vezzù, A. Patelli, S. Carmignato, E. Savio, Wear 271 (2011) 534–538.
- [21] A. Lazauskas, V. Grigaliūnas, A. Guobienė, M. Andrulevičius, J. Baltrusaitis, Thin Solid Films 520 (2012) 6328-6333.
- [22] ASTM Standard Practice A 262-93a, "Standard Practice for Detecting Susceptibility to Intergranular Attack in Austenitic Stainless Steels," in Annual Book of Standards, Vol. 3.02 (Philadelphia, PA: ASTM, 1988).
- [23] C. Cihal, A. Desestret, M. Froment, G. H. Wagner, "Tests for Evaluation of Sensibility of Stainless Steels to Intergranular Corrosion," Proc. 5th European Corros. Cong. (Paris, France: European Federation on Corrosion, 1973), p. 249.
- [24] M. Prazak, Corrosion 19 (1963) 75-80.
- [25] P. Novak, R. Stepec, F. Franz, Corrosion 31 (1975) 344-347.
- [26] M.K. Ahn, H.S. Kwon, J.H. Lee, Corrosion 51 (1995) 441-449.
- [27] Y.S. Lim, H.P. Kim, J.H. Han, J.S. Kim, H.S. Kwon, Corros. Sci. 43 (2001) 1321-1330.
- [28] M. Casales, V.M. Salinas-Bravo, A. Martinez-Villafane, J. G. Gonzalez-Rodriguez, Mater. Sci. Eng. A 332 (2002) 223-230.

- [29] Z. Ahmad, Principle of corrosion engineering and corrosion control, Ed: Zaki Ahmad, Elsevier, 2006.
- [30] J.R. Dygas, SolidState Ionics, 176 (2005) 2065-2078.
- [31] I. Betova, M. Bojinov, V. Karastoyanov, P. Kinnunen, T. Saario, Electrochim. Acta 55 (2010) 6163-6173.
- [32] R. Cabrera-Sierra, J.M. Hallen, J. Vazquez-Arenas, G. Vazquez, I. Gonzalez, J. Electroanal. Chem. 638 (2010) 51-58.
- [33] T. Ohtsuka, T. Otsuki, Corros. Sci. 40 (1998) 951-958.
- [34] M. Kendig, F. Mansfeld, S. Tsai, Corros Sci, 23 (1983) 317-329.
- [35] J.E.B. Randles, Discuss. Faraday Soc. 1 (1947) 11-19.

Chapter 3

*Pre-oxidation of stainless steel
surfaces*

3.1 Introduction

Pre-oxidation of the stainless steel (SS) surface prior to ZrO_2 deposition is the basic requirement for developing an adherent ZrO_2 coating [1]. ZrO_2 coatings do not grow on the plain polished SS surface. Prior to ZrO_2 deposition, it is mandatory to develop an oxide layer on the SS surface. The oxidation of SS surface creates suitable sites on the SS surface for the substrate to Zr-precursor chemical interaction and nucleation of the coating in the hydrothermal process. The surface chemical composition, structure and morphology of the substrate surface oxide layer influence properties of the ZrO_2 coatings deposited. Yeh et. al. [2] observed that the SS surface covered by oxides like hematite ($\alpha-Fe_2O_3$) structure results in more amount of nano-zirconia deposition compared to spinel oxides like magnetite (Fe_3O_4) under the same deposition conditions. The nature of bond between substrate and depositing material decide the degree of adhesion. The suitable chemical composition and lattice parameters of the substrate surface oxide lead to the formation of stable interface compound in between the surface and depositing material. Formation of a stable interface compound lead to adhesive and thick ZrO_2 coating. In addition, the interacting surface area is increased by increasing the surface roughness and reducing the substrate oxide particle size. SS surface oxide composed of nano-particles results in higher number of nucleation centers and inclusion of Zr-precursor on the substrate surface will be favorable.

In this thesis, different pre-oxidized SS surfaces were developed with varying surface composition and morphology. The physical properties like surface coverage, thickness of ZrO_2 coatings are observed to be highly influenced by the surface composition and morphology of the pre-oxidized layers. This chapter deals with the preparation and characterization of different types of pre-oxidized SS surfaces. Pre-oxidation of the SS specimens were performed by

different methods viz (i) by hydrothermal method in a static autoclave, (ii) hydrothermal method in a dynamic loop and (iii) by pulsed laser deposition (PLD) to form oxides on SS of different compositions. In the process of oxidation in static autoclave different water chemistry environments are used to grow different types of oxides on SS surfaces. The details of the aqueous environment of oxidation have been discussed chapter 2 as well as later in this chapter. Pre-oxidized specimens were characterized by various techniques like SEM-EDS, AFM, Raman spectroscopy, GI-XRD and XPS to understand the morphology and phases of the oxide films developed over SS surfaces. The use of the various characterization techniques specific to the pre-oxidized specimens is given below.

3.1.1 SEM

The surface morphologies of the oxide films grown on SS after pre-oxidation under different environments were examined by SEM images. SEM images reveal the uniformity and surface coverage of oxide films. Size and shape of the oxide particles developed are also studied. The shape of the oxide particles is useful for distinguishing the different kind of SS oxide like rhombohedral oxides and spinel oxides.

3.1.2 Raman Spectroscopy

SS oxides are mainly constituted of spinels such as Fe_3O_4 , NiFe_2O_4 , FeCr_2O_4 and rhombohedral structures like $\alpha\text{-Fe}_2\text{O}_3$ and $\text{Fe}_{2-x}\text{Cr}_x\text{O}_3$ [3, 4, 5]. Laser Raman spectroscopy is useful for identifying the structures like spinel oxides and rhombohedral oxide formed on stainless steel surface after oxidation [4]. Most of the spinel oxides show five Raman active modes, namely A_{1g} , E_g and $3T_{2g}$ peaks [6]. In ferrites, A_{1g} ranges from 700-680 cm^{-1} , E_g ranges from 336-306 cm^{-1} , $T_{2g}(1)$ ranges from 579-538, $T_{2g}(2)$ ranges from 490-486 and $T_{2g}(3)$ ranges from 226-193 cm^{-1} [7]. Rhombohedral structure like $\alpha\text{-Fe}_2\text{O}_3$ has D_{3d}^6 space group and shows

$2A_{1g}$ and $5E_g$ Raman active bands [8]. For $\alpha\text{-Fe}_2\text{O}_3$, peaks at 227 and 497cm^{-1} correspond to the A_{1g} mode while peaks at 226 , 245 , 291 , 298 , 413 , 611cm^{-1} correspond to the E_g mode [8]. Peak at 1320 cm^{-1} appears as the overtone of a forbidden peak at $661\text{-}662\text{ cm}^{-1}$ [9]. The depth of information in Raman spectroscopy is around $0.1\text{-}0.2\text{ }\mu\text{m}$. The thicknesses of pre-oxidized layers formed by autoclave oxidation are $< 0.1\text{ }\mu\text{m}$. Even then the SS substrate signal was not observed in the Raman spectra as SS is not Raman active. The analyses from the Raman spectra for the pre-oxidized SS samples are summarized in Table 3.1 given at the end of this chapter.

3.1.3. XPS

The surface chemical compositions of the pre-oxidized specimens are analyzed by XPS technique. It gives the information about the oxidation state of the elements forming the pre-oxidized layers which confirms the phases identified from Raman spectroscopy. Oxidation of SS in autoclave takes place in two ways; (i) oxidation of the alloy surface by the reaction and diffusion of the oxygen containing species into the alloy from water at high temperature and (ii) the dissolution of alloy components into water and re-deposition of the oxide particles formed in suspension on the oxide layer. These two mechanisms are responsible for the formation of two distinct layers on the SS. It is established that SS oxide layers are constituted of the very compact inner layer composed of smaller particles and the outer layer composed of scattered larger particles. The XPS technique gives the information from the outer layer ($\sim 5\text{nm}$ from the top surface). Different depths of information of Raman and XPS techniques give a complete understanding of the high temperature oxidation mechanism of SS surfaces. The elemental composition and binding energy of all the constituents for pre-oxidized SS specimens are summarized in Table 3.2 given at the end of this chapter.

3.1.4 GI-XRD

GI-XRD spectra are used to identify the metal oxide phases present in the oxide layers. It gives quite distinguished peaks for spinel and rhombohedral types of oxides. The conclusions from the Raman spectra and XPS analysis are confirmed by GI-XRD.

3.1.5 AFM

Particle size and surface morphology of the pre-oxidized SS specimens are studied by AFM. The grain size and shape of oxide particles grown during pre-oxidation treatment are examined by AFM topographic images. Surface roughnesses of pre-oxidized SS specimens are measured with respect to mirror finished Si (100). The AFM images of mirror finished Si (100) and plain SS are shown in Fig. 3.1.

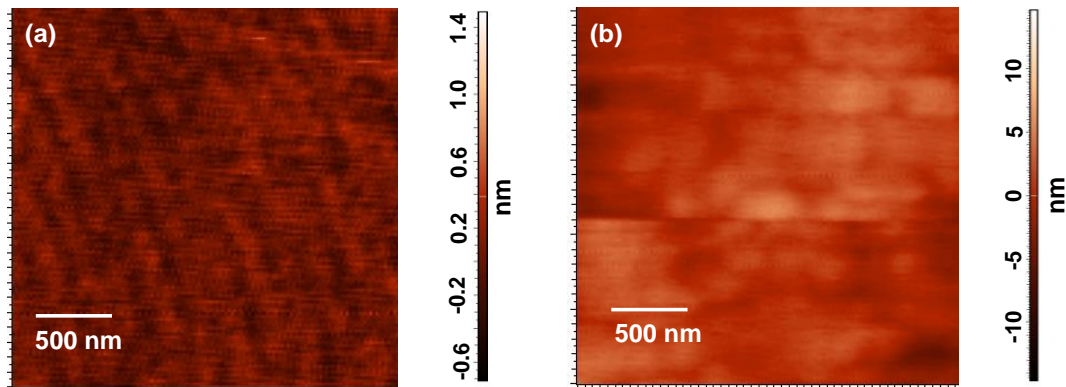


Fig. 3.1: AFM micrographs of the (a) Si (100) (b) Plain polished SS

Average surface roughness of Si (100) is 0.3 nm while the average surface roughness of plain polished SS substrate is 3 nm. AFM image of the plain SS Specimen (Fig. 3.1b) shows that the surface is neatly polished with no elevations present and polishing grooves are within the range of 10 nm.

3.2 Pre-oxidation of SS in static autoclave in reducing water chemistry conditions

Type 304L SS specimens were pre-oxidized in reducing water chemistry environment at 240°C for 5 and 21 days in a Teflon lined static autoclave. Pre-oxidized SS specimens are designated as POH-5 and POH-21 respectively. The experimental details of the preparation for both the specimens are already discussed in section 2.4.1.1.

3.2.1 Pre-oxidation for 5 days

The SEM image (Fig. 3.2) shows that the SS specimen surface is completely covered with the compact layer of oxide particles after SS oxidation in reducing environment for 5 days. The oxide particles developed are regularly shaped, having straight sides and sharp angles. Majority of the oxide particles are homogeneous in size ($<0.5 \mu\text{m}$). The Raman spectra (Fig. 3.3) show an intense sharp line at 687 cm^{-1} and smaller intensity peaks at 570 and 488 cm^{-1} . Weak signals at 570 and 488 cm^{-1} are the characteristic peaks of NiFe_2O_4 [10]. It is reported [6] that NiFe_2O_4 films show a characteristic strong peak at 701 cm^{-1} at 0.5 mw laser power. Here, the Raman spectrum shows the strong peak at 687 cm^{-1} instead of 701 cm^{-1} . Shift of the characteristic peak from 701 cm^{-1} to 687 cm^{-1} indicating that stoichiometry of NiFe_2O_4 is not maintained in the oxide particles. It is observed that peak at 687 cm^{-1} is very sharp toward the right side but it's significantly broad at its left side. A large amount of Cr rich spinel like NiCr_2O_4 , FeCr_2O_4 show their characteristic Raman peaks in this region [11]. The broadness of the peaks in range of $605\text{-}667 \text{ cm}^{-1}$ may correspond to chromite type of spinel oxides such as $\text{NiFe}_x\text{Cr}_{2-x}\text{O}_4$ ($x < 1$) and FeCr_2O_4 [5, 12]. So, it can be concluded from the Raman spectra that different type of spinel oxides with dominant non-stoichiometric nickel ferrite and significant amount of chromites are present on the surface of SS specimens. The analysis from the Raman spectra is summarized in Table 3.1.

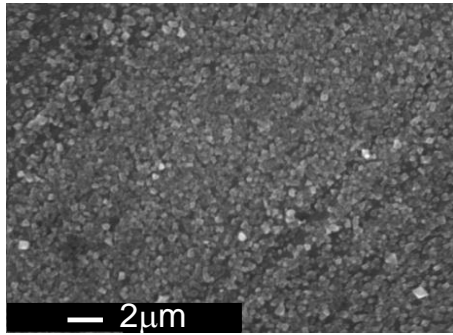


Fig. 3.2: SEM image of the pre-oxidized SS specimen POH-5

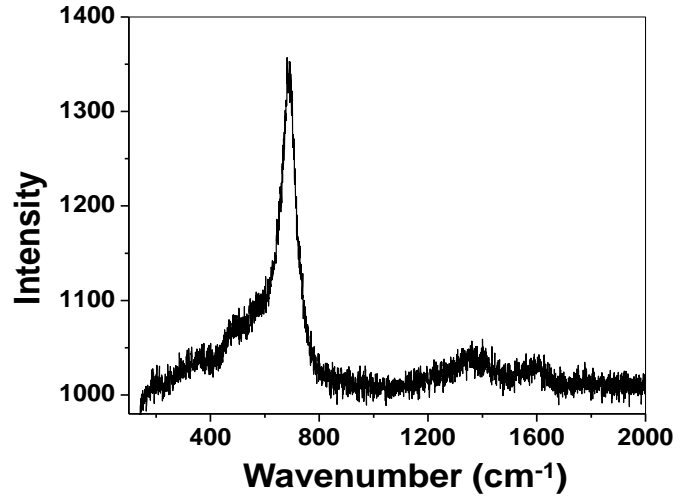


Fig. 3.3: Raman spectra the pre-oxidized SS specimen POH-5

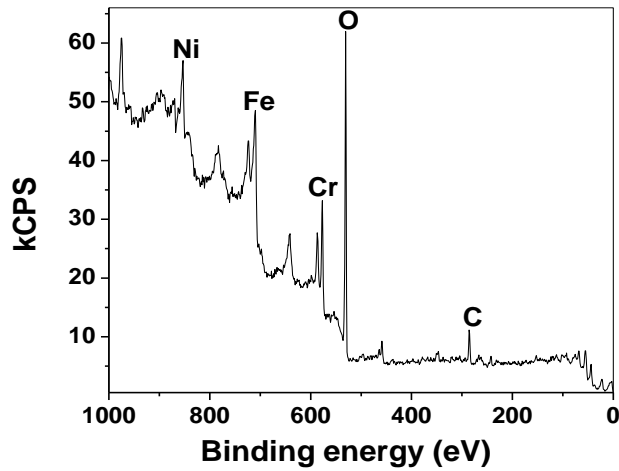


Fig. 3.4: XPS wide scan of the POH-5

The XPS wide spectrum of the pre-oxidized SS specimen is shown in Fig. 3.4. The surface composition obtained from XPS analyses shows that a significant amount of Fe, Cr and Ni (Table 3.2) are present on the surface. The binding energy of elements and atomic concentration (at %) of oxygen indicated that the surface is covered by ferrite type of structures. The binding

energy of Ni 2p peak at 855.2 eV indicates the formation of Ni-ferrite in the sample POH [13]. Ni enrichment (Table 3.2) indicates the dominance of Ni-ferrites on the surface.

3.2.2 Pre-oxidation for 21 days

The surface morphology of the POH-21 specimen is studied by SEM and AFM and the micrographs are represented in Fig. 3.5. The SEM image (Fig. 3.5a) shows that the surface is completely covered with oxides like the previous specimen (POH-5). Oxide particles are regularly shaped, having straight sides and sharp angles with size range of 200-500 nm (Fig. 3.5a). The AFM topographic image (Fig. 3.5b) shows the faceted oxide grains and calculated average roughness of the specimen surface is ~25 nm.

Raman spectra (Fig. 3.6a) show that the surface of POH-21 specimen is mainly composed of different types of spinel oxides [6, 7, 10-12, 14] (Table 3.1). The main peak at 690 cm^{-1} corresponds to non-stoichiometric ferrites like $\text{Ni}_x\text{Fe}_{3-x}\text{O}_4$, $\text{NiFe}_x\text{Cr}_{2-x}\text{O}_4$ and FeCr_2O_4 [4-6, 12]. The weak signals at 570 and 488 cm^{-1} belong to NiFe_2O_4 [7]. GI-XRD pattern (Fig. 3.6b) shows that all peaks are belonging to spinel oxides such as magnetite and Ni-ferrite [15-17]. A weak SS substrate signal (marked by S) is also observed.

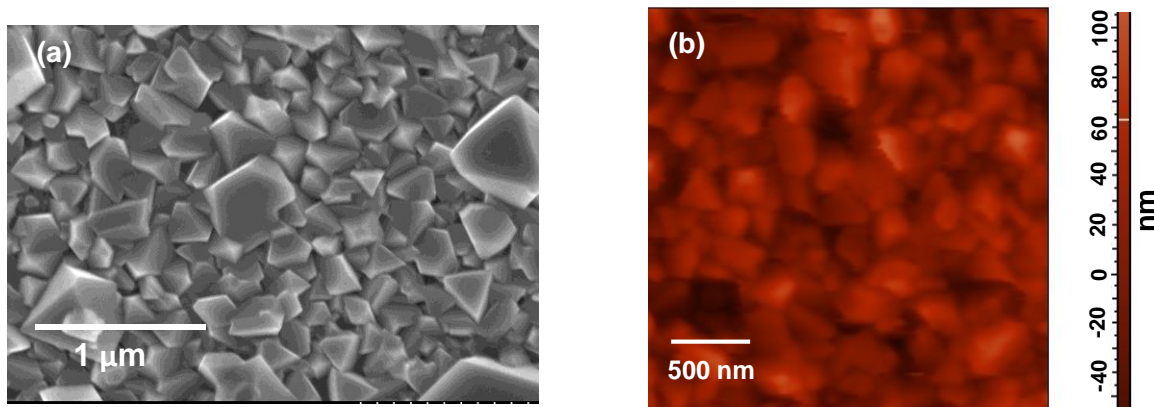


Fig. 3.5: Micrographs of POH-21 (a) SEM image, (b) AFM topographic image

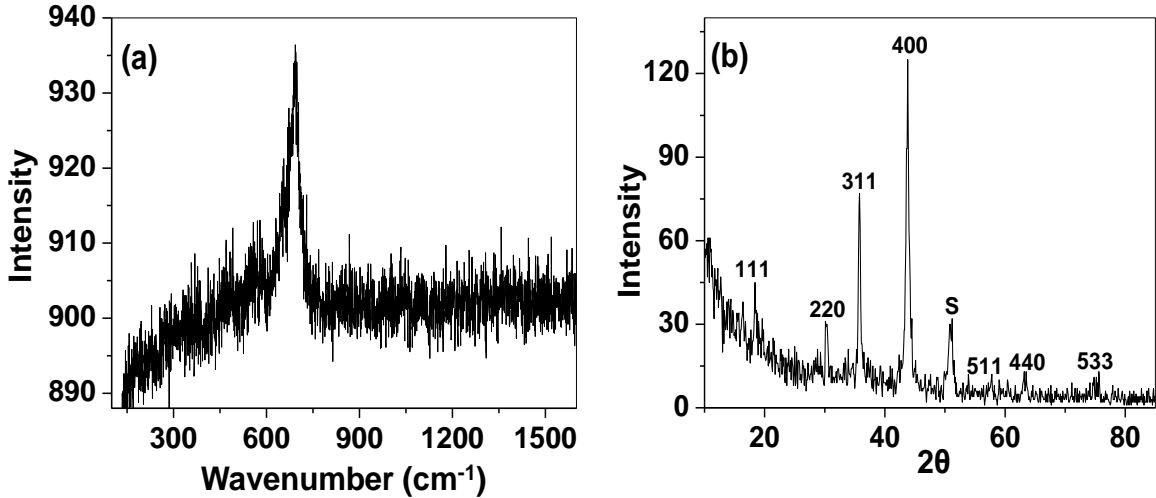


Fig. 3.6: (a) Raman spectra of POH-21, (b) GI-XRD of the POH-21

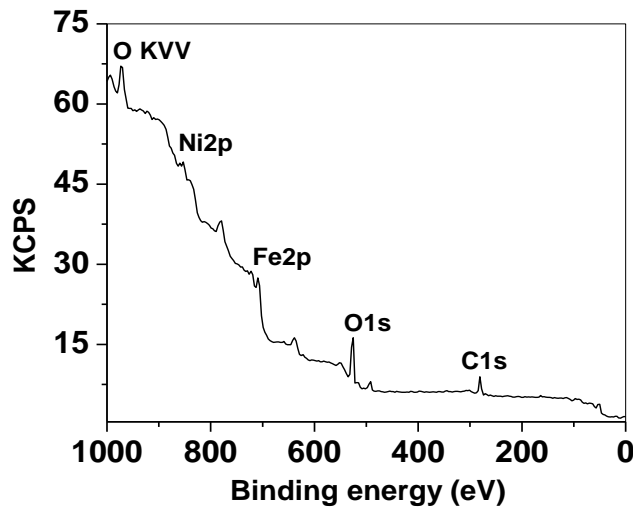


Fig. 3.7: XPS wide scan of the POH-21

The XPS wide scan (Fig. 3.7) and narrow scan (Fig. 3.8(a-d)) spectra are obtained for the elemental analysis and chemical composition of the pre-oxidized specimen POH-21 (Table 3.2). The binding energy of Ni 2p peak at 855.2 eV indicates the presence of Ni²⁺ in Ni-ferrite form [13]. Fe 2p_{3/2} peak is wider with full width at half maximum (FWHM) of 5.1 eV compared to that for pure Fe³⁺ (4.1 eV) which indicates the presence of both Fe³⁺ and Fe²⁺. Ni enrichment (Table 3.2) and Cr depletion on the surface confirms that the pre-oxidized surface is mainly

constituted of Ni-ferrites. It is clear from XPS, Raman and GI-XRD analysis that the specimen surface is composed mainly of spinel oxides like non-stoichiometric Ni-ferrites. Small amount of Ni-chromites and FeCr_2O_4 is also present on the surface.

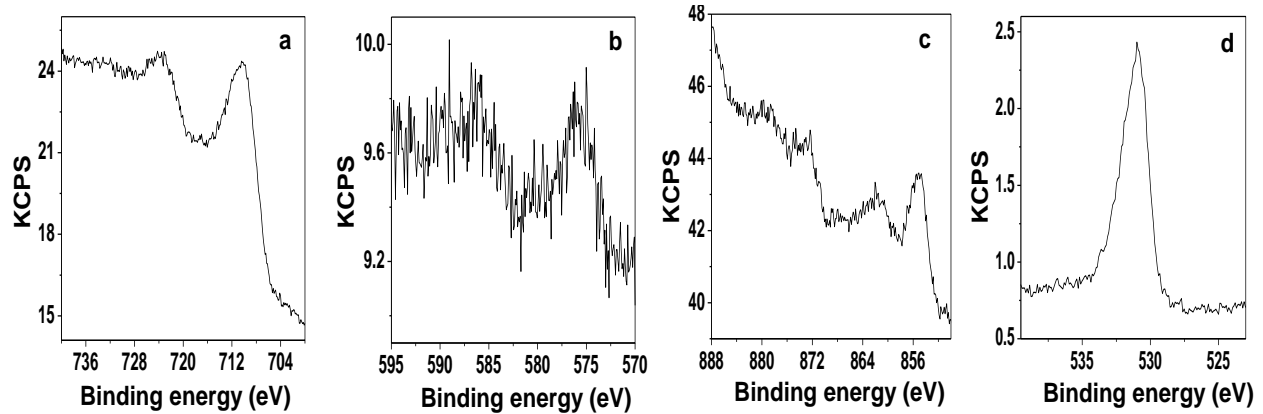


Fig. 3.8: XPS elemental scan of POH-21 specimen (a) Fe2p, (b) Cr2p, (c) Ni2p and (d) O1s

The pre-oxidized layers on the both sets of POH specimens are consisting of spinel oxides only with small difference in stoichiometry. There may be some difference in the thickness of the pre-oxidized layer, but it is assumed that the composition and surface morphology of the pre-oxidized surface has direct contribution to the growth of the ZrO_2 layer on SS surface.

3.2.3 Mechanism of oxide film formation

The SS oxide films developed under high temperature reducing water chemistry environments tend to show the presence of different type of non-stoichiometric spinel oxides like nickel ferrite and chromites [14, 18]. In this work, regular shaped grains of non-stoichiometric spinel oxides like Ni-ferrite and chromite are developed on the surfaces of SS specimens pre-oxidized under reducing water chemistry environments. XPS chemical composition analysis

shows that the Cr concentration is reduced to 3 at% after 21 days oxidation treatment. On the other hand, Ni got enriched on the surface with increase in exposure time (Table 3.2).

Growth of oxide layer on stainless steel surface in high temperature water is the result of both solid state reaction and solution transport process followed by precipitation of oxide particles [19]. At the early stage of oxidation, Fe and Ni cations released preferentially from the stainless steel surface. Fe and Ni dissolve in the solution in the form of hydroxides due to the reducing environment. So, the surface was enriched in oxides of remnant Cr forming spinel oxides like FeCr_2O_4 due to the reducing environment of the solution. At the same time inward diffusion of oxidant from solution also takes place that contribute to the formation of inner layer. Metastable hydroxides like $\text{Ni}(\text{OH})_2$ and $\text{Fe}(\text{OH})_2$ in solution might have diffused into the surface at preferential sites, where nucleation or growth of $\text{Ni}_x\text{Fe}_{3-x}\text{O}_4$ occur. So, the SS oxides are mainly constituted of non-stoichiometric Ni-ferrites and significant amount of chromites after the 5 days of immersion (POH-5). The $\text{Ni}(\text{OH})_2$ and $\text{Fe}(\text{OH})_2$ precipitated on Cr rich surface forming nickel and iron chromites having formula $\text{NiFe}_x\text{Cr}_{2-x}\text{O}_4$ as a result of solid state reaction [19, 20]. Fe and Ni oxides nucleate as ferrites due to the reducing environment. The long immersion time results in the nucleation of oxide particles in water (Fe, Ni oxides) that adsorbed on the surface oxide layer by precipitation thereby form the outer layer [20]. After 21 days of exposure, the surface will be mainly covered with the particles precipitated as nickel ferrites. The reducing water chemistry condition in the autoclave led to the conversion of Fe^{3+} to Fe^{2+} with formation of Ni-substituted magnetite type oxide. So the surface of POH-21 is mainly covered with oxides having spinel structure and mainly non-stoichiometric nickel ferrites like $(\text{Fe}_2^{3+}\text{Fe}^{2+}_x\text{Ni}_{1-x}^{2+})\text{O}_4^{2-}$.

3.3 Pre-oxidation of SS in static autoclave under normal water conditions

Type 304L SS specimens were pre-oxidized in double distilled water (initial oxygen concentration 7000 ppb) at 240°C for 14 and 21 days in a Teflon lined static autoclave. The pre-oxidized SS specimens are designated as POO-14 and POO-21 respectively. The experimental details of the preparation for both the specimens are discussed in section 2.4.1.2.

3.3.1 Specimens prepared in 14 days

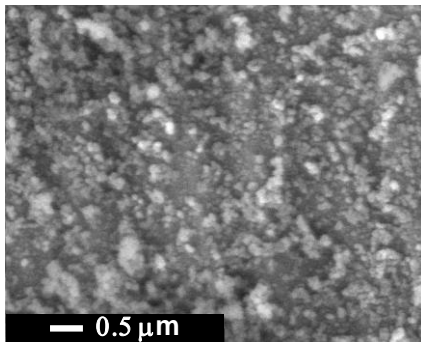


Fig. 3.9: SEM image of POO-14

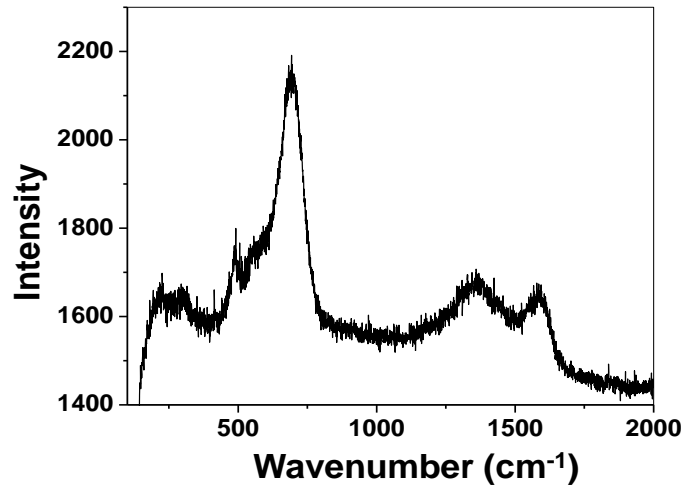


Fig. 3.10: Raman spectra of POO-14

The SEM image (Fig. 3.9) shows the formation of oxide film on the SS surface. The oxide film is consisting of very compact small grains ($\ll 0.1\mu\text{m}$) along with few large grains. Shape of the oxide particles is nearly spherical without any sharp sides and angles. The Raman spectra (Fig. 3.10) of the sample shows an intense broad peak at 692 cm^{-1} , weak and broad peaks at 222, 298, 546-556, 1359 and 1588 cm^{-1} and a sharp distinct peak at 489 cm^{-1} were observed. Peak at 489 cm^{-1} reflects the presence of the NiFe_2O_4 , while the broad peak at $546\text{-}556\text{ cm}^{-1}$ correspond to Cr_2O_3 [12] and solid solution of $\alpha\text{-Fe}_{2-x}\text{Cr}_x\text{O}_3$ ($2 > x > 1$). Weak signals at 222 cm^{-1} , 298 cm^{-1} and 1359 cm^{-1} correspond to the $\alpha\text{-Fe}_{2-x}\text{Cr}_x\text{O}_3$ phase where $x < 1$ [9, 21]. Intense and broad peak at

692 cm^{-1} represents the presence of both FeCr_2O_4 and rhombohedral oxides like $\alpha\text{-Fe}_{2-x}\text{Cr}_x\text{O}_3$ where $x > 1$ [22]. So surface of the specimen is dominated by $\alpha\text{-Fe}_{2-x}\text{Cr}_x\text{O}_3$ ($0 < x < 2$) type of rhombohedral systems, FeCr_2O_4 is present in significant amount while small amounts of NiFe_2O_4 is also present (Table 3.1).

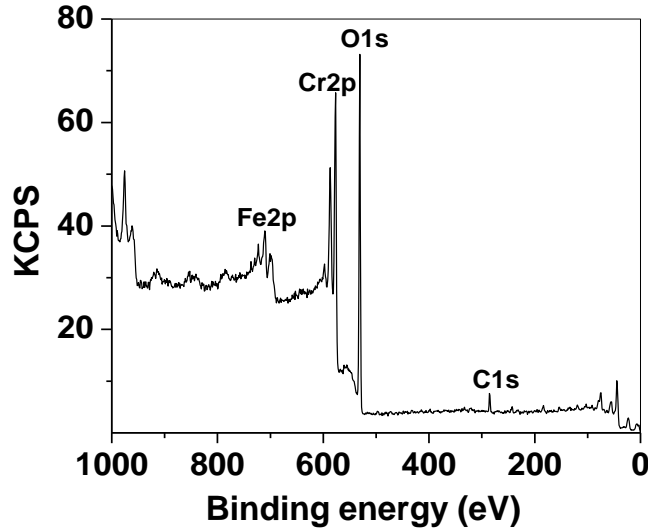


Fig. 3.11: XPS wide scan of the specimen POO-14

The XPS survey scan (Fig. 3.11) shows the presence of Cr dominantly on the surface (Table 3.2). Cr is present as Cr^{3+} on the surface which is seen from the binding energy at 577.1 eV [23]. In Raman analysis, the presence of chromium in two different phases has been observed. But, the narrow peak width of Cr $2p_{3/2}$ (FWHM 2.3 eV) in XPS analysis indicates the presence of Cr in single phase in the outer oxide layers. It appears from the XPS analysis that Cr is present as Cr rich Fe mixed oxide such as $\alpha\text{-Fe}_{2-x}\text{Cr}_x\text{O}_3$ on the outer surface. It can be concluded from the Raman analysis that inner layer of oxides is constituted of spinel structure oxides like NiFe_2O_4 and FeCr_2O_4 while XPS analysis reveal that outer layer is composed of rhombohedral structure oxides like $\alpha\text{-Fe}_{2-x}\text{Cr}_x\text{O}_3$ ($0 < x < 2$).

3.3.2 Specimens prepared in 21 days

The surface morphology of the pre-oxidized SS specimen POO-21 is shown by SEM and AFM images (Fig. 3.12). The SEM image (Fig. 3.12a) shows that the SS surface is completely covered with uniform size (~ 200 nm) SS oxides particles. The pre-oxidized layer is continuous and compact. The AFM topographic image (3.12b) also shows the uniform oxide particle and average roughness of the specimen surface is ~ 30 nm.

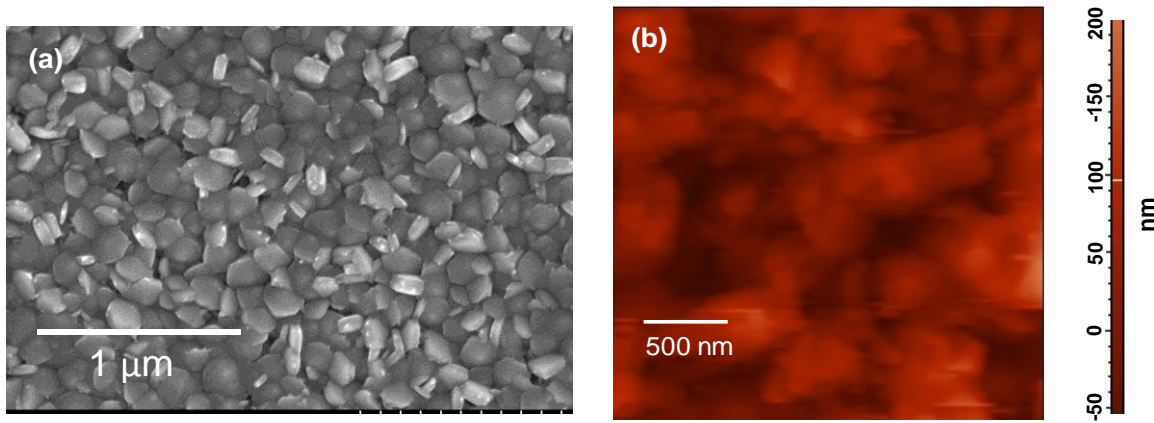


Fig. 3.12: Micrographs of POO-21 specimen (a) SEM image, (b) AFM topographic image

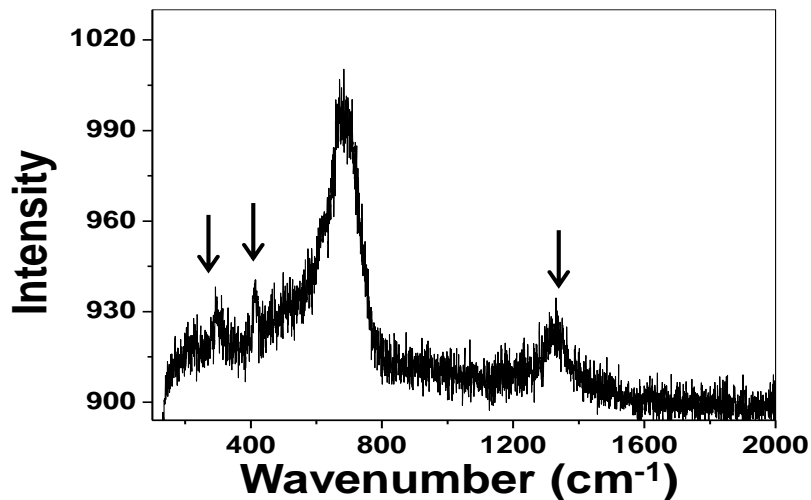


Fig. 3.13: Raman spectra of the pre-oxidized SS specimen POO-21, arrows indicate the signals from α - Fe_2O_3

The Raman spectrum (Fig. 3.13) shows that the surface oxides are constituted of both rhombohedral and spinel oxides (Table 3.1). The peaks at 222, 293 and 412 cm^{-1} correspond to $\alpha\text{-Fe}_2\text{O}_3$ [24]. Peak at 1312 cm^{-1} also correspond to $\alpha\text{-Fe}_2\text{O}_3$, it is the overtone of $\alpha\text{-Fe}_2\text{O}_3$ forbidden peak at 666 cm^{-1} [25]. 205 cm^{-1} peak correspond to $\alpha\text{-(Fe}_x\text{Cr}_{2-x})\text{O}_3(x<1)$ [24]. The intense broad peak at 685 cm^{-1} correspond to $\alpha\text{-(Fe}_x\text{Cr}_{2-x})\text{O}_3(x<1)$ as well as FeCr_2O_4 [25]. So the SS oxides are mainly constituted of rhombohedral oxides of Fe like $\alpha\text{-(Fe}_x\text{Cr}_{2-x})\text{O}_3(x<1)$ and $\alpha\text{-Fe}_2\text{O}_3$ while some amount of spinel oxides like FeCr_2O_4 are also present. GI-XRD pattern of POO-21 specimen (Fig. 3.14) shows that the surface is composed of both spinel oxides and rhombohedral oxides like $\alpha\text{-Fe}_2\text{O}_3$ and $\alpha\text{-(Fe}_x\text{Cr}_{2-x})\text{O}_3$ [15-17, 25, 26].

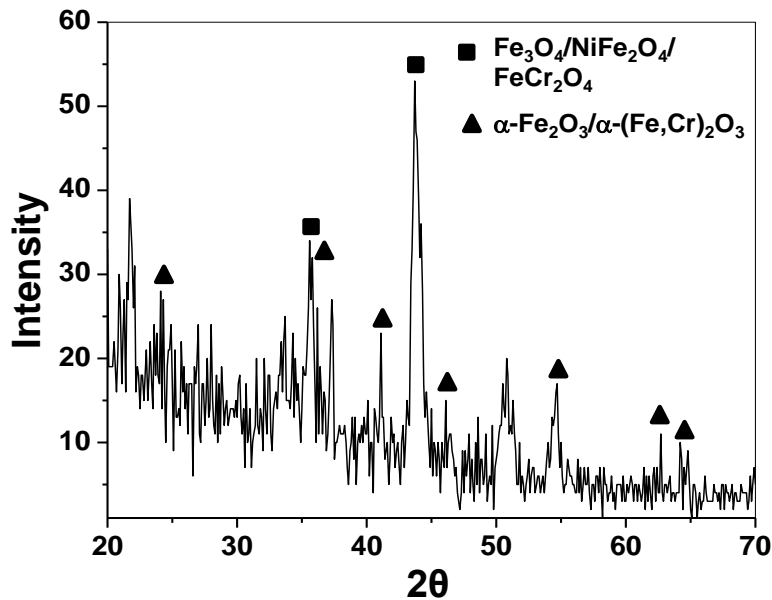


Fig. 3.14: GI-XRD pattern of the pre-oxidized SS specimen POO-21

The X-ray survey scan (Fig 3.15 & 3.16) primarily shows the enrichment of Cr (Table 3.2) on the surface. Narrow FWHM of Cr 2p_{3/2} (2.8 eV) (Fig 3.16 a-d) indicates the presence of Cr in a single phase. From the XPS analysis, it appears that Cr is mainly present as $\alpha\text{-Fe}_{2-x}\text{Cr}_x\text{O}_3$

[3, 10, 21]. It can be concluded from XPS, Raman and GI-XRD analysis, that the outer oxide layer of POO-21 specimen is composed of α -Fe_{2-x}Cr_xO₃ and α -Fe₂O₃ type of oxides while inner oxide layer is mainly composed of spinel oxides.

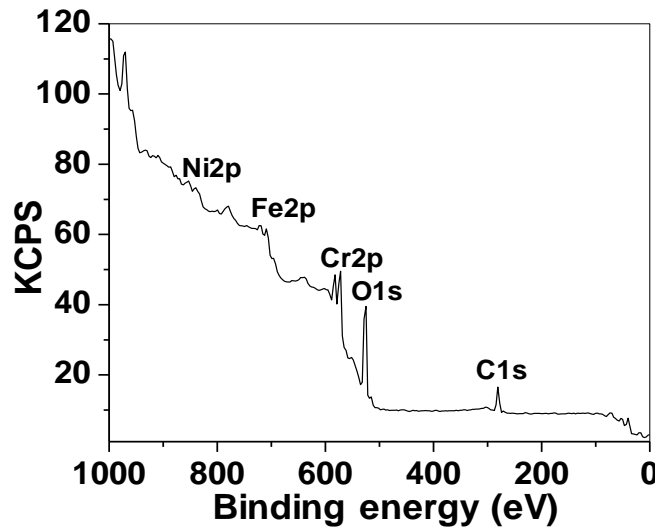


Fig. 3.15: XPS wide scan of the pre-oxidized SS specimen POO-21

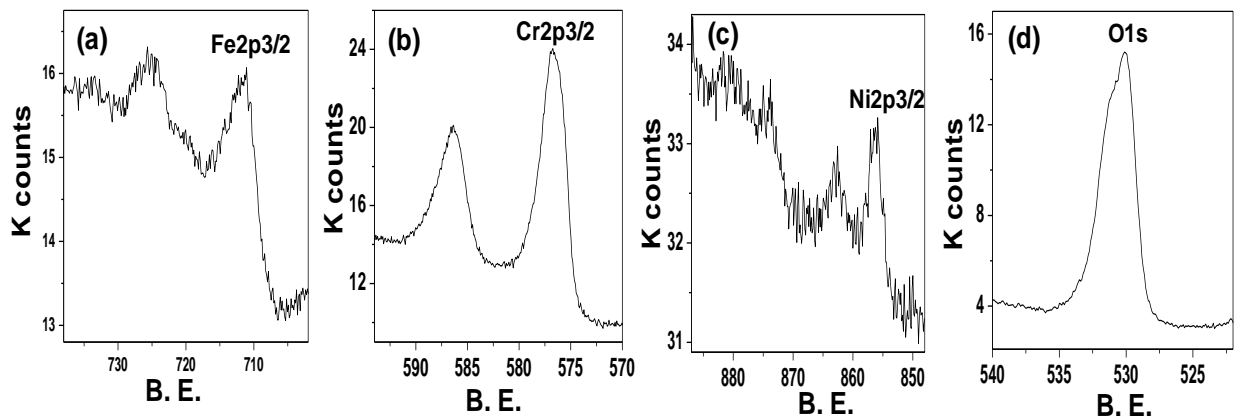


Fig. 3.16: XPS elemental scan of the pre-oxidized POO-21 SS specimen; (a) Fe2p, (b) Cr2p, (c) Ni2p and (d) O1s

The composition of the specimens POO-14 and POO-21 differ to some extent. The formation of rhombohedral structure oxides on the surface of POO-21 is more than that for POO-

14. The Cr dominating rhombohedral oxides (α -Fe,Cr) $_2$ O $_3$ got transformed into Fe dominating rhombohedral oxides with the increase in immersion time from 14 days to 21 days. ZrO $_2$ coating deposition was carried out on both these specimens.

3.3.3 Mechanism of oxide film formation

Pre-oxidation of type 304 SS in high temperature oxidizing aqueous medium led to the formation of several oxides observed earlier [3, 21]. It was observed that the oxides are mainly composed of spinel oxides and α -Fe $_2$ O $_3$ [3, 10, 21]. The TEM analysis by Kuang et. al. reveals the presence of similar oxides along with significant amount of α -Fe $_{2-x}$ Cr $_x$ O $_3$ when the oxidation was performed in oxygenated water at high temperature [5]. In general, Ni and Fe tend to dissolve away selectively from the stainless steel surface in high temperature water at the early stage of oxidation [18]. It was expected that some amount of Cr would also dissolve due to the presence of high concentration oxygen in the solution at the initial stage. But the dissolution of Cr would be totally controlled by the amount of dissolved oxygen and Cr dissolution would stop due to lack of continuous supply of oxygen. It is assumed that preferential dissolution of Ni and Fe caused Cr rich oxide layer at the early stage of oxidation. Simultaneously, the dissolved Cr in solution favored the formation of Cr containing oxides as observed in Raman spectroscopy. These two processes made a unique surface oxide on stainless steel mixed with FeCr $_2$ O $_4$ and α -Fe $_{2-x}$ Cr $_x$ O $_3$ oxides. The POO-14 specimen surface is mainly composed of Cr containing SS oxides like FeCr $_2$ O $_4$, Cr $_2$ O $_3$ and α -Fe $_{2-x}$ Cr $_x$ O $_3$. As the immersion time is increased, Cr concentration in solution reduces and only Fe oxides precipitate as α -Fe $_2$ O $_3$. After the 21 days, Cr at% got reduced from 28 at% to 21 at% while Fe at% increased to 9% from 6 at%. So, the POO-21 specimen surface is mainly constituted of α -Fe $_2$ O $_3$, α -Fe $_{2-x}$ Cr $_x$ O $_3$ and FeCr $_2$ O $_4$.

3.4 Pre-oxidation of SS in dynamic autoclave under simulated BWR water chemistry

Type 304L SS specimens were pre-oxidized in simulated BWR coolant environment at 285°C for ~6 months in a dynamic loop. The experimental details of the experiments are discussed in section 2.4.2. Pre-oxidized SS specimen is designated as POL.

3.4.1 Characterization of specimen

The SEM image (Fig. 3.17a) of the SS specimen, treated in simulated BWR environment for ~6 months shows the presence of densely packed inner layer composed of nano-size crystals on the surface. Over the compact inner layer, loosely packed large oxide particles of size 100-300 nm are present. The surface morphology of the specimen is shown by AFM image (Fig. 3.17b). The average roughness of the POL specimen surface is ~43 nm.

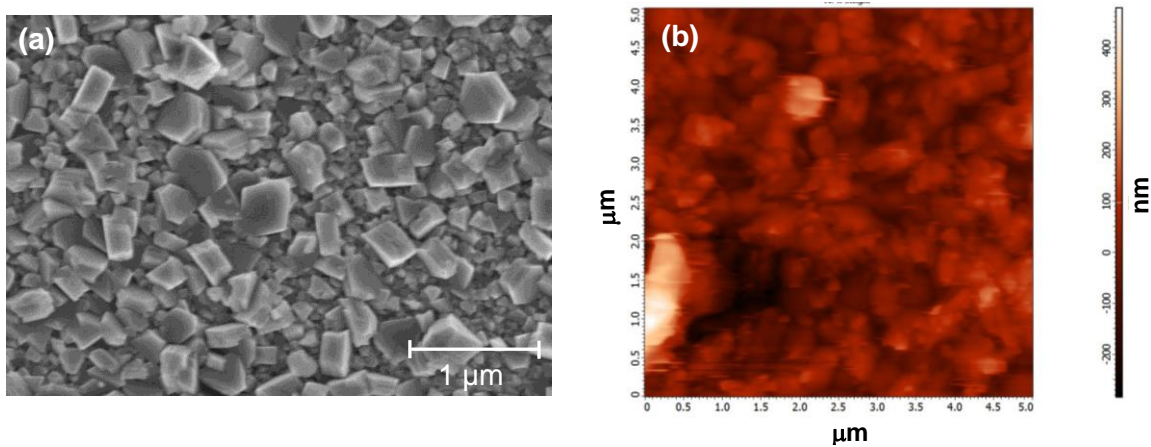


Fig. 3.17: Micrographs of POL (a) SEM image, (b) AFM topographic image

The Raman spectra and the GI-XRD pattern of the POL specimen are shown in Fig. 3.18. Raman spectra (Fig. 3.18 a) shows that the peaks at 226 cm^{-1} , 246 cm^{-1} , 295 cm^{-1} , 412 cm^{-1} , 498 cm^{-1} , 611 cm^{-1} , and 1325 cm^{-1} correspond to $\alpha\text{-Fe}_2\text{O}_3$ [24, 25]. Weak signals at 538 and 552 cm^{-1} correspond to Cr_2O_3 [11]. Intense peak at 664 cm^{-1} is quite broad and it appears that some peaks are merging into it. This peak corresponds to mixture of ferrites (mainly Fe_3O_4 and NiFe_2O_4) and

mixed compound of $\text{Fe}_2\text{O}_3\text{-Cr}_2\text{O}_3$ with high Cr content $\alpha\text{-(Fe}_x\text{Cr}_{2-x})\text{O}_3$ ($x < 1$) [27]. 701 cm^{-1} peak confirms the presence of NiFe_2O_4 . The GI-XRD pattern (Fig. 3.18b) reveal that the outer surface is mainly composed of rhombohedral structures like $\alpha\text{-Fe}_2\text{O}_3$ and mixed $\alpha\text{-(Fe,Cr)}_2\text{O}_3$ [24-26].

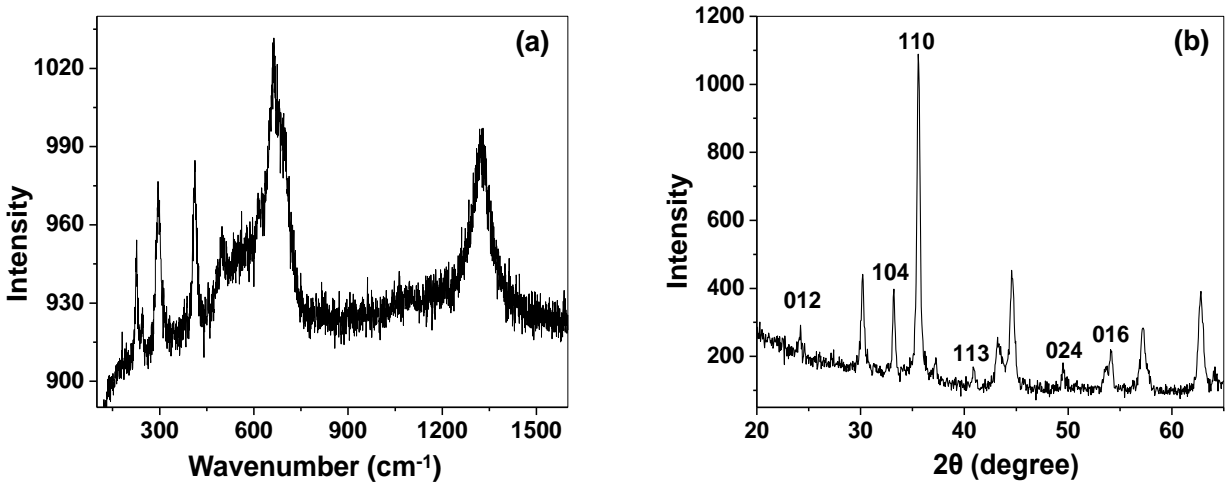


Fig. 3.18: (a) Raman spectra (b) GI-XRD of the pre-oxidized SS specimen POL

Wide scan and elemental scan XPS spectra of the POL specimen is given in Fig. 3.19 & 3.20 (a-d) respectively. The elemental analysis (Table 3.2) show that the surface is dominantly covered by Fe and Cr with very small amount of Ni. The binding energy of Fe $2p_{3/2}$ at 711.1 eV indicates the presence of Fe^{3+} on the surface. Narrow FWHM (4.2 eV) and distinguished satellite peak (marked by arrow) of $\text{Fe}2p_{3/2}$ confirms the presence of pure Fe^{3+} on the surface. Narrow FWHM of Cr $2p_{3/2}$ (2.8 eV) indicates the presence of Cr in single phase. Around 68.2% of oxygen concentration along with Fe^{3+} and Cr^{3+} on the outer surface indicates the presence of mainly $\text{(Fe,Cr)}_2\text{O}_3$ type of oxides on the surface. That supports the observation by GI-XRD that the outer surface is composed of rhombohedral structure oxides like $\alpha\text{-Fe}_2\text{O}_3$ and mixed $\alpha\text{-(Fe,Cr)}_2\text{O}_3$. So, the outer surface of the POL specimen is composed of large size $\alpha\text{-Fe}_2\text{O}_3$ and

mixed α -(Fe,Cr) $_2$ O $_3$ compounds while inner layer is composed of mainly nano-size spinel structures like Fe $_3$ O $_4$, FeCr $_2$ O $_4$, Ni $_x$ Fe $_{3-x}$ O $_4$, NiFe $_x$ Cr $_{2-x}$ O $_4$ and small amount of Cr $_2$ O $_3$.

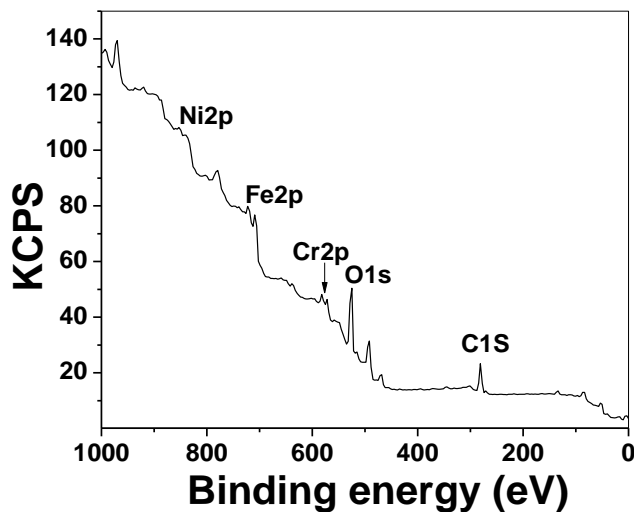


Fig. 3.19: XPS wide scan of the pre-oxidized SS specimen POL

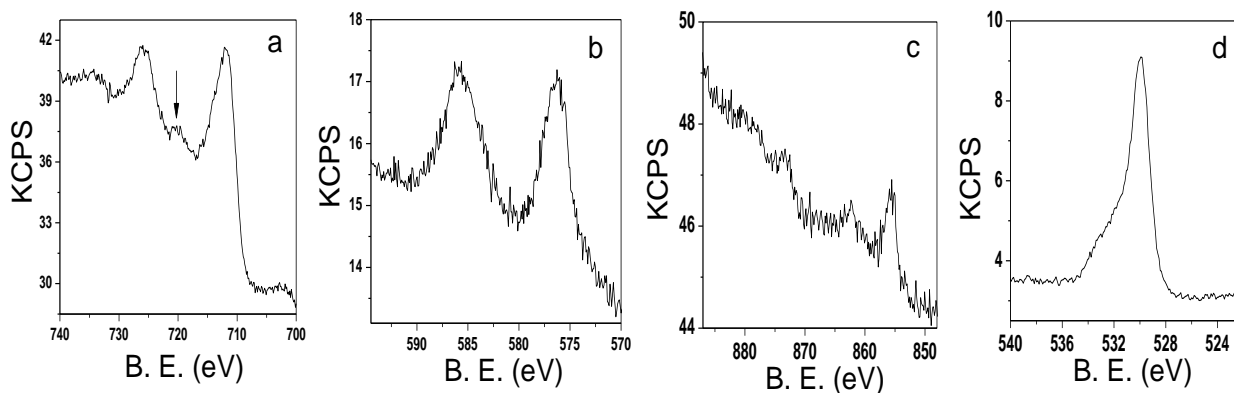


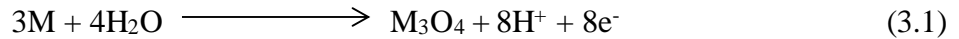
Fig. 3.20: XPS elemental scan of the POL (a) Fe2p, (b) Cr2p, (c) Ni2p, (d)O1s

Wide scan and elemental scan XPS spectra of the POL specimen is given in Fig. 3.19 & 3.20 (a-d) respectively. The elemental analysis (Table 3.2) shows that the surface is dominantly covered by Fe and Cr with very small amount of Ni. The binding energy of Fe 2p $_{3/2}$ at 711.1 eV indicates the presence of Fe $^{3+}$ on the surface. Narrow FWHM (4.2 eV) and distinguished satellite peak (marked by arrow) of Fe2p $_{3/2}$ confirms the presence of pure Fe $^{3+}$ on the surface. Narrow

FWHM of Cr 2p_{3/2} (2.8 eV) indicates the presence of Cr in single phase. Around 68.2 at% of oxygen concentration along with Fe³⁺ and Cr³⁺ on the outer surface indicates the presence of mainly (Fe,Cr)₂O₃ type of oxides on the surface. That supports the observation by GI-XRD that the outer surface is composed of rhombohedral structure oxides like α-Fe₂O₃ and mixed α-(Fe,Cr)₂O₃. So, the outer surface of the POL specimen is composed of large size α-Fe₂O₃ and mixed α-(Fe,Cr)₂O₃ compounds while inner layer is composed of mainly nano-size spinel structures like Fe₃O₄, FeCr₂O₄, Ni_xFe_{3-x}O₄, NiFe_xCr_{2-x}O₄ and small amount of Cr₂O₃.

3.4.2 Mechanism of oxide film formation

The mechanism of the oxide film formation is studied by assuming that the inner layer is developed by solid state growth processes while the outer layer is formed by metal dissolution and oxide precipitation mechanism [28]. The formation of inner compact layer (passive film) composed of spinel oxide can be described by the following reaction:



where M = Fe, Ni or Cr. In parallel with the solid state growth reactions, corrosion reactions by dissolution mechanism take place at the bare surface. At the early stage of oxidation, Fe and Ni selectively dissolve into high temperature water due to the low diffusion coefficient of Cr in the spinel lattice [18]. So, the formation of Cr-rich oxide take place and the enrichment of chromium in the inner layer can be explained. Higher affinity of Cr for oxygen also plays a role in forming the inner Cr-rich oxide layer. Simultaneously, solid state reactions, corrosion reactions/ dissolution of metal ions take place on the SS surface. Initially, small amount of Cr (due to oxidizing environment, dissolved high temperature O₂ conc. = 200-300 ppb) also dissolve from the stainless steel surface along with Ni and Fe at high temperature [18]. Metal oxides will be released as non-stoichiometric ferrites and will get embedded into the

growing passive film. Simultaneously, the inward diffusion of oxidant leads to the development of spinel oxides [19, 20]. With increasing exposure time, some oxide nuclei grew up to certain size. The hematite particles nucleate by solid-state reactions, and then grew up through precipitation of extraneous metallic ions from testing solution. The precipitation of oxides results in the formation of an oxide double layer. With the increase in immersion time, Fe content in the oxide film gradually increases, due to the precipitation of dissolved Fe ion from testing solution and the Cr content decreases. But Cr concentration is significantly high by XPS elemental composition analysis. The loop setup for the experiments was made of stainless steel, so higher Cr content in the outer layers may be attributed to the large surface of the structural material of loop system.

3.5 Pulsed laser deposition (PLD) of α -Fe₂O₃ on SS surface

It is quite difficult to grow pure α -Fe₂O₃ on the surface of SS by high temperature high pressure hydrothermal conditions. In order to study the role of different SS oxides during zirconia deposition, pure α -Fe₂O₃ film has been grown on the stainless steel surface by pulsed laser deposition (PLD) technique. Details of the PLD experiments are given in section 2.4.3. It has been observed that α -Fe₂O₃ could not be grown on plain SS surface without an intermediate oxide layer. It may be due to the lattice mismatch between 304L SS and α -Fe₂O₃ which prevents the growth of α -Fe₂O₃ directly on stainless steel substrate. Prior to PLD of α -Fe₂O₃, stainless steel substrates were oxidized in a static autoclave under two different conditions: 1. Aqueous solution containing H₂O₂ at 200°C for 14 days, 2. Normal water at 240°C for 21 days (POO-21).

The SS sample prepared in aqueous solution containing H₂O₂ was characterized by Raman spectroscopy (Fig. 3.21).

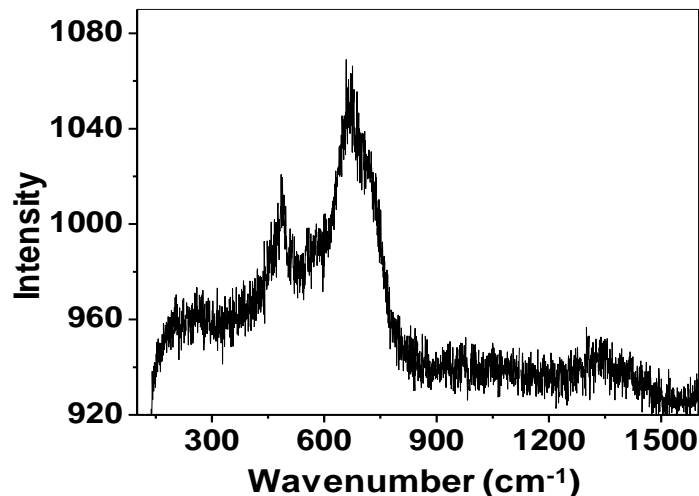


Fig. 3.21: Raman spectra of the SS specimen pre-oxidized in H₂O₂ environment at 200°C

The intense peak at 666 cm⁻¹ corresponds to Fe₃O₄, 490 cm⁻¹ peak corresponds to NiFe₂O₄ [10, 20, 21]. Weak signals at 200, 260 and 1330 cm⁻¹ show the formation of mixed α-(Fe,Cr)₂O₃ type of compounds [21]. So, Ni-ferrite and magnetite are present dominantly on the surface with very small amount of hematite. α-Fe₂O₃ was deposited by PLD process on pre-oxidized samples grown in two different water chemistry conditions. α-Fe₂O₃ coatings formed on both of the surfaces were found to be adherent and smooth and show similar surface characteristics. PL deposited SS specimen is designated as POP.

3.5.1 Characterization of PL deposited α-Fe₂O₃ films on SS surface

Thickness of the α-Fe₂O₃ film was measured by stylus profilometry and was about 0.5 μm (section 2.8.1). Fig. 3.22 shows the SEM and AFM micrographs of thin film of α-Fe₂O₃ deposited on stainless steel. SEM image (Fig. 3.22a) shows that shape of PL deposited α-Fe₂O₃ particles is nearly spherical and most of the particles deposited are of the order of 50-200 nm. Few particles are observed to be larger in size (~500 nm). AFM micrograph (Fig. 3.22 b) show

that size of α -Fe₂O₃ particles are approximately 50-75 nm and the surface roughness of α -Fe₂O₃ coated SS specimens is observed to be approximately 100 nm.

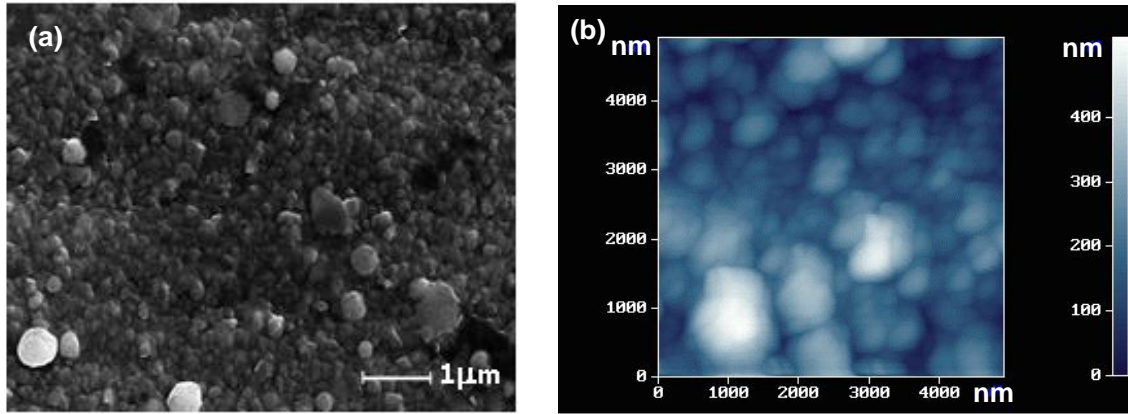


Fig. 3.22: Micrographs of the PL deposited SS specimen (POP) (a) SEM image, (b) AFM image

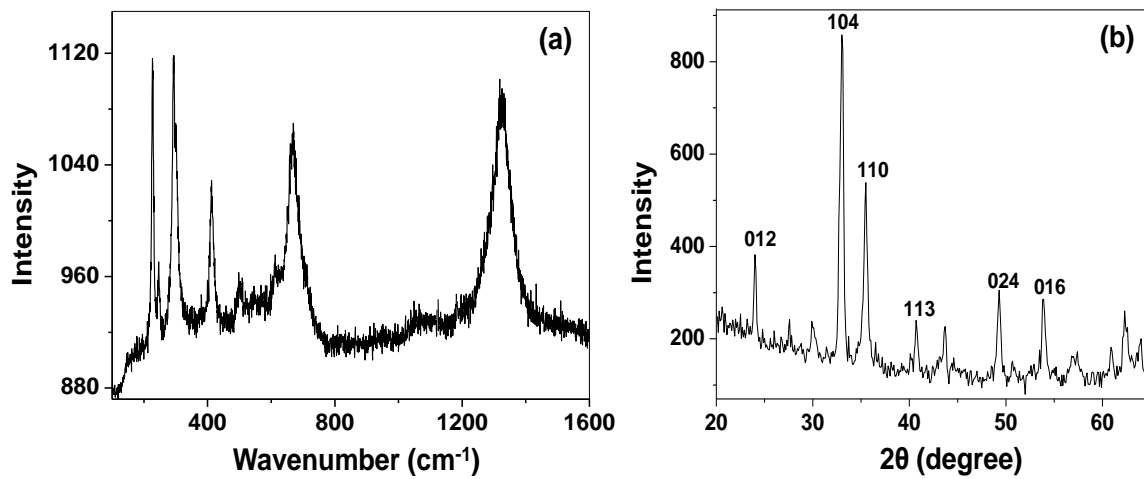


Fig. 3.23: (a) Raman spectra (b) GI-XRD of the PL deposited SS specimen POP

The phase analysis of the PL deposited SS specimen was performed by Raman spectroscopy and GI-XRD and shown in Fig. 3.23. The laser Raman spectra (Table 3.1) of PL deposited α -Fe₂O₃ sample show the several Raman modes at 227, 245, 291, 298, 413, 497, 611

and 668 cm^{-1} (Fig. 3.23a). $\alpha\text{-Fe}_2\text{O}_3$ belongs to $D63d$ space group and has 2 A_{1g} and 5 E_g Raman active bands. Peaks at 227 and 497 cm^{-1} belong to A_{1g} mode while the peaks at 245 , 291 , 298 , 413 , 611 cm^{-1} belong to the E_g mode of the $\alpha\text{-Fe}_2\text{O}_3$. The 668 cm^{-1} peak corresponds to Fe_3O_4 [20, 21]. It appears that Fe_3O_4 was also formed during the PL deposition process. GIXRD pattern (Fig. 3.23b) analysis shows that all the peaks are corresponding to $\alpha\text{-Fe}_2\text{O}_3$ only [24, 25]. It indicates that outer surface of the sample is free from magnetite contamination. Hence, the signal of magnetite detected by Raman analysis indicates its presence at the surfaces of substrates used for PL deposition.

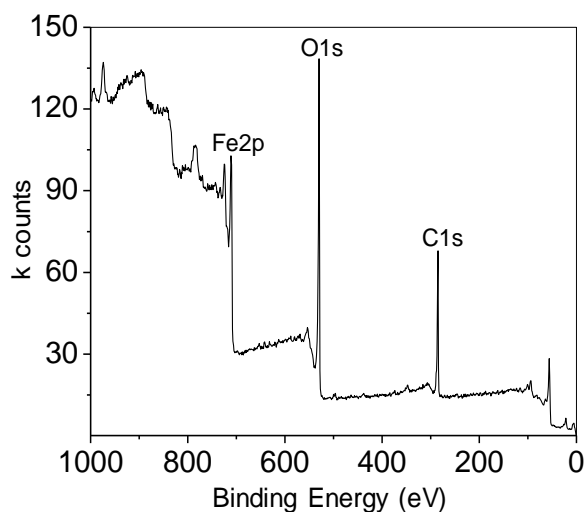


Fig. 3.24: XPS wide scan of the PL deposited pre-oxidized SS specimen POP

Fig. 3.24 shows the wide scan photoelectron spectrum of the PL deposited $\alpha\text{-Fe}_2\text{O}_3$ surface. The spectrum of PL deposited substrate surface (Fig 3.24) show the presence of Fe only along with oxygen and trace of C as contaminant. The quantification of Fe and O (Table 3.2) showed formation of stoichiometric Fe_2O_3 . The presence of pure Fe^{3+} in the oxide is also confirmed by the narrow scan of Fe2p (Fig. 3.25a) which shows the binding energy of Fe $2p_{3/2}$ at 710.6 eV with a distinct satellite at 8.0 eV above the main peak (marked by arrow) [29, 30]. The

O1s spectrum (Fig. 3.25b) shows the presence of a small signal at 531.3 eV along with intense peak at 529.4 eV. The narrow O1s peak indicates that the surface is free from other oxide contaminates. The small O1s peak at 531.3 eV represents the lattice OH⁻ from α -FeOOH [31, 32]. So, small amount of α -FeOOH also is formed during the PL deposition process or may be due to air exposure of the samples. XPS analysis did not show any signal from Fe₃O₄ that is in contradiction with the Raman spectra where Fe₃O₄ signals have been observed in addition to the Fe₂O₃ peaks. It is because of different depth of information of these two techniques. XPS technique gives the information of ~5 nm from the surface whereas Raman spectroscopy gives the information of much deeper levels from the surface. So, Fe₃O₄ is present only in inner layers on the substrate surface (H₂O₂ pre-oxidized). It is assumed that insufficient oxygen pressure during PLD process led to reduction of some of the Fe³⁺ ions to Fe²⁺ in the inner layers of the oxide film. This also results in formation of magnetite along with hematite in the inner layers of α -Fe₂O₃ film.

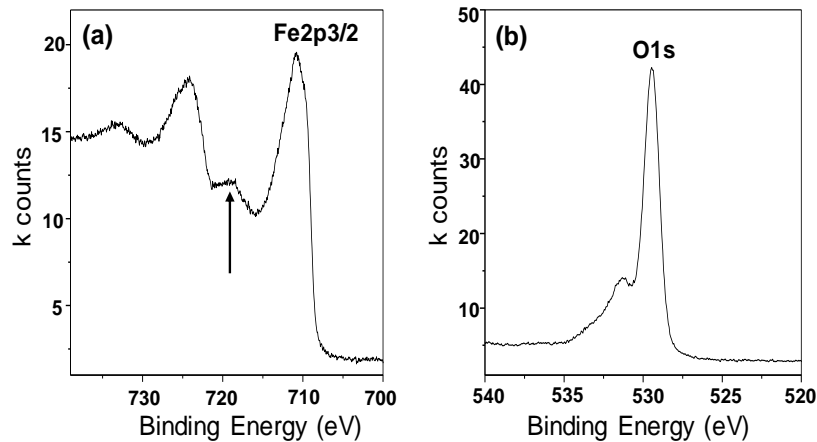


Fig. 3.25: XPS of narrow scan of the PL deposited pre-oxidized SS specimen POP (a) Fe2p, (b) O1s

3.5.2 Mechanism of PL deposition of α -Fe₂O₃

PL deposition is a type of physical vapor deposition technique, in which an intense high energy laser light pulses (typically $\sim 10^8$ Wcm⁻²) fall into the target (α -Fe₂O₃ pallet) material. Due to the high energy of laser beam, α -Fe₂O₃ melt, evaporate and ionize and removed from the surface of a target. This "ablation" event produces a transient, highly luminous plasma plume that expands rapidly away from the target surface and gets evaporated and removed from the surface in the form of plume. The material expands in plasma parallel to the normal vector of the target surface towards the substrate due to Coulomb repulsion and recoil from the target surface. The spatial distribution of the plume is dependent on the background pressure inside the PLD chamber. The high energetic species ablated from the target bombard on the substrate surface (SS oxide surfaces) where film of α -Fe₂O₃ to be deposited. The condensation of the target atoms (α -Fe₂O₃) from vapor phase to solid phase take place on the substrate surface. The atomistic condensation is known as nucleation which then grows to form a film by diffusion controlled process. The condensation of the vapor atom occurs due to interaction of atoms with surface and loss of velocity. The vapor atoms gets adsorbed on the substrate surface by releasing heat. After arriving at the substrate surfaces, the vapor atoms can either diffuse across the surface, encounter other clusters, or re-evaporated from the surface. The structural behavior of the thin film depends on the mode of growth process. Several factors like laser parameters, substrate surface temperature, and background pressure influence the nucleation and growth of the α -Fe₂O₃ film. The background pressure (O₂ pressure = 10^{-2} mbar) is very crucial parameter for maintaining the stoichiometry of target in the film [33]. α -Fe₂O₃ particles nucleate in the form of islands on the substrate surface. After an island is formed, an additional island can nucleate on top of the first island and at the same time continuous nucleation of islands on the substrate surface can take

place. As more material is added, the islands continue to grow and the islands coalesce into each other. Therefore, 3D growth of α -Fe₂O₃ particles take place on the substrate surface and it result in high surface roughness (~100 nm) of α -Fe₂O₃ layers.

3.6 Conclusions

The compositions of the pre-oxidized surfaces obtained from the Raman and XPS analyses are summarized in Table 3.1 and Table 3.2 respectively. The SS specimens pre-oxidized under reducing water chemistry condition have the surface composed of various spinel oxides. The SS specimens treated in normal water at 14 days shows the mixture of ferrites and rhombohedral α -(Fe,Cr)₂O₃ while after 21 days the surface was dominant of α -Fe₂O₃ and α -(Fe,Cr)₂O₃ with small amount of ferrites. The SS specimens prepared in BWR environment (in dynamic loop) have the surface composed of α -Fe₂O₃ and α -(Fe,Cr)₂O₃ while spinel oxides and Cr₂O₃ was present in the inner layers of SS oxide. The composition and structure of the oxides formed on SS surface in different water chemistry environments is varying because of the difference in dissolved ions in the solution under different water chemistry conditions. The SS oxide surface prepared by PL deposition of α -Fe₂O₃, shows the formation of stoichiometric α -Fe₂O₃ on the surface while some amount of Fe₃O₄ was present in the inner layers. The chemical composition, structure and morphology of the all sample prepared under various environments are given in Table 3.3.

Table 3.1: Analysis of Raman spectra acquired from different pre-oxidized SS specimens

Sample	Peaks Observed (cm ⁻¹)	Composition
POH-5	687 570, 488	Ni _k Fe _{3-x} O ₄ , NiFe _x Cr _{2-x} O ₄ , FeCr ₂ O ₄ NiFe ₂ O ₄
POH-21	690 575, 470	Ni _k Fe _{3-x} O ₄ , NiFe _x Cr _{2-x} O ₄ , FeCr ₂ O ₄ NiFe ₂ O ₄
POO-14	692 (broad) 489 222, 298, 1359 546	α -(Fe _x Cr _{2-x})O ₃ (x<1), FeCr ₂ O ₄ NiFe ₂ O ₄ α -(Fe _x Cr _{2-x})O ₃ (x<1) Cr ₂ O ₃ , α -(Fe _x Cr _{2-x})O ₃ (0<x<2)
POO-21	205, 222, 293, 412, 612, 1326 694 660	α -Fe ₂ O ₃ , α -(Fe _x Cr _{2-x})O ₃ (x<1) α -(Fe _x Cr _{2-x})O ₃ (x<1), FeCr ₂ O ₄ Fe ₃ O ₄
POL	227, 293, 414, 1325 662, 689	α -Fe ₂ O ₃ , α -(Fe _x Cr _{2-x})O ₃ (x<1) Fe ₃ O ₄ , α -(Fe _x Cr _{2-x})O ₃ (x<1), FeCr ₂ O ₄ , Ni _k Fe _{3-x} O ₄ , NiFe _x Cr _{2-x} O ₄
POP	1320, 497, 413, 298, 291, 245, 227, 611 668	α -Fe ₂ O ₃ Fe ₃ O ₄

Table 3.2: Atomic concentration (at %) and binding energy of different photoelectron peaks obtained from pre-oxidized SS specimens

Sample	Fe 2p _{3/2} (eV)	Cr 2p _{3/2} (eV)	Ni 2p _{3/2} (eV)	O1s (eV)
	at %	at %	at %	at %
POH-5	710.2	577.1	855.6	530.6
	26.0	10.0	8.0	56.0
POH-21	709.8	575.0	854.7	531.0
	45.8	2.7	16.8	34.7
POO-14	710.2	577.3	--	530.9
	6.0	28.0	~ 1.0	65.0
POO-21	711.3	577.0	856.1	530.4
	9.3	21.2	3.3	66.2
POL	711.6	576.8	856.0	530.4
	20.6	7.9	3.2	68.2
POP	710.6	-	-	529.4
	38.0	-	-	62.0

Table 3.3: Properties of pre-oxidized SS specimens prepared under different environments

Sample	Mode of surface preparation	Oxide structure	Surface composition	Oxide Particle Size	Surface Roughness
POH-5	Static Autoclave oxidation (Reducing environment)	Spinel oxides	$Ni_xFe_{3-x}O_4$ ($x=0-1$), $NiFe_xCr_{2-x}O_4$ ($x<1$), $FeCr_2O_4$	$< 0.5 \mu m$	-
POH-21	Static Autoclave oxidation (Reducing environment)	Spinel oxides	$Ni_xFe_{3-x}O_4$ ($x=0-1$), $NiFe_xCr_{2-x}O_4$ ($x<1$), $FeCr_2O_4$	200-500 nm	~25 nm
POO-14	Static Autoclave oxidation (oxidizing environment)	Rhombohedral, spinel oxides	$\alpha-Fe_{2-x}Cr_xO_3$ ($0<x<2$), $\alpha-Fe_2O_3$, Cr_2O_3 , $FeCr_2O_4$	$< 0.1 \mu m$	-
POO-21	Static Autoclave oxidation (oxidizing environment)	Rhombohedral, spinel oxides	$\alpha-Fe_xCr_{2-x}O_3$ ($0<x<2$), $\alpha-Fe_2O_3$, Cr_2O_3 , $FeCr_2O_4$, Fe_3O_4	~200 nm	~30 nm
POL	Dynamic loop oxidation (oxidizing environment)	Rhombohedral, spinel oxides	$\alpha-Fe_2O_3$, $\alpha-(Fe,Cr)_2O_3$, Cr_2O_3 , Fe_3O_4 , $FeCr_2O_4$, $NiFe_xCr_{2-x}O_4$ ($0<x<2$)	100-300 nm	~43nm
POP	PL deposition of $\alpha-Fe_2O_3$	Rhombohedral oxides	$\alpha-Fe_2O_3$	50-200 nm	~100 nm

3.7 References

- [1] F. Martin, R. Ayouchi, C. Ruiz, J. R. Ramos-Barrado, D. Leinen, *Surf. Interface Anal.* 34 (2002) 719-723.
- [2] T.-K. Yeh, Y.-C. Chien, B.-Y. Wang, C.-H. Tsai, *Corros. Sci.* 50 (2008) 2327-2337.
- [3] W. Kuang, X. Wu, E.-H. Han, *Corros. Sci.* 52 (2010) 4081-4087.
- [4] M. Takahiro, T. Takumi, U. Shunsuke, S. Tomonori, T. Takashi, S. Yoshiyuki, W. Yiochi, H. Hideyuki, *J. Nucl. Sci. Technol.* 43 (2006) 884-895.
- [5] W. Kuang, E.-H. Han, X. Wu, J. Rao, *Corros. Sci.* 52 (2010) 3654-3660.
- [6] P.R. Graves, C. Johnston, J.J. Campaniello, *Mater. Res. Bull.* 23 (1988) 1651-1660.
- [7] H.D. Lutz, B. Muller, H.J. Steiner, *J. Solid State Chem.* 90 (1991) 54-60.
- [8] D.L.A. de Faria, S. Venâncio Silva, M.T. de Oliveira, *J. Raman Spectrosc.* 28 (1997) 873-878.
- [9] D. Bersani, P.P. Lottici, A. Montenero, *J. Raman Spectrosc.* 30 (1999) 355-360.
- [10] A. Ahlawat, V.G. Sathe, *J. Raman Spectrosc.* 42 (2011) 1087-1094.
- [11] M.D.C. Belo, M. Walls, N.E. Hakiki, J. Corset, E. Picquenard, G. Sagon, D. Noel, *Corros. Sci.* 40 (1998) 447-463.
- [12] N. Boucherit, A. Hugot-Le Goff, S. Joiret, G. Beranger, H. Chaudason, *Thin Solid Films* 174 (1989) 111-116.
- [13] A.P. Grosvenor, M.C. Biesinger, R.St.C. Smart, N.S. McIntyre, *Surf. Sci.* 600 (2006) 1771-1779.
- [14] R.L. Tapping, R.D. Davidson, E. McAlpine, D.H. Lister, *Corros. Sci.* 26 (1986) 563-576.
- [15] M.C. Mascolo, Y. Pei, Terry A. Ring, *Materials* 6 (2013) 5549-5567.
- [16] S.B. Kondawar, A.I. Nandapure, B.I. Nandapure, *Adv. Mat. Lett.* 5 (2014) 339-344.

- [17] Z.-Q. Zhu, X.-D. Cheng, W.-P. Ye, J. Min, *International Journal of Minerals, Metallurgy, and Materials* 19 (2012) 266-270.
- [18] J. Robertson, *Corros. Sci.* 32(1991) 443-465.
- [19] W. Kuang, X. Wu, E.-H. Han, J. Rao, *Corros. Sci.* 53 (2011) 3853- 3860.
- [20] M. Sennour, L. Marchetti, F. Martin, S. Perrin, R. Molins, M. Pijolat, *J. Nucl. Mat.* 402 (2010) 147-156.
- [21] K.F. McCarty, D.R. Boehme, *J. Solid State Chem.* 79 (1989) 19-27.
- [22] J.H. Kim, I.S. Hwang, *Nucl. Eng. Des.*235 (2005) 1029-1040.
- [23] D. Owen, D.G. Zetaruk, N.S. McIntyre, *Electrochem. Soc.* 126 (1979) 750-760.
- [24] Q. Wei, Z. Zhang, Z. Li, Q. Zhou, Y. Zhu, *J. Phys. D: Appl. Phys.* 41 (2008) 202002-06.
- [25] M. Aronniemi, J. Lahtinen, P. Hautojarvi, *Surf. Interface Anal.* 36 (2004) 1004–1006.
- [26] K. Bhattacharya, A. Hartridge, K.K. Mallick, *J. Mat. Sci.* 32 (1997) 557-560.
- [27] M. Da C. Belo, M. Walls, N.E. Hakiki, J. Corset, E. Picquenard, G. Sagon and D. Noel, *Corros. Sci.* 40(1998) 447-463.
- [28] B. Stellwag, *Corros. Sci.* 40 (1998) 337-370.
- [29] S. Bera, A.A.M. Prince, S. Velmurugan, P.S. Raghavan, R. Gopalan, G. Panneerselvam, S.V. Narasimhan, *J. Mater. Sci.* 36 (2001) 5379-5384.
- [30] T. Yamashita, P. Hayes, *Appl. Surf. Sci.* 254 (2008) 2441–2449.
- [31] W. Temesghen, P.M.A. Sherwood, *Anal. Bioanal. Chem.* 373 (2002) 601–608.
- [32] A.P. Grosvenor, B.A. Kobe, N.S. McIntyre, *Surf. Sci.* 572 (2004) 217–227
- [33] A. Ohtomo, H.Y. Hwang, *J. Appl. Phys.*102 (2007) 083704-1-6.

Chapter 4

Preparation, characterization and adsorption of nano-ZrO₂ on SS surface

4.1 Introduction

Several approaches for ZrO_2 coating on SS 304L by hydrothermal process have been explored [1-3]. Direct adsorption of ZrO_2 nano particles over stainless steel surface by hydrothermal process is challenging but promising for alleviating the SCC problem [4-6.]. The advantages of forming ZrO_2 coating by directly depositing the ZrO_2 nano powder over SS surface by hydrothermal process are, (i) the phase of the coating can be controlled easily and (ii) it is simpler to apply in power plant and does not need any extra addition of chemicals. Tetragonal phase of zirconia is preferred as compared to monoclinic phase for a stable protective coating on stainless steel. In this work, the nanocrystalline zirconia powder has been prepared by precipitation route [7]. The efforts have been made to produce high quality nanocrystalline ZrO_2 particles of dominant tetragonal phase. Prepared zirconia powder was characterized for its phase determination, size distribution and chemical composition by x-ray diffraction (XRD), Raman spectroscopy, transmission Electron Microscopy (TEM) and x-ray photoelectron spectroscopy (XPS) techniques respectively. The role of chemical conditions and the reactants used in formation of tetragonal dominant powder are discussed in detail. In order to alleviate agglomeration, polyethylene glycol (PEG-8000) as dispersant was employed to refine the grain size of the precursor and 18% ethanol was used as solvent and for washing. It is found that the de-agglomeration treatments were effective and homogeneous zirconia nano-particles with weak agglomeration are obtained.

The adsorption of ZrO_2 nanoparticles on the pre-oxidized SS surface takes place due to the electrostatic interaction between the substrate and the suspended particles [8]. Surface charge is a function of two important experimental parameters such as pH and type of dispersants in the solution. It is essential to know the surface charge of ZrO_2 nano particles suspended in aqueous

solution under different conditions [9, 10]. Zeta potential of the nanocrystalline zirconia powder was studied as a function of pH at various temperatures and with the addition of surfactant. The adsorption of nano-zirconia particles on SS 304L surfaces have been studied at different temperatures viz. room temperature, 90°C and 150°C. The surfaces after adsorption have been characterized by SEM-EDS and XPS. Effect of surfactant (Sodium dodecylsulphate-SDS) on the adsorption of ZrO_2 on SS surfaces has also been studied at different temperatures.

4.2 Preparation and characterization of nanocrystalline ZrO_2 powder

4.2.1 Preparation of ZrO_2 powder

Nanocrystalline zirconia powder was prepared by direct precipitation route by using $ZrO(NO_3)_2 \cdot 6H_2O$ solution (water + ethanol mixture). The $NH_3 \cdot H_2O$ solution was added drop-wise to the solution of $ZrO(NO_3)_2$ and PEG-8000 at 80°C with continuous stirring. The precipitated hydroxides of zirconia was dried and calcined respectively. The details are given in section 2.5.

4.2.2 Characterization of prepared ZrO_2 powder

4.2.2.1 Microstructure and phase analysis by TEM and XRD

The microstructural analysis of the prepared ZrO_2 powder was carried out by TEM. The TEM bright field micrographs of agglomerates of the ZrO_2 powder on the carbon film is shown in Fig. 4.1. The images have been recorded at slight under focus in order to enhance the contrast at the boundaries of the particles. It is observed from the images that the powder particles are in nanometer size and these nano-particles are faceted indicating their crystalline nature. The sizes of these nano particles are observed to be typically in the range of 10–20 nm.

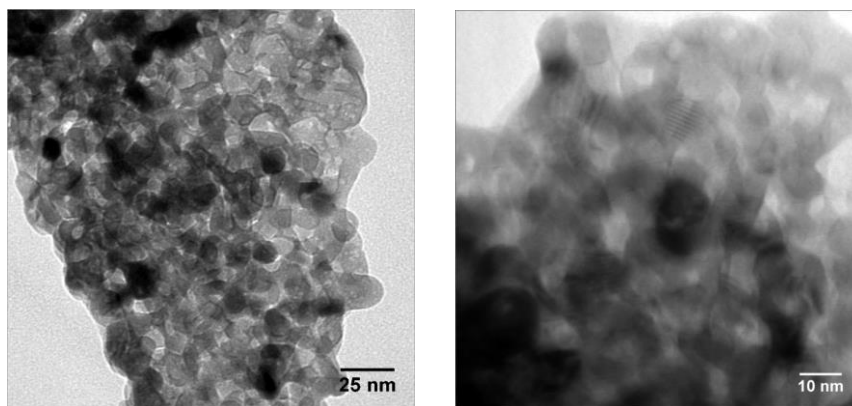


Fig. 4.1: Bright field TEM micrographs of the ZrO_2 powder showing the nano sized particles

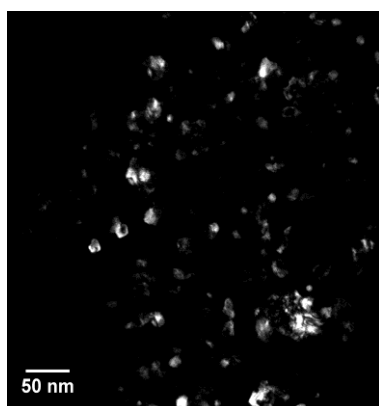


Fig. 4.2: Dark field TEM micrograph of the powder particles showing nanocrystalline ZrO_2

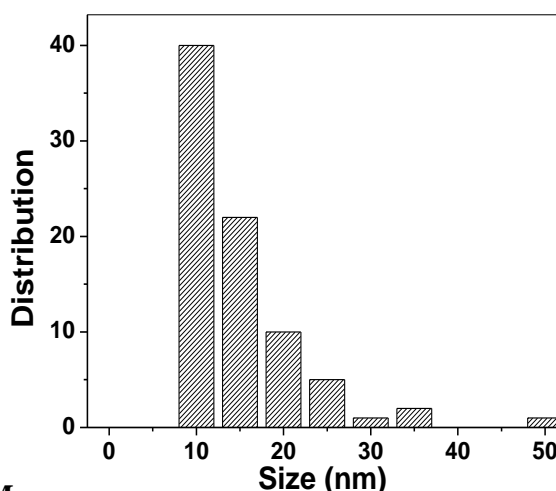


Fig. 4.3: ZrO_2 crystallite size distribution obtained from analysis of TEM dark field micrograph

For the accurate estimation of the crystallite size distribution, an image analysis technique was employed on a dark field micrograph shown in Fig. 4.2. This dark field micrograph was imaged using the objective aperture around the diffraction spots measuring 2.8–3.1 \AA . It is observed from the histogram (Fig. 4.3) that most of the nano crystals measure 10

mand some are in the size range of 15–25 nm while a few measure up to 50 nm. This result is consistent with the observation made from the bright field images in Fig. 4.1 earlier.

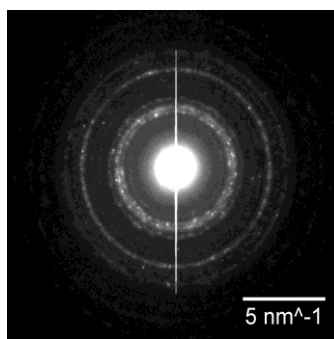


Fig. 4.4: Selected area electron diffraction pattern

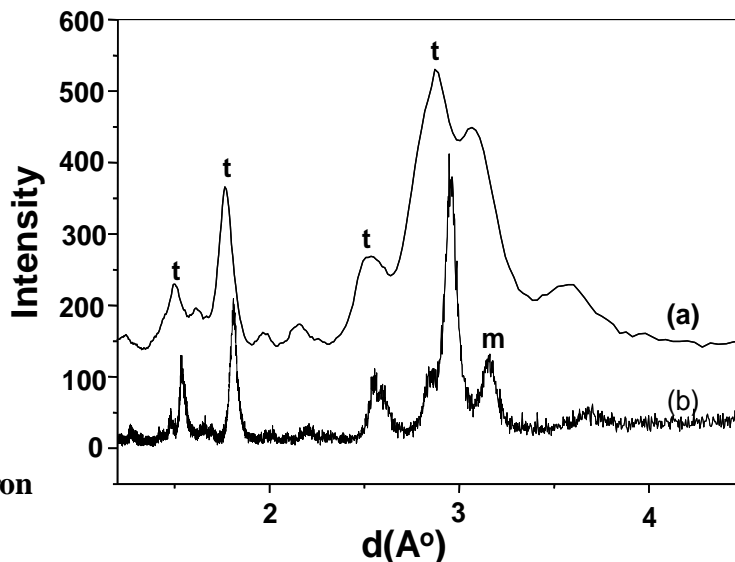


Fig. 4.5: (a) Electron diffraction pattern evaluated from the image processing technique from SAD pattern shown in Fig. 4.4, and (b) X-ray diffraction pattern (d vs Intensity) of the nano ZrO₂ powder

The electron diffraction pattern has been evaluated by image processing technique from the selected area diffraction (SAD) pattern and is shown in Fig. 4.4. The reciprocal space unit of the SAD pattern has been converted to actual lattice spacing (d in Å units) after calibration with respect to polycrystalline gold. The background, which contains undefined quantities of contribution from various inelastic scatterings from the sample, has been arbitrarily subtracted in order to compare the peak positions with those of the XRD pattern. The x-ray diffraction patterns as well as the electron diffraction pattern recorded from the sample are shown simultaneously in Fig. 4.5. Analysis of the XRD pattern reveals two phases of ZrO_2 , marked by ‘t’ and ‘m’ in the figure (Fig. 4.5b) for tetragonal and monoclinic phases, respectively [11, 12]. The peaks from

this viewgraph reveal the presence of major tetragonal phase and minor monoclinic phase of ZrO_2 powder. Analysis of the electron diffraction pattern reveals that all the diffraction peaks seen in the XRD pattern are present here as well. A small shift of the peak position in the SAD compared to the XRD pattern can be understood in terms of inherent inaccuracy in determining ‘d’ values from electron diffraction results and calibration. This result also indicates that there is an intimate mixture of the monoclinic and tetragonal ZrO_2 phases even at microscopic scales and not as local clusters of separate monoclinic and tetragonal phases. This observation is consistent with earlier observations by Chraska et. al. [13].

The XRD pattern of the sample in terms of 2θ vs intensity is shown in Fig. 4.6. The broadening of the XRD peaks is attributed to the nanometric sizes of the particles under investigation. The particle sizes (D) were calculated from the Scherrer’s formula, given in detail in section 2.9.5. The calculated observed size was approximately 15 nm. Since, XRD measurements reveal the average size of coherent crystalline domains; this result is consistent with our estimation of crystallite size from dark filed TEM imaging, wherein the actual distribution was presented.

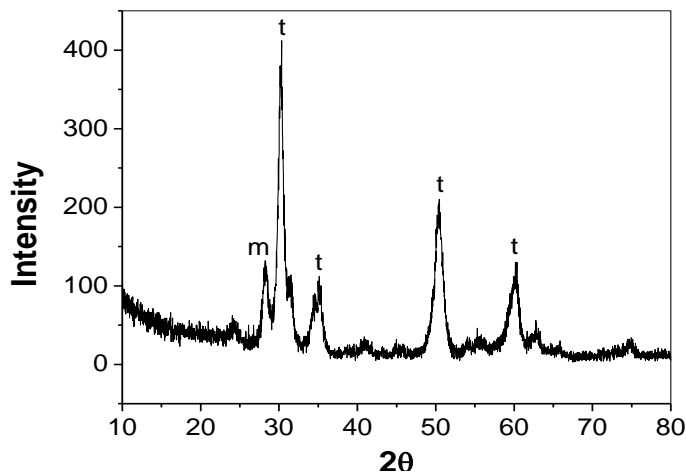


Fig. 4.6: X-ray diffraction pattern of the nano-crystalline ZrO_2 powder

4.2.2.2 Phase and volume fraction analysis from Raman spectroscopy

TEM and XRD analyses show that the nanocrystalline powder prepared was composed of both tetragonal and monoclinic phases. It is interesting to find the compositions of the phases in the powder. Raman spectroscopy was used to evaluate the quantity of each phase in the powder samples. The corresponding Raman spectrum is shown in Fig. 4.7. Raman peaks at 148, 269, 317, 462 and 646 cm^{-1} correspond to the tetragonal phase of zirconia, while 180, 192, 379 and 476 cm^{-1} peaks correspond to monoclinic zirconia [14]. The three peaks at 148, 180 and 192 cm^{-1} marked in the figure were taken to estimate the monoclinic phase in the powder. The fraction of the monoclinic phase (f_m) was estimated using the formula given in section 2.9.3 [15]. It was calculated that 35% as monoclinic and 65% as tetragonal phase is present in the powder. The stabilization of metastable tetragonal phase of ZrO_2 without the addition of any dopant is discussed later in this chapter.

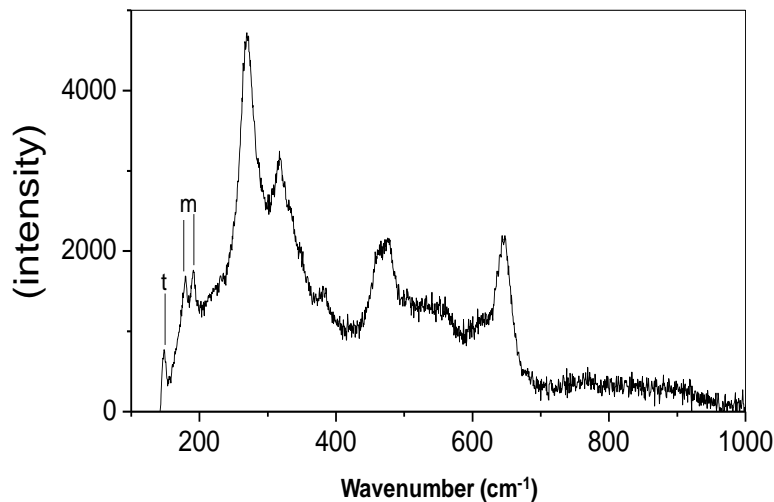


Fig. 4.7: Raman spectrum of the ZrO_2 powder showing the presence of both tetragonal and monoclinic phases (marked on the spectrum)

4.2.2.3 Chemical analysis from X-ray photoelectron spectroscopy

X-ray photoelectron spectroscopy measurements were performed to find the chemical composition of the material and the chemical state of Zr in the nanocrystalline ZrO_2 powder. A wide scan of XP spectrum has been presented in Fig. 4.8. It is observed that the photoelectron spectrum is composed of Zr peaks and O peaks. The absence of C indicated that the organic materials used for the preparation was completely burnt out. The indium 3d peak arises from the indium foil used for holding the ZrO_2 powder for XPS experiments

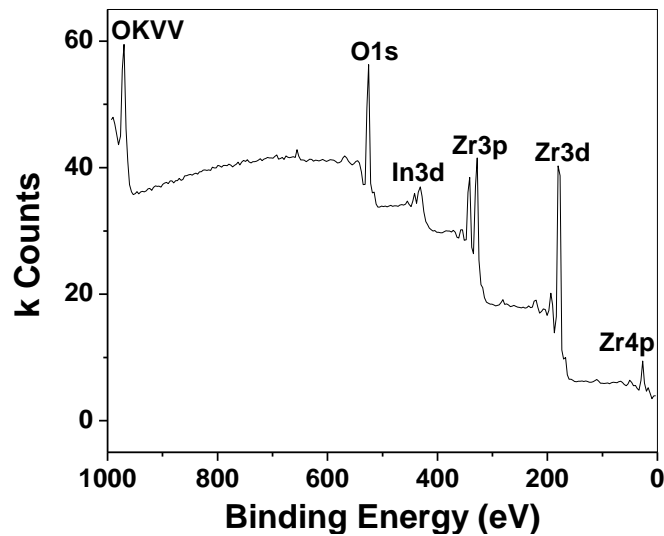


Fig. 4.8: XPS analysis of ZrO_2 powder on indium foil showing the composition of powder

Fig. 4.9 shows the Zr 3d peak that reveals the Zr3d binding energy at around 182 eV indicates the presence of only Zr^{4+} state in the prepared ZrO_2 powder [16]. The chemical analysis indicated that the material was not contaminated with any hydroxides or other chemical species. Fig. 4.10 shows the near Fermi level spectrum obtained from the ZrO_2 powder. The spectrum is associated with a broad peak from 0 to 7 eV indicating the formation of Zr–O hybridization bonding and non-bonding states [17]. The peak at around 15 eV is Zr 4d occupied states. Though, it is expected that the Zr 4d orbital should be completely unoccupied due to the

formation of Zr^{4+} states that gave rise to the $Zr4d-O2p$ conduction band states, the presence of the peak indicates that there is some reduction in Zr oxidation which led to the appearance of the occupied Zr 4d states. The peak around 8 eV is associated with the indium metal which was used for holding the powder for XPS measurements.

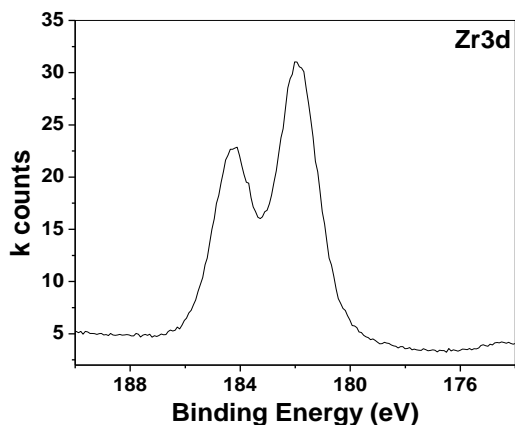


Fig. 4.9: Zr 3d photoelectron electron spectra of the ZrO_2 powder

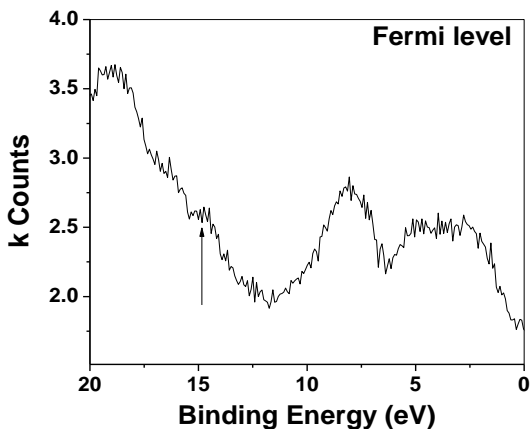


Fig. 4.10: Near Fermi levels spectral features of the ZrO_2 powder

4.2.3 The role of chemical conditions during ZrO_2 powder formation

The chemical conditions such as starting Zr-compound used for preparation, solvent, surfactants, temperature plays important role in the formation of nano-crystalline ZrO_2 powder. The use of $ZrO(NO_3)_2 \cdot 6H_2O$ as the starting material is found to be responsible for stabilization of metastable tetragonal phase at room temperature. The roles of various parameters during the powder formation are discussed in detail.

4.2.3.1 The role of solvent

Water containing ethanol (18%, v/v) was used as the solvent for the preparation of ZrO_2 nano powder. The solvent plays important role in ZrO_2 powder preparation during the precipitation of zirconium hydroxides by the addition of $NH_3 \cdot H_2O$. If water alone were used, the

hydroxide precipitate would have undergone agglomeration due to hydrogen bonds between the particles. This would lead to the formation of hard agglomerates during drying and calcinations. By using the ethanol, hydrogen bond between the adjacent precipitates that are responsible for formation of hard agglomerates were weakened [18] that resulted in the formation of small size nanocrystalline ZrO_2 .

18% ethanol is used for washing of the precipitate instead of pure water. The surfactant (PEG) adsorbed on the particle surfaces are rinsed out during washing due to weak Van der Waals forces between precipitates and PEG. Thus, the surface of zirconium hydrolysate is full of $-OH$ groups if pure water is used for washing. These $-OH$ groups form extensive hydrogen bonds between particles. When these $-OH$ groups were eliminated during the calcination and drying process, it would cause agglomeration. Here, as the precipitates are washed by ethanol, so $-OH$ groups on the surface of particles are replaced by $-OC_2H_5$ groups. Consequently, the possibility of the formation of strong chemical bonds and hard agglomerates is greatly eliminated. Surface tension of the washing solution is a critical component in the development of agglomerates. At room temperature, surface tension of water (0.07 Nm^{-1}) is nearly three times than surface tension of ethanol (0.02 Nm^{-1}) [19, 20]. The capillary pressure between the gels of ethanol is smaller than that of H_2O . So, hard agglomerates can be avoided in ethanol-water mixed washed gels. There is always some dissolution of Zr-hydroxides in water-ethanol mixture. During the drying of suspension, solute may re-precipitate between the particles and bonding them to form hard agglomerates. The lower solubility of Zr-hydroxides in ethanol than water results in softer agglomerates.

Optimum concentration of ethanol is important as low concentration lead to hard agglomerates consequently resulting in large grain size of ZrO_2 particles. High concentration of

ethanol cannot be used because zirconyl nitrate will not be soluble in solution having high fraction of ethanol.

4.2.3.2 The role of PEG-8000 as surfactant

It is believed that the use of PEG-8000 (Polyethylene glycol, molecular weight 8000) as steric dispersant controlled the particle size of ZrO_2 particles with narrow size distribution. The PEG interacts with precipitated particles in a very different manner. In the process of formation of nanoparticles through wet chemistry route, the colloidal stability plays an important role in the development of precipitate morphology [21]. PEG-8000 used in the preparation acts as a steric dispersant. Due to its amphiphilic nature, it can give steric stabilization to control the colloidal interaction potential with its hydrophobic ends adsorbed on the particle surface while the oxyethylene chain stretching into water phase. The surfactant cover the particles to form protecting layers, the connection due to the collision between the particles can be avoided. The precipitated particles are separated from each other due to the surrounding polymer matrix. Thus the growth of the particles was suppressed. So PEG adsorbed on the surface of precipitate prevents agglomeration during particle growth and both particle size and distribution would decrease [22].

4.2.3.3 Role of $ZrO(NO_3)_2$ as the starting material

It is observed that nitrate group in $ZrO(NO_3)_2$ has played the vital role in stabilizing the tetragonal phase in the zirconia powder. The oxygen vacancies seem to be responsible for stabilization of tetragonal phase at room temperature. Precursor obtained from $ZrO(NO_3)_2$ solution exist as $[Zr(OH)_2(OH_2)_2(NO_3)]^+$ chains in which zirconium atoms are eightfold coordinated by four bridging OH groups, two water molecules and one chelating nitrate. These chains are held together by hydrogen bonds through additional water molecules and non-

complexing nitrate groups located between the chains. Thus, half of the nitrate groups are covalently coordinated to the zirconium atoms and the other half are ionically bound in the crystal lattice between the chains. The stabilization of tetragonal phase occurred due to the presence of lattice defects or oxygen vacancies created because of the presence of nitrate group covalently bonded to zirconium ion [23, 24]. In addition, the presence of nitrate ions retarded the crystallization and delayed the growth of nanocrystalline ZrO_2 powder formed at $550^\circ C$. Metastable tetragonal phase of zirconia is possible to prepare at room temperature without dopants (stabilizers) when the particle sizes are below some critical crystallite size around 10–30 nm [25, 26]. In the present study, the ZrO_2 particle size distribution (Fig. 4.3) is in the range of 10–25 nm. This size distribution may be crucial for the tetragonal phase to be dominant in our case. It was observed that the ‘surface free energy’ favors the stabilization of tetragonal phase below the critical size [27, 28]. Thus, it can be concluded that small size of particles are responsible for stabilization of tetragonal phase owing to the lattice distortion caused by NO_3^- ions in the precursor solution. The concentration of $ZrO(NO_3)_2$ salt should be optimum to achieve the good dispersion of nano- ZrO_2 powder as high concentration of precursor results in poor dispersion of the nano-powder obtained [18]. In this context, it can be stated that $ZrOCl_2$ widely used for producing nanocrystalline ZrO_2 , is not a preferred material for producing predominant tetragonal phase of nanocrystalline ZrO_2 . In case of $ZrOCl_2$, Cl^- ions do not involve in the formation of Zr-complex in solution. So creation of oxygen vacancies during thermal annealing in this precursor is unlikely.

4.2.3.4 Role of temperature

In the process of precipitation, the mean size of particles depends on rate of nuclei formation and nuclei growth that depend on the reaction temperature. Viscosity decreases with

increase in temperature and mass transfer rate increases. Particle growth rate speed up and mean particle size increases. Along with this process, Brownian motion of particles intensified at high temperature and rate of particle growth was retarded. It leads to smaller particle size at high temperature. Optimum temperature ($\sim 80^\circ\text{C}$) is required to get the precipitates of small size.

4.2.4 Zeta potential of the zirconia powder in aqueous suspension

The surface charge behavior of the nanocrystalline zirconia powder in aqueous solution was studied [29]. Effect of temperature and dispersant on charge behavior of zirconia powder was experimentally measured using zeta potential technique. The zeta potential measurements of nanocrystalline ZrO_2 in aqueous suspension was performed at 25, 40 and 70°C as a function of pH. The preparations of all the suspensions prior to zeta potential measurements are described in section 2.9.8. All the solutions were sonicated for 1 h and then allowed to settle for 24 hrs to get a stable colloidal solution.

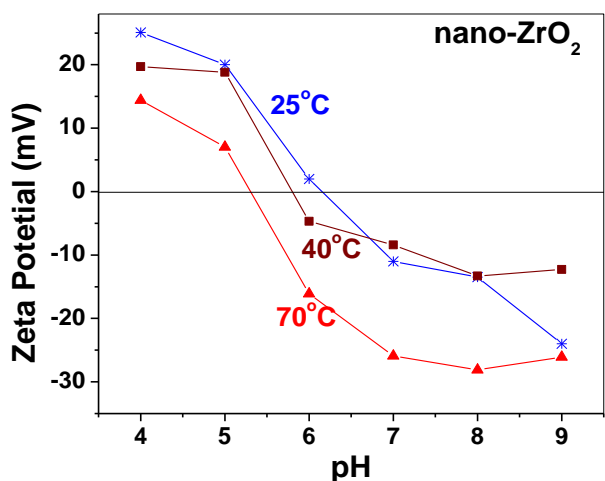


Fig. 4.11: The zeta potential of the nano- ZrO_2 at different temperature (a) 25°C , (b) 40°C and (c) 70°C , where pH_{pzc} was seen to reduce with increase in the temperature

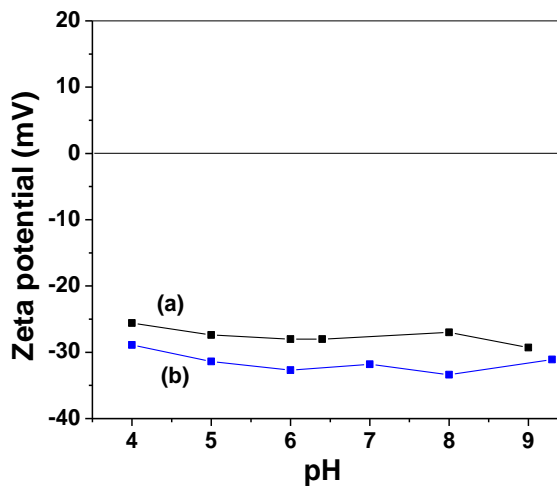


Fig. 4.12: The zeta potential of (a) nano- ZrO_2 in the aqueous solution containing SDS (b) $\alpha\text{-Fe}_2\text{O}_3$ in the aqueous solution containing SDS

The zeta potential values at different temperature and in the presence of surfactant are shown in Fig. 4.11. Fig. 4.11 shows the pH of zeta potential reversal (pH_{pzc}) decreased from 6.1 to 5.30 with the increase of temperature. Zeta potential values obtained from our work are in agreement with the Zhou et. al. [30]. Lower pH_{pzc} at higher temperature indicated that the surface hydroxyl groups were more ionized at higher temperature leading to a higher negative surface charge. Thus more protons are required to neutralize the surface charge. This results in shifting the pH_{pzc} to lower pH values [31].

The zeta potential of ZrO_2 in aqueous suspension in the presence of 10% sodium dodecyl sulfate (SDS) was determined as a function of pH at 25°C as shown in Fig. 4.12a. It shows almost a constant high negative zeta potential of ZrO_2 at all pH unlike the systems where SDS was not present. The high negative zeta potential corresponds to the increased stability of the system due to SDS dispersant. SDS is an electrosteric kind of dispersant. In presence of SDS, this behavior of zirconia suspension can be explained by double phase inversion [32]. SDS can interact with zirconia both electrostatically (through its sulfate group) and hydrophobically (via its alkane tail group). Adsorption of SDS molecules on the surface of nanocrystalline zirconia takes place because of Coulombic interaction. Beyond a certain SDS concentration (Initial SDS conc. 6 mM, [32]), hydrophobic interaction takes place between the alkyl chains of SDS adsorbed on nanocrystalline ZrO_2 in suspension. As a result, the sulfate functional groups are oriented outwards that lead to negative surface charge and negative zeta potential at high SDS concentration. Similar double phase inversion in SDS with CaCO_3 was also observed by Cui et al. [32]. This behavior also got confirmed when the zeta potential of $\alpha\text{-Fe}_2\text{O}_3$ powder was measured in aqueous solution containing 10% SDS (Fig. 4.12b). Here also, almost a constant high negative zeta potential of Fe_2O_3 has been observed at all pH. So, it is concluded that both

functional sulfate group at surface and its hydrophobic chain has influenced the adsorption of SDS on the zirconia/water interface.

4.3 Adsorption of nano-ZrO₂ on SS304L in aqueous medium

In this work, direct adsorption of zirconia nanoparticles on SS 304L surfaces have been carried out [33]. Effect of dispersant like SDS on the adsorption behavior of ZrO₂ has also been studied at different temperatures viz. 25°C, 90°C and 150°C. Substrates used are plain polished SS 304L and the pre-oxidized SS surface POO-21 described in section 3.3.2. The pre-oxidized surface was consisting of mainly α -Fe₂O₃, α -(Fe,Cr)₂O₃ with small amount of spinel oxides. Adsorption of ZrO₂ on the SS 304L surface is based on the electrostatic interaction between ZrO₂ nanoparticles and the substrate surface. For the attraction between the ZrO₂ nanoparticles and the substrate surface, surface charge (zeta potential) of suspended ZrO₂ particles in solution and the oxidized SS surface should be opposite. The pH of the solution decides the charge on the suspended ZrO₂ particles and the pre-oxidized surfaces. Prior to all the adsorption experiment, pH was adjusted to 6.2 with dilute NaOH. Point of zero charge (PZC) of ZrO₂ nanoparticles measured 6.1 at room temperature. The pH of the solution (6.2) is higher than the PZC of ZrO₂ (6.1), so ZrO₂ particles will be negative. PZC of α -Fe₂O₃, Cr₂O₃, Fe₃O₄ and NiFe₂O₄ are 8.4, 7, 6.5 and 6.7 respectively [34, 35]. The substrate surface will be positive in charge and the interaction between the depositing material and the substrate surface will be attractive. Aqueous solution containing ZrO₂ nano-particles was sonicated for 1 hr prior to the ZrO₂ deposition experiment to get the dispersion. The adsorption experiments are described in detail in section 2.6. The SS surfaces have been characterized by SEM-EDS and XPS after the adsorption experiments.

4.3.1 Adsorption of nano-ZrO₂ on plain SS304L surfaces at room temperature

The adsorption of ZrO₂ nano-particles were carried out on plain SS and POO-21 surfaces at pH 6.2 at 25°C. One set of experiments were carried out in the presence of SDS while another set were carried out without SDS. After the adsorption experiments, samples were characterized by XPS. Zr signal was not observed in the XPS spectra even after several scans. This implies that ZrO₂ nanoparticles could not be deposited on the substrate surfaces at room temperature. It is assumed that the energy required for nucleation of ZrO₂ particles on the substrate surface is not available at room temperature. As the temperature increases, nucleation events become more probable as the energy available for nucleation of ZrO₂ on the substrate surface increases. So, the same experiments are repeated at high temperature (90°C).

4.3.2 Adsorption of nano-ZrO₂ on SS304L surfaces at 90°C

The ZrO₂ nanoparticles were directly adsorbed on the plain SS and POO-21 surfaces at pH 6.2 at 90°C. Few specimens were treated with aqueous solution containing ZrO₂ nanoparticles and SDS while some specimens were treated with only ZrO₂ nano-particles without any surfactant. After the experiments, the ZrO₂ coated samples were characterized by SEM-EDX and XPS.

For the plain SS specimens, XPS analysis of the nano-ZrO₂ treated SS sample did not show any signal of Zr. That means nano-ZrO₂ cannot be adsorbed on plain SS surface without an intermediate oxide layer. It appears that plain SS surface cannot provide the sufficient surface energy even for physical adsorption of nano-ZrO₂ particles. Pre-oxidation of the SS prior to nano-ZrO₂ deposition is necessary for getting the adherent ZrO₂ deposition. Fig. 4.13 shows the SEM images of pre-oxidized SS specimen (POO-21) after the adsorption of ZrO₂ nano-particles. The ZrO₂ coated sample prepared without any surfactant is shown in Fig. 4.13a while the ZrO₂

coated sample prepared using SDS is shown in Fig. 4.13b. Both of the images show that the ZrO_2 particles have been deposited over the substrate surface. But the coating is not continuous and ZrO_2 islands are distributed unevenly on the pre-oxidized surface. The places where ZrO_2 particles seem to be deposited show the Zr counts ranging from 10 to 30 wt% in both samples. In both the cases (with and without SDS), EDS analysis shows very poor Zr counts at few places. The variation of EDS counts of Zr at different places is shown in Fig. 4.13.

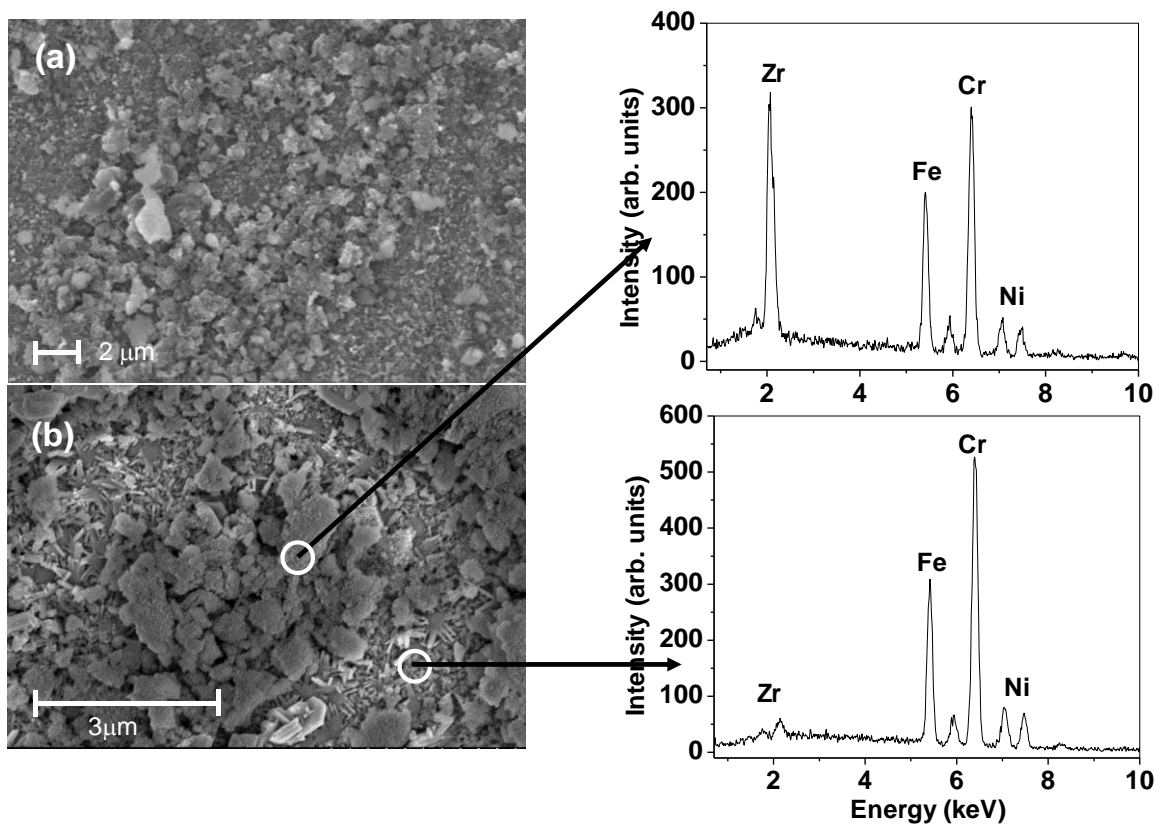


Fig. 4.13: SEM images of the pre-oxidized SS specimen after the adsorption of nano- ZrO_2 in the aqueous solution at 90°C (a) without any surfactant (b) containing SDS as surfactant; EDS results at two different zones showing different counts of zirconium

The XPS spectra of both of the ZrO_2 coated samples are shown in Fig. 4.14. Zr signals can be clearly seen in both the cases (Fig. 4.14 a & b). The presence of photoelectron peaks of Fe

2p and Cr 2p from the substrate reveal that the ZrO_2 coating is not continuous in both cases as shown by SEM images. The elemental analysis reveals that around 10 at% Zr was present on the pre-oxidized surface when the deposition was carried out without SDS. The nano- ZrO_2 deposition in the presence of SDS results in deposition of 9 at% of Zr. SDS as a surfactant does not seem to have a significant improvement on the ZrO_2 deposition, so further nano- ZrO_2 adsorption experiments are carried out without SDS.

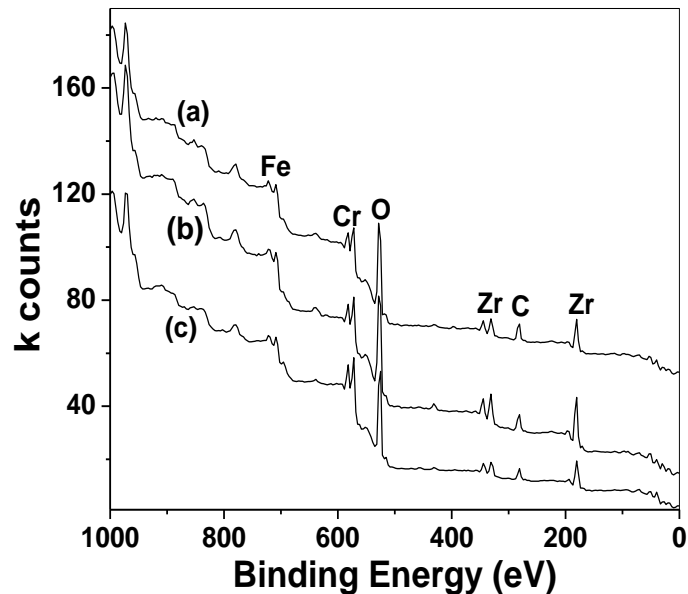


Fig. 4.14: XPS wide scan of the pre-oxidized SS specimen after the adsorption of nano- ZrO_2 in the aqueous medium (a) without any surfactant at $90^\circ C$, (b) containing SDS as surfactant at $90^\circ C$ and (c) without any surfactant at $150^\circ C$

4.3.3 Adsorption of nano- ZrO_2 on SS304L surface at $150^\circ C$

Direct deposition of ZrO_2 nano-particles is carried out on POO-21 surface at $150^\circ C$ and pH 6.2 (SDS is not used here). The SEM image (Fig. 4.15a) shows that ZrO_2 coating is not continuous. The EDS results (Fig. 4.15b) show the Zr counts as < 1 wt% at most of the places. It shows that the direct adsorption of ZrO_2 nano-particles is not favorable at $150^\circ C$. The XPS

spectrum reveals the presence of ZrO_2 on the surface (Fig. 4.14c) along with intense substrate signals. The elemental XPS analysis show the presence of 5 at% of Zr that is quite less compare to $90^\circ C$ deposited samples. It supports the observation of EDS analysis that direct adsorption of ZrO_2 nano-particles is less favorable at $150^\circ C$ compare to $90^\circ C$.

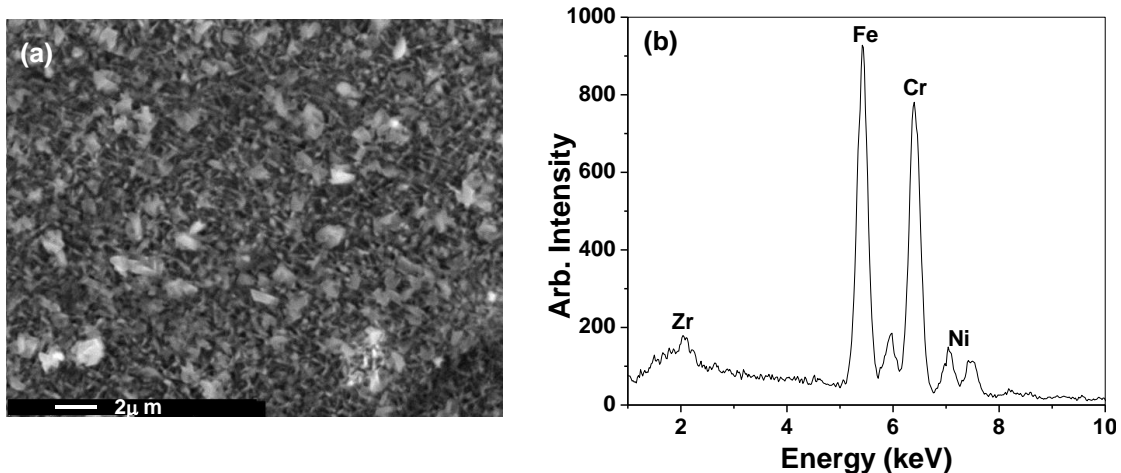


Fig. 4.15: SEM images (a) and EDS results (b) of the pre-oxidized SS specimen after the adsorption of nano- ZrO_2 in aqueous solution at $150^\circ C$

The direct adsorption of ZrO_2 nano-powder on the pre-oxidized SS surface is effective for the deposition of ZrO_2 nano-particles but it could not provide the full surface coverage. The adsorption of suspended nanocrystalline ZrO_2 particles from the aqueous solution to the SS surface is the result of electrostatic interaction between substrate surface and depositing material. The electrostatic interaction forces are not sufficient enough to grow a thick and continuous ZrO_2 coating on the SS surface. The direct adsorption of ZrO_2 nano-particles is very simple technique for application at industrial scale but the coating quality is not good. It is not advisable to use it on the fresh material. But the cases where cracks are already developed, the nano- ZrO_2 particles can sit into the cracks/ pits/ crevices and crack growth can be arrested.

4.4 Conclusions

Nanocrystalline ZrO_2 with dominant tetragonal phase has been synthesized by direct precipitation route. The ZrO_2 powder prepared consists of varying sizes but the majority of the nanocrystals are of the order of 10 nm. Use of $\text{ZrO}(\text{NO}_3)_2 \cdot 6\text{H}_2\text{O}$, choosing a suitable solvent and surfactant is important for preparing tetragonal dominant ZrO_2 nano-particles. The charge behavior of the nanocrystalline ZrO_2 in aqueous solution is observed by measuring the zeta potentials. Zeta potential of nanocrystalline ZrO_2 is seen to be negative and stable for a wide range of pH with SDS in solution. These observations help in deciding appropriate conditions for developing nanocrystalline ZrO_2 coating on steel through hydrothermal process. The adsorption of ZrO_2 nano-particles in aqueous solution is more favorable at 90°C compare to 150°C as observed by Yeh et. al. [6]. The direct adsorption of ZrO_2 nanoparticles on the pre-oxidized SS surface leads to the discontinuous ZrO_2 coating on the substrate surface. Along with electrostatic interaction forces, a further co-operative mechanism is required to promote the formation of covalent bond between ZrO_2 particles and substrate surface.

4.5 References

- [1] Z.F. Zhou, E. Chalkova, S.N. Lvov, P. Chou, R. Pathania, *Corros. Sci.* 49 (2007) 830-843.
- [2] Z.F. Zhou, E. Chalkova, S.N. Lvov, P.H. Chou, *J. Nucl. Mater.* 378 (2008) 229–237.
- [3] B. Stellwag, R. Killan, *Water Chemistry of Nuclear Reactor Systems* 8, BNES (2000) 127-131.
- [4] T.-K. Yeh, Y.-C. Chein, B.-Y. Wang, C.-H. Tsai, *Corros. Sci.* 50 (2008) 2327–2337.
- [5] T.-K. Yeh, Po-I. Wu, C.H. Tsai, *Prog. Nucl. Energ.* 57 (2012) 62-70
- [6] T.-K. Yeh, M.-Y. Lee, C.-H. Tsai, *J. Nucl. Sci. Technol.* 39 (2002) 531–539.

- [7] B. Djuricic, S. Pickering, D. McGarry, P. Glaude, P. Tambuyser, K. Schuster, *Ceram. Int.* 21 (1995) 195–206.
- [8] P. Jayaweera, S. Hettiarachchi, H. Ocken, *Colloids Surf. A Physicochem. Eng. Asp.* 85 (1994) 19–27.
- [9] Y. Huang, T. Ma, J.-L. Yang, L.-M. Zhang, J.-T. He, H.-F. LiY, *Ceram. Int.* 30 (2004) 675–681.
- [10] Z. Xie, J. Ma, Q. Xu, Y. Huang, Y.-B. Cheng, *Ceram. Int.* 30 (2004) 219–224
- [11] R. Srinivasan, R.J. De Angelis, G.I. Oak Ridge, H. Davis, *J. Mater. Res.* 6 (1991) 1287–1292.
- [12] E. Djurado, P. Bouvier, G. Lucazeau, *J. Solid State Chem.* 149 (2000) 399–407.
- [13] T. Chraska, A.H. King, C.C. Berndt, *Mater. Sci. Eng., A* 286 (2000) 169–178.
- [14] P. Barberis, T. Merle-Me´jean, P. Quintard, 246 (1997) 232–243
- [15] E. Djurado, P. Bouvier, G. Lucazeau, *J. Solid State Chem.* 149 (2000) 399–407.
- [16] D. Briggs, M.P. Seah, in: D. Briggs, M.P. Seah (Eds.), 2nd edition, vol. 1, John Wiley & Sons, New York, NY, USA, 1993.
- [17] R.H. French, S.J. Glass, F.S. Ohuchi, Y.-N. Xu, F. Zandiehnam, W.Y. Ching, *Phys. Rev. B* 49 (1994) 5133–5142.
- [18] S. Wang, X. Li, Y. Zhai, K. Wang, *Powder Technol.* 168 (2006) 53–58.
- [19] G. Vazquez, E. Alvarez, J. M. Navaza, *J. Chem. Eng. Data* 40 (1995) 611–614.
- [20] A.W. Adamson, A.P. Gast.; *Physical chemistry of surfaces*; 6Ed, Wiley, 1997.
- [21] J.L. Look, C.F. Zukoski, *J. Am. Ceram. Soc.* 75 (1992) 1587–1592.
- [22] H.-C. Yao, X.-W. Wang, H. Dong, R.-R. Pei, J.-S. Wang, Z.-J. Li, *Ceram. Int.* 37 (2011) 3153–3160

- [23] M. Tahmasebpour, A.A. Babaluo, M.K. Razavi Aghjeh, *J. Eur. Ceram. Soc.* 28 (2008) 773–778.
- [24] J. Livage, *Catal. Today* 41 (1998) 3–19.
- [25] L. Chen, T. Mashimo, E. Omurzak, H. Okudera, C. Iwamoto, A. Yoshiasa, *J. Phys. Chem. C* 115 (2011) 9370-9375.
- [26] R.C. Garvie, R.H. Hannink, R.T. Pascoe, *Nature* 258 (1975) 703–704.
- [27] M. Gateshki, V. Petkov, G. Williams, S.K. Pradhan, Y. Ren, *Phys. Rev. B* 71 (2005) 224107–224115.
- [28] Z. Qian, J.L. Shi, *Nanostruct. Mater.* 10 (1998) 235–244.
- [29] N. Garg, V.K. Mittal, S. Bera, A. Dasgupta, S. Velmurugan, *Ceram. Int.* 38 (2012) 2507-2512.
- [30] X.Y. Zhou, X.J. Wei, M.V. Fedkin, K.H. Strass, S.N. Lvov, *Rev. Sci. Instrum.* 74 (2003) 2501-2506.
- [31] P. Jayaweera, S. Hettiarachchi, *Rev. Sci. Instrum.* 64 (1993) 524–528.
- [32] Z.-G. Cui, K.-Z. Shi, Y.-Z. Cui, B.P. Binks, *Colloids Surf. A Physicochem. Eng. Asp.* 329 (2008) 67–74.
- [33] N. Garg, V.K. Mittal, S. Bera, S. Velmurugan, *AIP Conf. Proc.* 1447 (2012) 735-736.
- [34] G.A. Parks, *Chem. Rev.* 65 (1965) 177
- [35] R.C. Plaza, J. de Vicente, S. Gómez-Lopera, A.V. Delgado, *J. Colloid Interface Sci.* 242 (2001) 306-313.

Chapter 5

***Development of ZrO₂ coatings
from Zirconyl Salt
and
Role of Chemical Composition of
Pre-oxidized Layer***

5. 1 Introduction

It has been observed from the previous chapter that direct adsorption of nano-ZrO₂ could not produce a compact and thick film. Hence, a different hydrothermal method is approached using Zirconyl salt along with Na-EDTA and SDS to develop ZrO₂ coating on SS surface. The details of these experiments have been given in the Materials and Methods Chapter (section 2.7). This chapter deals with the different aspects of ZrO₂ coatings on different pre-oxidized SS surfaces by hydrothermal method using ZrO(NO₃)₂.6H₂O.

During the hydrothermal deposition, molecular level chemical interactions take place in between depositing material and substrate surface at high temperature and high pressure. This leads to atom by atom interaction between substrate surface and depositing material [1, 2]. Hence, the chemical composition of SS surface oxide layer is very important for the growth of adherent and continuous ZrO₂ coatings on SS surface [3]. Type 304L stainless steel coupons were pre-oxidized under different conditions as discussed in Chapter 3 to form different type of oxide surfaces. Three different types of pre-oxidized surface are chosen; (i) Pre-oxidized surfaces composed of spinel oxides like NiFe₂O₄, FeCr₂O₄, Fe₃O₄ etc, (ii) pre-oxidized surface composed of mixed spinel and rhombohedral type oxides like α -Fe₂O₃, Cr₂O₃ etc. and (iii) pre-oxidized surface composed of pure α -Fe₂O₃. zirconia films were developed on these surfaces under identical deposition conditions by hydrothermal technique. The ZrO₂ coated samples were characterized by different techniques like SEM, XPS and Raman spectroscopy and GI-XRD. Detailed characterization of the zirconia coatings led to the establishment of the most suitable SS oxide surface required for ZrO₂ deposition.

5.2 Role of chemical composition of oxide layer on stainless steel surface for hydrothermal deposition of ZrO₂ coating

Surface chemical composition of the pre-oxidized SS specimen is important because the top few layers are involved in the initial stage of nucleation of ZrO₂. Preparation and characterization details of the pre-oxidized SS surfaces are mentioned in chapter 2 and Chapter 3. The pre-oxidized surfaces used were: 1. POH-5, 2. POO-14 and 3. POP. The substrate surface compositions of all the three samples used for comparison are given in Table 5.1.

Table 5.1: The details of substrate surfaces used for studying the role of substrate surface during ZrO₂ deposition

Sample Name	Experimental conditions for preparation	Composition of the pre-oxidized surface on SS
POH-5	1ppm LiOH, 24ppm Hydrazine, 250°C, pH 10.3, 5 days (reducing conditions)	Ni _x Fe _{3-x} O ₄ (x=0-1), NiFe _x Cr _{2-x} O ₄ (x<1), FeCr ₂ O ₄ (spinel oxides)
POO-14	Normal water, Initial oxygen concentration 7000ppb, 240°C, 14 days (oxidizing conditions)	α-Fe _{2-x} Cr _x O ₃ (0<x<2), α-Fe ₂ O ₃ , Cr ₂ O ₃ , FeCr ₂ O ₄ , NiFe ₂ O ₄ (Mixture of rhombohedral and spinel oxides)
POP	Pulsed laser deposition	α-Fe ₂ O ₃ only

5.2.1 Preparation and characterization of the ZrO₂ coatings on pre-oxidized SS surfaces

The ZrO₂ coatings were deposited on all the pre-oxidized SS specimens in a static autoclave using 1:1 ZrO(NO₃)₂ and Na-EDTA, SDS at 200°C, pH 6.2 for 5 days. The details of the ZrO₂ deposition by hydrothermal method are discussed in section 2.7.1. After the ZrO₂ deposition on POH-5, POO-14 and POP specimens, the coated samples are designated as ZPOH, ZPOO, ZPOP respectively. Subsequent to the ZrO₂ deposition, the ZrO₂ coated samples were examined by SEM- EDS, Raman spectroscopy, XPS and GI-XRD.

5.2.1.1 SEM-EDX characterization and thickness analysis

The SEM images from the zirconia coated samples are shown in Fig. 5.1 and the EDS spectra for the same are shown in Fig. 5.2.

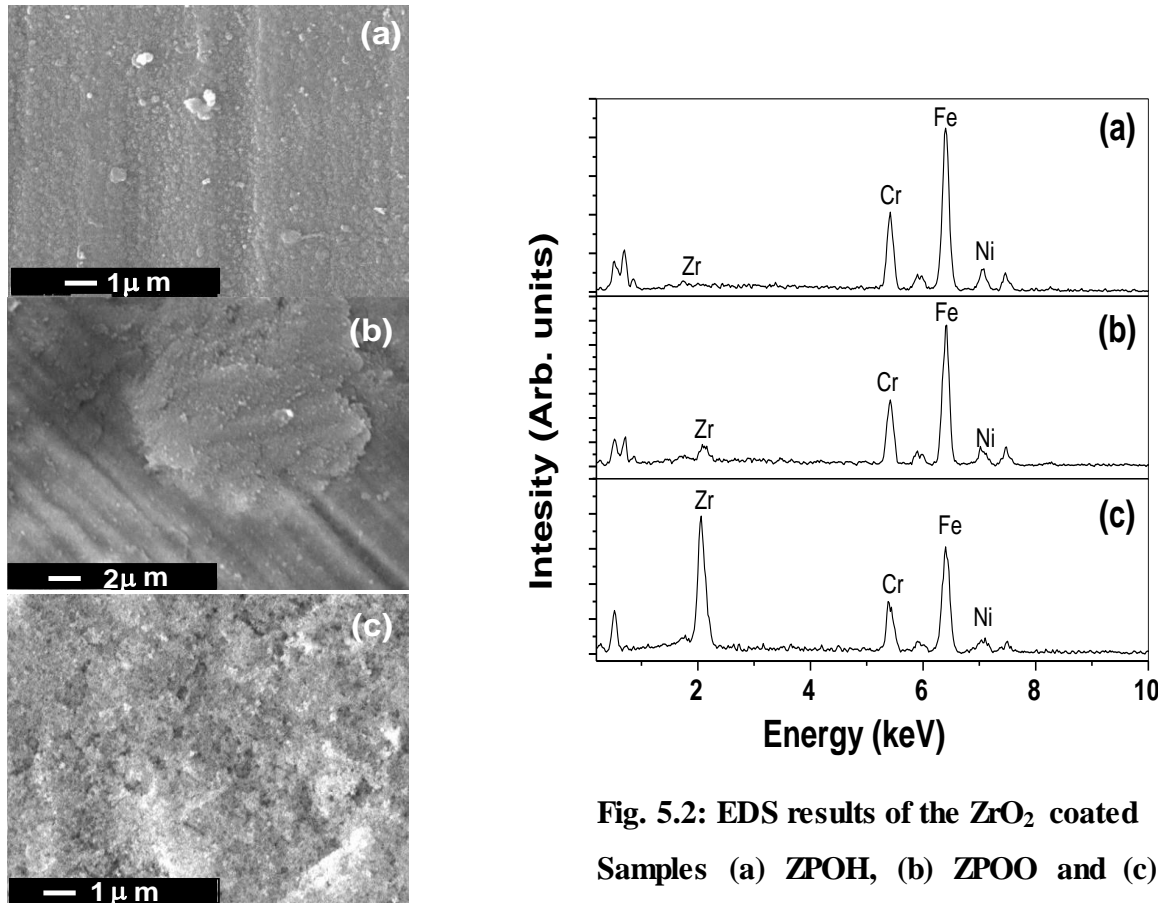


Fig. 5.1: SEM micrographs of ZrO₂ coated samples (a) ZPOH, (b) ZPOO and (c) ZPOP

Fig. 5.2: EDS results of the ZrO₂ coated Samples (a) ZPOH, (b) ZPOO and (c) ZPOP

Zirconia coating on POH-5 (Fig. 5.1 a) is thin. The EDS data (Fig. 5.2a) recorded at different places of the sample ZPOH showed that zirconium is present but with relatively low zirconium counts (<1wt %). It can be concluded that a very thin zirconia layer was developed on the surface of spinel oxides. In the case of ZPOO, zirconia film is present in heterogeneous

topology, forming zones of thicker and thinner deposits. EDS analysis done at different points on the coating indicated that zirconia film was covering the surfaces completely but having a huge difference in zirconium counts at different places (Fig. 5.3) varying from 3 to 48 wt%. It can be concluded that a continuous but non-uniformly thick coating developed on the ZPOO surface. For the specimens ZPOP, ZrO_2 particles seem to deposit more evenly on the surface (Fig. 5.1c). This inference is further supported by the EDS result (Fig. 5.2c) showing relatively constant and fairly high (approximately 31 wt%) zirconium counts at every place. It can be inferred that a thick, uniform and continuous zirconia coating developed on pre-oxidized specimen composed of $\alpha-Fe_2O_3$ as surface oxide.

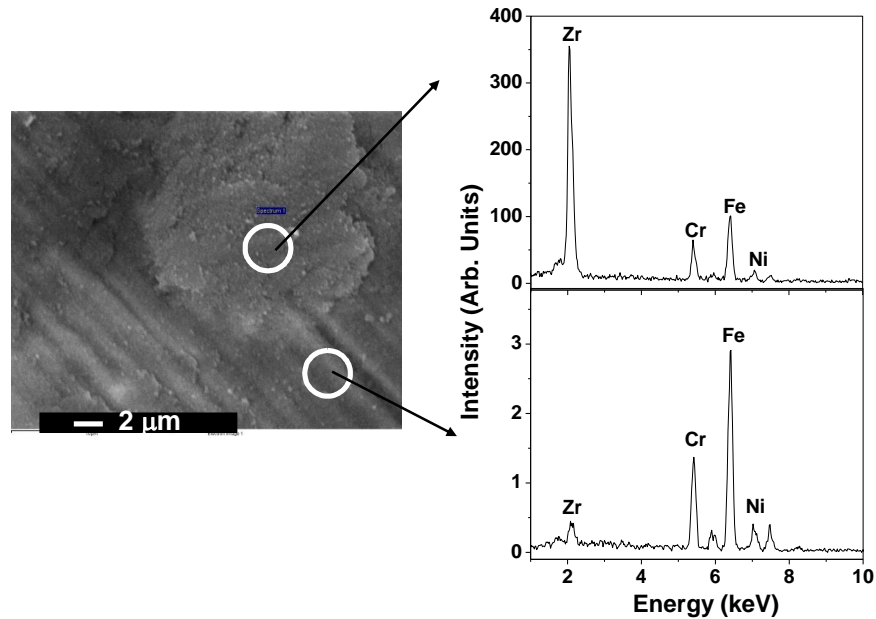


Fig. 5.3: EDS results of ZrO_2 coated ZPOO specimen at two different places showing different counts of zirconium

The average thickness of ZrO_2 coatings in the case of ZPOH, ZPOO and ZPOP are found to be 60 nm, 120 nm and 250 nm respectively measured by ZrO_2 coating dissolution followed by UV-Vis spectroscopy (section 2.8.2).

5.2.1.2 Raman and GI-XRD analysis

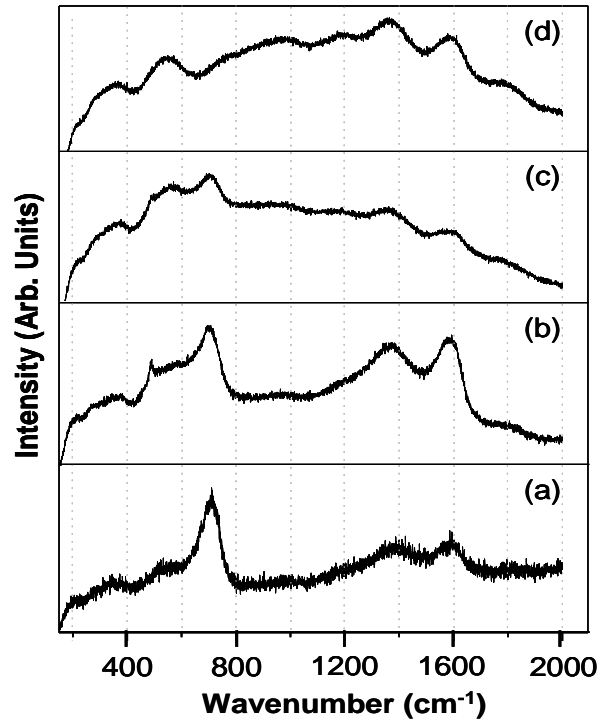


Fig. 5.4: Raman spectra of ZrO₂ coated specimens (a) ZPOH, (b) and (c) ZPOO at two different points and (d) ZPOP

The Raman spectra of zirconia coated samples are shown in Fig. 5.4. Raman spectra are taken at several points of ZPOH and no difference was observed in the spectra. The intensity of all the Raman peaks of POH-5 (Fig. 3.3) got reduced in ZPOH which indicates the presence of a thin layer of ZrO₂ on the surface of ZPOH. Raman spectra acquired from ZPOO showed a significant difference between the Raman spectra taken from different regions of the sample but the intensity of the substrate signals got reduced significantly for all the regions. This implies that, in ZPOO, zirconia is present all over the surface but the thickness of ZrO₂ layer is different at different places. This evidence is supported by SEM and EDS measurements where excessive growth of zirconia can be seen clearly at some places. Two spectra taken from ZPOO are shown

in Figs. 5.4b and 5.4c. It appears that, ZrO_2 coated sample has lost the substrate features corresponding of $\alpha-Fe_2O_3$ while the intense peak corresponds to spinel oxides is present after the ZrO_2 coating. In case of ZPOP sample, the substrate signals belonging to the POP disappeared after the ZrO_2 coating (Fig. 5.4c). This might be due to the formation of a thick and uniform layer of ZrO_2 . This fact is further supported by the presence of ~ 31 wt% of Zr in the EDS spectra. Loss of Raman spectral feature related to $\alpha-Fe_2O_3$ in both ZPOP and ZPOO samples is a direct evidence of involvement of $\alpha-Fe_2O_3$ for mediating the growth of the ZrO_2 grains on stainless steel.

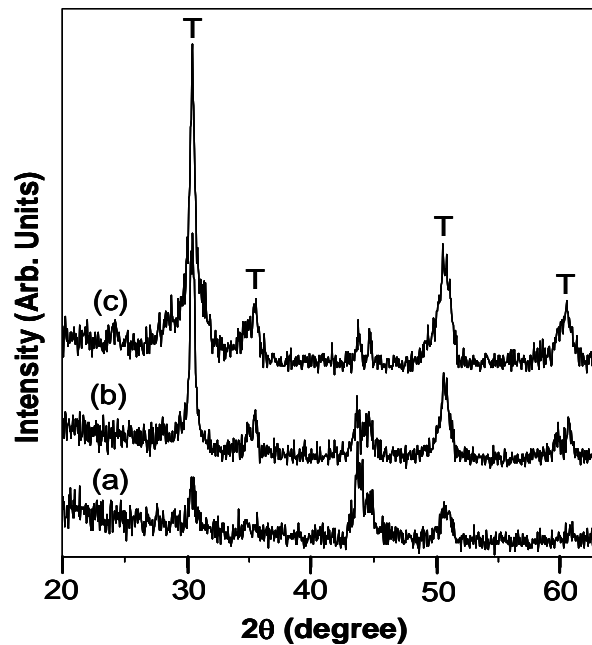


Fig. 5.5: GIXRD patterns obtained from ZrO_2 coated samples (a) ZPOH, (b) ZPOO and (c) ZPOP; T - tetragonal zirconia

Grazing incidence x-ray diffraction (GI-XRD) patterns are used for phase analysis of ZrO_2 coatings deposited (Fig. 5.5). The detailed analysis of the patterns indicates that tetragonal or cubic ZrO_2 is the major phase of ZrO_2 coatings. Pure ZrO_2 cannot crystallize in the cubic

phase by synthesis, a stabilizer like yttria or calcium oxide needs to be added to the source powder in order to crystallize it in cubic phase. As there is no source of such dopants in the reactor system, hence the phase formed in the coating is most likely to be tetragonal ZrO_2 . Stabilization of tetragonal phase of ZrO_2 indicates that the particles are nano-crystalline in nature with particles size below 25 nm [4, 5], which is evident from the broad peaks in the XRD patterns (Fig. 5.5). Average particle size of coated ZrO_2 particles is calculated by using Scherrer formula (section 2.9.5) and found to be ~15 nm. Use of $ZrO(NO_3)_2 \cdot 6H_2O$ as the starting material may be responsible for the stabilization of tetragonal phase [6, 7].

5.2.1.3 XPS analysis

The photoelectron spectra of the ZrO_2 coated samples are shown in Fig. 5.6.

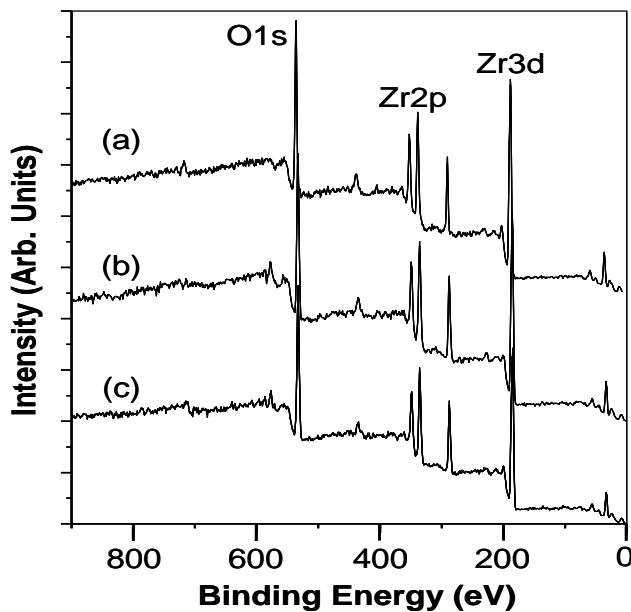


Fig. 5.6: XPS of ZrO_2 coated specimens (a) ZPOP, (b) ZPOO and (c) ZPOH

It is evident from the spectra that significant amount of ZrO_2 was deposited in all cases. Though a huge variation in Zr counts was observed in EDS measurement of the ZrO_2 coated

samples, there is hardly any variation observed in the photoelectron spectra (Fig. 5.6). The depth of information in XPS is limited to few nanometers (5-10 nm). The coatings formed on the three specimens are certainly higher than the depth of information of the XPS technique where as the EDS spectra are mixed with signals from both coatings and the substrates.

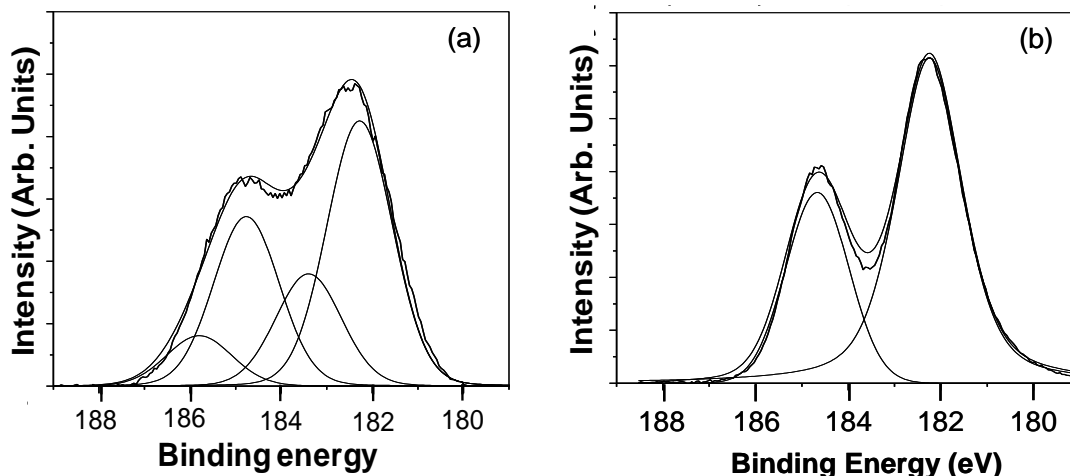


Fig. 5.7: (a) Deconvolution of Zr 3d_{5/2} photoelectron peak acquired from ZrO₂ coated specimen (ZPOP) showing the presence of ZrO₂ (182.2 eV) and small amount of zirconium hydroxide (183.0 eV), (b) the same peak after Ar⁺ ion sputtering

Zr 3d_{5/2} spectrum acquired from one of the coated specimens (ZPOP) is shown in Fig. 5.7. The binding energy of Zr 3d_{5/2} was found to be 182.2 eV in all cases which is well matching with the literature value for the ZrO₂ [8]. The FWHM for Zr 3d_{5/2} for standard ZrO₂ was found to be 1.7 eV, whereas in the present case the FWHM was seen to be 2.2 eV. The spectrum was deconvoluted by fitting Gaussian-Lorentzian mixed function on a Shirley background and an additional peak was observed at 183.0 eV. The peak at higher energy can be marked for Zr(OH)₄. After Ar⁺ sputtering for 30 seconds, the spectra became narrower as shown in Fig. 5.7b. Many metal hydroxides tend to reduce into metal oxides by Ar ion Sputtering [9]. So from

binding energy values it appears that the coating is composed of mainly ZrO_2 with small amount of Zr-hydroxide at surface which was removed in few seconds of sputtering.

5.2.2 Interaction of ZrO_2 with pre-oxidized SS surfaces

The hydrothermal conditions used in this study lead to formation of nano-size zirconia particles in the aqueous solution at $200^\circ C$. The mechanism of ZrO_2 nano-particles formation in aqueous solution is discussed in section 5.3 in detail. The zirconia nano-particles remain suspended in solution due to the small size. In addition, the surfactant SDS in the solution keeps particles in suspension and prevents agglomeration. To initiate the adsorption of ZrO_2 particles on substrate surface, suspended zirconia particles and the target substrate surface should have opposite charges. Surface charge (zeta potential) of the suspended ZrO_2 particles in solution and the pre-oxidized stainless steel surface are primarily decided by the solution pH. The room temperature pH of the starting solution was 6.2. Corresponding pH could be ~ 5.0 at $200^\circ C$. PZC values of various oxides at different temperatures are given in Table 5.2 [10-14]. As pH of the solution is higher than the PZC of ZrO_2 at $200^\circ C$, zeta potential of ZrO_2 particles will be negative [11]. Due to negative zeta potential of ZrO_2 particles in the solution, maximum number of surface sites of ZrO_2 would be occupied by $-O^-$. The solution pH is lower than the PZC of $Fe_2O_3/Fe_3O_4/NiFe_2O_4$, so zeta potential of $Fe_2O_3/Fe_3O_4/NiFe_2O_4$ will be positive [11-14] and $-OH_2^+$ ions will prevail on surface sites of all the pre-oxidized surfaces. Due to the opposite surface charges, suspended zirconia particles would experience electrostatic force of attraction towards all pre-oxidized surfaces mentioned here. Opposite charges on the suspended ZrO_2 nano-particles (ZrO^-) and target pre-oxidized SS surfaces ($Fe-OH_2^+$) leads to form an interface bond between zirconia particles and the substrate surface through oxygen bridging. This may be the reason of ZrO_2 deposition on all of the pre-oxidized surfaces.

Table 5.2: Point of zero charge (PZC) values of ZrO₂ and different iron oxides [2]

Sample	PZC at 25°C	PZC at higher temperature	References
ZrO ₂	6.1, 6.05	5.3 at 70°C 4.7 at 200°C	[6, 10,11]
α-Fe ₂ O ₃	>8.4	5.9 at 200°C	[11,12]
Fe ₃ O ₄	6.5	6.0 at 100°C	[11-13]
NiFe ₂ O ₄	6.7	-	[14]
Cr ₂ O ₃	7.0	-	[12]

Table 5.3: Lattice parameters of tetragonal ZrO₂, α-Fe₂O₃ and spinel oxides

Sample	Structure	Lattice parameters	Reference
ZrO ₂	Tetragonal	a =b =5.0813Å, c = 5.1989Å°	15, 16
α-Fe ₂ O ₃	Rhombohedral	a =b = 5.0355Å°, c = 13.747Å°	17
NiFe ₂ O ₄	Cubic	a = b= c = 8.37 Å°	18
Fe ₃ O ₄	Cubic	a = b= c = 8.407 Å°	19

In addition to PZC of pre-oxidized surfaces, ZrO₂ coating growth process is strongly influenced by the crystal structure of substrate surface oxides. ZrO₂ coating is thick, uniform and crystalline when the substrate surface was composed of pure α-Fe₂O₃. ZrO₂ coating is having the minimum thickness when the substrate surface was constituted of only spinel oxides. Substrate surface composed of α-Fe₂O₃ has a preference for nucleation of crystalline zirconia because lattice parameters of tetragonal zirconia and α-Fe₂O₃ are nearly equal [15-17]. Spinel oxides (Fe₃O₄, ferrites or chromites) are less preferred for nucleation of ZrO₂ crystallites as lattice parameters of spinel oxides are larger [15, 16, 18, 19] than ZrO₂ lattice parameters. The lattice parameters of the tetragonal ZrO₂, α-Fe₂O₃ and spinel oxides are given in Table 5.3.

The adsorbed zirconia particles nucleate as the tetragonal ZrO_2 crystallites on the pre-oxidized SS surfaces. The ZrO_2 crystallites grow 20% faster relative to the amorphous ZrO_2 [20], abundance of ZrO_2 crystallite on the pre-oxidized surface decides the thickness of ZrO_2 film. The matching lattice parameters of $\alpha\text{-Fe}_2\text{O}_3$ with the tetragonal zirconia lead to higher number of nucleation centers for ZrO_2 crystallites. The substrate surface composed of $\alpha\text{-Fe}_2\text{O}_3$ results in formation of uniform and thicker ZrO_2 coating. Substrate surface consisting of both the spinel and rhombohedral ($\alpha\text{-Fe}_2\text{O}_3$, $\alpha\text{-Fe}_{2-x}\text{Cr}_x\text{O}_3$) type of oxide structures lead to varying number of nucleation sites at different regions of substrate surface and result in non-uniform growth of ZrO_2 coating. Spinel oxides do not seem to be the favorable oxide for the nucleation of ZrO_2 crystallites. Low nucleation density of ZrO_2 crystallites on spinel oxides results in limited growth of ZrO_2 crystallites and lead to a very thin coatings.

5.3 Study of $\text{Fe}_2\text{O}_3\text{-ZrO}_2$ interface and mechanism of ZrO_2 coating

To understand the mechanism of ZrO_2 coating formation on $\alpha\text{-Fe}_2\text{O}_3$ surface and the interface of $\alpha\text{-Fe}_2\text{O}_3$ with the ZrO_2 coating, very thin zirconia coatings were developed on the $\alpha\text{-Fe}_2\text{O}_3$ surface by hydrothermal method [3]. ZrO_2 deposition by hydrothermal process were carried out for very small durations (< 1 hr) to prepare very thin ZrO_2 films on $\alpha\text{-Fe}_2\text{O}_3$. Another ZrO_2 coated sample was prepared by carrying out the ZrO_2 coating experiment at low temperature (90°C) under the same deposition conditions for 5 hours. The samples were characterized by different techniques like FE-SEM, AFM, XPS, Raman spectroscopy and GIXRD. Monitoring of different stages of growth of zirconia coating led to the establishment of the growth mechanism of ZrO_2 on $\alpha\text{-Fe}_2\text{O}_3$ surface. XPS technique has been used to study the $\text{Fe}_2\text{O}_3\text{-ZrO}_2$ interface of ZrO_2 coating grown by hydrothermal process.

5.3.1 Preparation of ZrO₂ coated samples at different durations and temperatures

The SS specimen having the pre-oxidized layer of pure α -Fe₂O₃ was used as the substrate surface. The details of the substrate preparation and characterization are described in chapter 2 and chapter 3 respectively. The SS specimens are oxidized in H₂O₂ medium in a static autoclave followed by PL deposition of α -Fe₂O₃. Zirconia was coated on α -Fe₂O₃ surface for the duration of 30 mins, 60 mins and 5 days by hydrothermal process at 200°C. In order to find the initial stage of the chemical reaction of Zr-precursor with α -Fe₂O₃, deposition experiment was carried out at 90°C instead of 200°C for 5 hours. The details of preparations of zirconia coated samples at 200°C as well as 90°C are given in section 2.7.2.

5.3.2 Surface Morphology by SEM and AFM

Fig. 5.8 shows the SEM images of thin film of α -Fe₂O₃ and ZrO₂ films grown on α -Fe₂O₃ surfaces for different durations (30 mins, 60 mins, 5 days) by hydrothermal process. Deposition of ZrO₂ on α -Fe₂O₃ has been monitored by EDS measurements. Zr signal in the EDS spectrum was observed even after the 30 min of deposition although the counts were very low (<1%). In high resolution images, nucleation of zirconium oxide nano-particles is seen at few places marked by circles (Fig 5.8b). After 60 min (Fig. 5.8c), a large number of ZrO₂ particles of size approximately 5-20 nm were spread uniformly on the entire α -Fe₂O₃ surface. Surface was fully covered with thick, continuous and uniform layer of zirconium oxide nano particles after 5 days of exposure (Fig. 5.8d). Zr counts in EDS measurement increased to ~36%. The size of the most of the particles are < 20nm.

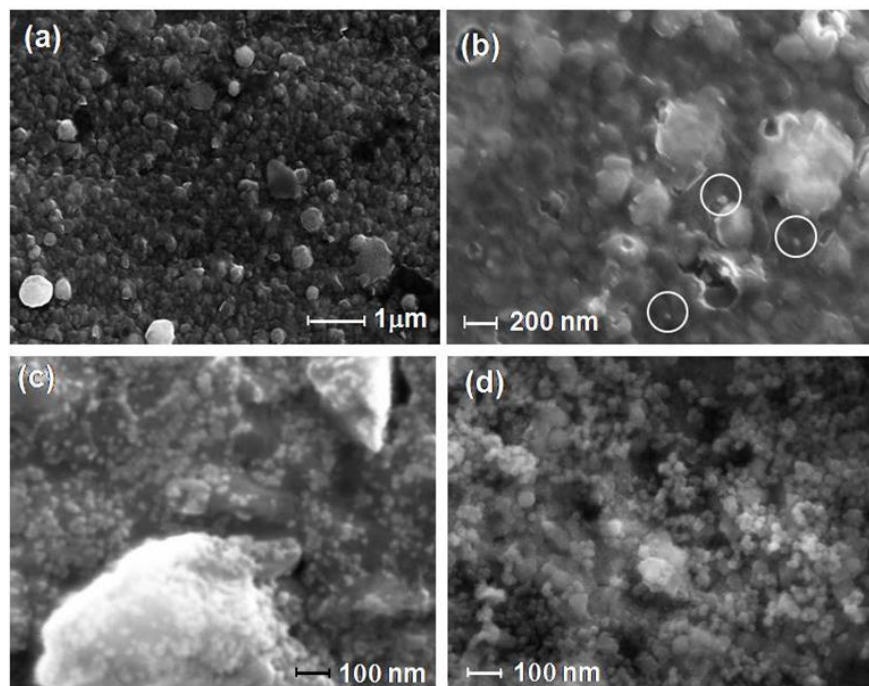


Fig. 5.8: SEM micrographs of samples before and after ZrO₂ deposition; (a) thin film of α -Fe₂O₃ on stainless steel (b) ZrO₂ deposited for 30 min, (c) ZrO₂ deposited for 60 min and (d) ZrO₂ deposited for 5 days

The surface morphology of the SS specimens after PL deposition of α -Fe₂O₃, and the 5 days ZrO₂ coated samples are studied by AFM images. Roughness of surfaces was measured by AFM mapping with respect to mirror finished Si(100) substrate. The 2D and 3D images of the Si(100) surface, plain polished SS specimen, SS specimen after oxidation in H₂O₂ solution are presented and given in Fig. 5.9a-f. The mirror finished Si(100) (Fig. 5.9a) shows the average roughness of 0.330 nm. Plain polished stainless steel samples were having the roughness of 1.660 nm while after oxidation in H₂O₂ solution surface roughness was observed to be 1.610 nm.

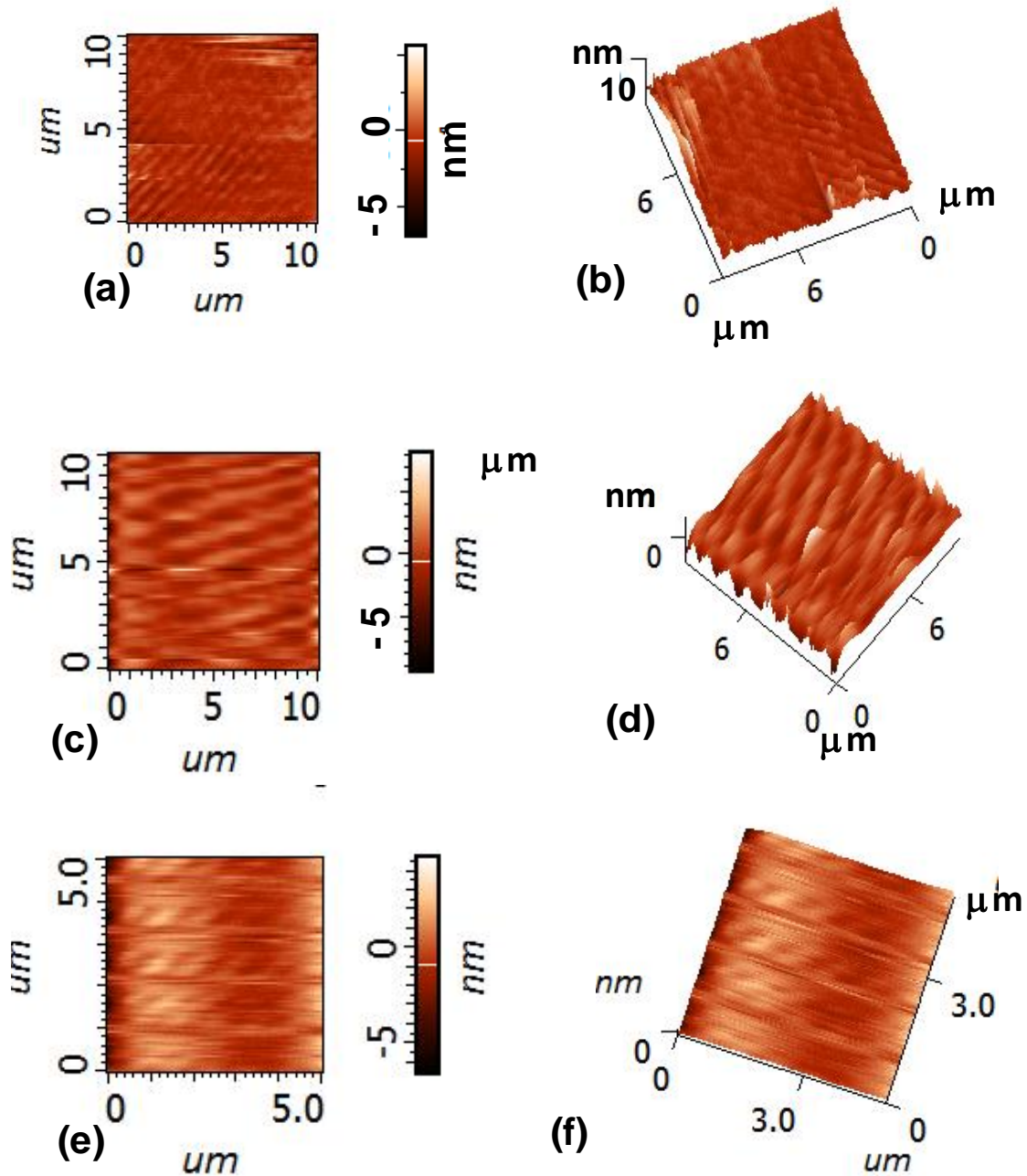


Fig. 5.9: AFM images in 2D and 3D profiles; (a & b) stainless steel surface pre-oxidized in H_2O_2 environment, (c & d) Plain SS and, (e & f) mirror finished Si (100) surface

AFM images of PL deposited $\alpha\text{-Fe}_2\text{O}_3$ specimen and 5 days ZrO_2 coated sample are shown in Fig. 5.10. The 3D AFM image (Fig. 5.10a) show that the PL deposition of $\alpha\text{-Fe}_2\text{O}_3$ leads to hills/valley type of morphology on the SS surface. The grain size of deposited $\alpha\text{-Fe}_2\text{O}_3$ particles

are approximately 50-75 nm. The surface roughness of the α -Fe₂O₃ coated surface is around 100 nm (Fig. 5.10 a&b) that got reduced after the hydrothermal deposition of ZrO₂. After the 5 days of ZrO₂ coating, roughness of sample surface observed is approximately 70-80 nm (Fig. 5.10d). The average size of ZrO₂ particles is around 25-40 nm (5.10c). From both AFM and SEM images taken after 5 days experiment, ZrO₂ particles seem to have a small amount of agglomeration, no large grains of ZrO₂ have been observed.

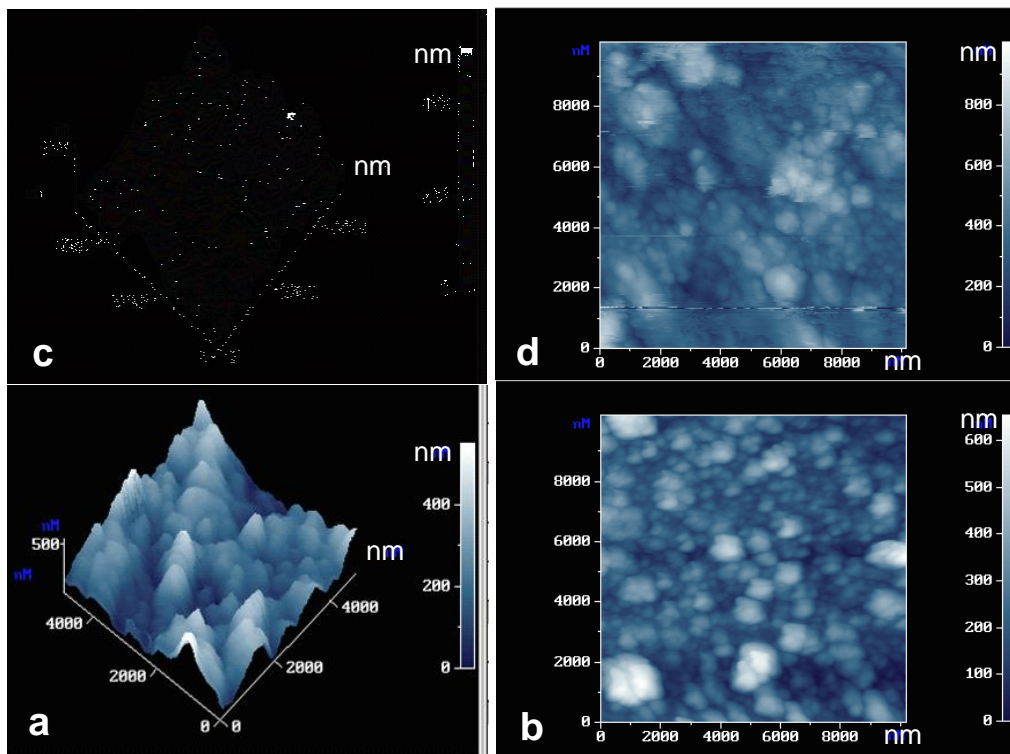


Fig. 5.10: AFM images in 3D and 2D profiles (a & b) thin film of α -Fe₂O₃ deposited on stainless steel and (c & d) ZrO₂ deposited on α -Fe₂O₃ for 5 days

5.3.3 Phase Analysis by Raman Spectroscopy and GIXRD

Raman spectra of thin film of α -Fe₂O₃ and the ZrO₂ films grown on α -Fe₂O₃ surfaces for different durations are shown in Fig 5.11. After ZrO₂ coating, intensity of all the peaks corresponding to substrate (α -Fe₂O₃) reduce systematically as the duration of ZrO₂ deposition

experiments increases (Fig 5.11b, 5.11c and 5.11d). After 5 days of coating (Fig 5.11d), substrate signals disappeared completely because substrate surface is fully covered by thick ZrO_2 coating. It is observed that the intensity of the Raman signals of $\alpha\text{-Fe}_2\text{O}_3$ reduced considerably even at the initial stage of ZrO_2 coating formation (Fig 5.11b and 5.11c). This implies that the strong chemical interaction of $\alpha\text{-Fe}_2\text{O}_3$ with ZrO_2 at the initial stage of ZrO_2 deposition modified the Raman modes of $\alpha\text{-Fe}_2\text{O}_3$.

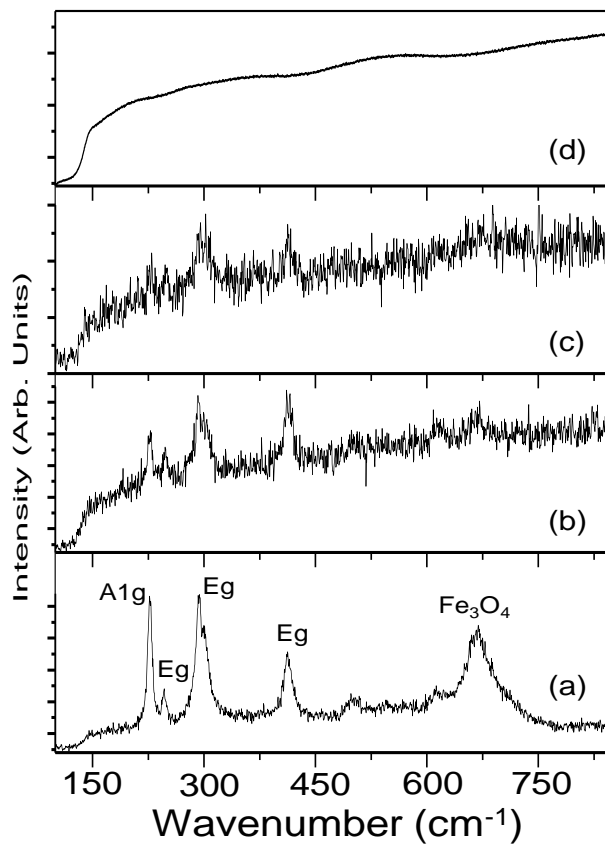


Fig. 5.11: Raman spectra of samples prior and after ZrO_2 deposition (a) thin film of $\alpha\text{-Fe}_2\text{O}_3$ on stainless steel, (b) ZrO_2 deposited for 30 min, (c) ZrO_2 deposited for 60 min and (d) ZrO_2 deposited for 5 days

GIXRD spectra of all the samples are presented in Fig 5.12. All the peaks in Fig 5.12a correspond to $\alpha\text{-Fe}_2\text{O}_3$ coating on stainless steel [21]. In Fig 5.12b, no significant changes in the

diffraction patterns have been observed. This implies that the amount of ZrO_2 deposited in 30 min may be too small to be detected by GIXRD technique or deposited ZrO_2 may be amorphous in nature. After 60 min of deposition (Fig 5.12c), a small peak (shown by arrow) at $2\theta = 50.5^\circ$ starts appearing which corresponds to tetragonal (112/020) [22] or cubic (220) [23] phase of ZrO_2 or metastable $Zr(Fe)O_2$ tetragonal phase at the interface plane [24]. This shows the growth of particular planes of crystalline ZrO_2 at the initial stage of coating formation. The diffraction pattern of 5 days ZrO_2 coated sample shows no signal from $\alpha-Fe_2O_3$ and peaks correspond to mainly tetragonal ZrO_2 .

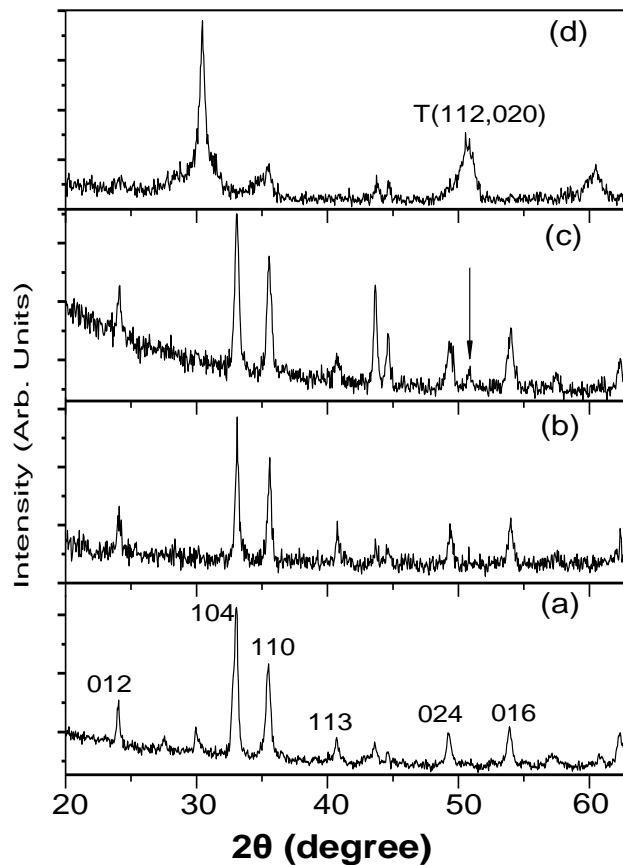


Fig. 5.12: GIXRD patterns obtained from samples prior and after ZrO_2 deposition (a) thin film of $\alpha-Fe_2O_3$ on stainless steel, (b) ZrO_2 deposited for 30 min, (c) ZrO_2 deposited for 60 min and (d) ZrO_2 deposited for 5 days. T- tetragonal zirconia

5.3.4 Chemical state analysis by XPS

Fig. 5.13 shows the wide scan photoelectron spectra of the samples at various stages of ZrO_2 coating formation.

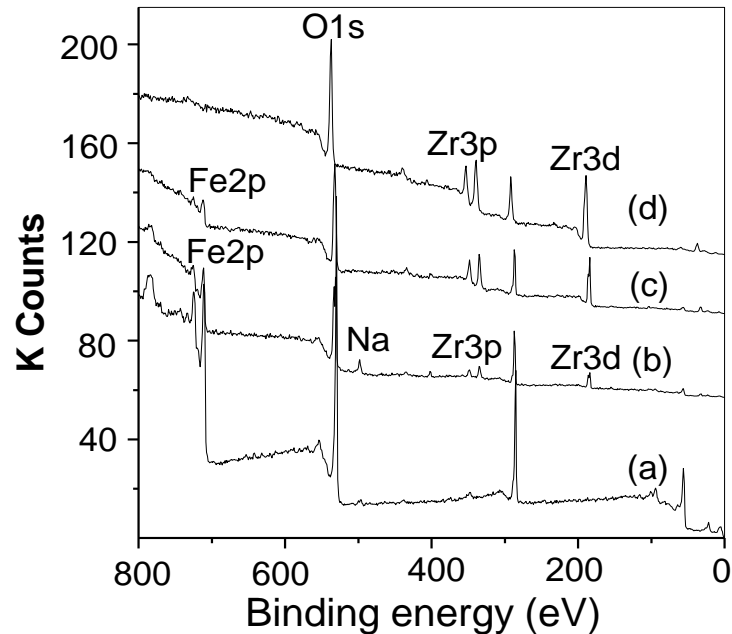


Fig. 5.13: XPS of different samples prior and after ZrO_2 deposition (a) thin film of $\alpha\text{-Fe}_2\text{O}_3$ on stainless steel, (b) ZrO_2 deposited for 30 min, (c) ZrO_2 deposited for 60 min and (d) ZrO_2 deposited for 5 days

Systematic growth of zirconium oxide on $\alpha\text{-Fe}_2\text{O}_3$ surface has been observed in the XP spectra taken at different stages of coating formation process (Fig. 5.13b, 5.13c and 5.13d). Presence of Zr was observed along with Fe from the substrate surface after 30 min of deposition (Fig 5.13b). Zr counts increased to significant extent after 60 min of deposition but the zirconium oxide layer was not thick enough to stop the photoelectrons from the underlying $\alpha\text{-Fe}_2\text{O}_3$ surface (Fig 5.13c). Quantitative analysis of Zr/Fe (section 2.9.4) shows the presence of 13 and 31 atomic % of Zr on the surface of the 30 min and 60 min samples respectively. The surface was fully covered by zirconium oxide (Fig 5.13d) in 5 days coated sample and no signal of Fe was detected. In the XP spectrum of the sample deposited for 30 min (Fig. 5.14b), Na (KLL around

480 eV) was present on the surface along with Fe and Zr. The Na signal become very weak in the case of 60 min sample that means concentration of Na is almost negligible. Na signal has not been observed in the 5 days ZrO₂ coated sample. This implies that the Na-EDTA (only source of Na in autoclave) plays a direct role in the deposition process only at the initial stage when the particles in solution start interacting with the substrate surface.

Fig. 5.14 shows that the narrow scan of Fe 2p peak for the PL deposited α -Fe₂O₃ sample, 30 mins and 60 mins ZrO₂ coated samples. Fe 2p_{3/2} peak for the PL deposited α -Fe₂O₃ sample was observed at 710.6 eV (Fig. 5.14a). The peak intensity reduced systematically and peak position was shifted to lower binding energy by 0.6 eV after ZrO₂ deposited for 30 min and 60 min. Fig. 5.15 shows the narrow scan of Zr3d peak for 30 mins, 60 mins and 5 days ZrO₂ coated samples. The intensity of Zr peak increased systematically with increasing time as expected. Zr3d_{5/2} peak was seen around 182.5 eV in both 30 min and 60 min ZrO₂ deposited samples. Narrow peak widths (~1.6 eV) of Zr 3d_{5/2} of these two samples imply that zirconium oxide is present in single valence state (Fig. 5.15a & 5.15b). Zr 3d_{5/2} peak was seen at 182.0 eV (Fig 5.15c) after 5 days of ZrO₂ deposition which is approximately 0.5 eV lower [25, 26] compared to both 30 min and 60 min samples.

In the case of 30 mins and 60 mins ZrO₂ coated samples, the shifts in Fe 2p_{3/2} towards the lower binding energy compare to pure Fe₂O₃ and Zr 3d_{5/2} shift towards the higher binding energy compare to pure ZrO₂ indicate the strong chemical interaction between the substrate α -Fe₂O₃ and deposited ZrO₂. As Fe³⁺ is more electronegative compare to Zr⁴⁺; Fe-O-Zr bond formation leads to increase the effective positive charge on Zr atom and decrease it on Fe atom [27]. Because of increase of positive charge on Zr atom, Zr 3d peaks has been observed at higher binding energy values in 30 min and 60 min samples compare to 5 days ZrO₂ coated sample (Fig

5.15). Shift of Fe 2p_{3/2} peak from 710.6 in PL deposited α -Fe₂O₃ sample to 710.0 eV in both 30 min and 60 min coated samples is also the result of Fe-O-Zr bond formation (Fig 5.14).

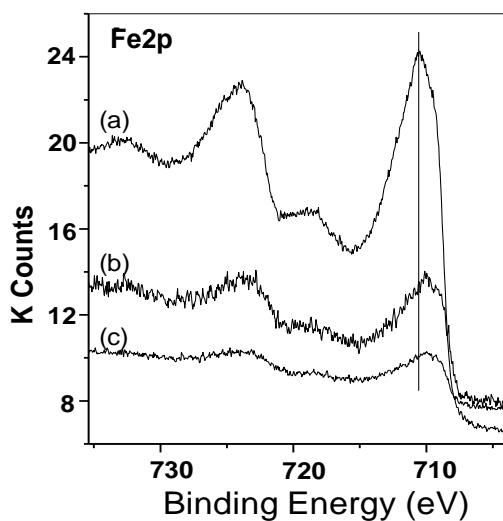


Fig. 5.14: Fe2p photoelectron spectra obtained from samples (a) thin film of α -Fe₂O₃ on SS, (b) ZrO₂ deposited for 30 min, (c) ZrO₂ deposited for 60 min

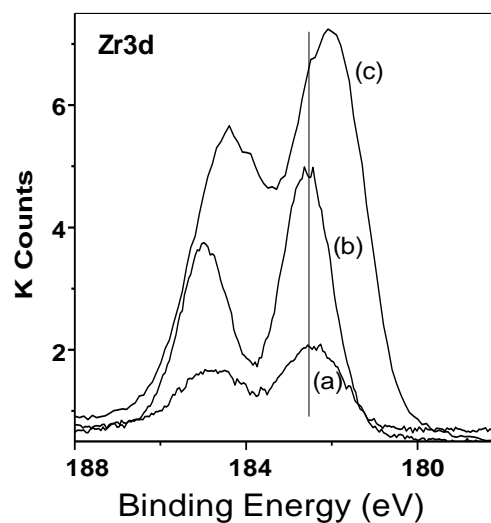


Fig. 5.15: Zr3d photoelectron spectra from samples (a) ZrO₂ deposited for 30 min, (b) ZrO₂ deposited for 60 min and (c) ZrO₂ deposited for 5 days

Valance band spectra acquired from the samples are presented in Fig 5.16. The spectrum from the PL deposited α -Fe₂O₃ sample (Fig 5.16a) is mainly composed of peaks due to Fe3d states hybridized with O2p states [28]. Three main peaks at \sim 2.0, \sim 5.0 and \sim 7 eV have been observed due to major contribution from d⁴, d⁵L and d⁶L² final states originated due to L(O2p) \rightarrow Fe3d Charge transfer (L, L² signify one or two holes in the ligand) [29-33]. In the VB spectra of 30 min and 60 min deposited samples (Fig 5.16b and 5.16c), intensity of all the peaks got reduced systematically and a broad band appeared primarily due to O2p-Zr4d derived states after 5 days deposition (Fig 5.16d). However no special features related to Fe-O-Zr type of bonding have been observed. It is assumed that characteristic features might have been buried in

the broad band of Fe-O or/and Zr-O bands due to low contribution from Fe-O-Zr type bonding states.

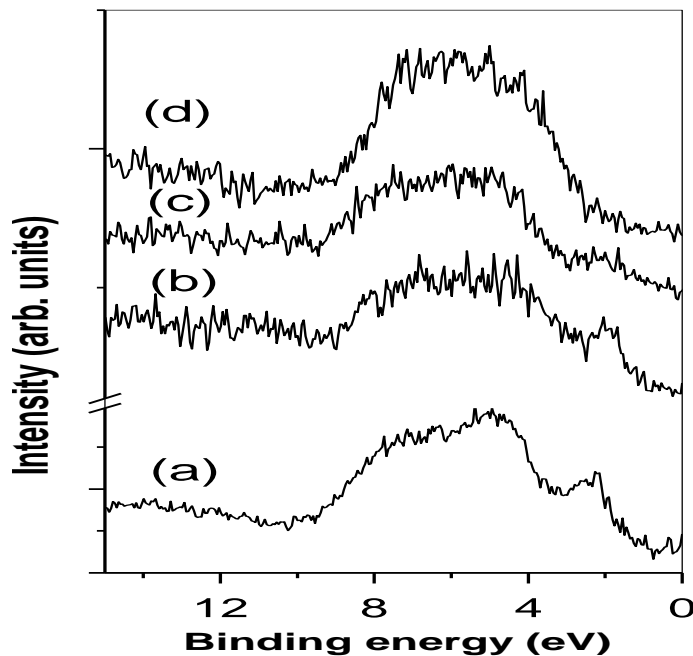


Fig. 5.16: Valance band spectra of (a) thin film of Fe_2O_3 on stainless steel, (b) ZrO_2 deposited on Fe_2O_3 for 30 min, (c) ZrO_2 deposited on Fe_2O_3 for 60 min and (d) ZrO_2 deposited on Fe_2O_3 for 5 days

The interaction of the solutes with $\alpha\text{-Fe}_2\text{O}_3$ surface at low temperature (90°C) has been studied by XPS. The wide scan of ZrO_2 coated sample at 90°C and for 5 hours is shown in Fig. 5.17 and the narrow scan spectra of elements (Zr, C, Na and N) are given in Fig 5.18. Presence of Zr signals in the XP spectrum confirms the interaction of precursor solution and substrate surface at lower temperature. Quantitative analysis of Zr/Fe shows the presence of around 10 at% of Zr on the Fe_2O_3 surface after 5 hours which is definitely much lower compared to that deposition experiments carried out at high temperature in autoclave. This shows that the zirconia growth is limited to surface only at 90°C and coating does not grow even after 5 hours of the

experiment. The presence of Na and N signals in XP scan point out the involvement of Na-EDTA in interaction between substrate surface and depositing material at low temperature.

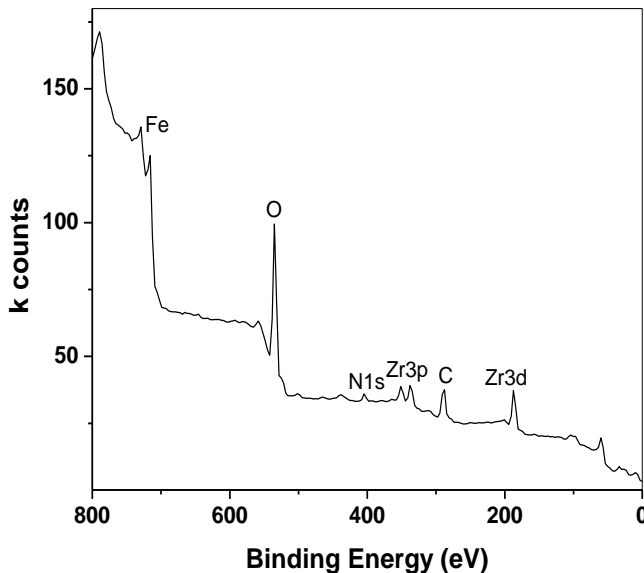


Fig. 5.17: XPS wide scan of the ZrO₂ coated sample prepared at 90°C for 5 hours

Presence of Zr 3d_{5/2} at 181.6 eV in the XP spectra (Fig.5.18a) shows the adsorption of Zr-compounds on the substrate surface and binding energy is lower than that for binding energy of ZrO₂ (182.0 eV). Zr 3d binding energy is influenced by the surrounding atoms of Zr, the lower binding energy of Zr3d_{5/2} is due to the presence of Zr in the form of Na salt of Zr-EDTA complex [34]. In the earlier three cases (high temperature deposited 30 min, 60 min and 5 days ZrO₂ deposited sample), Zr was surrounded by O (i.e. ZrO₂). The different surroundings of Zr in ZrO₂ and Na salt of Zr-EDTA lead to different binding energies of Zr3d_{5/2}. C1s spectrum (Fig 5.18b) shows the presence of two distinct peaks, at around 285 and at 288.2 eV. The higher energy peak of C1s indicates the presence of carboxylic species from the EDTA compound on the surface [35, 36]. The N1s peak was observed at 400 eV (Fig. 5.18c) which is from the diamine chain of EDTA, the presence of NO₃⁻ group (source ZrO(NO₃)₂) is ruled out which

generally shows binding energy at around 407 eV [37, 38]. The detailed XPS analysis confirm that the formation of ZrO_2 phase is not complete at 90°C and Zr is present as Na salt of Zr-EDTA. At least 170°C temperature is required to detach the EDTA from zirconia [43, 44].

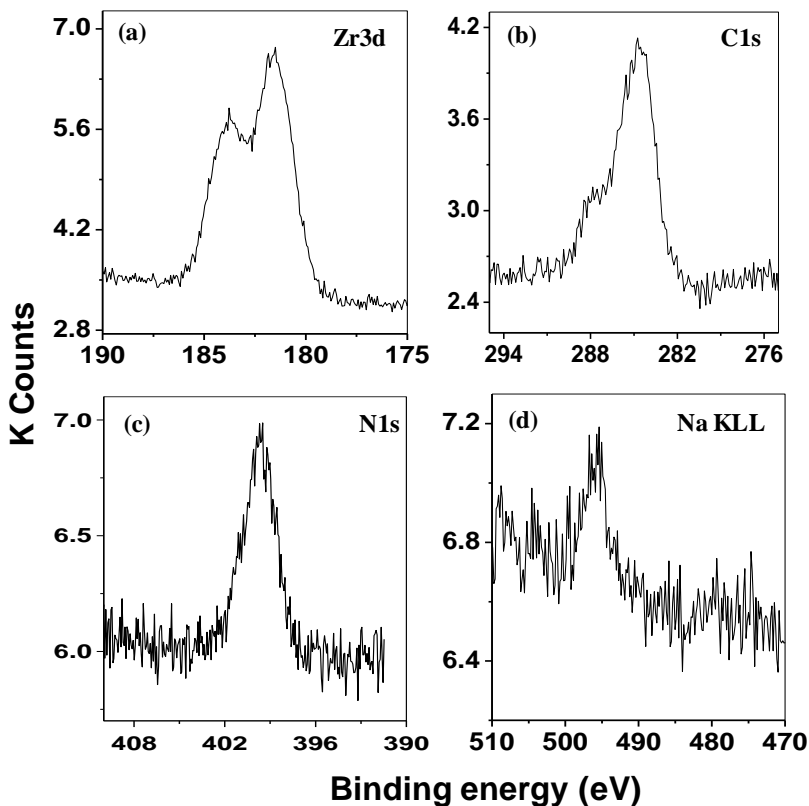


Fig. 5.18: XPS of ZrO_2 coated sample prepared at 90°C for 5 hrs, (a) Zr 3d spectrum, (b) C1s spectrum, (c) N1s spectrum and (d) Na KLL Auger peak

5.3.5 Interaction and growth mechanism of ZrO_2 on the α - Fe_2O_3 surface

$ZrO(NO_3)_2 \cdot 6H_2O$ along with Na-EDTA and SDS has been used as chelating agent and surfactant respectively for developing the ZrO_2 coating by hydrothermal process. On the basis of interface samples study, the nucleation and growth model of ZrO_2 layer on the α - Fe_2O_3 surface is developed and it is assumed to occur in three steps:

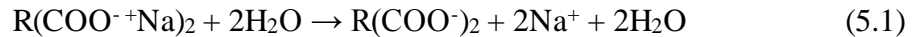
(1) Formation of Na-salt of Zr-EDTA in aqueous solution

(2) Interaction between α -Fe₂O₃ surfaces with Na salt of Zr-EDTA

(3) Nucleation and growth of crystalline ZrO₂ coating

5.3.5.1 Formation of Na-salt of Zr-EDTA in aqueous solution

In the process of hydrolysis of ZrO(NO₃)₂, parallel cation chains in solution exist as the precursor with the repeating units of [Zr(OH)₂(OH₂)₂(NO₃)]⁺ where zirconium atom is eightfold coordinated by four bridging OH groups, two water molecules and one chelating nitrate. These chains are held together by hydrogen bonds through additional water molecules and non-complexing nitrate groups located between the chains. Thus, half of the existing nitrate groups is directly (covalently) coordinated to the zirconium atoms and the other half is ionically bound in the crystal lattice between the chains [7, 41]. Na-EDTA acts as a complex compound R(COONa)₂, produces an ionized complexing agent by hydrolysis; i.e.



OH₂ and OH⁻ and NO₃⁻ functional groups of the chain unit [Zr(OH)₂(OH₂)₂(NO₃)]⁺ reacts with the anion of the ionized complex agent R(COO⁻ Na⁺)_n to produce a large complex molecules by replacing NO₃⁻, OH and OH₂ sites by RCOO⁻ groups partially or completely. The RCOO⁻ groups mainly replace the NO₃⁻ sites [42] and a bond between ionized complex agent and the Zr ions is formed by these replacement reactions. The absence of NO₃⁻ groups in the films prepared at 90°C has been observed in XPS analysis. It confirms the replacement of nitrate group from the zirconium oxynitrate and formation of Na salt of Zr-EDTA complex. Langer et al [43] reported the formation of Na salt of Zr-EDTA at pH 7 by adding NaOH into the solution of Zr-EDTA complex. Na-salt of Zr-EDTA is represented by Na[Zr(OH)Y] where ‘Y’ is EDTA anions (C₁₀H₁₂N₂O₈). Na[Zr(OH)Y] is a binuclear complex with two bridged hydroxyl groups. Detailed structure of binuclear Na[Zr(OH)Y] is shown in Fig 5.19. It is observed that stable suspension of

Zr compounds cannot be formed in the absence of Na-EDTA in precursor solution. Hydrated zirconia particles used to get precipitate while maintaining the solution pH by addition of NaOH.

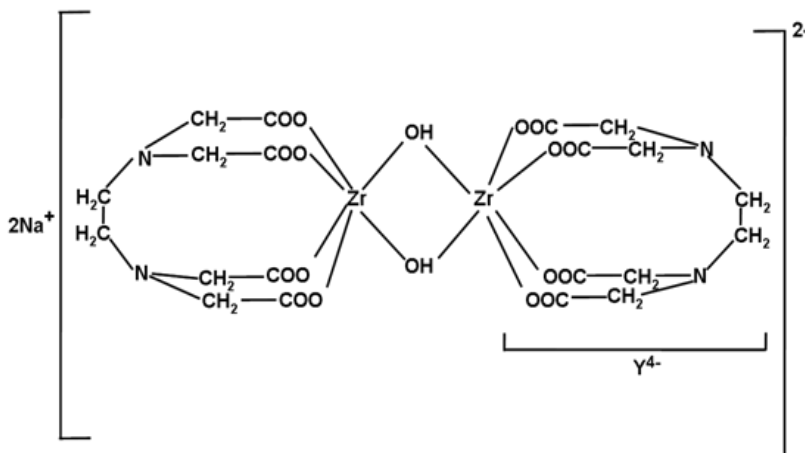


Fig. 5.19: Binuclear complex structure of Na-salt of Zr-EDTA

5.3.5.2 Interaction between α -Fe₂O₃ surfaces with Na salt of Zr-EDTA

Chemisorption of water on α -Fe₂O₃ surface takes place by the dissociation of water molecules. Fe³⁺ ions present in the oxide layer of α -Fe₂O₃ surface combine with hydroxyl ions in aqueous solution to form Fe(OH)₃. The hydroxyl group of Fe(OH)₃ becomes positive [Fe(OH)₂]⁺ at solution pH due to the adsorption of H₃O⁺ from solution [44]. The positively charged α -Fe₂O₃ surface provide a conducive environment for the adsorption of Na[Zr(OH)Y] on the stainless steel substrate. The possible interaction mechanism between the hydroxylated α -Fe₂O₃ surface and Na salt of Zr-EDTA is shown in Fig 5.20. The bridged hydroxyl groups of the complex (Na salt of Zr-EDTA, Fig. 5.19) are quite reactive and electropositive in nature. One of these hydroxyl groups reacts with the positively charged hydroxylated Fe₂O₃ surface and release as water molecule by combining with the proton. This leads to the attachment of Na salt of Zr-EDTA to the Fe-O of the substrate surface through Fe-O-Zr bond formation and nucleation of

ZrO₂ takes place on the substrate surface. After the adsorption, remaining hydroxyl group of the complex molecule react with the adjacent Fe-OH⁺ (Fig. 5.20) at surface and form Fe-O-Zr bond as discussed above. It shows that the giant molecule of Na[Zr(OH)Y] forms a surface complex on the Fe₂O₃ surface.

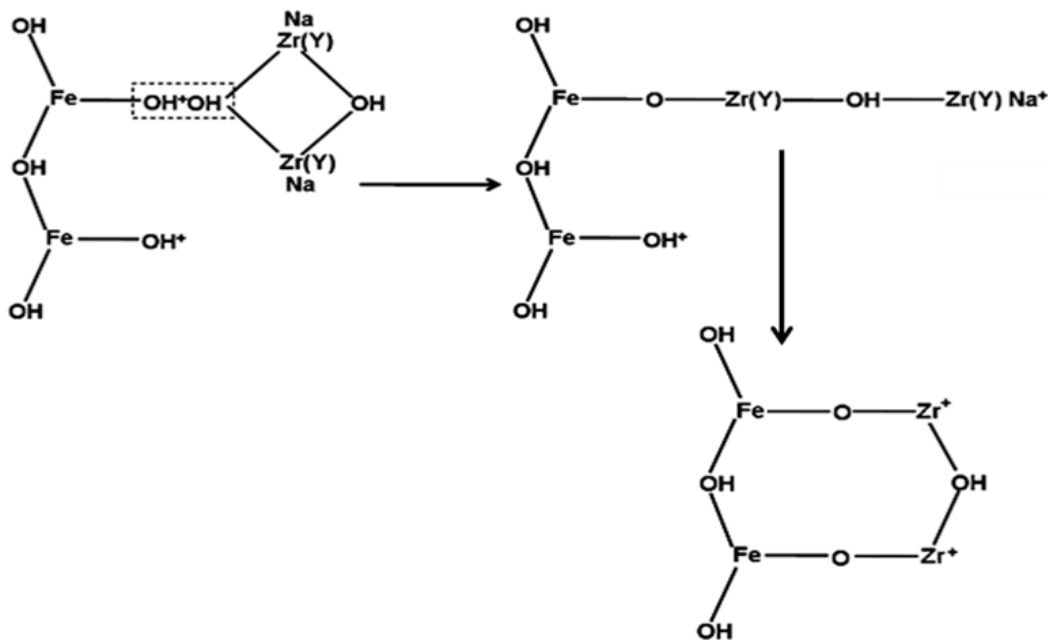


Fig. 5.20: Interaction mechanism of Zr-EDTA complex with α -Fe₂O₃ in the hydrothermal conditions

The presence of Na[Zr(OH)Y] on the Fe₂O₃ surface has been observed by XPS analysis when the ZrO₂ deposition was carried out at 90°C (Fig 5.18a-d). At high temperature (>170°C), EDTA ions lose their complexing capability with Zr [39, 40]. Hence EDTA ions are released into the solution leaving behind the zirconium oxide particles on the α -Fe₂O₃ surface as well as in the solution. At 200°C, Zr deposited on α -Fe₂O₃ gets hydrolyzed to form a strong interface bond with the α -Fe₂O₃ surface (Fig. 5.20). Slight reduction in binding energy and peak broadening of Fe 2p_{3/2} for the 30 min and 60 min ZrO₂ deposited samples (Fig 5.14 b & c)

indicate the interaction of α -Fe₂O₃ with ZrO₂ at the interface. Simultaneously, Zr 3d_{5/2} peak was seen at higher binding energy in both 30 min and 60 min coated sample compared to the 5 days ZrO₂ coated sample. The higher binding energy of Zr is due to the formation of Fe-O-Zr type of bonding at the interface of substrate and ZrO₂ coating. Chemical interaction between α -Fe₂O₃ and ZrO₂ is also observed in the Raman spectroscopy (Figs. 5.11 b & c) where the peaks belonging to α -Fe₂O₃ got disturbed to large extent although the ZrO₂ coating thickness was very low.

5.3.5.3 Nucleation and growth of crystalline ZrO₂ coating

Interaction of Na[Zr(OH)Y] with Fe₂O₃ of the substrate surface results in the formation of Fe-O-Zr bond and initiation of nucleation of ZrO₂ particles on the substrate surface. At high temperature, EDTA ions lose their complexing ability and zirconium oxide particles released into the solution from Na[Zr(OH)Y]. The released ZrO₂ particles are likely to precipitate at high temperature but the sizes of released particles are too small (nm order) to precipitate. So, released zirconia particles remain suspended in solution. In addition, the surfactant SDS in the solution keeps particles in suspension and prevents agglomeration. The suspended zirconium oxide particles lead to nucleation of new ZrO₂ particles on the Fe₂O₃ surface and simultaneous growth of already deposited ZrO₂ particles on the substrate surface take place. Suspended zirconium oxide particles having surface as ZrO⁻ due to the reaction conditions are attracted towards the substrate surface by electrostatic forces discussed earlier in sec. 5.2.2 [2]. As Fe₂O₃ provides a favorable crystal structure [41-43] for growing ZrO₂ crystallites, attached zirconium oxide particles on the surface rearrange themselves to form tetragonal ZrO₂ crystallites.

Miscibility of ZrO₂ with α -Fe₂O₃ crystallites [45] is important for the nucleation and growth of the ZrO₂ coating. ZrO₂ is known to form a wide range of Fe₂O₃-ZrO₂ metastable

compositions with Fe_2O_3 [45]. It has been observed from XPS and Raman analyses that the hydrothermal conditions in the autoclave provide a suitable environment for the formation of Fe_2O_3 - ZrO_2 interfacial bonds prior to the nucleation and growth of the crystalline ZrO_2 coating. The lattice parameters of metastable Fe_2O_3 - ZrO_2 with Fe_2O_3 amount ranging from 10 to 30 mole% remain within 0.506 nm to 0.5 nm [45]. It provides a suitable surface crystallography for the growth of the tetragonal ZrO_2 as the lattice parameter of tetragonal ZrO_2 is around 0.508 nm. GIXRD shows the formation of crystalline coating after 60 min of the reaction with Fe_2O_3 . Tetragonal ZrO_2 grows on Fe_2O_3 - ZrO_2 interfacial compound in the form of islands. These crystallite islands on the surface grow in all directions. Radial crystal growth will cease at some time as surface will be completely covered with crystallites. But the growth of ZrO_2 particles in vertical direction of the surface will continue and results in thickening of the film [20]. ZrO_2 crystallites assume to have a columnar structure and each individual crystallite has a cone-like top that is confirmed by AFM image (Fig 5.10).

Selection of optimum pH, temperature and concentration of Na-EDTA which lead to the formation of Zr-EDTA complex is very important for deposition of ZrO_2 . At high pH zirconium ions precipitate in the form of $\text{Zr}(\text{OH})_4$ instead of forming Zr-EDTA complex while at low pH, Zr-EDTA complex is highly insoluble and tend to precipitate in solution. To avoid these consequences and forming a stable suspension of Zr-EDTA complex, solution pH should be in optimum range. Na-EDTA in precursor solution plays a major role in controlling the particle size by the formation of Zr-EDTA complex. It limits the ion concentrations available for nucleation and growth and results in deposition of nanometric and homogeneous size particles. But at the same time excess concentration of Na-EDTA should be avoided. ZrO_2 particles will completely dissolve in solution in presence of excess EDTA salt. Temperature influences the growth process

at two stages, (i) release of EDTA from Na[Zr(OH)Y] complex attached with Fe₂O₃ surface at high temperature which results in the formation of Fe-O-Zr bond. At 90°C, Zr observed in the XPS spectra is from the Na salt of Zr-EDTA that is chemisorbed on the substrate surface. EDTA retains its complexing ability till ~170°C and that restricts the nucleation and growth of ZrO₂ at low temperature. (ii) At 200°C nucleation events become more probable as the energy available for atom to nucleate on the substrate surface increases. Further bond strengthening, increase in crystallinity and growth of nucleated ZrO₂ crystallites becomes more favorable at high reaction temperature [20]. If the reaction temperature exceeds 230°C, EDTA salts tend to decompose [42] and this decomposition can drastically modify the solution pH. The modeling of hydrothermal deposition parameters like temperature, pH and precursor concentration is very important for deposition of adherent and continuous ZrO₂ coating on the SS surface.

5.4 Conclusions

Thin films of ZrO₂ have been developed on the pre-oxidized stainless steel surfaces using zirconyl nitrate and Na-EDTA by hydrothermal method. The pre-oxidized SS surfaces with varying compositions were used as the substrate for ZrO₂ deposition and role of chemical composition of pre-oxidized layer for the growth of ZrO₂ film has been explained. The variation in thicknesses and uniformity of ZrO₂ films have been observed for different compositions of intermediate SS surface oxides. The pre-oxidized layer composed of pure α -Fe₂O₃ results in thick and uniform ZrO₂ coating while the pre-oxidized layer composed of mixed α -Fe₂O₃ and spinel oxides result in thinner and non-uniform ZrO₂ layer. The matching of lattice parameters of substrate surface oxide with the zirconia decides the probability of nucleation of zirconia crystallites. The higher nucleation density of ZrO₂ crystallites result in thick zirconia coating. α -Fe₂O₃ layer with the lattice parameters close to zirconia crystals favors the maximum growth of

ZrO₂ coatings among all pre-oxidized SS surfaces. The mismatch in the lattice parameters of spinel oxides and crystalline zirconia delays the nucleation events and growth of zirconia coating is limited.

The mechanism of formation of ZrO₂ coating on α -Fe₂O₃ surface has been explored. Na-EDTA plays a vital role during the initial stage of interaction of Zr complex with α -Fe₂O₃ as well as in controlling the size of suspended ZrO₂ particles. At the initial stage of the film formation, Na salt of Zr-EDTA interacts with α -Fe₂O₃ to form an unstable surface complex. Subsequent to this complex formation, EDTA ions are released into the solution at high temperature leaving zirconium oxide on the surface of α -Fe₂O₃. This leads to the formation of interfacial states of Fe-O-Zr which provides the adhesion and initiates the nucleation of ZrO₂. XPS technique established the formation of Fe-O-Zr bonding states at the interface. The formation of metastable Fe₂O₃-ZrO₂ compositions takes place at high temperature due to the matching lattice parameters of α -Fe₂O₃ and ZrO₂. The metastable t-(Fe,Zr)O₂ compound at the interface provides suitable crystal structure at the interface for the nucleation of tetragonal ZrO₂ coating. Nucleated ZrO₂ particles grow in the form of islands on the α -Fe₂O₃ surface at the initial stage and these islands grow and coalesce to form the thick and uniform coating on α -Fe₂O₃ surface.

5.5 References

- [1] T.-K. Yeh, Y.-C. Chien, B.-Y. Wang, C.-H. Tsai, Corros. Sci. 50 (2008) 2327.
- [2] N. Garg, V.K. Mittal, S. Bera, P. Chandramohan, C.R. Das, S. Velmurugan, Thin Solid Films 545 (2013) 222-228.

- [3] N. Garg, S. Bera, G. Mangamma, V.K. Mittal, R. Krishnan, S. Velmurugan, *Surf. Coat. Technol.* 258 (2014) 597–604.
- [4] L. Chen, T. Mashimo, E. Omurzak, H. Okudera, C. Iwamoto, A. Yoshiasa, *J. Phys. Chem.C* 115 (2011) 9370-9375.
- [5] R.C. Garvie, R.H. Hannink, R.T. Pascoe, *Nature* 258 (1975) 703-704.
- [6] N. Garg, V.K. Mittal, S. Bera, A. Dasgupta, V. Sankaralingam, *Ceram. Int.* 38 (2012) 2507-2512.
- [7] M. Tahmasebpour, A.A. Babaluo, M. K.R. Aghjeh, *J. Eur. Ceram. Soc.* 28 (2008) 773–778.
- [8] Yu. M. Shul'ga, A.V. Bulatov, R.A.T. Gould, W.V. Konze, L.H. Pignolet, *Inorg. Chem.* 31 (1992) 4704-4706.
- [9] O. Bohmann, P. Ahlberg, R. Nyholm, N. Martenson, K. Siegbahn, J. M. Lehn, *Chem. Scripta* 18 (1981) 44-46.
- [10] X.Y. Zhou, X.J. Wei, M.V. Fedkin, K.H. Strass, S.N. Lvov, *Rev. Sci. Instrum.* 74 (2003) 2501-2506.
- [11] S.N. Lvov, S.R. Narayanan, D.D. Macdonald, D.J. Wesolowski (Ed.), *Interfacial Electrochemistry and Chemistry in High Temperature Media*, ECS Transactions, vol. 11, New Jersey, USA, 2008, 181-188.
- [12] G.A. Parks, *Chem. Rev.* 65 (1965) 177-198.
- [13] P.H. Tewari, A.W. McLean, *J. Colloid Interface Sci.* 40 (1972) 267-272.
- [14] R.C. Plaza, J. de Vicente, S. Gómez-Lopera, A.V. Delgado, *J. Colloid Interface Sci.* 242 (2001) 306-315.
- [15] T. Chraska, A.H. King, C.C. Berndt, *Mater. Sci. Eng., A* 286 (2000) 169-178.
- [16] H. Ding, A.V. Virkar, F. Liu, *Solid State Ionics* 215 (2012) 16-23.

- [17] M. Cao, T. Liu, S. Gao, G. Sun, X. Wu, C. Hu, Z. L. Wang, *Angew. Chem. Int. Ed.* 44 (2005) 4197–4201.
- [18] S. Bid, P. Sahu, S.K. Pradhan, *Physica E* 39 (2007) 175–184.
- [19] M.P. Gonzalez-Sandoval, A.M. Beesle, M. Miki-Yoshida, L. Fuentes-Cobas, J.A. Matutes-Aquino, *Journal of Alloys and Compounds* 369 (2004) 190–194.
- [20] D.M. Hausmann, R.G. Gordon, *J. Cryst. Growth* 249 (2003) 251–261.
- [21] M. Aronniemi, J. Lahtinen, P. Hautojarvi, *Surf. Interface Anal.* 36 (2004) 1004–1006.
- [22] J. Malek, L. Benes, T. Mitsuhashi, *Powder Diffraction* 12 (1997) 96-98.
- [23] V.I. Khitrova, V.V. Klechkovskaya, *Sov. Phys. Crystallogr. (Engl. Transl)* 30 (1985) 70-73.
- [24] P.K. Narwankar, F.F. Lange, C.G. Levi, *J. Am. Ceram. Soc.* 80 (1997) 1684-1690.
- [25] B.F. Dzhurinskii, D. Gati, N.P. Sergushin, V.I. Nefedov, Y.A.V. Salyn, *Russ. J. Inorg. Chem.* 20 (1975) 2307-2314.
- [26] D. Briggs, M.P. Seah, Eds., *Practical Surface Analysis*, D. Briggs and M. P. Seah, Eds., vol. 1, John Wiley & Sons, New York, NY, USA, 2nd edition, 1993, 30.
- [27] J.R. Sohn, J.S. Lim, *Mater. Res. Bull.* 41 (2006) 1225–1241.
- [28] Th. Schedel-Niedrig, W. Weiss, R. Schlogl, *Phys. Rev. B: Condens. Matter* 52 (1995) 17449-17461.
- [29] N. Uekawa, K. Kaneko, *J. Phys. Chem. B* 102 (1998) 8719-8724.
- [30] D.M. Sherman, T.D. Waite, *Am. Mineral.* 70 (1985) 1262-1269.
- [31] C.-Y. Kim, M.J. Bedzyk, E.J. Nelson, J.C. Woicik, L.E. Berman, *Phys. Rev. B: Condens. Matter* 66 (2002) 085115-4.
- [32] W. Temesghen, P.M.A. Sherwood, *Anal. Bioanal. Chem.* 373 (2002) 601-608.

- [33] A. Fujimori, M. Saeki, N. Kimizuka, M. Taniguchi, S. Suga, *Phys. Rev. B: Condens. Matter* 34 (1986) 7318-7328.
- [34] R.D. Feltham, P. Brant, *J. Am. Chem. Soc.*, 104 (1982) 641–645.
- [35] A.M. Dennis, R.A. Howard, K.M. Kadish, J. L. Bear, J. Brace, N. Winograd, *Inorg. Chim. Acta* 44 (1980) L139-L141.
- [36] V.I. Nefedov, Y.V. Salyn, A.G. Maiorova, L.A. Nazarova, I.B. Baranovskii, *Russ. J. Inorg. Chem.* 19 (1974) 1353-1357.
- [37] Yu. M. Shul'ga, A.V. Bulatov, R.A.T. Gould, W.V. Konze, L.H. Pignolet, *Inorg. Chem.* 31 (1992) 4704-4706.
- [38] O. Bohmann, P. Ahlberg, R. Nyholm, N. Martenson, K. Siegbahn, J. M. Lehn, *Chem. Scripta* 18 (1981) 44-46.
- [39] R.J. Motekaitis, X.B. Cox III, P. Taylor, A.E. Martell, B. Miles, T.J. Tvedt Jr, *Can. J. Chem.* 60 (1982) 1207-1213.
- [40] B. Stellwag, R. Kilian, *Water Chemistry of Nuclear Reactors System*, BNES 8 (2000) 127-131.
- [41] J. Livage, *Catal. Today* 41 (1998) 3-19.
- [42] M.-L. Wang, B.-L. Liu, C.-C. Ren, Z.-W. Shih, *Ind. Eng. Chem. Res.* 36 (1997) 2149-2155.
- [43] H.G. Langer, *J. Inorg. Nucl. Chem.* 26 (1964) 59-72.
- [44] T.P. Trainor, A.M. Chaka, P. J. Eng, M. Newville, G. A. Waychunas, J.G. Catalano, G.E. Brown Jr., *Surf. Sci.* 573 (2004) 204-224.
- [45] O. Fabrichnaya, *Ternary Alloy Systems: Phase Diagrams, Crystallographic and Thermodynamic Data*, Landolt-Börnstein - Group IV Physical Chemistry 11D5 (2009) 490-511.

Chapter 6

Electrochemical and adhesion properties of ZrO₂ coatings

6.1 Introduction

Different physical properties of the ZrO_2 coatings such as coating thickness, coating coverage, porosity etc., strongly depend on the nature of the pre-oxidized layer on SS substrate [1-3]. Hence it is expected that the adhesion and the corrosion resistance properties of the ZrO_2 coatings will be strongly influenced by the chemical composition and surface morphology of the pre-oxidized layer. In the present chapter, adhesion and corrosion resistance behavior of the ZrO_2 coatings developed on different pre-oxidized SS specimens by hydrothermal process have been studied. Thermally sensitized austenitic Type 304 SS (size $15*10*2\text{ mm}^3$) alloy is used for this study. The sensitized SS coupons were polished, cleaned and pre-oxidized in different environments. The pre-oxidation treatment and characterization details of the pre-oxidized SS specimens are described in detail in chapter 2 and chapter 3.

The corrosion resistant properties of ZrO_2 coatings developed on different pre-oxidized samples were studied and compared. Corrosion protection efficiency of ZrO_2 coated samples have been studied by potentiodynamic polarization tests and electrochemical impedance spectroscopy (EIS) at ambient temperature and 90°C . The PDP measurements reveal the corrosion resistance and insulating properties of the ZrO_2 film. EIS analysis explains the impact of different coating properties like porosity, thickness and compactness on the corrosion protection behavior. The standard tests for studying the resistance of stainless steel to IGC or SCC involve the immersion of coated test specimens in concentrated highly acidic solution. As the hydrothermally deposited ZrO_2 coatings are expected to be porous in nature, highly aggressive solution will penetrate to the underlying substrate material. The SS surface or the SS oxide layer will subsequently dissolve and results in detachment of ZrO_2 layer. The corrosion tests involving highly corrosive electrolytes like $0.1\text{ N H}_2\text{SO}_4$ does not provide any significant

analytical information as the parameters for specimens studied for comparison are identical. The determination of the polarization curve must be performed in a proper electrolyte to extract the maximum information about the corrosion resistance properties. Na_2SO_4 is an inert electrolyte which resulted from a strong acid and a strong base; and the polarization curves recorded in Na_2SO_4 electrolyte are found to be very sensitive to the insulating properties of surface films. The polarization measurements and EIS tests in Na_2SO_4 electrolyte at room temperature can be used as short term tests for characterization of the quality of hydrothermally deposited ZrO_2 coatings.

Qualitative analysis of nano-mechanical properties such as adhesion and hardness of ZrO_2 coatings is carried out by scanning probe microscope (SPM) to establish a relation between corrosion resistance behaviors of ZrO_2 coated samples and the adhesion of the ZrO_2 film to the substrate. Nano-indentation is the most commonly used technique for studying the nano-mechanical properties of thin films (thickness $> 1 \mu\text{m}$). The ZrO_2 coatings prepared by the hydrothermal route in this work are very thin (50-350 nm). So, present studies make the use of force-distance (FD) spectroscopy along with atomic force acoustic microscopy (AFAM) to study the adhesion behavior. The adhesion behavior is very important for the corrosion resistance behavior of thin films as the adherent film does not allow the direct contact of the electrolyte with the substrate. Corrosion resistance improves when the insulating film is adherent to the substrate. In addition, decrease in grain size of nanocrystalline ZrO_2 coatings enhances the adhesion and hardness of the coating [4].

6.2 Sensitization of Type 304L stainless steel

Type 304L stainless steel (SS) specimens were sensitized in a vacuum furnace under two different conditions. One set of samples was heated at 650°C for 24 hrs while the another set of

specimens were heated at 625°C for 100 hrs. Details of the sensitization experiments are given in Chapter 2. The susceptibility for IGC was studied for both types of sensitized SS specimens with respect to non-sensitized SS specimens. Oxalic acid etch test and Double-loop electrochemical potentiokinetic reactivation (DL-EPR) are carried out for the qualitative and quantitative analysis of the degree of sensitization.

6.2.1 Oxalic acid etch test

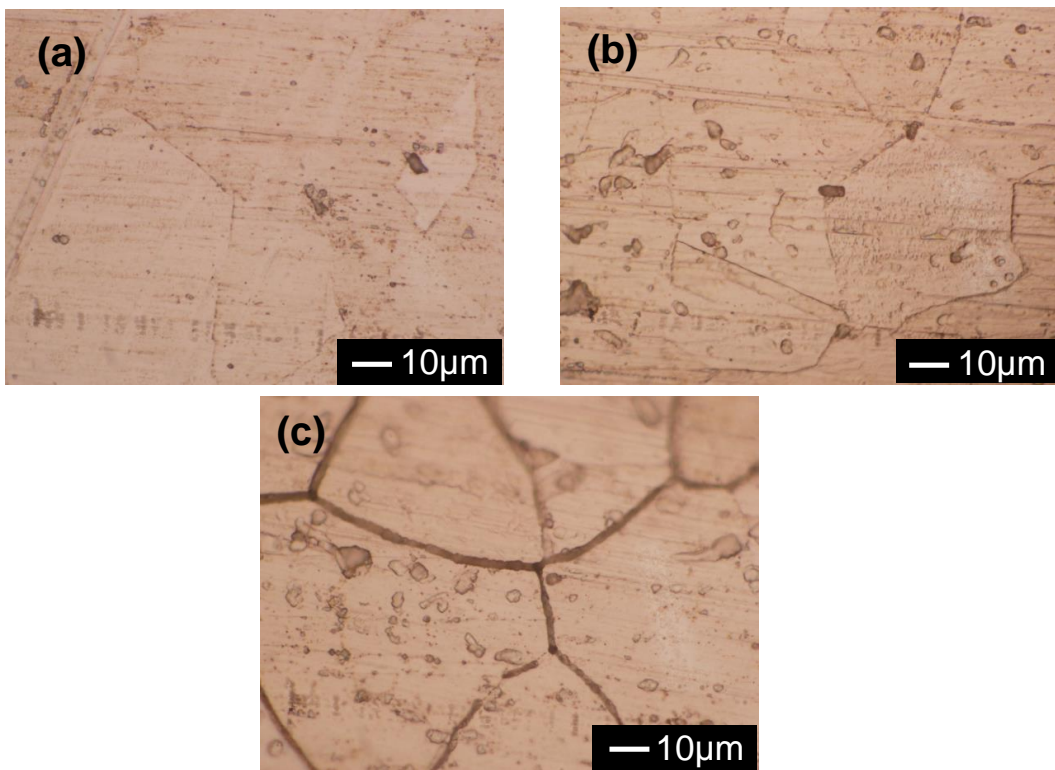


Fig. 6.1: Optical micrographs of the SS specimens after 10% oxalic acid etching at 1A/cm² (a) non-sensitized (as received), (b) sensitized at 650°C for 24 h and (c) sensitized at 625°C for 100 h

The oxalic acid etch test (ASTM A262-Practice A), described in section 2.10.2.1 is carried out on all the SS specimens and the resultant structures are shown in Fig. 6.1. The structures in Fig. 6.1 a, b and c are classified as "Step", "Dual" and "Ditch" structures

respectively. The "Step" and "dual" structures are resistant to IGC while the "Ditch" structure may be prone to IGC.

6.2.2 DL-EPR Test

DL-EPR tests are conducted to quantify the degree of sensitization (DOS) of SS specimens (section 2.10.2.2). The plots obtained from the DL-EPR test of different specimens are shown in Fig. 6.2.

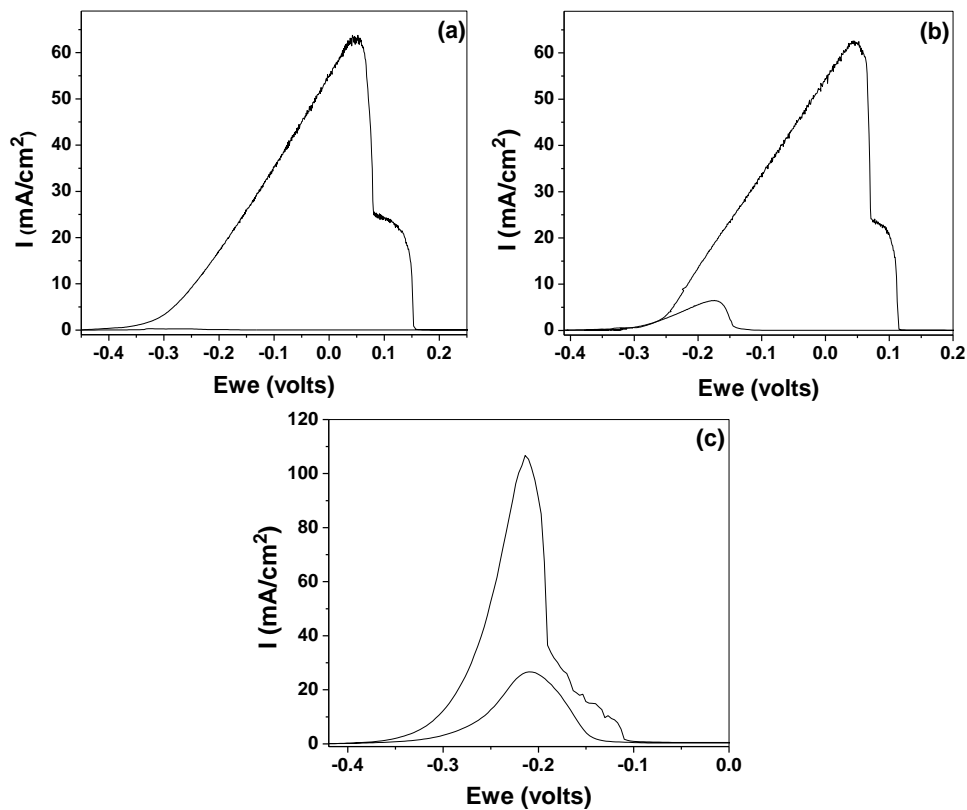


Fig. 6.2: DL-EPR curves of SS specimens (a) non-sensitized (as received), (b) sensitized at 650°C for 24 h and (c) sensitized at 625°C for 100 h

According to the ratio of peak reverse current density to peak forward current density in voltammetric curves (equation 2.12), DOS is calculated. For the plain (non-sensitized) SS specimen, 0% DOS was obtained for all the five test specimens. For the SS specimens sensitized

for 24 hours at 650°C, the degree of sensitization obtained was 3-4%. When the DL-EPR test was carried out on the SS specimens sensitized at 625°C and for 100 hrs, the nominal values of 25-30% were measured for five tested specimens. The results from DL-EPR study are consistent with the oxalic acid etch test studies. For example, no sensitization refer to a step structure, 3-4% and 25-30% of sensitization refer to dual and ditch structures respectively. The set of sensitized SS specimens with ditch structure and 25-30% of sensitization (sensitized for 625°C, 100 hrs) is used for further studies.

6.3 Electrochemical studies of sensitized and non-sensitized SS 304L specimens

SS304L specimens sensitized at 625°C for 100 hrs and the non-sensitized (as received) SS304L specimens are compared by PDP measurements and EIS analysis. The electrochemical measurements are carried out in 0.1M Na₂SO₄ solution at room temperature and 90°C respectively.

6.3.1 PDP measurements

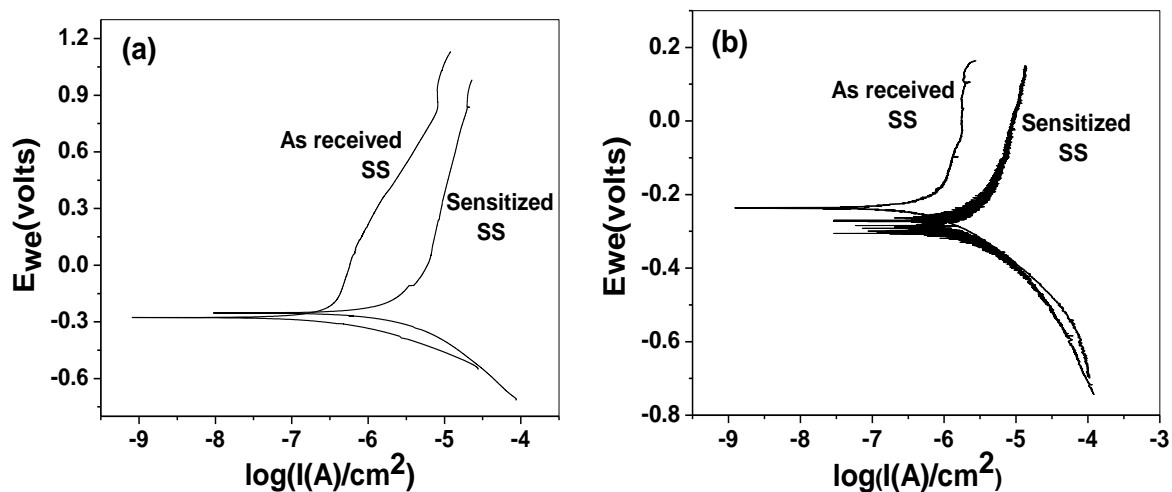


Fig. 6.3: Potentiodynamic polarization plot of plain 304 SS (sensitized and as received) specimens in 0.1 M sodium sulphate solution at (a) Room temperature (b) 90°C

Fig. 6.3 shows the potentiodynamic polarization plots for the sensitized and non-sensitized type 304L SS specimens at ambient temperature and 90°C. Corrosion current density (I_{corr}) of the SS specimens increased 3-5 times after the sensitization treatment (Table 6.1).

Table 6.1: Average value of polarization parameters for the plain as received 304L SS and sensitized 304L SS in 0.1 M sodium sulphate

<i>Sample Name</i>	<i>Temperature (°C)</i>	<i>E_{corr} (mV)</i>	<i>I_{corr} (μA/cm²)</i>	<i>β_a (mV)/decade</i>	<i>β_c (mV)/decade</i>
As received SS	R.T.	-277.31	0.3126	975.6	119.1
Sensitized SS	R.T.	-252.84	1.572	376	212
As received SS	90°C	-234.72	0.7955	561.2	152.1
Sensitized	90°C	-280.91	2.4627	408.3	203.6

6.3.2 EIS measurements

Fig. 6.4a and Fig. 6.4b show the Nyquist plots (Real vs. Imaginary impedance spectra) for the sensitized and non-sensitized type 304L SS specimens at ambient temperature and 90°C respectively. The existence of single depressed capacitive loop in the Nyquist plot indicates that the corrosion behavior is controlled by charge transfer process. The corresponding impedance parameters derived after fitting are presented in Table 6.2 and the equivalent circuit is shown in Fig 6.5. The constant phase element (Q) is used instead of pure capacitor to account for various kinds of defects such as surface roughness, porosity. R_s represents the solution resistance. The charge transfer resistance (R_{ct}) value of SS specimens decreased by 4-7 times after the sensitization treatment which is in agreement with the I_{corr} values obtained from PDP measurements.

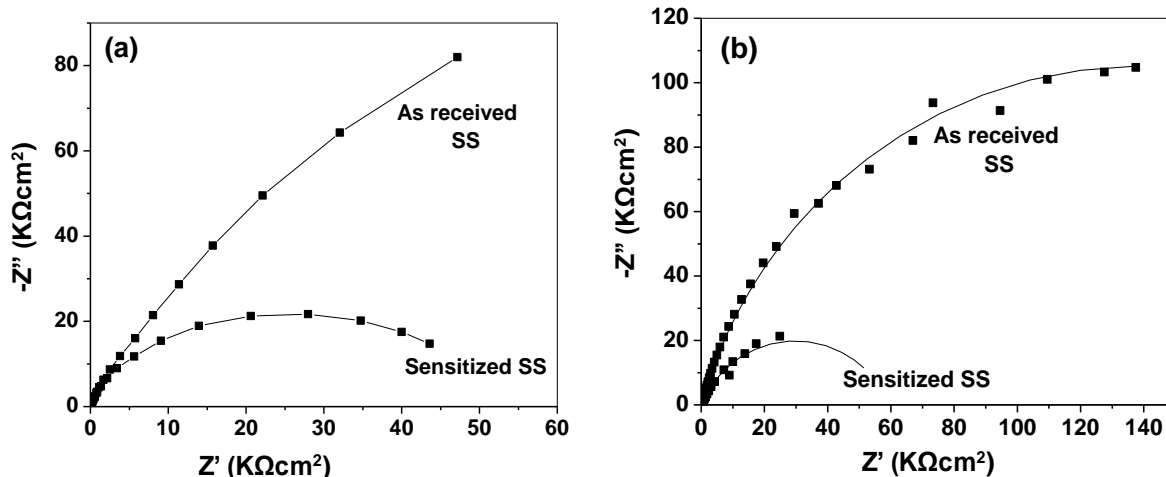


Fig. 6.4: Impedance spectra of plain SS 304L (sensitized and as received) specimens in 0.1 M sodium sulphate solution (a) Room temperature (b) 90°C

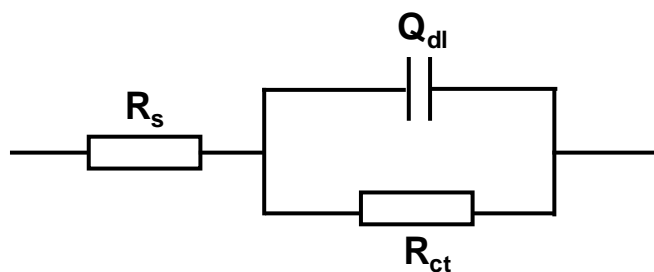


Fig. 6.5: Equivalent circuit used for fitting the electrochemical data of plain non-sensitized and sensitized 304L SS specimens

Table 6.2: Parameters of electrical equivalent circuits for the plain as received 304L SS and sensitized 304L SS specimens

Sample	Temperature	R_s ($\Omega \text{ cm}^2$)	Q_{dl} ($\mu\text{F cm}^{-2} \text{ s}^{n-1}$)	n_2	R_{ct} ($\Omega \text{ cm}^2$)
Plain SS	R. T.	3	102.63	0.83	350.46
Sensitized SS	R.T.	7	70.13	0.885	52.1
Plain SS	90°C	7	36.01	0.8246	277.86
Sensitized SS	90°C	19	35.75	0.75	59.46

6.4 Pre-oxidation of sensitized SS specimens

The 25-30% sensitized SS coupons were polished, cleaned and pre-oxidized under different conditions as given.

1. One set of specimens were oxidized in autoclave under reducing water conditions at 240°C for 21 days. Specimens are designated as POH-21.
2. Another set of specimens were oxidized in normal water at 240°C for 21 days. Specimens are designated as POO-21.
3. Thin films of α -Fe₂O₃ were deposited on few POO samples by PLD technique. These specimens are designated as POP.

The pre-oxidation and characterization of all the specimens have already been discussed in details in chapter 3. The properties of pre-oxidized SS specimens are summarized in Table 6.3 for comparison.

Table 6.3: Surface chemical composition and morphology of the pre-oxidized layers on SS

Sample Name	Experimental conditions	Composition of SS oxides	Surface Roughness	Particle size (nm)
POH-21	1ppm LiOH, 24ppm Hydrazine, 240°C, pH 10.3, 21 days (reducing conditions)	NiFe ₂ O ₄ , FeCr ₂ O ₄ etc. (Spinel oxides)	~25 nm	200-500
POO-21	Normal water, Initial oxygen concentration 7000 ppb, 240°C, 21 days (oxidizing conditions)	FeCr ₂ O ₄ , NiFe ₂ O ₄ , α -Fe ₂ O ₃ , α -(Fe,Cr)O ₃ etc. (Mixture of rhombohedral and spinel oxides)	~30 nm	~200
POP	Pulsed laser deposition of α -Fe ₂ O ₃ on sensitized POO specimen	Only α -Fe ₂ O ₃	~ 100 nm, hills-valley type morphology	50-200

6.5 Preparation and surface characterization of ZrO₂ coated samples

ZrO₂ coatings were developed on all the three types of pre-oxidized SS specimens. The coatings were developed by hydrothermal route given in section 2.7.1. The sample surfaces were characterized by different techniques and the electrochemical measurements were carried out.

6.5.1 SEM-EDS results

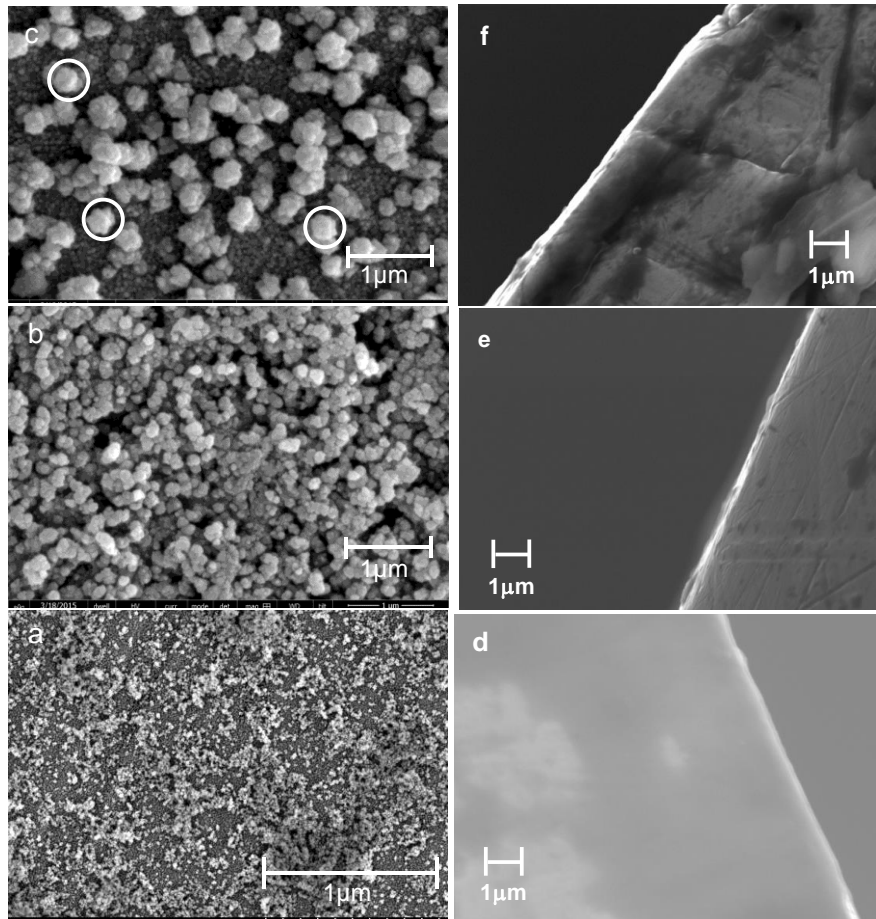


Fig. 6.6: SEM micrographs of ZrO₂ coated samples (a) ZPOH, (b) ZPOO and (c) ZPLD the circles indicates the large size grains of ZrO₂. Cross-sectional SEM micrographs of ZrO₂ coated samples; (d) ZPOH, (e) ZPOO and (f) ZPLD

The SEM images from the zirconia coated samples are shown in Fig. 6.6. The energy dispersive x-ray spectroscopy (EDS) analyses were performed at various regions for all the

samples including darkest to brightest zones. The EDS area analyses are also performed and the results obtained from the analyses are shown in Fig. 6.7.

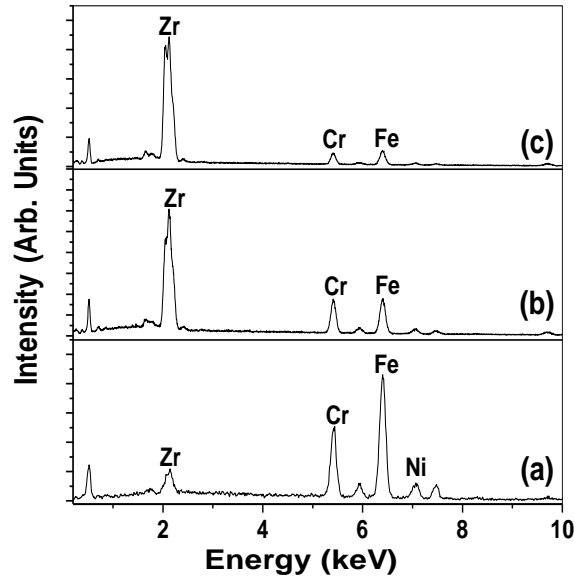


Fig. 6.7: EDS patterns of the ZrO_2 coated samples (a) ZPOH, (b) ZPOO and (c) ZPLD

The surface morphology of ZPOH sample (Fig. 6.6a) indicates that surface was covered with small grains of ZrO_2 particles, ZrO_2 particle size is of the order of 10-20 nm. Coating does not appear to be continuous; it seems that the islands of zirconia did not grow to the extent to completely cover the surface. The EDS data recorded at different places of the sample showed the presence of low concentration (1-6 wt%) of zirconium all over the surface. In ZPOO sample (Fig. 6.6b), ZrO_2 coating was continuous and individual grains of uniform size (~50 nm) were deposited all over the surface. The grains are composed of ZrO_2 nanoparticles of the order of 10-20 nm. The coating was porous at few places and various sizes of pores are present on the surface (black regions in Fig. 6.6b). Most of the pores are the order of 50-400 nm in size. EDS analysis done at different spots of the coating indicates the presence of 15-30 wt% of Zr. In ZPLD sample (Fig. 6.6c), ZrO_2 nano-particles are deposited uniformly and form a dense coating.

Over the dense ZrO₂ coating, large (~100 nm) grains of ZrO₂ are developed by the agglomeration of ZrO₂ nano-particles (indicated by circles in Fig. 6.6c). Very few, nano-size pores are present in the ZrO₂ coating in ZPLD sample. EDS analysis shows that 35-45 wt% of Zr was present on the entire sample.

By the cross-sectional SEM analysis (Fig. 6.6 (d-f)), thickness of ZrO₂ coatings for the ZPOH, ZPOO and ZPLD samples are found to be 50-100 nm, ~200 nm and ~350 nm respectively. So, a very thin zirconia layer was developed on pre-oxidized surface composed of spinel oxides while the surface composed of α -Fe₂O₃ leads to thick zirconia coating.

6.5.2 XPS and Raman analysis

The photoelectron spectra of all the ZrO₂ coated samples are shown in Fig. 6.8. From the intense Zr 3d peak at around 182 eV, it can be concluded that significant amount of ZrO₂ is deposited on all the pre-oxidized specimens. Very low intensity Fe and Cr signals from substrate are observed in the case of ZPOH. This supports the SEM image of ZPOH (Fig 6.8a) which shows that ZrO₂ coating is not continuous. In the case of ZPOO and ZPLD samples, substrate signals are completely absent that supports the SEM analysis where substrate surface was found to be fully covered with ZrO₂ particles.

The chemical interaction of ZrO₂ with the pre-oxidized surface has been investigated by Raman spectroscopy (Fig. 6.9). In the Raman spectrum of ZPOH (Fig. 6.9a), the presence of Raman mode at ~690 cm⁻¹ (Fig. 6.9a) even after the ZrO₂ coating implies that the interaction of ZrO₂ particles with spinel oxides of the substrate surface is not sufficient enough to modify the Raman modes. Raman spectra acquired from ZPOO (Fig. 6.9b) shows that most of the features from the POO specimen (Fig. 3.13) are almost disappeared; a weak signal of ferrites at around 690cm⁻¹ is only present. Raman modes from the POP specimen disappeared completely (Fig.

6.9c) due to the thick ZrO_2 coating. In the case of ZPOO and ZPLD, the Raman modes that belong to $\alpha-Fe_2O_3$ and $\alpha-(Fe_xCr_{2-x})O_3(x<1)$ disappeared completely indicating a strong chemical interaction of ZrO_2 with rhombohedral oxides [5].

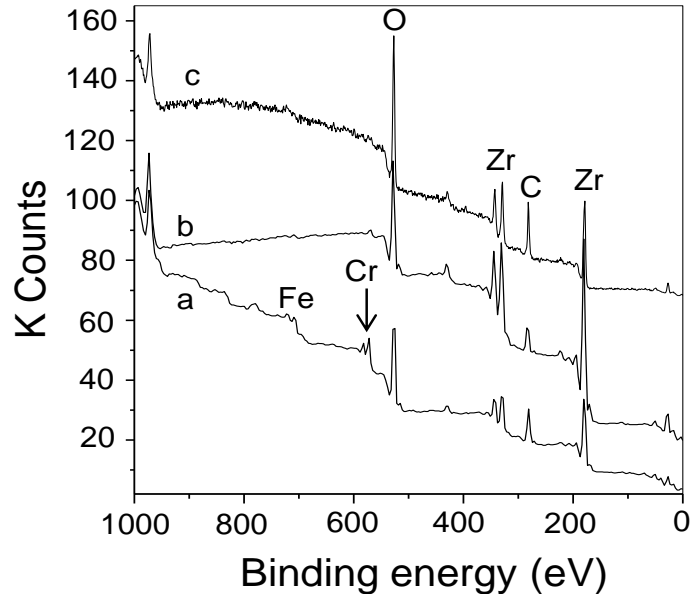


Fig. 6.8: XPS of ZrO_2 coated samples (a) ZPOH, (b) ZPOO and (c) ZPLD

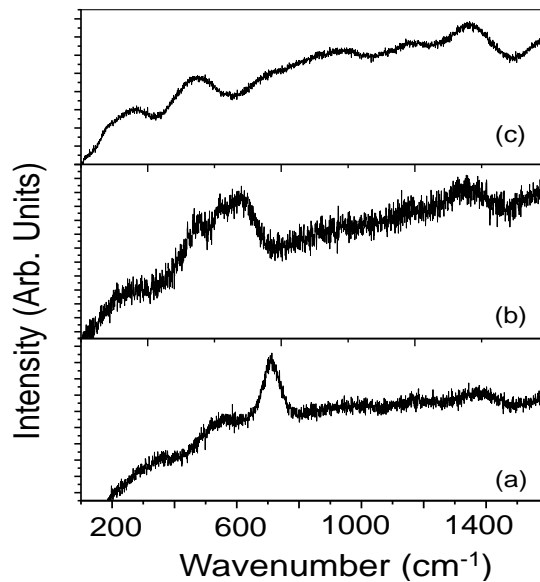


Fig. 6.9: Raman spectra of ZrO_2 coated samples (a) ZPOH, (b) ZPOO and (c) ZPLD

6.6 Topography and adhesion studies by AFM

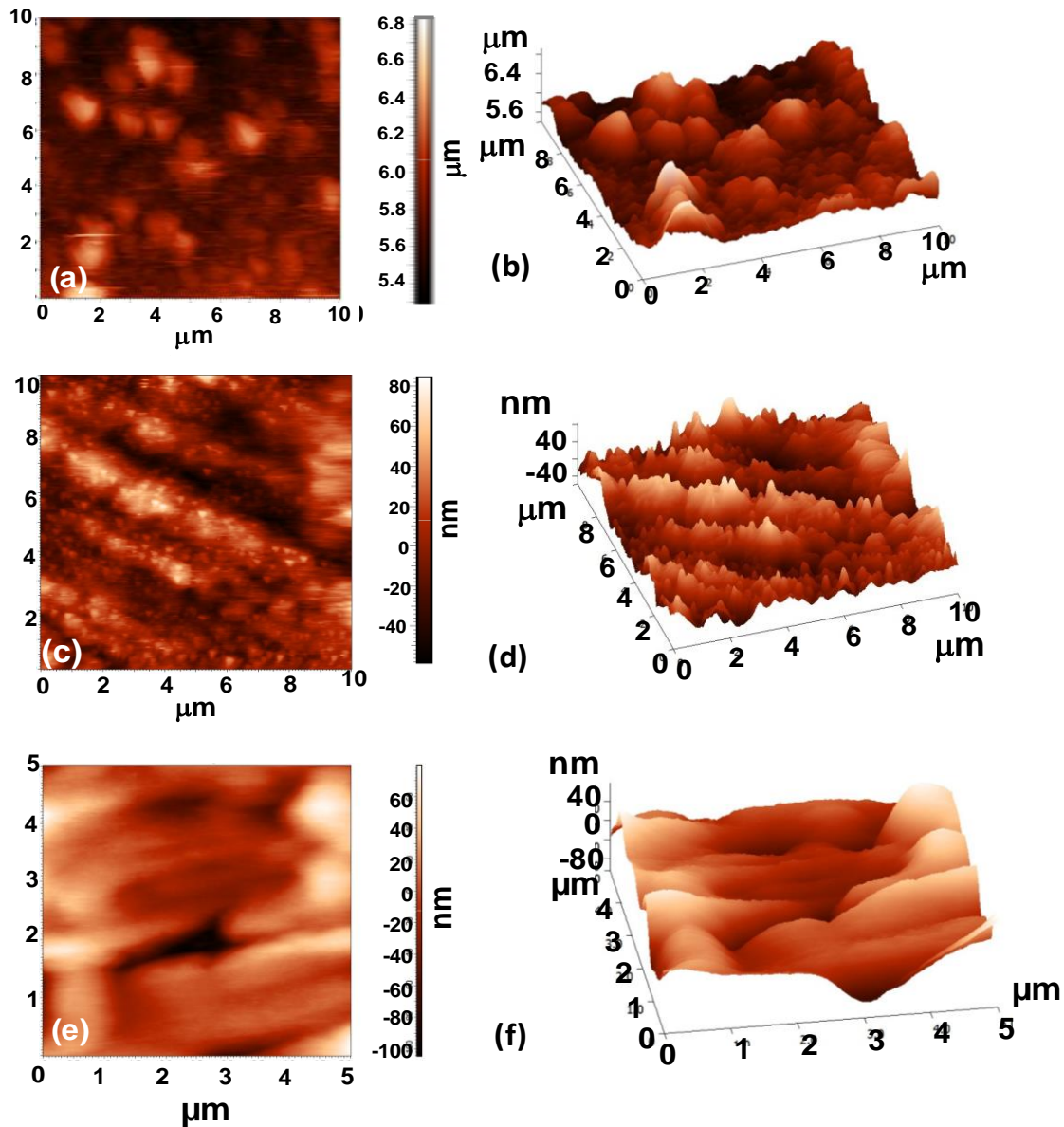


Fig. 6.10: AFM 2D and 3D topographic images of ZrO_2 coated samples (a, b) ZPLD, (c, d) ZPOO and (e, f) ZPOH

In the previous chapter it was established that Na salt of Zr-EDTA formed in the solution interacts with the pre-oxidized surface leading to the formation of interfacial bonding between the substrate oxide and ZrO_2 (section 5.3.5). The extent of the chemical interaction of the Na salt of Zr-EDTA with the substrate surface is directly influenced by the chemical composition,

surface roughness and the particle size of the pre-oxidized layer. Topography of all the ZrO_2 coated samples has been studied by AFM and topography images are shown in Fig. 6.10.

Topography analyses of the ZrO_2 coated samples (Fig 6.10 a-f), reveal that nano- ZrO_2 particles have been deposited on different substrates in different manners. Surface roughness of ZPOH sample (Fig 6.10e) is ~ 35 nm. Large surface oxide particles (200-500nm) of POH-21 could limit the diffusion of Zr-precursor (Na salt of Zr-EDTA, discussed in section 5.3.5.1) [1] on to the substrate surface during the ZrO_2 deposition process. So, continuity in between the ZrO_2 particles deposited is lost at several places and it results in the porous nature of ZrO_2 film as observed in both AFM and SEM images (Fig 6.10e, f & 6.6a). From AFM images of ZPOO sample (Fig 6.10c), very fine crystals of nano- ZrO_2 have been deposited with surface roughness of 15 nm. Smaller (~ 200 nm) and uniform size oxide particles of the substrate (POO-21) surface leads to continuous ZrO_2 coating as nano-nano composites with no agglomeration (Fig. 6.10b & 6.10c, d respectively). AFM image of ZPLD sample (Fig. 6.10a & b) shows the surface roughness of ~ 100 nm that is very high compared to other two cases. High surface roughness of ZPLD sample is reflecting the high surface roughness of the substrate (POP). Surface oxide of POP specimen has been deposited by PL deposition process that leads to high substrate surface roughness and hills and valleys type special topography shown by 3D images in chapter 5 (Fig. 5.10a) [1]. Inclusion of depositing material into the substrate will be more and ZrO_2 particles sit in the valleys resulting in the highly adhesive coating. Smaller substrate surface particle size (50-200 nm) in POP specimen (Table 6.1) results in better interaction of Zr-precursor due to higher surface area. It leads to the formation of continuous and dense nano- ZrO_2 coating as shown by SEM image (Fig. 6.6c). In this case, ZrO_2 particles seem to be a nano-micro composites, as very few large grains are observed along with mostly small grains (Fig 6.10 a & b).

AFAM images (Fig. 6.11) of the ZrO_2 coated specimens are acquired to study the variation in local nano-mechanical properties like hardness and adhesion. These images give the impact of surface mechanical properties on the tip with respect to topography. Hardness is depicted by the deflection of AFM cantilever in AFAM images (Fig 6.11a-f). The contrast in AFAM images shows the hardness variation in ZrO_2 coatings within the sub-structures. Bright region corresponds to stiff/hard regions and dark region corresponds to soft regions. Change in bright and dark zones in AFAM images with respect to topography is very less in the case of ZPOH and ZPOO samples (Fig. 6.11c-f). This indicates uniform hardness at different location of the samples. The change is prominent in ZPLD sample (Fig. 6.11a, b) that depicts the cantilever deflection is due to the variation in hardness at different locations. Different impact on cantilever results in dark and bright regions indicating the variation of hardness at different local nano-structures. The ZPLD sample shows the highest hardness. From AFAM images of ZPLD sample (Fig. 6.11 a & b), it appears that certain fraction of ultrafine ZrO_2 nano-particles get entrapped in grain boundaries during the growth process. This entrapment adds to hardening of grain boundaries [6]. This behavior is not observed in ZPOH and ZPOO samples, where growth of ZrO_2 coating is limited due to the unfavorable substrate surfaces. Particularly, the ZPOH sample shows the lowest hardness due to very limited growth of ZrO_2 coating.

Measurements of local adhesion force of thin films by FD spectroscopy have been performed in the past by few researchers [7, 8]. To measure the local adhesion forces, FD spectroscopy was used for each sample at several points and average value of the impact on the cantilever deflection was calculated. All the samples were analyzed by constant force. Force versus distance curve (FD curves) of the Si, SS reference, and ZrO_2 coated samples at different regions were measured and shown in Fig. 6.12 (a-e). The particular points from which the FD

curves are presented are marked by circles. The blue lines in the Fig. 6.12 represent the loading of cantilever while the red lines represent the unloading process. Uniform deflection at different areas depicts the homogeneous adhesion in all ZrO_2 coated samples. Adhesion force was calculated with respect to deflection of cantilever. Adhesion force for the ZPLD sample is around 100 nN, around 55 nN for ZPOO and around 48 nN for ZPOH samples.

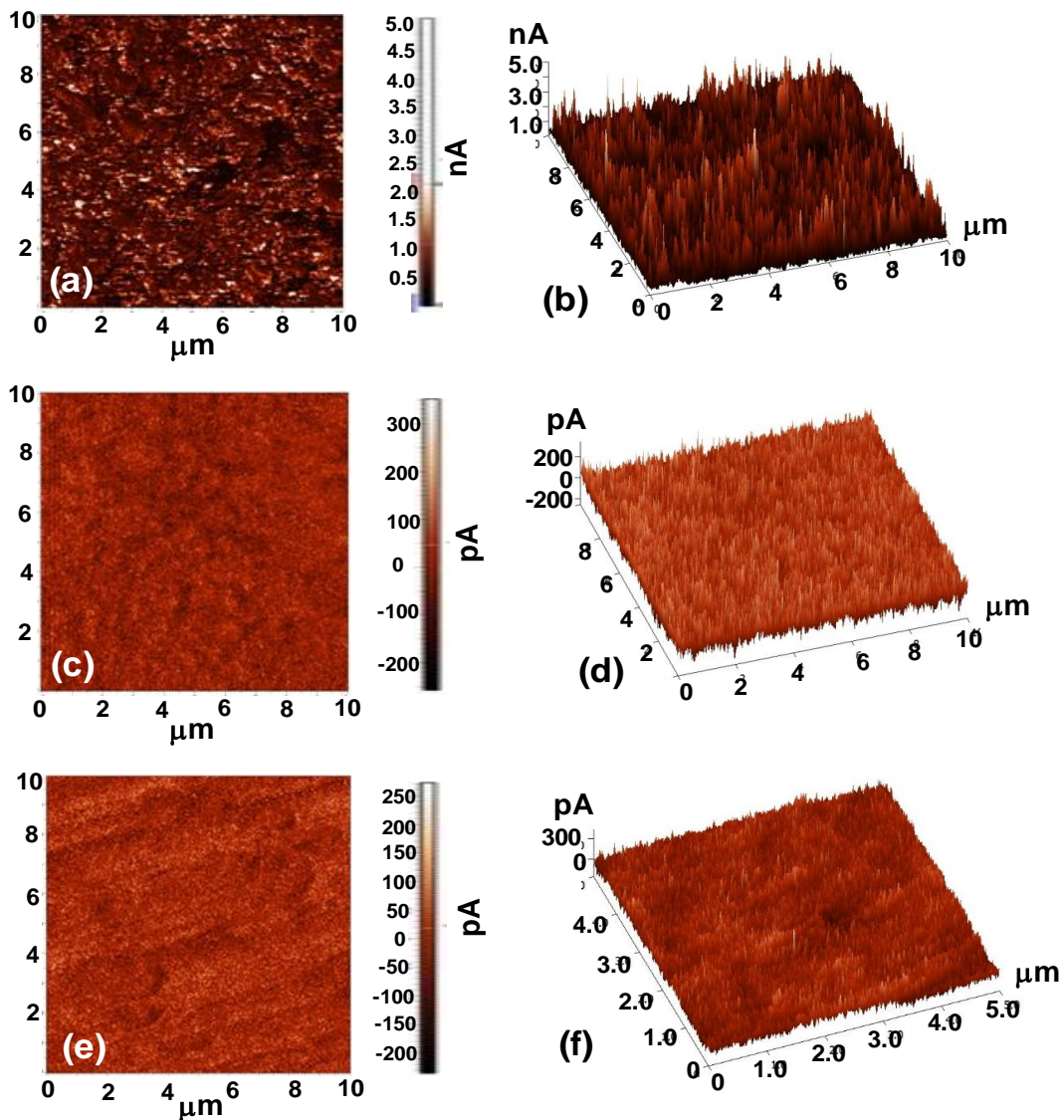


Fig. 6.11: Acoustic 2D and 3D images acquired during AFAM scans ZrO_2 coated samples (a, b) ZPLD, (c, d) ZPOO and (e, f) ZPOH

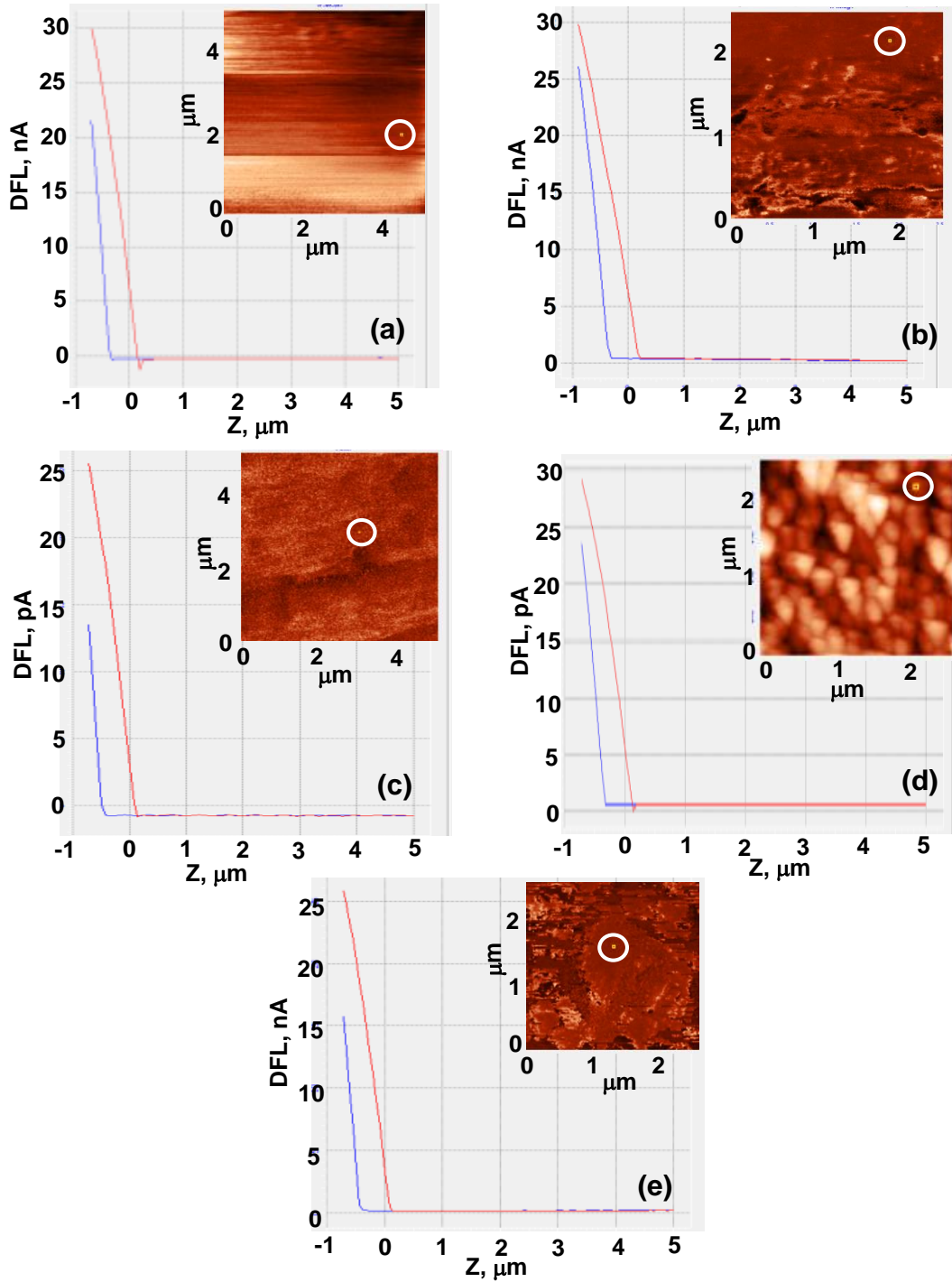


Fig. 6.12: Force-distance curves for the (a) Si, (b) Plain SS and ZrO₂ coated samples (c) ZPOH, (d) ZPOO, (e) ZPLD. Force is given in terms of cantilever deflection (DFL). The particular zones from where the FD curves are presented are marked by circles in AFM images in the insets of FD curves

It is concluded that ZrO_2 film developed on $\alpha-Fe_2O_3$ coated substrate is more adhesive compared to other two ZrO_2 coated samples. Hence, intermediate oxide surface roughness, oxide composition and particle size strongly contribute to the adhesion and hardness of ZrO_2 coatings.

6.7 Electrochemical studies of zirconia coatings at room temperature:

6.7.1 Potentiodynamic polarization test

Potentiodynamic current-potential plots for all the samples were recorded in sodium sulfate solution to examine the corrosion behavior of ZrO_2 coated samples in comparison to the uncoated SS specimens. Fig. 6.13 shows the potentiodynamic polarization plots from the pre-oxidized specimens and Fig. 6.14 shows the same for ZrO_2 coated samples and plain stainless steel. Corresponding electrochemical parameters are presented in Table 6.4. After the pre-oxidation, a strong passivation behavior is observed in the specimens prepared in autoclave (POH-21 and POO-21). Similar passivation behavior was not observed in the case of POP specimen.

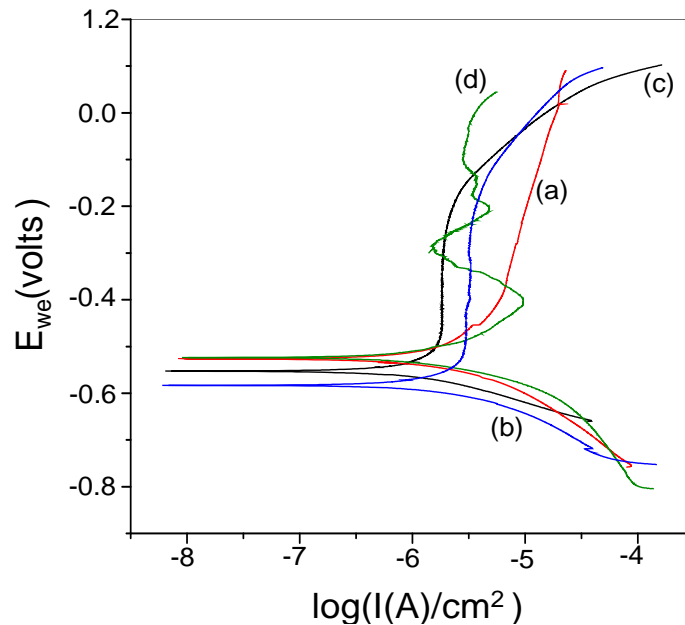


Fig. 6.13: Potentiodynamic polarization plots of plain SS and pre-oxidized SS specimens in 0.1M sodium sulphate solution (a) Plain SS, (b) POH-21, (c) POO-21 and (d) POP

It is observed that the corrosion potentials (E_{corr}) of zirconia coated samples are shifted towards positive values indicating that the corrosion resistance of samples improved after ZrO_2 coating (Fig. 6.14). I_{corr} values got reduced to significant extent for all the samples after ZrO_2 coating (Table 6.4). Cathodic current densities of ZPOO and ZPLD samples (Fig. 10) are approximately 100 times lower in comparison to plain SS. In these cases, ZrO_2 coatings act as physical barrier and alleviate the cathodic reactions on the surface [9]. Zirconia coating is not thick enough in the case of ZPOH sample to act as a barrier. The anodic current densities of all the zirconia coated samples are lowered by more than one order in comparison to plain SS. This is due to inertness of ZrO_2 in electrochemical environment. ZrO_2 coatings inhibit the anodic dissolution process due to its insulating nature, and provide the alloy a stable and protective surface. Anodic current densities of ZPOH sample during anodic polarization show a steep increase after the potential is raised above +0.25V. This behavior shows the onset of the film breakdown [10]. The presence of porosity and defects on the surface increase the diffusion of electrolytes through coating, resulting in the decrease of corrosion resistance. In the case of ZPOO and ZPLD samples, ZrO_2 films are stable during the polarization tests. High dielectric strength of ZrO_2 resists the collapsing of films during polarization [11]. Although I_{corr} for ZPOO (0.046 μA) is lower compared to ZPLD (0.104 μA), but anodic current density is higher in ZPOO than ZPLD. In the case of ZPOO, anodic current density rises when the potential is raised from -0.072V to 0.248V and then becomes constant and shows the passive behavior. This shows the disturbance of film in this region due to effect of porosity. In general, pores and continuous boundaries in between the columnar grains on the coated surface create solution paths. Once the solution reaches the bottom of the coated surface, the exposed areas of the substrate will be subject to accelerated anodic dissolution resulting in an increase in passive current density as

well as corrosion current density. As the coating thickness is high for ZPLD, pore formation is limited and film disturbance is not observed.

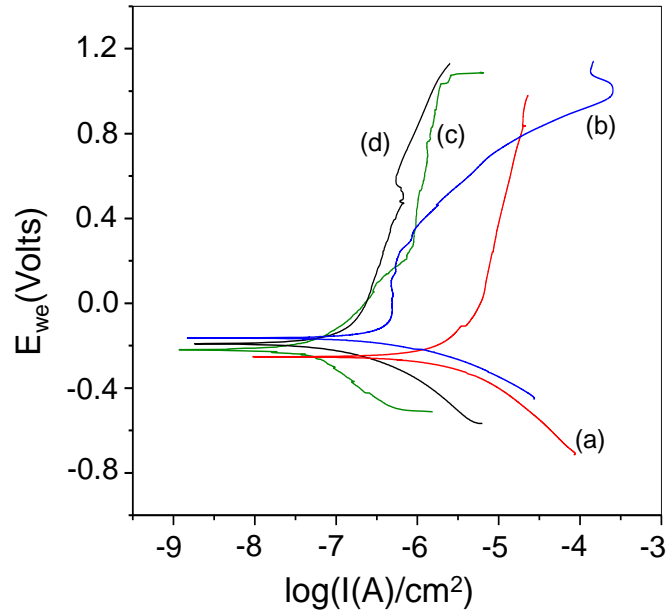


Fig. 6.14: Potentiodynamic polarization plots of plain SS and ZrO_2 coated SS samples in 0.1M sodiumsulphate solution (a) Plain SS, (b) ZPOH, (c) ZPOO and (d) ZPLD

Table 6.4: Average value of polarization parameters for plain, pre-oxidized and ZrO_2 coated 304L SS in 0.1 M sodium sulphate

<i>Sample Name</i>	E_{corr} (mV)	I_{corr} ($\mu A/cm^2$)	β_a (mV)/decade	β_c (mV)/decade
Sensitized SS	-252.8	1.572	376	212
POH-21	-366.2	1.632	352	194
POO-21	-305.6	0.925	400	135
POP	-247.5	1.972	300	189
ZPOH	-164.0	0.383	548	157
ZPOO	-219.6	0.046	281	308
ZPLD	-192.2	0.104	156	298

6.7.2 Electrochemical Impedance Spectroscopy

EIS technique has been used to evaluate the barrier properties of the ZrO_2 thin films on SS surfaces. It has been reported that these barrier coatings prevent the electrode reactions strongly since they act as isolators [12]. Fig. 6.15 shows the Nyquist plots (Real vs. Imaginary impedance spectra) for the pre-oxidized specimens and plain SS and Fig. 6.16 shows the bode-phase plots for the same. The corresponding impedance parameters derived after fitting are presented in Table 6.5. In the case of plain SS, POH-21 and POP specimens (Fig. 6.15 a, b & d), existence of single depressed capacitive loop in the impedance spectra indicates that the corrosion behavior is controlled by charge transfer process. Their equivalent circuit model is presented in Fig. 6.5. Here, resistance of the surface is indicated by charge transfer resistance (R_{ct}) value that is highest for POH-21 ($58 \text{ k}\Omega \text{ cm}^2$) and lowest for POP ($26 \text{ k}\Omega \text{ cm}^2$) specimen. The high capacitance value for the POH-21 specimen indicates the porous nature of the oxide. The equivalent circuit for the POO-21 specimen is described in Fig 6.17 that is comprised of two time constants in parallel. R_{ct} of POO-21 specimen is $90 \text{ k}\Omega \text{ cm}^2$ (Table 6.5). Porous nature of the oxide film in POO-21 leads to the high capacitance value.

The Bode-phase plot of the plain SS (Fig 6.16 a) shows the typical characteristic feature of thin passive oxide film on the surface that may be formed while the SS sample was immersed in electrolyte during the electrochemical measurements [13]. For the POP specimen (Fig. 6.16 d), a single time constant refers to a non-porous oxide layer. For the POH-21 specimen (Fig. 6.16 b), low frequency bode plot shows the diffusion of electrolyte through the oxide layer that supports the porous nature of POH-21. For the POO-21 specimen (Fig. 6.16 c), two time constants and the porous nature got confirmed by the Bode-phase plot.

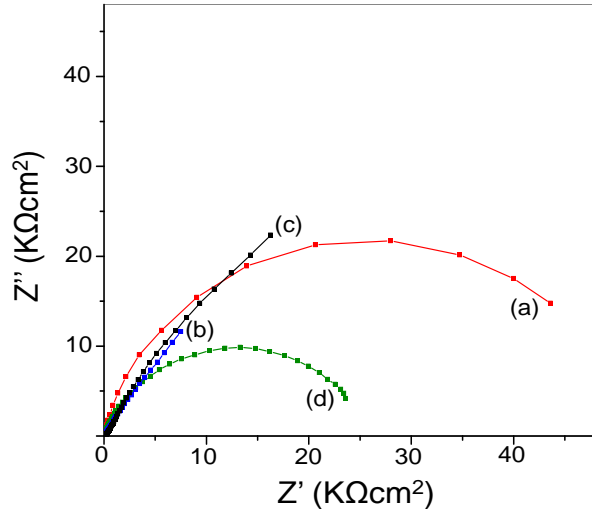


Fig. 6.15: Impedance spectra (Nyquist plot) of plain SS and pre-oxidized specimens in 0.1 M sodium sulphate solution (a) Plain SS, (b) POH-21, (c) POO-21 and (d) POP

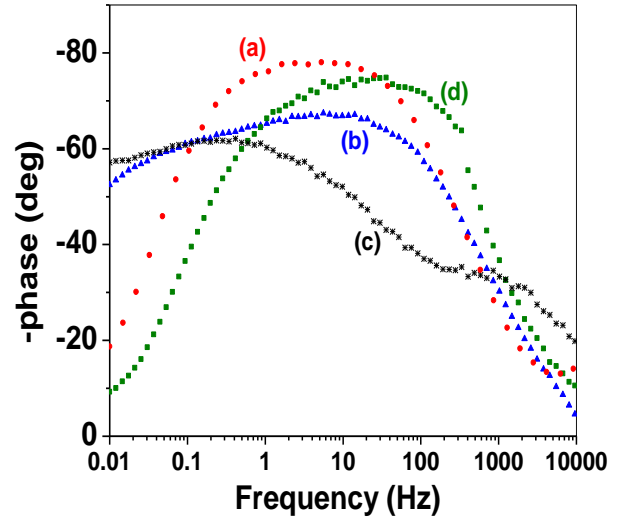


Fig. 6.16: Bode-phase plot of plain SS and pre-oxidized specimens in 0.1 M sodium sulphate solution (a) Plain SS, (b) POH-21, (c) POO-21 and (d) POP

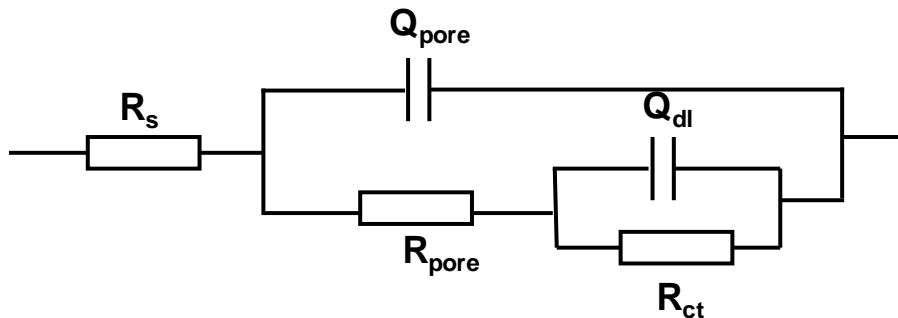


Fig. 6.17: Equivalent circuit used for fitting the electrochemical data of pre-oxidized SS specimen POO-21

Impedance spectra of ZrO_2 coated samples and plain SS specimen are presented in the form of Nyquist plots and bode-phase plots in Fig. 6.18 and Fig. 6.19 respectively. In the inset of Fig. 6.18, enlarged view of Nyquist plots at high frequencies is presented. The equivalent circuits for all the ZrO_2 coated samples are fitted with the single equivalent circuit shown in Fig. 6.20 which represents two time constants in series. The impedance parameters derived are given in

Table 6.6. The first time constant (R_2Q_2) belongs to the microstructural defects of the coatings such as pores, grain boundaries. The second time constant (R_3Q_3) represents the electrode resistance in terms of charge transfer resistance and coating capacitance. The value of n (Table 6.6) is related to pores, coating defects; $n = 0.5 \pm \epsilon$ and $0 \leq \epsilon \leq 0.1$, implies Warburg impedance [14] where constant phase element is related to the diffusion of electrolyte through the pores of coatings. It implies that ZrO_2 coatings in ZPOH and ZPOO samples are porous and results in high coating capacitance (252.8 and $400 \mu F cm^{-2} s^{n-1}$ respectively). Porous nature of ZrO_2 coating in ZPOO and thin, discontinuous coating in ZPOH lead to microstructural defects in ZrO_2 coatings. These defects results in low charge transfer resistances for ZPOH and ZPOO (345 and $368 k\Omega cm^2$ respectively) although it is quite high when compared to plain and pre-oxidized SS specimens. The higher pore resistance of ZPOO ($45 k\Omega cm^2$) compared to ZPOH ($29 k\Omega cm^2$) is attributed to continuous and thicker ZrO_2 coating in ZPOO than ZPOH. EIS results are in agreement with the observations from polarization tests where ZPOH and ZPOO coatings are porous in nature.

Table 6.5: Parameters of electrical equivalent circuits for plain SS and pre-oxidized specimens

<i>Sample</i>	R_s (Ωcm^2)	Q_{pore} ($\mu F cm^{-2} s^{n-1}$)	n_2	R_{pore} (Ωcm^2)	Q_{dl} ($\mu F cm^{-2} s^{n-1}$)	n_{dl}	R_{ct} ($k\Omega cm^2$)
Plain SS	7	-	-	-	70.13	0.89	52.1
POH-21	5	-	-	-	432	0.72	58
POO-21	6	133.6	0.69	52.2	314	0.72	90
POP	9	-	-	-	59.8	0.82	26

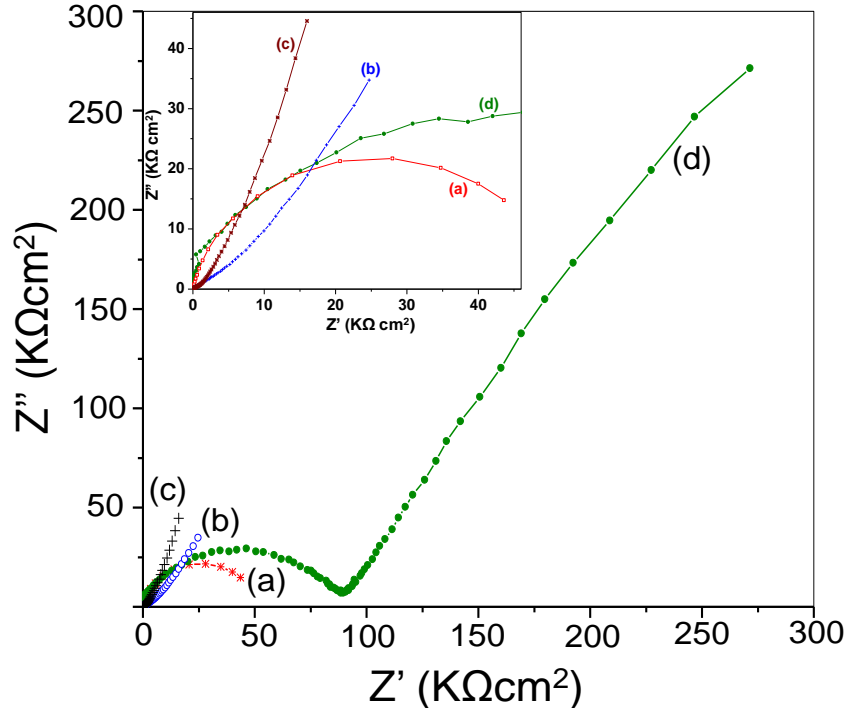


Fig. 6.18: Impedance spectra (Nyquist plot) of plain SS and ZrO_2 coated samples in 0.1 M sodiumsulphate solution (a) Plain SS, (b) ZPOH, (c) ZPOO and (d) ZPLD, The inset shows the enlarged view of the (a) plain SS, (b) ZPOH and (c) ZPOO

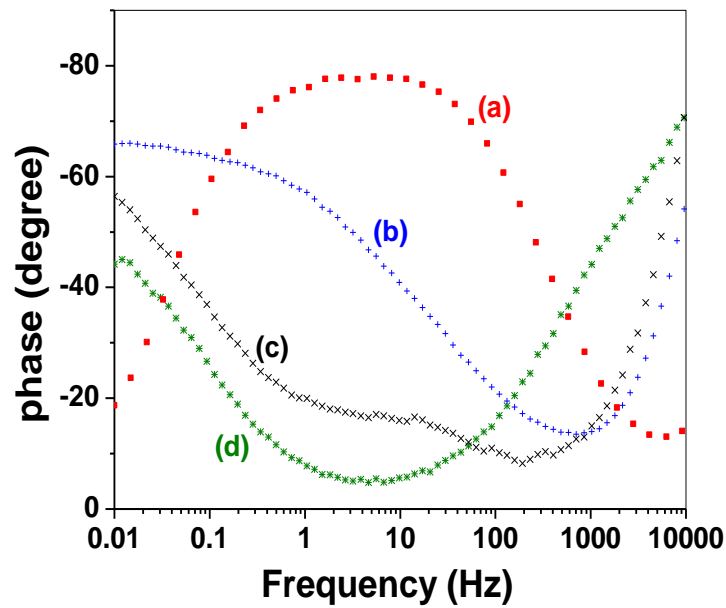


Fig. 6.19: Bode-phase plot of plain SS and ZrO_2 coated samples in 0.1 M sodiumsulphate solution (a) Plain SS, (b) ZPOH, (c) ZPOO and (d) ZPLD

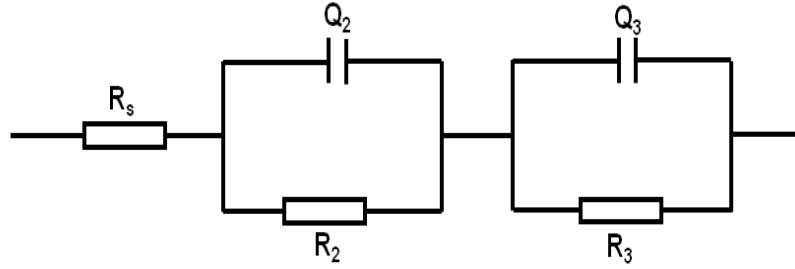


Fig. 6.20: Equivalent circuit used for fitting the electrochemical data of ZrO_2 coated samples

Table 6.6: Parameters of electrical equivalent circuit for ZrO_2 coated samples

Sample	R_s (Ωcm^2)	Q_2 ($\mu F cm^{-2} s^{n-1}$)	n_2	R_2 ($k\Omega cm^2$)	Q_3 ($\mu F cm^{-2} s^{n-1}$)	n_3	R_3 ($k\Omega cm^2$)
ZPOH	3	107.2	0.5	29	252.8	0.78	345
ZPOO	2	170	0.43	45	400	0.95	368
ZPLD	2	0.035	0.72	90	19.1	0.7	3000

In the Bode-phase plot, the high frequency region ($>10^3$ Hz) shows the properties of reference electrode and solution resistance R_s , the medium frequency region ($1-10^3$ Hz) shows capacitive behavior and the low frequency region (<1 Hz) explains the charge transfer process occurring at solution/coating interface [15]. The Bode-phase plot of ZPOH (Fig 6.19b) confirms the diffusion of electrolyte through the ZrO_2 layer where high and continuous phase angle (-65°) has been observed at the low frequency region (10^{-2} -1 Hz). Bode-phase plot of ZPOO sample (Fig 6.19c) shows phase angle minima of -17° at 1-10 Hz of frequency range depicts the insulating behavior of ZrO_2 coating in ZPOO. It also shows the capacitive characteristics in the high frequency region (10 - 10^4 Hz). So, the corrosion process is controlled by diffusion in ZPOH sample while both diffusion and charge transfer mechanism controls the corrosion process in ZPOO sample.

In the Nyquist plot of ZPLD sample (Fig. 6.18d), the semicircle portion at high frequency represents the resistance (R_2) of $90 \text{ k}\Omega \text{ cm}^2$ and capacitance value (Q_2) of $0.035 \mu\text{F cm}^{-2}\text{s}^{n-1}$. The first time constant (R_2Q_2) in the equivalent circuit (Fig 6.20) belonging to semicircle provides information about the grain boundary resistance and capacitance [16]. In the high frequency region (10^3 - 10^5 Hz), impedance spectrum shows the significant contribution from the intergranular component of the nano-particles (size ~ 15 nm) of thick ZrO_2 coating in ZPLD [16, 17]. Smaller grain size results in more number of grain boundaries across the sample with increase in grain boundary resistance [18]. The second time constant (R_3Q_3) shows the highest charge transfer resistance ($3000 \text{ k}\Omega \text{ cm}^2$) and lowest value of coating capacitance ($19.1 \mu\text{F cm}^{-2}\text{s}^{n-1}$) of ZPLD sample compared to ZPOH and ZPOO samples. It is the indicative of an insulating, barrier like compact and thick (~ 350 nm) zirconia coating in the ZPLD sample [19]. The well connected ZrO_2 grains all over $\alpha\text{-Fe}_2\text{O}_3$ surface leading to the continuous and dense ZrO_2 coating. In the Bode-phase plot of ZPLD (Fig 6.19d), the occurrence of a lowest phase angle (-5°) at 1-10 Hz confirms the barrier layer characteristics and existence of a compact coating where the diffusion of electrolyte through the ZrO_2 coating is very low and ZrO_2 film is highly resistive in nature. The steep increase in the phase angle at high frequency region (10^2 - 10^4 Hz) shows the capacitive behavior of the ZrO_2 coatings that may be attributed to the grain boundaries [16, 20,].

6.8 Electrochemical studies of zirconia coatings at 90°C

Electrochemical studies of the pre-oxidized SS specimens prepared in autoclave under reducing and oxidizing water chemistry conditions (POH-21 and POO-21 respectively) and their respective ZrO_2 coated samples were carried out at 90°C . The 90°C studies may provide the insight of high temperature applications of ZrO_2 coatings.

6.8.1 Potentiodynamic polarization tests

The PDP studies of zirconia coated samples (ZPOH and ZPOO) are carried out with respect to pre-oxidized and plain SS specimens at 90°C. Fig. 6.21 shows the potentiodynamic polarization plots for the plain SS, pre-oxidized SS (POH-21, POO-21) and zirconia coated SS (ZPOH, ZPOO) samples. All the samples show the tendency to increase the corrosion current density (I_{corr}) compared to ambient temperature studies. The zirconia coated samples shows the significant protection from corrosion at 90°C also like the room temperature experiments (Table 6.7). The cathodic and anodic current densities as well as I_{corr} values of zirconia coated samples are 5 to 7 times lower than that in plain and pre-oxidized SS specimens.

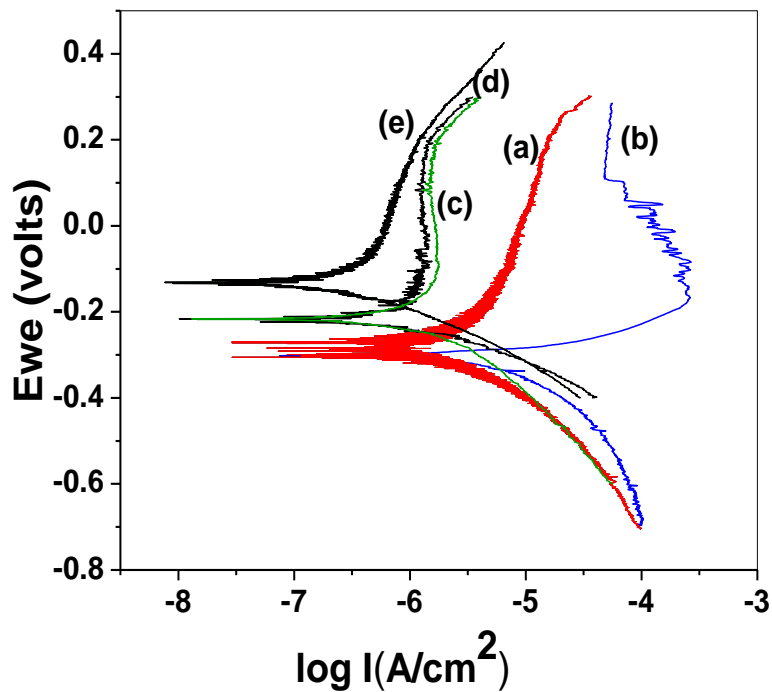


Fig. 6.21: Potentiodynamic polarization plots of plain, pre-oxidized and ZrO_2 coated SS samples in 0.1M sodium sulphate solution at 90°C (a) Plain SS, (b) POH-21, (c) POO-21 and (d) ZPOH and (e) ZPOO

Table 6.7: Average value of polarization parameters for plain, pre-oxidized and ZrO₂ coated 304L SS in 0.1 M sodium sulphate at 90°C

<i>Sample Name</i>	<i>E_{corr}</i> (mV)	<i>I_{corr}</i> (μA/cm ²)	<i>β_a</i> (mV)/decade	<i>β_c</i> (mV)/decade
Plain SS	-280.91	2.463	408	204
POH-21	-300.6	9.84	109	214
POO-21	-270.8	1.678	581	169
POL	-233.92	1.177	480	170
ZPOH	-215.07	1.338	-	119
ZPOO	-133.97	0.372	616	135
ZPOL	-166.17	0.7383	572	149

6.8.2 EIS studies

Fig. 6.22 shows the Nyquist plots for the pre-oxidized (POH-21 and POO-21) while the Fig. 6.23 shows the same for zirconia coated samples (ZPOH and ZPOO) with respect to plain SS. The corresponding equivalent circuits and electrochemical parameters are presented in Table 6.8 and Table 6.9 respectively. The increase in capacitance values of ZrO₂ coated samples correspond to increase in number of pores at high temperature. The charge transfer resistance of ZPOH sample decreased significantly compare to room temperature studies. The discontinuous zirconia coating in the case of ZPOH sample lead to enhanced diffusion of electrolyte at higher temperatures. The ZPOO sample did not show much deviation in the charge transfer resistance compare to room temperature studies. It means zirconia coating is able to act as a barrier at high temperatures and can be used for high temperature corrosion protection applications.

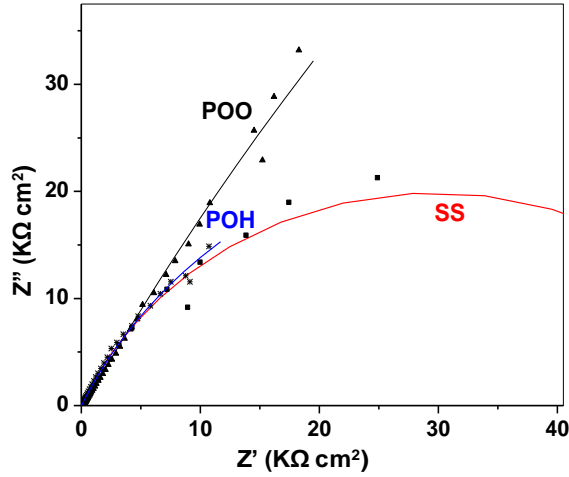


Fig. 6.22: Nyquist plots of the plain SS and pre-oxidized SS specimens (POH-21 and POO-21) in 0.1M sodium sulphate solution at 90°C

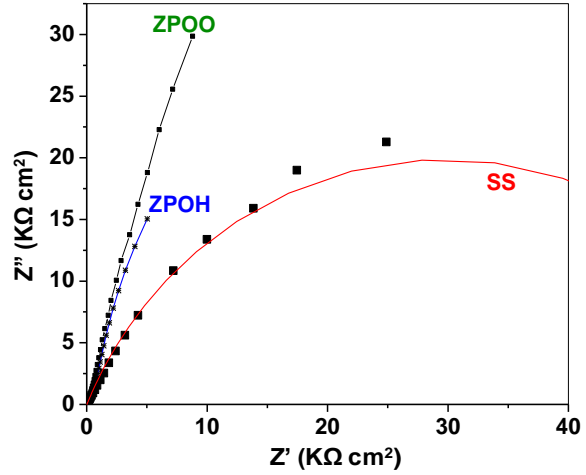


Fig. 6.23: Nyquist plots of the plain SS and ZrO₂ coated SS specimens (ZPOH and ZPLD) in 0.1M sodium sulphate solution at 90°C

Table 6.8: Equivalent circuits used for fitting the electrochemical data of samples

Sample	Equivalent circuit
Plain SS, POH-21	$R_s + Q_2/R_2$
POO-21	$R_s + Q_1/(R_2 + W_2) + C_3/R_3, s_2 = 1.407 \text{ Ohm.s}^{-1/2}$
ZPOH, ZPOO	$R_s + Q_2/R_2 + Q_3/R_3$

Table 6.9: Parameters of electrical equivalent circuit for different samples at 90°C

Sample	R_s (Ω)	Q_2 ($\mu\text{F cm}^{-2} \text{s}^{n-1}$)	n_2	R_2 ($k\Omega \text{ cm}^2$)	Q_3 ($\mu\text{F cm}^{-2} \text{s}^{n-1}$)	n_3	R_3 ($k\Omega \text{ cm}^2$)
SS	18.7	-	-	-	35.75	0.75	59.46
POH-21	9.0	-	-	-	342.6	0.73	76.99
POO-21	8.8	18.87	0.78	74.84	850.4	0.82	140.81
ZPOH	7.7	1418	0.4	25	901.5	0.95	75.0
ZPOO	6.4	3574	0.34	25	360.2	0.87	480.60

6.9 Impact of coating physical properties on adhesion and corrosion resistance

Adhesion of ZrO_2 coatings directly depends on the chemical composition and the surface morphology of the pre-oxidized layer. Chemical composition of the pre-oxidized surface is very important to form a stable molecular interface (eg. (Fe, Cr, Ni)-O-Zr) of metal oxides with the ZrO_2 for an adhesive and thick coating. Miscibility of ZrO_2 with substrate particles like $\alpha-Fe_2O_3$ crystallites and different spinel oxides is the deciding property for the nucleation and growth of ZrO_2 coating. ZrO_2 is known to form a wide range of $Fe_2O_3-ZrO_2$ metastable compositions with Fe_2O_3 and $\alpha-Fe_2O_3-ZrO_2$ metastable compounds are more thermodynamically stable compare to $Fe_3O_4-ZrO_2$ compounds [22, 23]. Favorable interfacial sites in ZPLD sample results in higher adhesion and surface coverage of ZrO_2 nano-particles on the substrate surface (section 5.3.4). In ZPOH sample, unfavorable composition of the pre-oxidized layer leads to unstable or less stable interfacial states. Thin, porous and less adhesive behaviors of ZPOH coating are observed by SEM, AFM and AFAM images as well as PDP technique. The ZPOO is having the mixed substrate surface composed of rhombohedral oxides of Fe like $\alpha-Fe_2O_3$, $\alpha-(Fe_{2-x}Cr_x)O_3$ and spinel oxides like $FeCr_2O_4$ and Fe_3O_4 . It is showing the adhesion and coating thickness higher than ZPOH but lower than ZPLD. The adhesion and surface coverage of ZrO_2 coatings deposited over different pre-oxidized SS surfaces are partially influenced by their respective substrate surface roughness and oxide particle sizes. In the case of ZPLD, small $\alpha-Fe_2O_3$ particles (50-200 nm) and hills/valley type high roughness substrate surface in POP sample provide the maximum surface area for interaction of Zr-precursor. ZrO_2 particles deposited in the valleys improve the adhesion of the coating to the substrate. Favorable topography and small $\alpha-Fe_2O_3$ particles lead to maximum inclusion of depositing material in POP sample. POO-21 does not have the morphology like hills/valleys but have low particle size (~200 nm). Small particles offer the high

surface area for interaction. The POH-21 with smooth surface and large particles (200-500 nm) offers the least favorable morphology for ZrO₂ deposition.

Electrochemical properties of the coated specimens are strongly influenced by the coating physical and adhesion properties. The electrochemical properties of ZrO₂ coatings with respect to their substrate surface properties are summarized in Table 6.10.

Table 6.10: Comparison of properties of ZrO₂ coated samples for different pre-oxidized SS surfaces

Sample	ZPOH	ZPOO	ZPLD
Substrate surface	Spinel oxides	Spinel oxides, α -($\text{Fe}_x\text{Cr}_{2-x})\text{O}_3$ (x = 0-2)	α -Fe ₂ O ₃
Substrate oxide particle size (nm)	200-500	~200	50-200
ZrO ₂ coating thickness (nm)	50-100	~250	~350
Adhesion Force (nN)	~55	~48	~100
Porosity	Porous	Less Porous	Non-porous
Total resistance (k Ω cm ²)	374	413	3090
Roughness (nm)	~35	~15	~100
I _{corr} ($\mu\text{A}/\text{cm}^2$)	0.383	0.046	0.104

It appears that the properties of ZrO₂ coatings like adhesion, surface coverage, coating thickness and porosity effect the corrosion resistance behavior of ZrO₂ coated samples. The ZPOO sample shows better corrosion resistance properties compare to ZPOH due to higher surface coverage and thickness although adhesion force for ZrO₂ coatings is nearly equal for both. The total resistance offered by ZPLD sample (3.01 M Ω) was highest among all the ZrO₂

coated samples by EIS as it is best in terms of thickness, adhesion and density of coating. Though compact and thick ZrO_2 coating of ZPLD shows the highest corrosion resistance, even a thin and porous layer of ZrO_2 can also reduce the I_{corr} at both ambient temperature and $90^\circ C$ to a significant extent by alleviating the redox reactions on SS surface which is observed in ZPOH. These results are similar to the observations by Yeh et al. [24, 25] where just physical deposition of ZrO_2 particles on the SS surface was able to reduce the I_{corr} to significant extent.

6.10 Zirconia coating on SS specimen pre-oxidized in simulated BWR environment

Zirconia coating is developed on the pre-oxidized SS specimens prepared under simulated Loop with BWR coolant conditions (designated as POL). Zirconia coated samples (designated as ZPOL) are characterized by SEM-EDS, AFM and PDP measurements are performed for analysis of corrosion resistance properties. After the zirconia deposition treatment on pre-oxidized POL specimen, The SEM image (Fig. 6.24a) shows that the surface of ZPOL is fully covered with ZrO_2 particles and the EDS analysis (Fig. 6.24b) confirms the presence of uniformly thick ZrO_2 coating with 27-35% Zr counts everywhere.

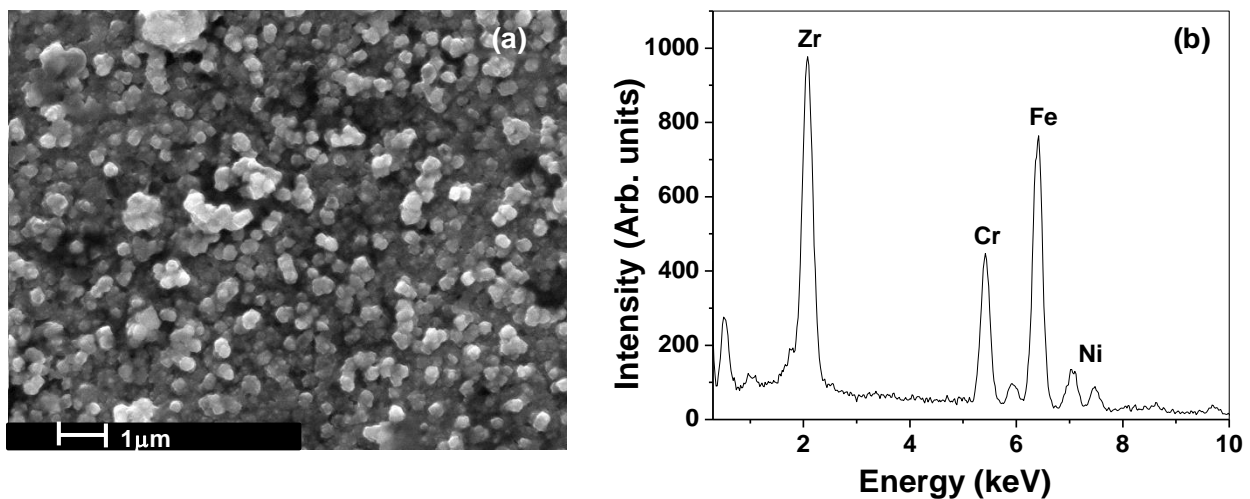


Fig. 6.24: (a) SEM image of the ZPOL sample and (b) EDS results for the ZPOL sample

The AFM analysis (Fig. 6.25a) shows grains of ZrO_2 with uniform size on the ZPOL surface. The surface roughness of the ZPOL specimen is >100 nm. The AFAM (Fig. 6.25b) analysis indicates that the deposited ZrO_2 coating is hard and the hardening of grain boundaries is also observed like ZPLD sample. It means that the thick and adhesive ZrO_2 coating is developed in the ZPOL sample leading to high hardness. The adhesion force of the ZrO_2 coating is measured by FD spectroscopy and the value of adhesion force is found to be ~ 75 nN. The presence of major α - Fe_2O_3 phase in the surface of POL specimen leads to the higher adhesion force compare to ZPOH and ZPOO samples.

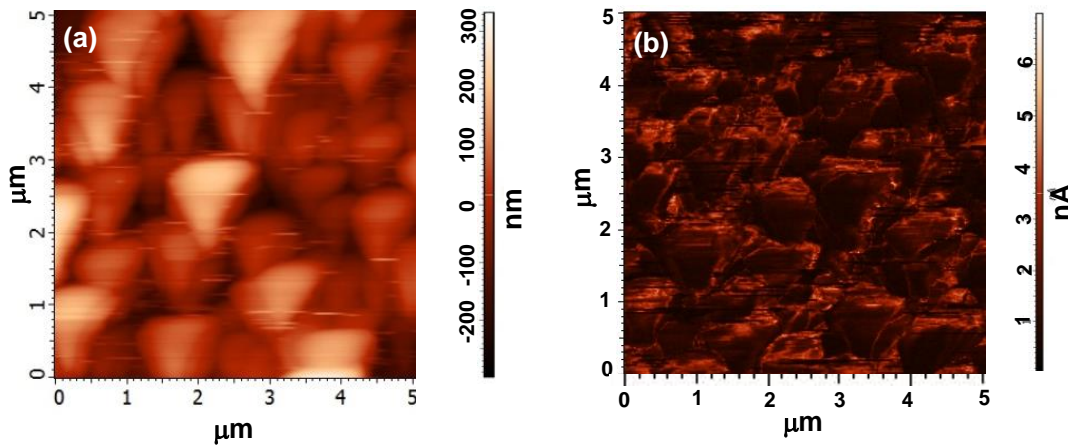


Fig. 6.25: The AFM images of the ZPOL sample; (a) AFM topographic image and (b) Acoustic image acquired during AFAM scan

The corrosion resistance properties of the ZrO_2 coated POL specimen (ZPOL) in comparison to pre-oxidized POL specimen are studied by potentiodynamic polarization test at $90^\circ C$ (Fig. 6.26). The corresponding electrochemical parameters are given in Table 6.7. There is a shift in E_{corr} towards the positive value after the ZrO_2 deposition along with a significant decrease in I_{corr} values. It means that the ZrO_2 coatings are effective on the pre-oxidized SS specimens prepared in simulated BWR water chemistry environments.

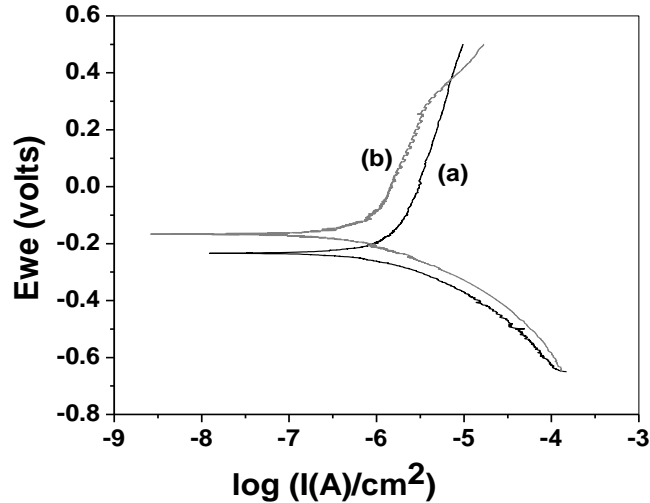


Fig. 6.26: Potentiodynamic polarization plots of (a) pre-oxidized POL specimen and (b) ZrO_2 coated ZPOL sample in 0.1M sodium sulphate solution at 90°C

6.11 Conclusions

ZrO_2 films have been deposited on pre-oxidized stainless steel substrates with different surface compositions and morphologies by hydrothermal process. The effects of surface composition, particle size and roughness of the pre-oxidized surface on the properties of ZrO_2 coatings have been studied. Pre-oxidized surface composed of $\alpha\text{-Fe}_2\text{O}_3$ with special morphology is found to provide the highest adhesion of the coatings and most suitable surface oxide for the growth of compact and thick ZrO_2 coating. The thickness of around 350 nm has been achieved on such pre-oxidized layer on SS. Pre-oxidized surface composed of mixed rhombohedral and spinel oxides results in porous ZrO_2 coating with thickness of around 200 nm. Pure spinel oxides lead to deposition of discontinuous ZrO_2 coating with coating thickness of 50-100 nm. AFAM and FD spectroscopy analyses show that ZrO_2 coating is hard when the pre-oxidized layer is PL deposited $\alpha\text{-Fe}_2\text{O}_3$ and the adhesion force is around 100 nN. Small particle size and hills/valley type morphology of the PL deposited $\alpha\text{-Fe}_2\text{O}_3$ provide the large surface area for interaction with Na salt of Zr-EDTA during the hydrothermal process which improves the adhesion. Adhesion

force for ZrO₂ coatings grown on other surface oxides like spinel oxides or mixed rhombohedral and spinel oxides is approximately 50nN. Significant improvements in corrosion resistant behavior of SS specimens have been observed after ZrO₂ coatings on all the pre-oxidized specimens. ZrO₂ coatings are able to provide sufficient corrosion protection at high temperature (90°C) and ZrO₂ coatings are effective for the pre-oxidized SS specimens prepared in simulated BWR environment. However, the best corrosion resistance properties have been observed in the case of ZrO₂ coatings deposited on α -Fe₂O₃ surface where corrosion resistance value increased to 3090 k Ω cm² from 52.1 k Ω cm² of plain SS.

6.12 References

- [1] N. Garg, S. Bera, G. Mangamma, V.K. Mittal, R. Krishnan, S. Velmurugan, *Surf. Coat. Technol.* 258 (2014) 597–604.
- [2] N. Garg, V.K. Mittal, S. Bera, P. Chandramohan, C.R. Das, S. Velmurugan, *Thin Solid Films* 545 (2013) 222-228.
- [3] F. Martin, R. Ayouchi, C. Ruiz, J.R. Ramos-Barrado, D. Leinen, *Surf. Interface Anal.* 34 (2002) 719–723.
- [4] M. Trunec, *Ceram-Silikaty* 52 (2008) 165-171.
- [5] T.K. Yeh, Po-I. Wu, C. H. Tsai, *Prog. Nucl. Energ.* 57 (2012) 62-70.
- [6] G. Mangamma, K.M. Kant, M.S.R. Rao, S. Kalavathy, M. Kamruddin, S. Dash, A. K. Tyagi, *J. Nanosci. Nanotechnol.* 7 (2007) 2176-2181.
- [7] A. Lazauskas, V. Grigaliūnas, A. Guobienė, M. Andrulevičius, J. Baltrusaitis, *Thin Solid Films* 520 (2012) 6328–6333.

- [8] T.-G. Kim, Y.-S. Yoo, J. Ahn, J.-M. Lee, J.-S. Choi, A.A. Busnaina, Jin-Goo, *Microelectron. Eng.* 86 (2009) 150–154.
- [9] R.R. Pareja, R.L. Ibáñez, F. Martín, J.R. Ramos-Barrado, D. Leinen, *Surf. Coat. Technol.* 200 (2006) 6606–6610.
- [10] R.A. Antunes, M.C.L. de Oliveira, M.F. Pillis, *Int. J. Electrochem. Sci.* 8 (2013) 1487 - 1500.
- [11] N. Padhy, S. Kamal, R. Chandra, U.K. Mudali, B. Raj, *Surf. Coat. Technol.* 204 (2010) 2782-2788.
- [12] S.M. Lee, S.H. Oh, W.I. Cho, H. Jang, *Electrochim. Acta* 52 (2006) 1507-1513.
- [13] E. Kobayashi, T.J. Wang, H. Doi, T. Yoneyama, H. Hamanaka., *Journal of Materials Science: Materials in Medicine* 9 (1998) 567-574.
- [14] X. Yuan, C. Song, H. Wang, J. Zhang, *Electrochemical impedance spectroscopy in PEM fuel cells – fundamentals and applications*, Springer-Verlag, London, UK (2010).
- [15] M. Metikoš-Huković, E. Tkalčec, A. Kwokal, J Piljac, *Surf. Coat. Technol.* 165 (2003) 40-50.
- [16] R. Heung, X. Wang, P. Xiao, *Electrochim. Acta* 51 (2006) 1789–1796.
- [17] Y. Zhu, C. Ding, *J. Eur. Ceram. Soc.* 20 (2000) 127-132.
- [18] S.H. Jo, P. Muralidharan, D.K. Kim, *SolidState Ionics* 178(2008) 1990-1997.
- [19] J.G. Fletcher, A.R. West, J.T.S. Irvine, *J. Electrochem. Soc.* 142 (1995)2650-2654.
- [20] J. Hitzig, K. Jüttner, W.J. Lorenz, W. Paatsch, *Corros. Sci.* 24 (1984) 945-952.
- [21] F. Mansfeld, M.W. Kendig, *J. Electrochem. Soc* 135 (1988) 828-833.
- [22] O. Fabrichnaya, *Ternary Alloy Systems: Phase Diagrams, Crystallographic and Thermodynamic Data*, Landolt-Börnstein - Group IV Physical Chemistry 11D5 (2009) 490-511.

- [23] P.K. Narwankar, F.F. Lange, C.G. Levi, *J. Am. Ceram. Soc.* 80 (1997) 1684-1690.
- [24] T.-K. Yeh, Y.-C. Chien, B.-Y. Wang, C.-H. Tsai, *Corros. Sci.* 50 (2008) 2327–2337.
- [25] T.-K. Yeh, M.-Y. Lee, C.-H. Tsai, *J. Nucl. Sci. Technol.* 39 (2002) 531-539.

Chapter 7

Increase of zirconia coating thickness and electrochemical measurements

7.1 Introduction

The corrosion resistance of SS samples improved significantly after the ZrO₂ coatings. It is expected that the thicker ZrO₂ coating will lead to better corrosion protection. It was discussed in chapter 2, ZrO(NO₃)₂.6H₂O (Zr precursor) along with Na-EDTA and SDS was used for the formation of ZrO₂ coating on pre-oxidized stainless steel by hydrothermal process [1, 2]. In the present chapter, two different methods are adopted for improving the ZrO₂ coating thickness by hydrothermal process. The first method involves the increase of concentration of precursor materials (ZrO(NO₃)₂.6H₂O) while maintaining the other hydrothermal deposition conditions like pH, temperature, pressure identical. In second method, repetition of the hydrothermal deposition process several times using same concentration of Zr-precursor (discussed in chapter 2) with fresh reactants to improve the ZrO₂ coating thickness.

The samples after the coating formation are characterized by different techniques like SEM-EDS, XPS and Raman spectroscopy. Thicknesses of the ZrO₂ coatings are measured by cross-sectional SEM analysis. Several rounds of ZrO₂ deposition is found to be effective for improving the ZrO₂ coating thickness. The corrosion resistance properties of the coated samples have been measured by PDP and EIS techniques. The resistance of ZrO₂ coated samples found to be increased with the increase in coating thickness but it deteriorated after a certain thickness. The optimum thickness of the ZrO₂ coating for corrosion resistance applications is evaluated by electrochemical measurements.

7.2 Attempt for coating thickness improvement by increasing the precursor concentrations

Preparation and characterization details of the pre-oxidized SS specimens are given in chapter 2 and chapter 3. Pre-oxidized SS specimens POH-21 and POO-21 are used for this study.

POH-21 specimens are composed of mainly spinel oxides while the POO-21 specimens are composed of both spinel oxides and rhombohedral oxides like $\alpha\text{-(Fe,Cr)}_2\text{O}_3$ and $\alpha\text{-Fe}_2\text{O}_3$.

ZrO_2 coatings are developed on these pre-oxidized SS specimens by hydrothermal method using 3.33 mM, 6.66 mM and 10 mM of $(\text{ZrO}(\text{NO}_3)_2) \cdot 6\text{H}_2\text{O}$. Zirconia coated POH-21 samples are designated as ZPOH and 2ZPOH for the 3.33 mM and 6.66 mM concentration respectively. Zirconia coated on POO samples are designated as ZPOO, 2ZPOO and 3ZPOO for the 3.33 mM, 6.66 mM and 10 mM concentration respectively.

7.2.1 Improvement of ZrO_2 coating thickness on POH-21

7.2.1.1 Surface characterization

In chapter 6, it is observed that hydrothermal deposition process leads to the development of discontinuous and porous zirconia coating on the pre-oxidized specimen POH-21. In order to attain a continuous and thicker ZrO_2 coating, hydrothermal deposition is carried out with higher concentration of reactants. It was expected to increase the interaction between suspended Zr-precursor and pre-oxidized SS surface. The surface morphology of the zirconia coatings developed on POH-21 at different precursor concentrations are shown by SEM images (Fig. 7.1).

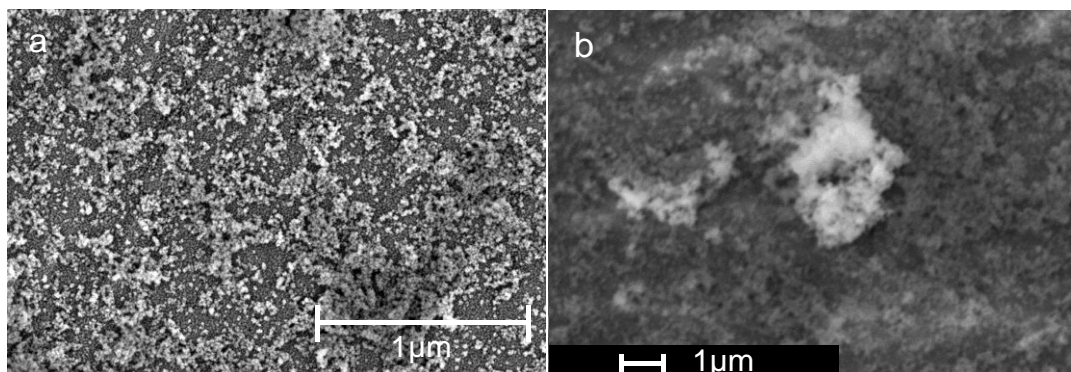


Fig. 7.1: SEM micrographs of the zirconia coated SS samples, (a) ZPOH and (b) 2ZPOH

Both of the ZPOH and 2ZPOH samples show that the zirconia coatings are discontinuous at several places. EDS analysis show that 0-6 and 0-18 wt% of Zr is present for the ZPOH and 2ZPOH samples respectively. It confirms that the both of the ZrO_2 coatings are very thin and discontinuous at several places. XPS spectra (Fig. 7.2) show the presence of weak substrate signals from both ZPOH and 2ZPOH samples. It confirms that the ZrO_2 particles could not completely cover the substrate surface for both samples as depth of information of XPS is very small (5-10 nm). So, it can be concluded that interaction between spinel oxides (POH-21) and deposited ZrO_2 particles could not be enhanced significantly by doubling the precursor concentration. Although continuous coating could not be achieved by doubling the precursor concentration, electrochemical studies are performed to compare the corrosion protection ability of both samples.

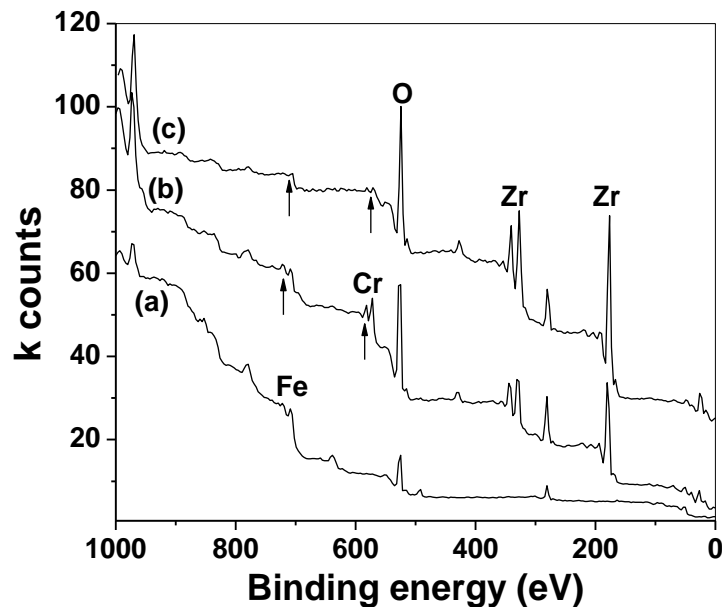


Fig. 7.2: XPS survey scan of the pre-oxidized and ZrO_2 coated SS samples; (a) POH, (b) ZPOH and (c) 2ZPOH

7.2.1.2 Electrochemical studies

Potentiodynamic current-potential plots and EIS plots for ZPOH and 2ZPOH samples were recorded in sodium sulfate solution at ambient temperature (25°C) and 90°C. Fig. 7.3 shows the potentiodynamic polarization plots for the zirconia coated samples ZPOH and 2ZPOH at ambient temperature and 90°C. The onset of film breakdown is observed in the anodic region of room temperature measurements for both the cases [3]. ZPOH and 2ZPOH samples show similar cathodic and anodic current densities and I_{corr} values during the polarization measurements at ambient temperature and 90°C (Table 7.1).

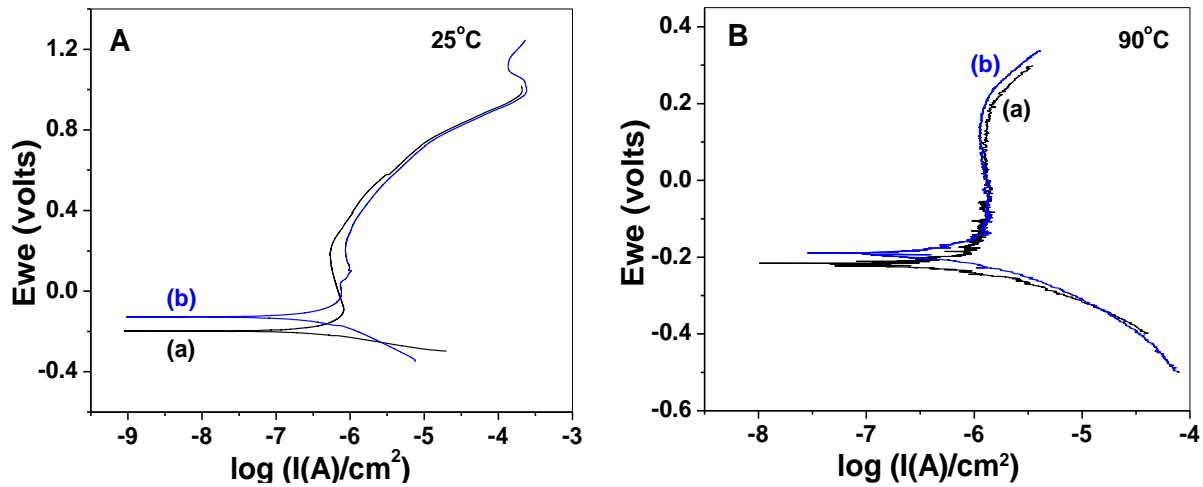


Fig. 7.3: A. Potentiodynamic polarization plots of ZrO_2 coated SS samples obtained at 25°C, (a) ZPOH and (b) 2ZPOH, B. Potentiodynamic polarization plots of ZrO_2 coated SS samples obtained at 90°C (a) ZPOH and (b) 2ZPOH

The EIS analysis (Fig. 7.4) also shows that same observations as PDP tests that there is no significant difference between the ZrO_2 coated samples prepared at different precursor concentrations. The electrochemical parameters obtained from the EIS analysis are given in Table 7.2. All the EIS spectra are fitted with two time constants in series (Fig. 6.20). Both of the samples show porous behavior at both 25°C and 90°C. The PDP plots and EIS analysis confirms

that diffusion of electrolyte is taking place to the substrate due to discontinuous and porous ZrO_2 coatings. It confirms that there is no significant improvement in the corrosion resistance properties of 2ZPOH samples compare to ZPOH samples.

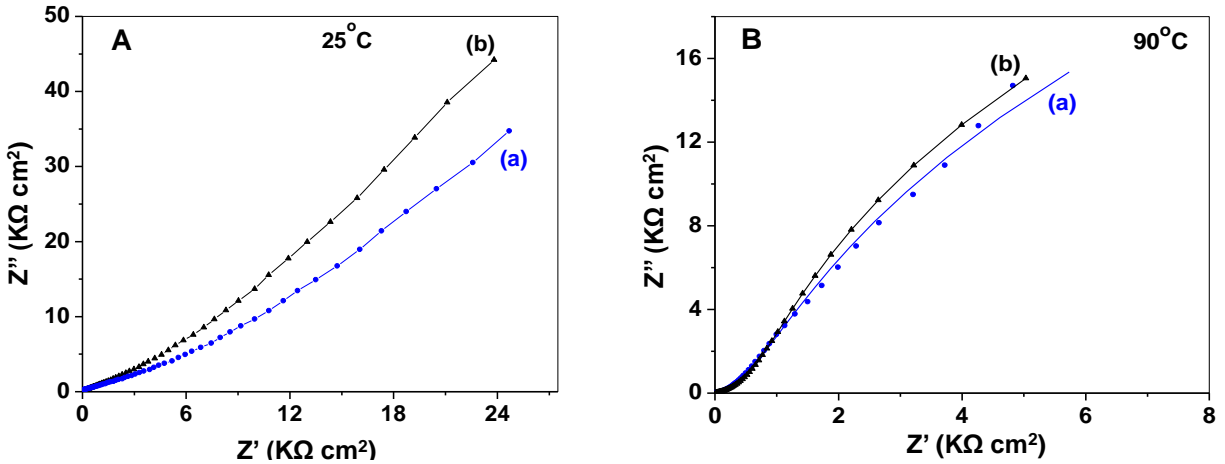


Figure 7.4: A. Impedance spectra of ZrO_2 coated samples in 0.1 M sodium sulphate solution at 25°C, (a) ZPOH and, (b) 2ZPOH, B. Impedance spectra of ZrO_2 coated samples in 0.1 M sodium sulphate solution at 90°C, (a) ZPOH and, (b) 2ZPOH

7.2.2 Improvement of ZrO_2 coating thickness on POO-21

7.2.2.1 Surface Characterization

Zirconia coatings are developed on pre-oxidized SS specimens composed of both rhombohedral and spinel oxides (POO-21) at different precursor concentrations (3.33, 6.66 and 10 mM). Fig.7.5 Shows the SEM micrographs of zirconia coated samples ZPOO, 2ZPOO and 3ZPOO. In ZPOO and 2ZPOO samples (Fig. 7.5a & b respectively), ZrO_2 coating was continuous and individual grains of uniform sizes were deposited on the entire surface. For both the ZPOO and 2ZPOO samples, zirconia coatings were porous at few places and various sizes of pores (50-400 nm) are present on the surface (black regions in Fig. 7.5a & b). EDS analysis done at different spots of the coating indicates the presence of 15-30 wt% and 4-11 wt% of Zr counts

in ZPOO and 2ZPOO samples respectively. It indicates that the increase in precursor concentration does not improve the thickness of ZrO_2 coating. Fig. 7.5c shows the SEM image of 3ZPOO sample, where zirconia coating was not continuous. It was non-adherent and peeled off from the substrate. SEM images (marked by arrows in Fig. 7.5c) show the several zones where zirconia film could not deposit. EDS analysis confirms the absence of Zr in these regions. Further studies are not carried out for this sample because of poor coating properties.

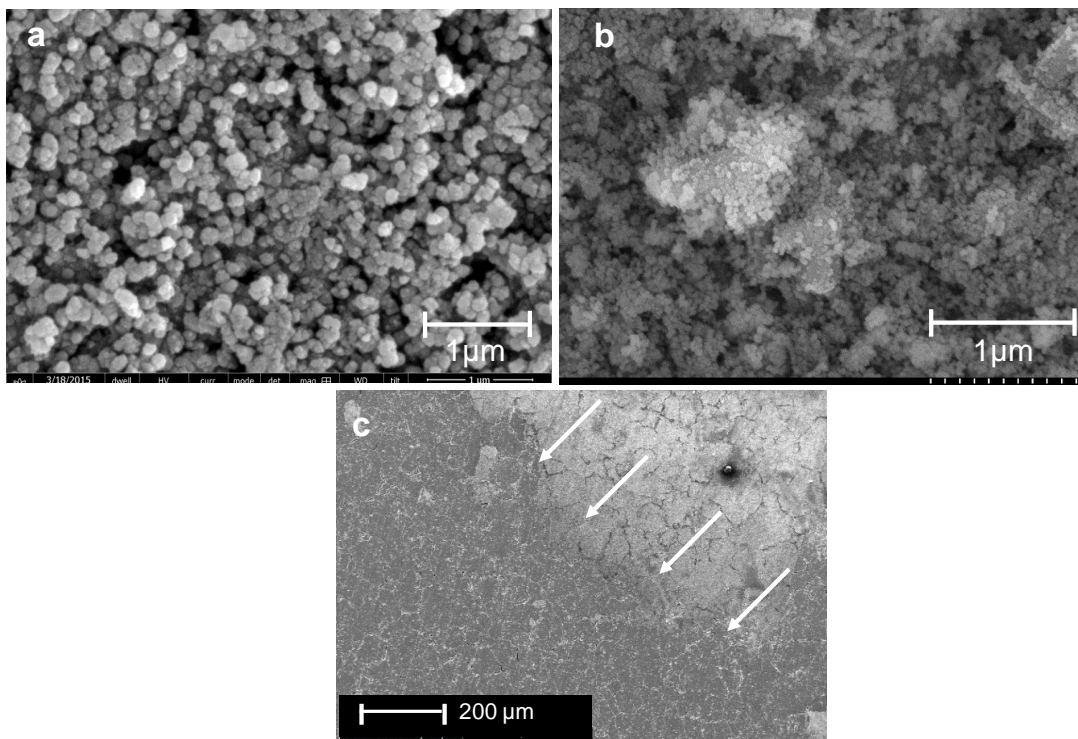


Fig. 7.5: SEM micrographs of the ZrO_2 coated samples (a) ZPOO, (b) 2ZPOO and (c) 3ZPOO

XPS survey spectra (wide scan) of the pre-oxidized SS specimen POO-21, ZPOO and the 2ZPOO samples are shown in Fig. 7.6. No substrate signal has been observed for both ZPOO and 2ZPOO sample that support the SEM observation (Fig. 7.5a & c) where continuous ZrO_2 coatings was observed.

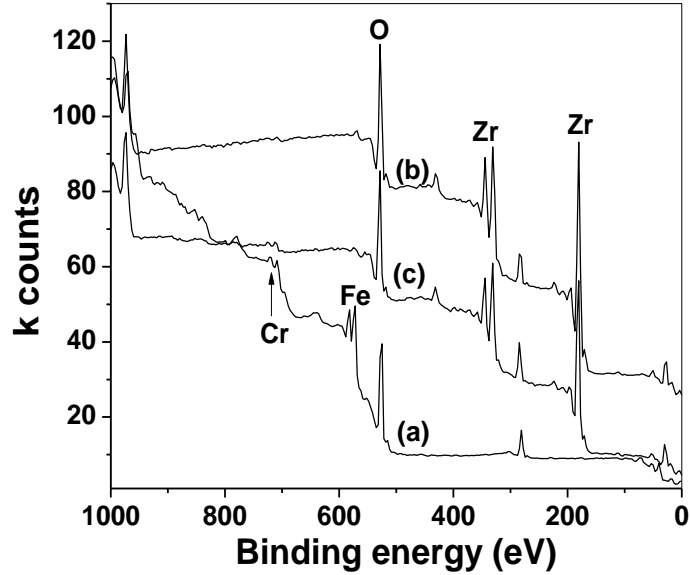


Fig. 7.6: Survey scan of the pre-oxidized and ZrO_2 coated SS samples (a) POO, (b) ZPOO and (c) 2ZPOO

7.2.2.2 Electrochemical Characterization

Fig. 7.7 shows the potentiodynamic polarization plots for the zirconia coated samples ZPOO and 2ZPOO at both ambient temperature and 90°C for comparison. Corresponding electrochemical parameters are presented in Table 7.1. The I_{corr} value for the 2ZPOO sample is approximately double compare to ZPOO samples for both room temperature and 90°C polarization measurements (Table 7.1). The cathodic and anodic current densities also rise by increasing the precursor concentration. Polarization measurements (Fig. 7.7A) show the disturbance of the film at room temperature in the anodic region of both ZPOO and 2ZPOO due to the effect of porosity. It can be concluded that corrosion resistance of ZrO_2 coated SS could not be improved by increasing the precursor concentration. It leads to more porous and non-adherent ZrO_2 films. An alternate approach of multiple rounds of ZrO_2 deposition with the same Zr-precursor concentration is attempted.

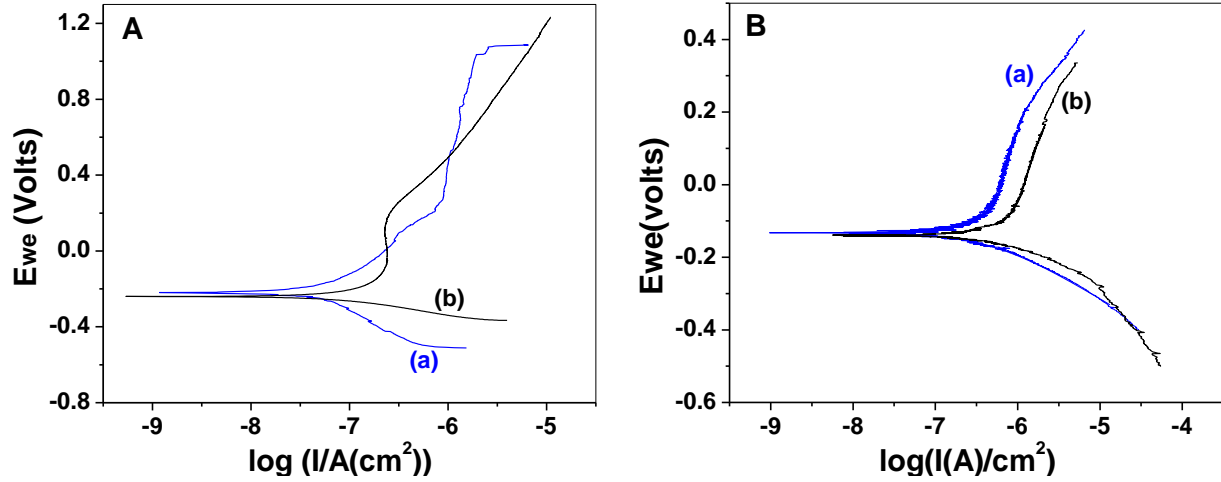


Fig. 7.7: A. Potentiodynamic polarization plots of ZrO_2 coated SS samples at 25°C (a) ZPOO and (b) 2ZPOO, B. Potentiodynamic polarization plots of ZrO_2 coated SS samples at 90°C (a) ZPOO and (b) 2ZPOO

Table 7.1: Average value of polarization parameters for the ZrO_2 coated 304L SS samples in 0.1 M sodium sulphate

Sample Name	Temperature (°C)	E_{corr} (mV)	I_{corr} ($\mu A/cm^2$)	β_a (mV/decade)	β_c (mV/decade)
ZPOH	R.T.	-125.61	0.394	177.0	249.0
2ZPOH	R.T.	-197.13	0.398	333.7	53.8
ZPOH	90°C	-215.07	1.338	-	118.9
2ZPOH	90°C	-189.21	1.519	-	155.1
ZPOO	R.T.	-219.55	0.046	280.8	308.5
2ZPOO	R.T.	-39.71	0.096	411.4	75.2
ZPOO	90°C	-133.97	0.372	615.7	134.7
2ZPOO	90°C	-139.64	0.727	481.1	160.8

Table 7.2: Parameters of electrical equivalent circuits for ZrO₂ coated 304L SS samples in 0.1 M sodium sulphate

<i>Sample</i>	<i>Temperature (°C)</i>	R_s ($\Omega \text{ cm}^2$)	Q_2 ($\mu\text{F cm}^{-2} \text{ s}^{n-1}$)	n_2	R_2 ($k\Omega \text{ cm}^2$)	Q_{dl} ($\mu\text{F cm}^{-2} \text{ s}^{n-1}$)	n_{dl}	R_{ct} ($k\Omega \text{ cm}^2$)
ZPOH	25°C	2	107.2	0.5	29	252.8	0.78	345
2ZPOH	25°C	2	145.4	0.45	113	337.2	0.9	403.5
ZPOH	90°C	8	1418	0.4	25	901.5	0.95	75
2ZPOH	90°C	8	1300	0.4	19	1038	0.99	70

7.3 Improvement of ZrO₂ coating thickness by multiple rounds of ZrO₂ deposition

Attempt was made to increase the ZrO₂ coating thickness by the repetition of hydrothermal deposition process several times using fresh reactants. The concentration of the Zr-precursor is kept 3.33 mM every time [4]. The pre-oxidized SS specimen POO-21 is used for this study. After the 2nd, 3rd and 4th rounds of ZrO₂ deposition, samples are designated as POO2Z, POO3Z and POO4Z respectively.

7.3.1 Surface characterization of Zirconia coated samples

The SEM images of the zirconia coated samples prepared by multiple deposition rounds (2-4 rounds) are shown in Fig. 7.8. The zirconia coatings seem to be thick and pore free. After every round of zirconia deposition, Zr counts in EDS measurement increased significantly. For the 2nd, 3rd and 4th round of zirconia coating, EDS analyses show the presence of 20-51 wt%, 37-65 wt% and ~69 wt% of Zr respectively. The first round zirconia deposition results is continuous but porous coating with pores of size 50-400 nm (Fig. 7.5a). During the second round of zirconia deposition, the newly formed ZrO₂ nanoparticles cover these pores. So, the porosity of ZrO₂ coatings is reduced after the 2nd round of ZrO₂ deposition.

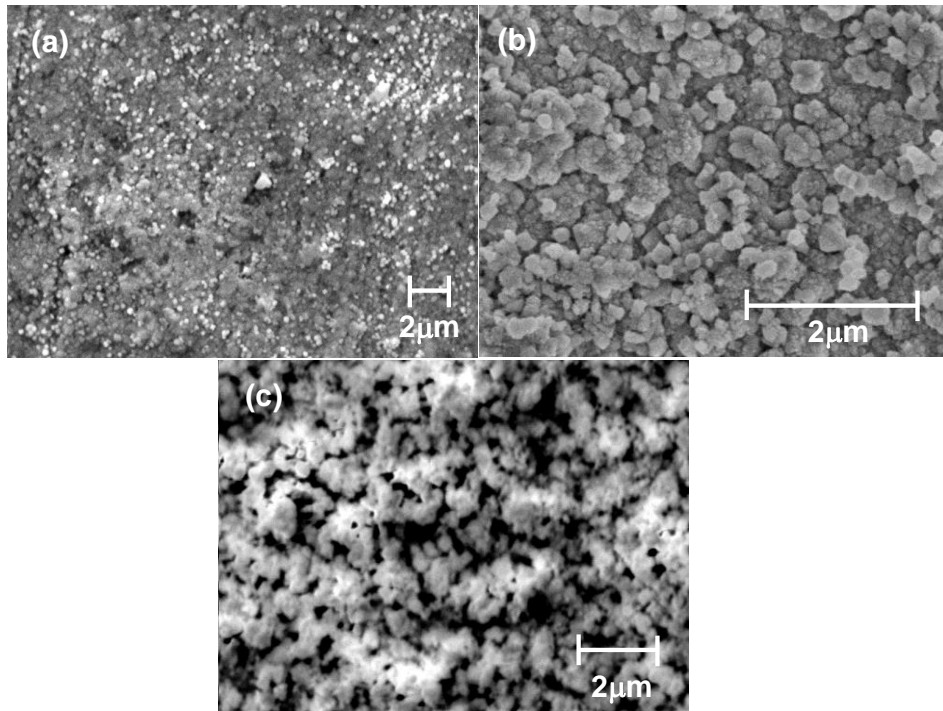


Fig. 7.8: SEM images of several rounds of ZrO_2 coated SS samples; (a) POO2Z: second, (b) POO3Z: third and (c) POO4Z: fourth round

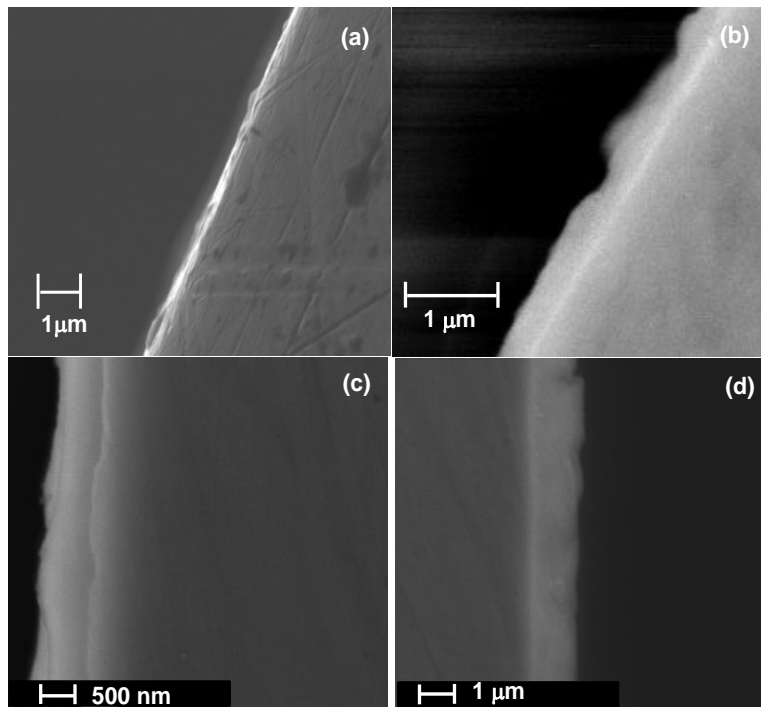


Fig. 7.9: Cross-sectional images of several rounds of ZrO_2 coated SS samples (a) ZPOO, (b) POO2Z, (c) POO3Z and (d) POO4Z

The high Zr counts in EDS supports the compact zirconia coating for multiple rounds deposited samples. The thickness of zirconia coatings are measured by cross-sectional SEM analysis after every round of zirconia deposition. The cross-sectional SEM images of all the rounds of ZrO₂ deposited samples are shown in Fig. 7.9. The thickness of ZrO₂ coating after the 1st, 2nd, 3rd and 4th round of ZrO₂ deposition are ~200 nm, 300-550 nm, 750 nm-1.1 μm and 0.9-1.2 μm respectively.

Raman spectra of the multiple round ZrO₂ coated samples with respect to 1st round of ZrO₂ coated sample are shown in Fig. 7.10. Raman spectra of zirconia coated samples show that intensity of substrate signals is reduced systematically with every round of ZrO₂ deposition. After the 3rd and 4th round of zirconia coating, substrate signals disappeared completely indicating the formation of thicker ZrO₂ coating in these samples (Fig. 7.10d & 4e).

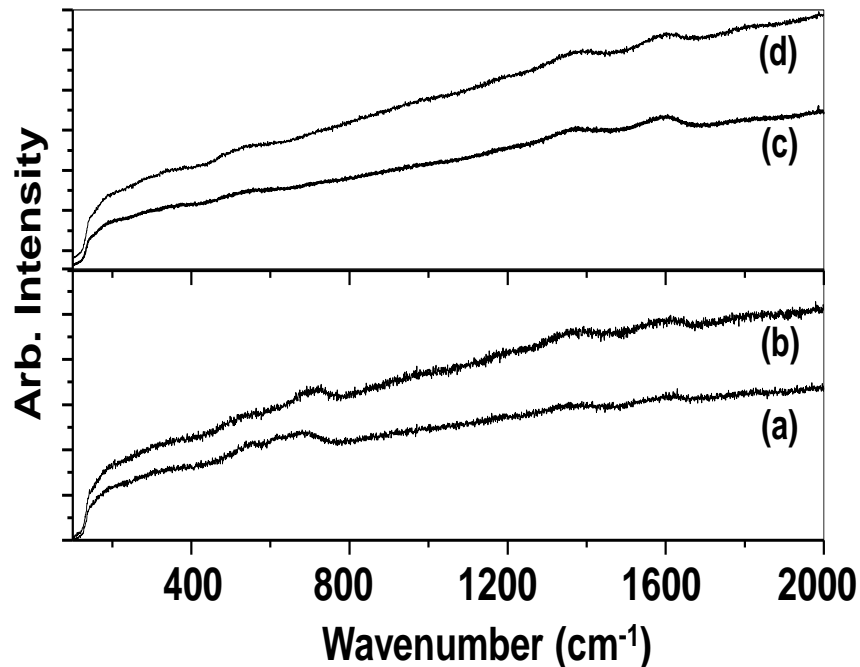


Fig. 7.10: Raman spectra of the several rounds of ZrO₂ coated SS samples; (a) ZPOO (b) POO2Z, (c) POO3Z and (d) POO4Z

7.3.2 Electrochemical studies

7.3.2.1 Potentiodynamic polarization test

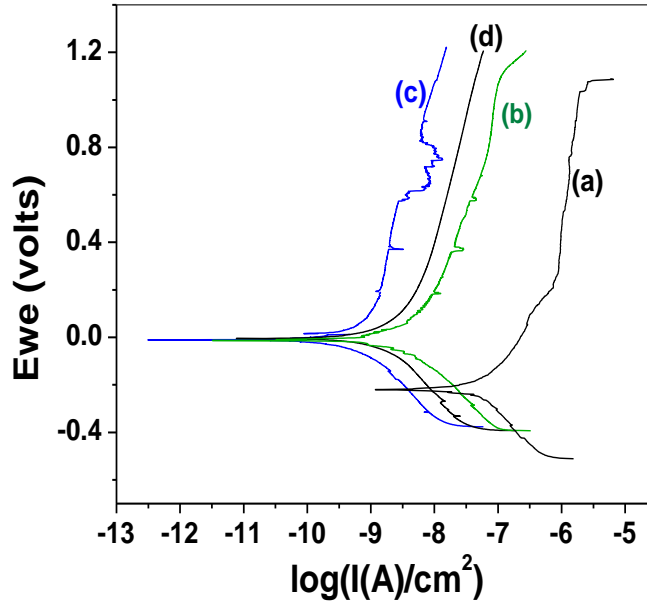


Fig. 7.11: Potentiodynamic polarization plot of several rounds of ZrO_2 coated SS samples (a) ZPOO (b) POO2Z, (c) POO3Z and (d) POO4Z

Potentiodynamic current-potential plots for multiple rounds of ZrO_2 coated samples with respect to 1st round of ZrO_2 coated sample are recorded in sodium sulfate solution to examine the corrosion resistance behavior of different thicknesses of ZrO_2 coated samples (Fig. 7.11). The corresponding electrochemical parameters are presented in Table 7.3. The 2nd round of zirconia coated samples show a remarkable decrease in I_{corr} values compared to first round of zirconia deposited sample (Fig. 7.11a & b). After the second round of zirconia deposition, I_{corr} value reduced from $4.63 \times 10^{-8} A$ to $2.16 \times 10^{-9} A$ (> 20 times). After the third round of zirconia deposition, I_{corr} value got further reduced to $5.25 \times 10^{-10} A$. Stable anodic current densities of the second and third rounds of zirconia deposited samples confirm that the coatings are non-porous. After the fourth round of zirconia coating, I_{corr} value ($1.495 \times 10^{-9} A$) increased compared to third

round zirconia coated sample. Both cathodic and anodic current densities of the fourth round zirconia deposited sample are higher compared to that in third round zirconia deposited sample. This implies that after the fourth round of zirconia deposition, although coating thickness increased, corrosion resistance deteriorated instead of improving it.

Table 7.3: Average value of polarization parameters for the multiple rounds ZrO₂ coated 304L SS samples in 0.1 M sodium sulphate

<i>Sample Name</i>	<i>E_{corr}</i> (mV)	<i>I_{corr}</i> (μA/cm ²)	<i>β_a</i> (mV)/decade	<i>β_c</i> (mV)/decade
ZPOO	-219.55	0.046	280.8	308.5
POO2Z	-13.68	2.161*10 ⁻³	275.7	203.3
POO3Z	-10.61	5.25*10 ⁻⁴	441.6	235.3
POO4Z	-5.00	1.495*10 ⁻³	377.6	269.5

7.3.2.2 EIS studies

The EIS technique has been used to evaluate the barrier layer properties and structural defects of the ZrO₂ films on SS surfaces. The structural defects in ceramics, especially in zirconia-based materials have been studied by EIS by many researchers [5-11]. Fig. 7.12 shows the Nyquist plots (Real vs. Imaginary impedance spectra) for the 1st, 2nd, 3rd and 4th rounds of ZrO₂ deposited samples. The enlarged view of the 2nd, 3rd and 4th rounds of ZrO₂ deposited samples is shown in Fig. 7.13. The corresponding equivalent circuits are presented in Fig. 7.14 and electrochemical impedance parameters obtained after fitting are presented in Table 7.4.

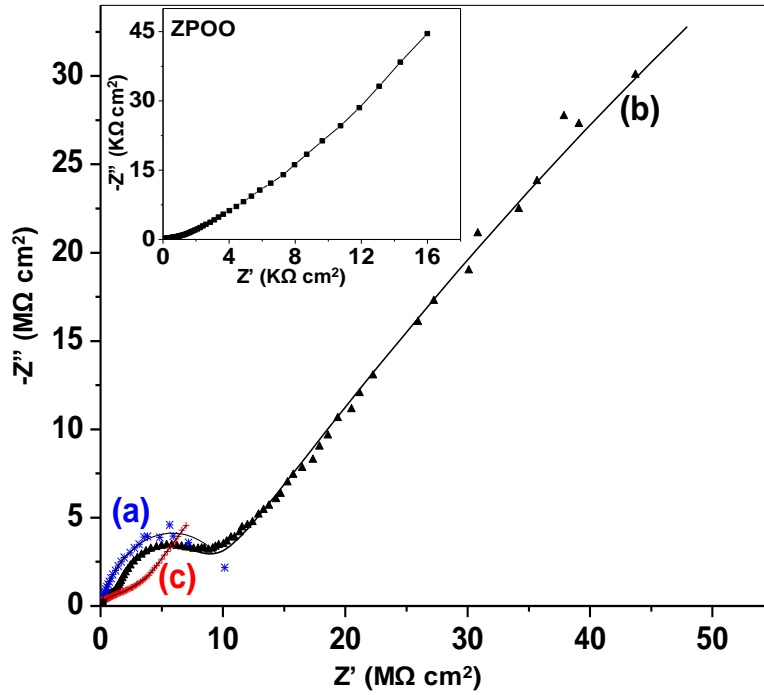


Fig. 7.12: Nyquist plots of the several rounds of ZrO_2 coated samples (a) POO2Z, (b) POO3Z and (c) POO4Z; the inset of figure shows the Nyquist plot for first round of ZrO_2 deposited sample

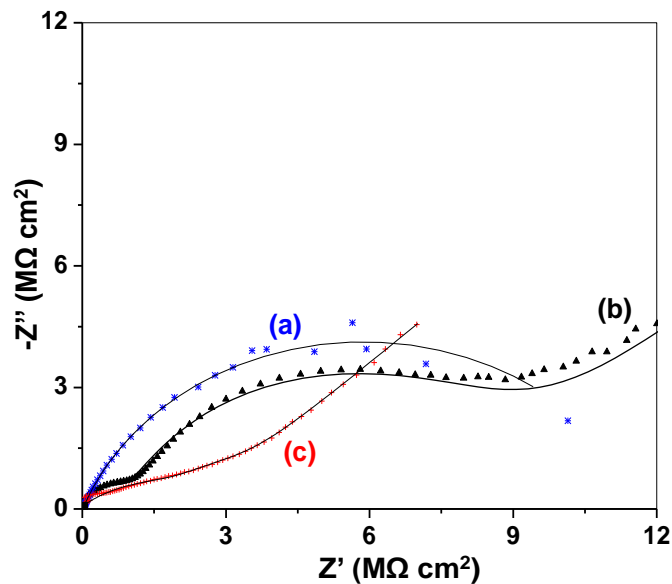


Fig. 7.13: Enlarged view of the several rounds of ZrO_2 deposited samples (a) POO2Z, (b) POO3Z and (c) POO4Z; markers represent the experimental data whereas solid lines represent the fitted spectrum

Table 7.4: Parameters of electrical equivalent circuits for ZrO₂ coated samples

Sample	R_s (Ω)	C_2 ($\mu F cm^{-2}$)	R_2 ($k\Omega cm^2$)	Q_3 ($\mu F cm^{-2} s^{n-1}$)	n_3	R_3 ($k\Omega cm^2$)	Q_4 ($\mu F cm^{-2} s^{n-1}$)	n_4	R_4 ($k\Omega cm^2$)
ZPOO	2	-	-	170	0.43	45	400	0.95	368
POO2Z	2	-	-	$9.67*10^{-3}$	0.92	9.5	0.284	0.78	$1.17*10^4$
POO3Z	5	$29.8*10^{-6}$	733.2	$1.65*10^{-3}$	0.8	7250	0.067	0.5	$4*10^5$
POO4Z	10	1.46	310.4	$66.4*10^{-3}$	0.49	2472	0.664	0.52	$2.1*10^5$

Very high resistance values for the 2nd, 3rd and 4th rounds of ZrO₂ deposited samples indicate the barrier like characteristics of ZrO₂ coatings. The thick, compact coating and insulating nature of ZrO₂ results it to behave like a resistor and this behavior is also observed by Zhang et. al. [12]. After the 2nd round of ZrO₂ deposition, capacitance of ZrO₂ coating decreases as porosity of ZrO₂ coating reduces (Table 7.4). Impedance spectra of POO2Z sample is dictated by intergranular component unlike the impedance behavior dominated by pores in ZPOO sample. The intergranular component become dominant as the ZrO₂ coatings is thick and constituted of nano-sized grains of ZrO₂. The impedance spectrum of the POO2Z sample is fitted with two time constants in series with solution resistance (R_s). The values obtained for first time constant (Q_3R_3) is associated with the grain boundaries while the second time constant (Q_4R_4) values reveal the coating capacitance and charge transfer resistance. The capacitance value ($1.65*10^{-3}\mu F cm^{-2}s^{n-1}$) supports that time constant Q_3R_3 is representing the grain boundary capacitance and grain boundary resistance [13]. The grain and grain boundary behaviors cannot

be analyzed separately for the 2nd round of ZrO₂ deposited sample (POO2Z) because of overlapping in the impedance spectrum. The grain and grain boundary behavior can be distinguished separately while fitting the EIS spectrum of POO3Z. Its equivalent circuit is shown in Fig. 7.14; first time constant C₂R₂ represents the grain, second time constant Q₃R₃ represents the grain boundary and third time constant Q₄R₄ represents the coating capacitance and charge transfer resistance.

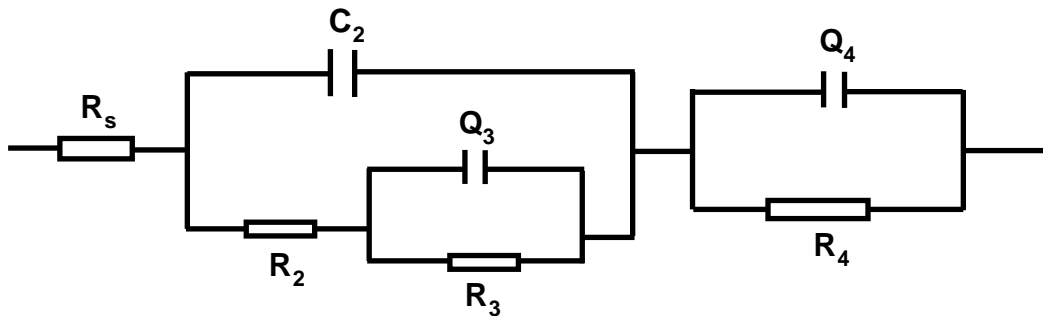


Fig. 7.14: Equivalent circuit used for fitting the electrochemical data of POO3Z

For the better understanding, Bode-phase and Bode-mod plot for the 3rd round ZrO₂ deposited sample are shown in Fig. 7.15. The impedance values ($\sim 10^8 \Omega\text{cm}^2$) from the Bode-mod plot (Fig. 7.15a) are in agreement with the high impedance values obtained from fitting of equivalent electrical circuits. It further confirms the highly insulating behavior shown by ZrO₂ coatings. The electrical properties of ZrO₂ coatings are closely associated with the nano structure and intergranular component which is largely dependent on coating thickness. The EIS spectra for POO4Z sample is also fitted with three time constants but in series. The high value of capacitance ($1.46 \mu\text{F cm}^{-2}$) for the first time constant (C₂R₂) reveals that it represents the coating defects rather than the grains of ZrO₂ coating. The capacitance values (Q₃) of 2nd, 3rd and 4th round of ZrO₂ deposited samples (10^{-8} - 10^{-9} Farads) confirms that the time constant R₃Q₃ is associated with grain boundary [13]. Both grain boundary and the charge transfer resistance

reduced by 2-3 times for the POO4Z compare to POO3Z sample. It is attributed to the generation of coating defects after a certain thickness. It appears that the grain size increases along with increase of stress between the zirconia coating and the substrate that lead to generation of defects in the zirconia coatings. Due to the strain between zirconia coating and the substrate, corrosion resistance properties of the zirconia film also are affected.

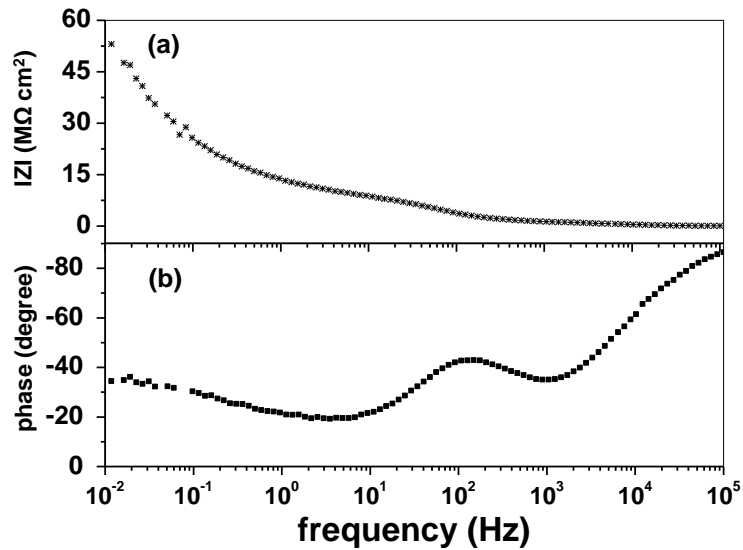


Fig. 7.15: Bode plot of ZrO₂ coated sample POO3Z (a) Bode-plot (|Z| vs frequency) (b) Bode-phase plot (phase angle vs frequency)

7.4 Mechanism of film thickening by hydrothermal method

In order to increase the thickness of ZrO₂ coatings on pre-oxidized SS specimens for corrosion protection applications, two methods have been proposed and discussed. The increase in concentration of reactants did not result in increase of thickness of ZrO₂ coatings. After the deposition experiment, precipitation was observed at the bottom of the autoclave. It appears that the ZrO₂ particles could not remain suspended in aqueous solution of the autoclave at high concentration and tend to precipitate. So, the nucleation of zirconia deposition on the pre-oxidized surface is low and result in thin and porous coatings in 2ZPOH/ 2ZPOO samples.

Repetition of ZrO_2 deposition process using 3.33 mM of $\text{ZrO}(\text{NO}_3)_2 \cdot 6\text{H}_2\text{O}$ is the suitable method for improving the thickness of ZrO_2 coatings by hydrothermal method. As discussed in the chapter 5 and chapter 6, hydrothermal process follows nucleation and island formation for the growth of ZrO_2 coating. The 1st round of ZrO_2 deposition results in ~200 nm porous coating of tetragonal nano- ZrO_2 particles. During the 2nd round of ZrO_2 deposition, ZrO_2 nanoparticles cover the pores formed in the 1st round of zirconia deposited sample and result in dense and non-porous coating. During the 2nd round, ZrO_2 crystals grow and coalesce to form a thick coating of 300-550 nm. The formation of grain boundaries is enhanced at this stage as the crystals coalesce and the energy associated with the growth of crystallites is balanced by the elimination of the surface. During the 3rd round of ZrO_2 deposition, ZrO_2 crystallites further grow to form a thicker coating (750-1100 nm). The preferential attachment of atoms at the grain boundaries result in nucleation of a new rows of particles at grain boundaries [14]. The higher mobility of ZrO_2 nanoparticles for the thicker coatings and diffusion of nano-particles into the grain boundaries favors the grain coarsening along with hardening of grain boundaries [14]. The hardening of grain boundaries for thick coatings has been already discussed in chapter 6. During the 4th round of ZrO_2 deposition, ZrO_2 crystallites further grow to a coating thickness of 900-1200 nm. The grain coarsening continues and the fraction of grain boundaries is reduced at the surface as observed by EIS.

The corrosion resistance behavior of nano- ZrO_2 coatings improves significantly with the increase in ZrO_2 coating thickness and becomes saturated at around 750-1000 nm thickness (3rd round of ZrO_2 deposition). The presence of nanoparticles mechanically strengthens the film and provides longer diffusion paths to the corrosive electrolyte, leading to improved barrier property of the coatings. The total resistance offered by 3rd round zirconia deposited sample is the highest

followed by 4th and 2nd round of ZrO₂ deposited samples (Table 7.3). This behavior is supported by the potentiodynamic polarization tests. It means after the third layer of zirconia deposition, further zirconia coating treatment although lead to increase in thickness but it result in decrease of corrosion resistance properties. The total resistance offered by 3rd round of zirconia deposited sample is >7000 times compared to plain SS specimen.

It appears that coating develops some strain with the substrate when the thickness exceeds the certain range. Hence, a reduction in corrosion protection ability is observed after a certain thickness that is around 1000 nm in the present case. It can be concluded that the optimum thickness for zirconia coating for corrosion protection applications is around 1000 nm. Repetition of hydrothermal ZrO₂ deposition process is suitable method for improving the thickness of ZrO₂ coatings by hydrothermal method. Continuous supply of 3.33 mM concentration of zirconia precursor material in a dynamic loop with continuous thickness monitoring device for longer duration will lead to a coating with controlled thickness.

7.5 Conclusions

ZrO₂ films of different thicknesses have been deposited on pre-oxidized stainless steel specimens by hydrothermal method. Thick and compact ZrO₂ films on SS can be achieved by multiple round of deposition using 3.33 mM of ZrO(NO₃)₂.6H₂O by hydrothermal process. The corrosion resistance of zirconia coated SS samples increases with the increase in ZrO₂ coating thickness and the total resistance of ZrO₂ coated samples increases by 5000-7000 times compared to uncoated SS samples when coating thickness is around 1000 nm. The corrosion performance decreased when the coating thickness is above ~1000 nm. It is assumed that coating thickness above 1000 nm results in coating defects due to lattice strain and causes the deterioration of corrosion resistance behavior [15].

7.6 References

- [1] N. Garg, V.K Mittal, S. Bera, P. Chandramohan, C.R. Das, S. Velmurugan, *Thin Solid Films* 545 (2013) 222-228.
- [2] N. Garg, S. Bera, G. Mangamma, V.K. Mittal, R. Krishnan, S. Velmurugan, *Surf. Coat. Technol.* 258 (2014) 597–604.
- [3] R.A. Antunes, M.C.L. de Oliveira, M. F. Pillis, *Int. J. Electrochem. Sci.* 8 (2013) 1487- 1500.
- [4] N. Garg, S. Bera, V.S. Tripathi, V. Karki, S. Velmurugan, *Symposium on Water Chemistry and Corrosion in Nuclear Power Plants in Asia – 2015*, Paper No. AWC-183.
- [5] S. Lanferdi, A.C.M. Rodrigues, *J. Appl. Phys.* 86 (1999) 2215-2219.
- [6] M.C. Steil, F. Thevenot, M. Kleitz, *J. Electrochem. Soc.* 144 (1997) 390-398.
- [7] M. Keitz, L. Dessemond, M.C. Steil, *SolidState Ionics* 75 (1995) 107-115.
- [8] L. Dessemond, R. Muccillo, M. Henault, M. Kleitz, *Appl. Phys.* A57 (1993) 57-60.
- [9] R. Muccillo, E.N.S. Muccillo, N.H. Saito, *Mater. Lett.* 34 (1998) 128-132.
- [10] E.N.S. Muccillo, M. Kleitz, *J. Euro. Ceram. Soc.* 16 (1996) 453-465.
- [11] W.J. McCarter, S. Garvin, N. Bouzid, *J. Mater. Sci. Lett.* 7 (1988) 1056-1057.
- [12] Z. Dan-hua, G. Hong-bo, G. Sheng-kai, *Trans. Nonferrous Met. Soc. China* 21(2011) 1061–1067.
- [13] J.G. Fletcher, A.R. West, J.T.S. Irvine, *J. Electrochem. Soc.* 142 (1995) 2650-2654.
- [14] W.D. Nix, B.M. Clemens, *J. Mater. Res.* 14 (1999) J. Mater. Res. 3467-3473.
- [15] Y. Liu, Jiamu Huang, J.B. Claypool, C. E. Castano, M. J. O’Keefe, *Appl. Surf. Sci.* 355 (2015) 805–813.

Chapter 8
Conclusions

8.1 Conclusion

The present work describes the development of a simple hydrothermal deposition method for growing ZrO_2 coatings on pre-oxidized stainless steel (SS) substrates. The oxide layers on type 304L SS surfaces were developed by high temperature oxidation under different water chemistry conditions and pulsed laser deposition (PLD) technique. The pre-oxidation of SS specimens under high temperature reducing water chemistry conditions leads to the development of SS oxides constituted of various non-stoichiometric spinel oxides like $Ni_xFe_{3-x}O_4$. The mixture of spinel oxides and rhombohedral oxides like $\alpha-(Fe,Cr)_2O_3$ developed on the SS specimens surface when it is treated at high temperature under normal water chemistry conditions. The SS oxide surface prepared by PL deposition of $\alpha-Fe_2O_3$ shows the deposition of stoichiometric, spherical and small size $\alpha-Fe_2O_3$ particles on the SS surface. ZrO_2 coatings were developed on these pre-oxidized SS by hydrothermal methods either by using nano- ZrO_2 powder or by using solution of $ZrO(NO_3)_2 \cdot 6H_2O$ and Na-EDTA at high temperature.

In the first method, nanocrystalline zirconia powder was produced by precipitation from the reaction of $ZrO(NO_3)_2 \cdot 6H_2O$ with NH_4OH followed by drying and calcination. The use of $ZrO(NO_3)_2 \cdot 6H_2O$ as Zr-precursor results in the formation of tetragonal dominant nanocrystalline ZrO_2 powder. Narrow size distribution of ZrO_2 nanoparticles was obtained by using PEG-8000 as dispersant. The adsorption of nano- ZrO_2 particles on SS surface oxides take place due to the electrostatic interaction between ZrO_2 particles and SS surface oxides in aqueous medium. The coatings prepared are not continuous and ZrO_2 islands were seen distributed unevenly on the pre-oxidized surfaces.

Continuous, thick and tetragonal ZrO_2 coatings were developed on SS oxide composed of $\alpha-Fe_2O_3$ by the hydrothermal deposition in autoclave using $ZrO(NO_3)_2 \cdot 6H_2O$ with Na-EDTA.

Na-salt of Zr-EDTA produced in the aqueous solution combines with the positively charged hydroxylated α -Fe₂O₃ surface through Fe-O-Zr bond formation. At high temperature (>170°C), EDTA loses its complexing ability and Zr deposited on α -Fe₂O₃ surface gets hydrolyzed to form a strong interface bond with the α -Fe₂O₃ surface. Nucleated nano-ZrO₂ particles grow in the form of islands on the α -Fe₂O₃ surface and these islands grow and coalesce to form the thick and uniform coating.

The hydrothermal deposition of ZrO₂ coatings is carried out on different oxide layers on stainless steel surfaces composed of spinel oxides or mixed α -(Fe,Cr)₂O₃ and spinel oxides or pure α -Fe₂O₃. The pre-oxidized layer composed of spinel oxides or mixed α -(Fe,Cr)₂O₃ and spinel oxides results in thinner ZrO₂ coatings compared to pre-oxidized layer composed of pure α -Fe₂O₃. Though the interaction between spinel oxides and suspended nano-ZrO₂ particles is electrostatically favorable, but the lattice mismatch between spinel oxides and tetragonal ZrO₂ do not favor the nucleation of ZrO₂ particles over the spinel oxides. The inability of the spinel oxides for the formation of suitable interface compounds limits the growth of ZrO₂ islands and coating developed on spinel oxides is thin and porous.

Higher miscibility of ZrO₂ with α -Fe₂O₃ results in formation of metastable Fe₂O₃-ZrO₂ interfacial compounds. The metastable interfacial compound t-(Fe,Zr)O₂ provides the adhesion as well as suitable surface crystallography for the growth of tetragonal ZrO₂. Small size and hills/valley type morphology of the PL deposited α -Fe₂O₃ surface leads to efficient inclusion of Zr-precursor into the substrate surface and improves the adhesion. This is due to larger surface area of interaction of Zr-precursor with the pre-oxidized surface. The chemical composition and morphology of the substrate surface largely influence the adherence, thickness, continuity and porosity of ZrO₂ coatings deposited. The study of qualitative nano-mechanical properties by

scanning probe microscopy reveal that the ZrO₂ coatings developed on small size α -Fe₂O₃ particles show the highest hardness along with hardening of grain boundaries. The limited island growth of ZrO₂ nanoparticles lead to lower hardness of ZrO₂ coatings when the deposition is carried out on the spinel oxides.

It is important to improve the thickness of the ZrO₂ coatings to improve the coating quality and corrosion resistance properties of SS. Multiple rounds of hydrothermal deposition of ZrO₂ using 3.33 mM precursor concentration every time found to be a suitable method for improving the thickness of ZrO₂ coatings. The porosity of ZrO₂ coatings reduce drastically after the 2nd round of zirconia deposition itself. The thickness of ZrO₂ coatings increase systematically with every round of ZrO₂ deposition. The coating thickness is increased from ~200 nm to ~1.2 μ m from the 1st to 4th round of ZrO₂ deposition.

Electrochemical properties of the ZrO₂ coatings developed on different pre-oxidized SS surfaces are studied and all the pre-oxidized SS specimens show the significant improvement in their corrosion resistance behavior after the ZrO₂ coating. The corrosion current density (I_{corr}) values reduced drastically and charge transfer resistance (R_{ct}) values increased significantly after the ZrO₂ coatings. Thin and porous ZrO₂ coating on the spinel oxides is also able to improve the corrosion resistance of SS specimens. The diffusion of electrolyte is observed during the electrochemical measurements for the porous zirconia coatings developed on SS oxides composed of spinel oxides or mixed rhombohedral and spinel oxides. Thick, compact, insulating and barrier like ZrO₂ coating on the α -Fe₂O₃ surface show the best electrochemical properties in terms of highest charge transfer resistance.

The multiple rounds of ZrO₂ deposited samples (thickness ~200 nm to ~1.2 μ m) were analyzed by PDP tests and EIS analysis for optimizing the ZrO₂ coating thickness for corrosion

protection applications. The impedance behavior of thick coatings is significantly influenced by the intergranular component as ZrO_2 coatings are composed of ultra-fine particles. The corrosion resistance behavior of ZrO_2 coatings improves with the increase in coating thickness till the thickness of $\sim 1 \mu m$. It is assumed that defects are generated after a certain coating thickness due to the development of lattice strain in the coatings.

8.2 Future Directions

1. The PL deposited nano-sized $\alpha-Fe_2O_3$ particles resulted in thick, compact and adherent ZrO_2 coatings. Efforts should be made to grow SS oxides composed of mainly nano size $\alpha-Fe_2O_3$ on the SS surface by hydrothermal method.
2. The study of stabilized ZrO_2 coatings like yttria stabilized zirconia and magnesia stabilized zirconia is necessary to attain the maximum corrosion protection and desirable mechanical properties for nuclear reactor applications. Mechanical properties of already developed ZrO_2 coatings and stabilized ZrO_2 coatings should be studied in detail.
3. The high temperature performance of zirconia coatings should be studied for nuclear power plant applications. Although the ZrO_2 coatings performed satisfactorily during adhesion testing and electrochemical measurements at R.T. and $90^\circ C$ but it is mandatory to do the high temperature electrochemical measurements to accommodate the high temperature effects like ionic conductivity of ZrO_2 and decrease in adhesion of ZrO_2 coatings (if any) with the substrate surface. The high temperature measurements of I_{corr} and slow strain rate tests should be carried out for the ZrO_2 coated samples to confirm their applicability.